Superconducting Pb(_1-x)Eu(_x)Mo(_6)S(_8) measured between 300 mK and T(_c) in high magnetic fields, using a new field-gradient torque magnetometer

Morley, Nicola Ann

Superconducting $Pb_{1-x}Eu_xMo_6S_8$ measured between 300 mK and T_c in high magnetic fields, using a new field-gradient torque magnetometer

Nicola Ann Morley

A thesis in partial fulfilment of the requirements for the degree of Doctor of Philosophy

Department of Physics, University of Durham

2003

Superconducting $Pb_{1-x}Eu_xMo_6S_8$ measured between 300 mK and T_c in high magnetic fields, using a field-gradient torque magnetometer

Nicola Ann Morley

Abstract

A field-gradient torque magnetometer has been designed and constructed which measures the magnetic moment of isotropic superconductors using a Quantum Design torque chip. The magnetometer fits onto the base of an Oxford Instruments Heliox probe; thus the temperature range is 300 mK to 20 K, in magnetic fields up to 15 T. The superconductors measured on the torque magnetometer in vacuum were NbTi wire, $PbMo_6S_8$, and $Pb_{0.75}Eu_{0.25}Mo_6S_8$ as a function of magnetic field, magnetic field-gradient and temperature. The utility of the torque magnetometer was demonstrated by determining the critical current density $\left(J_c\right)$ and the upper critical field $\left(B_{c2}(0)\right)$ of the samples. These superconducting properties were compared with the vibrating sample magnetometer (VSM) values, for the same samples.

The change in the superconducting parameters and properties of $Pb_{1-x}Eu_xMo_6S_8$, for x = 0.0 & 0.25 were investigated. The samples were fabricated using two different heat treatment methods, which finished with hot isostatic pressing (HIP'ing) at 2000 bar and 800 °C for 8 hours. To characterise the superconductors, ac resistivity, ac susceptibility, specific heat and magnetic measurements were carried out, as a function of magnetic field and temperature. From the magnetisation data, the GL parameter (κ) and the Sommerfeld constant (γ) were determined for the magnetic superconductor x = 0.25. For both samples, κ was determined in the temperature range 6 K to T_c, from the magnetisation data. For x = 0.0 & 0.25, the critical temperature $\left(T_c\right)$, the upper critical field $\left(B_{c2}(0)\right)$, the critical current density $\left(J_c\right)$ and the irreversibility fields $\left(B_{irr}\right)$ were determined from the experimental data.

Declaration and Copyright

I hereby declare that the work contained within this thesis is my own original work and nothing that is result of collaboration unless stated. No part of this thesis has been submitted for a degree or other qualification at this or any other university

N. A. Morley
May 2003

Acknowledgements

Throughout the course of this study many people have provided invaluable assistance and I would like to take this opportunity to express my gratitude.

First of all I would like to thank my supervisor Dr. Damian Hampshire, who has helped me through the PhD with great support and encouragement. Also the Engineering and Physical Sciences Research Council (EPSRC) for providing the financial support. I would also like to thank Prof. M R Pennington for use of the Department of Physics facilities.

Thanks also goes to the many members of the support staff of the Physics Department in Durham, including Phil Armstrong, Steve Lishman and the other members of the mechanical workshop, and to Mike Lee, Vicky Greener and Pauline Russell in Audio-Visual and to Norman Thompson, John Dobson and Paul Foley for providing technical support in the laboratories.

I would also like to thank St John's College for providing fellowship and support, especially the Principal Prof. Stephen Sykes, Dr. Chloe Starr, and the other residential tutors I have got to work with, Dr Scott Mason, Dr Thomas Hobel, Rachel Jepson, Matthew Eddy, Brad & Kori Embry and Archie Wright.

Special thanks go to Dr Tom Hase, Dr Lars Palsson, Dr Beth Hartland and Christine Carey, without whose support and encourage this work would not have been finished. Many thanks go to all the guys who I got to work with in the superconductivity group. These include Dr Simon Keys, Dr Nigel Leigh, and Dr Adrian Sneary, who were willing to show me the ropes, and more recently to David Taylor, George Carty, and Dr Hongjun Niu, for their support and discussions during my time of study. I also would like to thank Sean Giblin, James Buchanan, Dr Stuart Wilkins, Neil Parkinson, Paul Tulip and all the other physicists who have provided light relief from my work during coffee breaks.

I would like to thank all the people who have let me play sport with them, especially the Gradsoc Netball girls, and the boat club, to all those outside of physics who have provided friendship and relaxation during the last few years.

Of course to my Mum, Dad and Gran for their great support, motivation and love. Special thanks go to Ros, Cas, Deb and Kel for being great friends and putting up with a rather grumpy older sister for so long.

This thesis is dedicated to my Granddad, who was an inspiration in my life, and never got the chance to see its complication.

Variables

The following list contains the variables and constants, which occur in this thesis:

α_V – voltage calibration constant of the QD torque chip

α_R – resistance calibration constant of the QD torque chip

α_p – variable in the flux pinning scaling law

α_K – constant in the Kramer law

$\mathbb{A}$ – The magnetic potential vector

$\hat{\mathbb{A}}$ - Area in vector form

A – Area

a – radius of model sample

a(T) – parameter in the Ginsburg-Landau equation

$B_{c2}(T)$ - The upper critical field of a type II superconductor, at temperature T.

$B_{c1}(T)$ - The lower critical field of a type II superconductor, at temperature T.

$B_c(T)$ – The critical field for a type I superconductor, and the thermodynamic critical field for a type II superconductor, at temperature T.

B_{c3} – upper critical field at the superconductor-insulator boundary

B_{in} – The internal magnetic field within a superconductor.

B_{irr} – the irreversible magnetic field of a type II superconductor.

B_{loc} – magnetic field experienced by the sample when in a field gradient

B_{app} – external magnetic field

B^* - characteristic field from the Bean's model

B_J(y) – Brillouin function

b – the reduced magnetic field; the ratio of the applied magnetic field to the irreversible magnetic field.

b_{max} – the reduced field at which the peak in the normalised flux pinning force occurs

b(T) – parameter in the Ginsburg-Landau equation

$\frac{dB}{dz}$ - magnetic field gradient

$\frac{dB_{c2}}{dT}$ - change in the upper critical field with temperature

β_A – Abrikosov constant

C – Curie's constant

c – specific heat

Δc – discontinuity in the specific heat

d – position of the wavefunction

D – demagnetisation factor

$\Delta(T)$ – energy gap at temperature T

$\varnothing$ - diameter

e - electron charge

e* - effective electron charge

$\mathbf{E}$ – electric field strength

Φ_o - quantised magnetic flux

ϕ_o – one quanta of magnetic flux

ϕ - magnetic flux

F_p – the volume flux pinning force

F_{pmax} – the maximum volume flux pinning force

F_s – Helmholtz free energy in the superconducting state

F_n – Helmholtz free energy in the normal state

γ_{sf}- shape factor, used to determine the critical current density

γ_m – mass anisotropy ratio

γ - Sommerfeld constant

γ_{cp} - Sommerfeld constant determined from specific heat measurements

$\gamma_{\omega_{ln}}$ - Sommerfeld constant determined from the BSC equation, using the weighted phonon frequency

γ_{Δ} - Sommerfeld constant determined from the BSC equation, using the energy gap

g_J – Lande factor

G_s – Gibbs free energy in the superconducting state

G_n – Gibbs free energy in the normal state

H_{app} – the applied magnetic field strength

H_{loc} – local magnetic field

$H_{app\text{-}loc}$ – applied local magnetic field

H_c – thermodynamic critical field

H_{c1} – lower critical field

H_{c2} – upper critical field

$\frac{dH_{app}}{dz}$ - applied magnetic field gradient

$\frac{dH_{loc}}{dz}$ - local magnetic field gradient

h – the half the length of a cylindrical sample

$\hbar$ – reduced Planck's constant

I_{ex} – excitation current through the calibration loop of the QD chip

I - current

φ - angle between the normal to the QD chip platform and the applied magnetic field

J_c – The critical current density of a superconductor.

$J_{c||}$ - critical current density measured for the field parallel to the symmetry axis

$J_{c\perp}$ - critical current density measured for the field perpendicular to the symmetry axis

$\mathbf{J_s}$ – current density in a superconductor

J – critical current density

J_m – angular momentum

κ - the ratio between the Ginsburg-Landau penetration depth and the coherence length; also known as the GL parameter.

κ_1 - GL parameter determined from the upper critical field

κ_2 - GL parameter determined from the magnetisation

k – wavevector of an electron

k_b – Boltzman's contstant

λ_L – the London penetration depth.

λ_{GL} – the Ginsburg-landau penetration depth.

$\lambda(0)$ – penetration depth at 0 K

λ_χ - fraction of the susceptibility, used to determine the internal field of a paramagnetic material

l – the distance between the centre of the magnetic moment and the centre of the torque chip stage.

μ_o – permeability of free space

μ_B - Bohr magnetron

m – magnetic moment

Δm_{+-} - difference in magnetic moment across the torque magnetometry hysteresis loop

$\mathbb{m}_I$ - magnetic moment due to the excitation current around the calibration loop on the QD chip platform

m_z - magnetic moment in the z-direction

m_e – electron mass

m_e* - effective electron mass

$m_{a,b}$ – effective electron mass in the a,b plane

m_c – effective electron mass in the c-direction

M_i – ionic mass

M – magnetisation

M_+ - magnetisation measured for increasing magnetic field

M_- - magnetisation measured for decreasing magnetic field

M_{rev} – reversible magnetisation

M_{irr} – irreversible magnetisation

ΔM - difference in magnetisation across the hysteresis loop

N – the number of filaments within a wire.

N_M – the number density of magnetic ions within a sample.

N_o – density of electronic levels for a single spin population in the normal level

$\tilde{N}$ – demagnetisation tensor

$\bar{N}$ - demagnetisation constant

$N_{||}$ - demagnetisation constant parallel to the applied magnetic field

$N_{\perp}$ - demagnetisation constant perpendicular to the applied magnetic field

n – electron density in the superconductor

^{n} – temperature scaling variable of the flux pinning force scaling law

$\hat{\mathbb{n}}$ - unit vector perpendicular to the chips' platform

|| - parallel to

$\perp$ - perpendicular to

p – exponent in the flux pinning force scaling law

θ - angle between the samples' magnetic moment and the applied field

q – exponent in the flux pinning force scaling law

ρ - the density of a sample

ρ_N – normal resistivity of the superconductor

r – the radius of a cylindrical sample

ΔR_{+-} - difference in resistance across the ΔR hysteresis loop

σ - surface energy

S – entropy

$\hat{s}$ – unit vector parallel to the direction of the torque

τ - The torque applied by the superconducting magnetic moment in a magnetic field.

T_c – The critical temperature of a superconductor.

t – reduced temperature (T/T_c)

V – voltage

V_{ac} – applied ac-voltage of the Stanford lockin

ΔV - change in voltage across the QD chip's Wheatstone bridge

ΔV_{+-} - change in voltage across the ΔV hysteresis loop

vol – volume of a sample

V_o – electron-electron potential

w – the width of a rectangular sample

ω_D – Debye frequency

ω_{ln} - weighted phonon frequency

χ – susceptibility

χ' - ac lossless susceptibility

χ'' - ac loss susceptibility

χ_m – mass susceptibility

χ_{vol} – volume susceptibility

ψ - order parameter

ψ^* - complex conjugate of the order parameter

ψ_∞ - order parameter at infinity

ψ_H – angle between the symmetry axis of a sample and the applied magnetic field

Y – Young's modulus

ξ - coherence length

$\xi(0)$ – coherence length at 0 K

z – height from the sample to the magnet field centre for the torque magnetometer experiment

In this thesis superscripts are used to describe variables determined from different experiments.

$B_{c2}^{0.9\rho_N}(0)$ - upper critical field determined at 90 % of the normal resistivity

$B_{c2}^{0.5\rho_N}(T)$ - upper critical field determined at 50 % of the normal resistivity

$B_{c2}^{J_c=0}(T)$ - upper critical field determined when the transport J_c is zero

$B_{c2}^{M\to 0}(0)$ - upper critical field determined from the VSM magnetic moment data

$B_{irr}^{M\to 0}(T)$ - irreversibility field determined from the VSM magnetic moment data

$B_{irr}^{\tau}(T)$ - irreversibility field determined from the torque magnetometer data

J_c^{VSM} - critical current density determined from the VSM data

J_c^{τ} - critical current density determined from the torque magnetometer data

γ_{cp} - Sommerfeld constant determined from the specific heat data

$\gamma_{\omega_{\ln}}^{0.9\rho_N}$ - Sommerfeld constant determined from the weighted phonon BCS equation, using the resistivity data

$\gamma_{\omega_{\ln}}^{M\to 0}$ - Sommerfeld constant determined from the weighted phonon BCS equation, using the VSM data

$\gamma_{\Delta}^{0.9\rho_N}$ - Sommerfeld constant determined from the energy gap BCS equation using the resistivity data

$\gamma_{\Delta}^{M\to 0}$ - Sommerfeld constant determined from the energy gap BCS equation using the VSM data

Contents

Chapter 1

Introduction and Motivation

Superconductivity is an exciting and very interesting area of solid state physics. Superconductors are distinguished by two fundamental properties, and these are zero resistance and expelling all magnetic flux. One of the main commercial areas, they are used in is high-field magnets. These magnets are used in particle accelerators, magnetic resonance imaging (MRI) and the levitating trains (Maglev). At the moment superconductors such as NbTi and Nb_3Sn are used in these applications. They are limited by their upper critical field, which means the highest magnetic fields reached are 22 T. Thus as technology moves on, new superconductors are being researched in to with the aim of increasing the magnitude of the magnetic fields possible for a continuous superconducting magnet. These materials include the low temperature superconductors MgB_2, Nb_3Al and Chevrel phase superconductors, and the high temperature superconductors $YBa_2Cu_3O_7$ and $Bi_2Sr_2Ca_2Cu_3O_{10}$.

Chevrel phase materials are isotropic, polycrystalline, low temperature superconductors. $PbMo_6S_8$ has a critical temperature (T_c) of 15 K and an upper critical field ($B_{c2}(0)$) of 60 T. This makes it an ideal candidate for the next generation of superconducting magnets. $PbMo_6S_8$ limiting property is its critical current density (J_c), which is a factor 5 lower than Nb_3Sn. Research is continuing to increase J_c to the required standard for industry. Chevrel phase superconductors are also studied as magnetic ions can be introduced into the lattice in the place of the Pb ion. This means superconductivity and magnetism are observed in these materials. They are one of the few materials where this interaction occurs. Part of this thesis investigates how the properties such as T_c, J_c and $B_{c2}(0)$ of $PbMo_6S_8$ change with the addition of the magnetic europium ions. To determine whether doping with a 2+ magnetic ion improves the intrinsic and extrinsic superconducting properties of the material. Also studied is the interaction between the magnetism and the superconductivity.

The main part of this thesis was to design and construct a new magnetic technique, which would measure the critical current density of isotropic superconductors. The

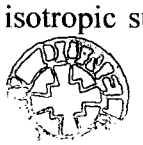

main methods used to measure the J_c of superconductors, are transport and magnetic measurements. For the magnetic measurements the two commercial instruments most commonly used are the vibrating sample magnetometer (VSM) and the superconducting quantum interference device (SQUID). Both methods have disadvantages in measurements of the magnetic moment. For commercial VSMs the base temperature is 4.2 K, while for SQUIDs the maximum field that can be applied is 7 T. The magnetic technique used in this thesis was torque field-gradient magnetometry, using a silicon piezoresistive cantilever. It was designed to work below 2 K, and in magnetic fields up to 15 T. Thus bridging the gap between the other two techniques.

In chapter 2 the general theories of superconductivity are presented. These include the microscopic theory by Bardeen, Cooper and Schrieffer (BCS) and the phenomenological Ginsburg-Landau theory. The behaviour of type II superconductors in the mixed state is described. This includes the Abrikosov lattice, Bean's model and the volume flux-pinning force. Chapter 3 reviews the different magnetic techniques used to measure the magnetic moment of superconductors. This includes the VSM, SQUID and Faraday force balance. Torque magnetometry is reviewed from the original torque balances to the new cantilever techniques. The different piezoresistive and capacitance cantilevers are described and compared. The theory behind the torque field-gradient magnetometer is also derived, including the definitions of the demagnetisation factor and the shape factor.

The investigation into the introduction of Eu ions in the Chevrel phase superconductor $PbMo_6S_8$ is presented in chapter 4. This includes a description of the heat treatments used to fabricate the samples and the measurements carried out to characterise them. These measurements included resistivity, ac susceptibility and VSM. N Leigh also measured the specific heat of the samples. From the measurements the upper critical field ($B_{c2}(0)$), the fundamental parameters ($B_{c1}(0)$, $B_c(0)$, $\xi(0)$ & $\lambda(0)$), the GL parameter (κ) and the Sommerfeld constant (γ) were determined. How these parameters and variables change with the addition of Eu ions is discussed.

The design and circuitry of the torque field-gradient magnetometer, which fits on to the base of an Oxford Instruments Heliox probe, are described in chapter 5. The problems, which occurred with the torque magnetometer and their solutions are

discussed. The experimental procedure to measure the critical current density of the isotropic superconductors as a function of magnetic field and temperature is described. The preliminary measurements were carried out on NbTi wire as a function of angle in liquid helium. The critical current densities of NbTi wire as a function of magnetic field and temperature are compared with the corresponding critical current densities measured on the VSM. The advantages and disadvantages including the sensitivity of each technique are presented.

The critical current densities of 1 mm length samples of NbTi wire, $PbMo_6S_8$ and $Pb_{0.75}Eu_{0.25}Mo_6S_8$ as a function of temperature and magnetic field measured on the torque field-gradient magnetometer and the VSM are presented in chapter 6. On the torque magnetometer these were measured in the temperature range 300 mK up to 10 K, in fields up to 15 T. On the VSM the critical current densities were measured with the field parallel to the c-axis, and perpendicular to the c-axis. Also determined from the VSM data were the critical current densities of the 4 mm length bulk samples of $PbMo_6S_8$ and $Pb_{0.75}Eu_{0.25}Mo_6S_8$. The different flux pinning mechanisms in NbTi wire are discussed using the torque data taken from 0.3 K to 8 K. The upper critical field was also determined from the torque magnetometer and VSM measurements.

The temperature dependence of the magnetic moments of titanium alloys and copper-beryllium are presented in chapter 7. This work is an independent study, which does not relate to the other chapters in this thesis. It was carried out to investigate, which of these high-strength materials had the smallest change in susceptibility with temperature, as it is important in magnetic measurements. The magnetic moments of CuBe, Ti-64 and Ti-550 were measured as a function of magnetic field and temperature on the VSM. The change in magnetic moment with temperature is compared for the three samples. In chapter 8, there is a summary of the work, and the future work that could be carried out based upon the findings in this thesis.

Chapter 2

General Theory of Metallic superconductors

2.1 Introduction

This chapter introduces the general theories of superconductivity. The history and the fundamental properties of superconductors are described in section 2.2. The two main theories are presented, which describe the behaviour and properties of low temperature superconductors. The first theory is BCS microscopic theory in section 2.3. It predicts the properties including the energy gap, the critical temperature and the thermodynamic critical field. The thermodynamic theory (section 2.4) and the London equations (section 2.5) are presented. The second main theory is Ginzburg-Landau phenomenological theory (section 2.6), which introduces the GL parameters, type I & II superconductors and Abrikosov's lattice. Section 2.7 presents the critical state model proposed by Bean, and the Flux pinning force scaling laws. These are important as they describe the behaviour of type II superconductors in an external magnetic field. The on going theories for high-temperature superconductors are reviewed in section 2.8.

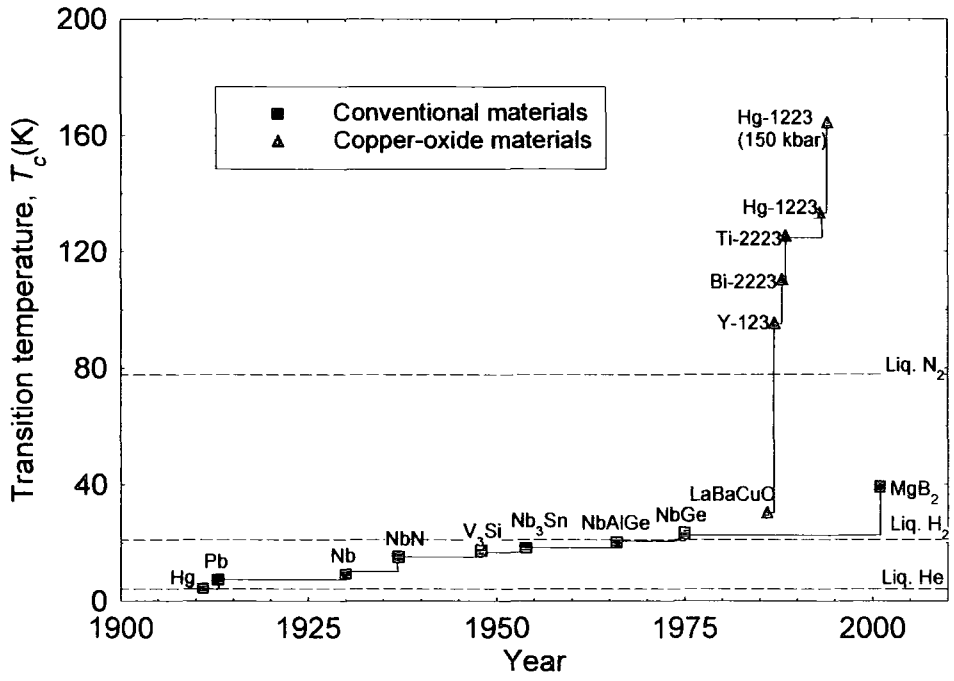

Figure 2.1. The increase in critical temperature of superconductors since their discovery in 1911, till the present day [3].

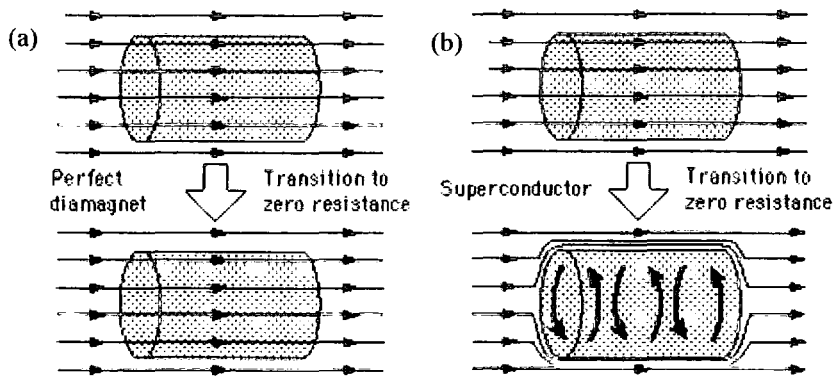

Figure 2.2. The behaviour of a superconductor in an applied magnetic field, for H_{app} less than the thermodynamic critical field (H_c) (a) $T > T_c$ (b) $T < T_c$.

2.2 History of superconductivity

Kamerlingh Onnes discovered superconductivity in 1911[1], since then the area of research has expanded greatly. The range of superconductors has grown from just the elements to the ternary isotropic superconductors and layered high-T_c superconductors. The critical temperature of superconductors has increased from 4.2 K (mercury)[1] up to 133 K ($HgBa_2Ca_2Cu_3O_{8+\delta}$) [2], in the last hundred years.

2.2.1 Intrinsic properties of superconductors

All superconductors have two fundamental properties. The first property is they have no resistance, at temperatures below their critical temperature (T_c). They are perfect conductors.

The second property is they expel magnetic flux[4] below the critical field (H_c). This effect is known as the Meissner effect (fig. 2.2). Superconductors are perfect diamagnets ($\chi = -1$), below H_c and T_c.

2.2.2 Critical Parameters of superconductors

Superconductors are characterised by three critical parameters. The critical temperature (T_c), is the temperature at which the superconducting phase transition occurs, in zero field. The upper critical field (B_{c2}) is the magnetic field at the superconducting phase transition, at constant temperature. The critical current density is the maximum current density (J_c) that a superconductor can sustain at a given field and temperature.

2.3 BCS theory

2.3.1 Cooper pairs

In 1956, Cooper[5] proposed a model based on two electrons, pairing up in a bound state. The first electron, with wavevector $+k$, deforms the lattice, by attracting the positive ions. This creates a phonon, which propagates through the lattice (range ~ coherence length) and interacts with another electron, with wavevector $-k$. The overall interaction is attractive. The effective attractive interaction is strong enough to override the Coulomb repulsion between the electrons. Cooper pairs have anti-parallel spins. They have zero net spin and zero net angular momentum. All Cooper pairs are in the ground state, as the total wavevector is zero. This is a condensation in k-space. The ground state is separated from the first excited state by an energy gap. The pairs have charge $2e$ and effective mass $2m_e^*$.

2.3.2 Microscopic Theory

Bardeen, Cooper and Schrieffer first proposed BCS theory in 1957[6]. It is a microscopic theory, which qualitatively predicts the properties of low temperature superconductors. BCS theory involves Cooper pairs and is supported by experimental observations. From experiments the critical temperature is proportional to the ionic mass M. BCS theory predicts the empirical law:

$$T_c \propto M_i^{-a} \tag{2.1}$$

where $a = 0.5$, which holds for most non-transition metals. Eqn. 2.1 is known as the isotope effect. BCS theory predicts the critical temperature and the energy gap. The critical temperature is the temperature where the energy gap tends to zero ($\Delta(T) \to 0$). In zero field, the critical temperature is given by:

$$k_b T_c = 1.13\hbar\omega_D e^{-1/N_o V_0} \tag{2.2}$$

where ħ is the reduced Planck's constant and the energy gap at 0 K by:

$$\Delta(0) = 2\hbar\omega_D e^{-1/N_o V_o} \tag{2.3}$$

where N_o is the density of electronic levels for a single spin population in the normal metal, ω_D is the Debye frequency and V_o is the electron-electron potential. The weak-coupling approximation is $N_o V_o << 1$. Equating eqns 2.2 & 2.3, gives a relation between critical temperature and the energy gap:

$$2\Delta(0) = 3.52 k_b T_c \tag{2.4}$$

Eqn 2.4 is in terms of $2\Delta(0)$, as it is measured in tunnelling experiments. Eqn 2.4 is independent of any phenomenological parameters. The energy gap near the critical temperature, in zero field, is an universal law, from mean-field theory, given by:

$$\frac{\Delta(T)}{\Delta(0)} = 1.74\left(1-\frac{T}{T_c}\right)^{1/2} \qquad T \approx T_c \tag{2.5}$$

The thermodynamic critical field $H_c(T)$, is predicted from BCS theory. It is taken from the empirical law:

$$\frac{H_c(T)}{H_c(0)} \approx 1-\left(\frac{T}{T_c}\right)^2 \tag{2.6}$$

BCS theory predicts the discontinuity in the specific heat from the normal phase to the superconducting phase. It is a first order transition. The size of the discontinuity is given by:

$$\Delta c = 9.4Nk_b^2T_c \tag{2.7}$$

2.4 Thermodynamic theory

Thermodynamics is used to describe the phase transition from the normal state to the superconducting state[3].

The Gibbs free energy is minimised with respect to temperature and magnetic field, at the transition:

$$dG = -SdT - \mu_o \mathbf{M} \cdot d\mathbf{H} \tag{2.8}$$

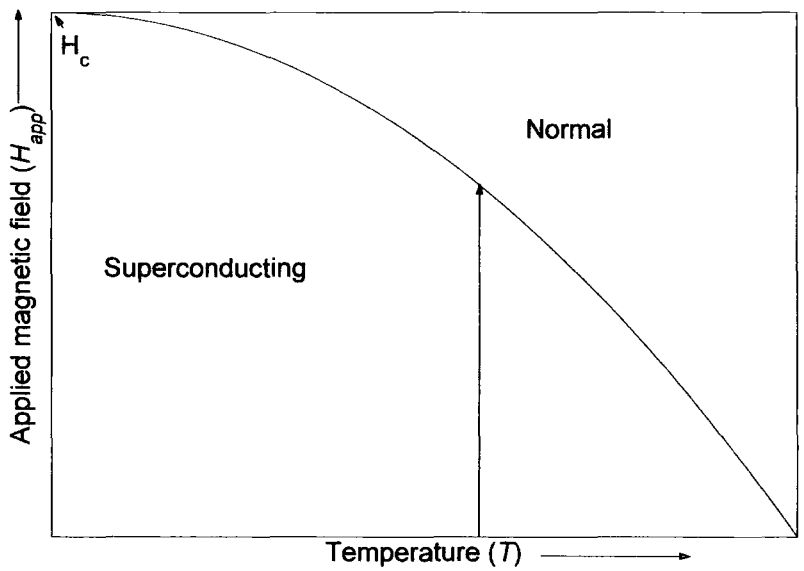

Figure 2.3. The (H, T) phase diagram for a type I superconductor [3].

The Gibbs potential is integrated along the vertical line in fig. 2.3. In the superconducting state it is a perfect diamagnet ($H = -M$), and thus:

$$G_s(T,H_c) - G_s(T,0) = \int_0^{H_c} \mu_o M dH = \mu_o \frac{H_c^2}{2} \qquad (2.9)$$

Across the transition, the Gibbs energy is constant $G_s(T,H_c) = G_n(T,H_c)$. In the normal state, the magnetisation is zero (neglecting paramagnetism and diamagnetism.) If the sample was normal below H_c, then the Gibbs energy is given by:

$$G_n(T,H_c) - G_n(T,0) = \int dG = -\int_0^{H_c} \mu_o M dH \approx 0 \qquad (2.10)$$

Equating eqns 2.9 & 2.10, the difference in free energy between the superconducting state and normal state is given by:

$$G_s(T,0) - G_n(T,0) = -\mu_o \frac{H_c^2}{2} \qquad (2.11)$$

The minimised Gibbs free energy is lower in the superconducting state. Therefore it is thermodynamically stable.

From $F = G - \mu_o HM$, with $H = 0$, the equation for the Helmholtz free energy is given by:

$$F_s(T,0) - F_n(T,0) = -\frac{\mu_o H_c^2}{2} \qquad (2.12)$$

The quantity $\mu_o H_c^2/2$ is the condensation energy per unit volume. It is an important in determining the surface energy.

2.5 London Equations

In 1935 the London brothers presented a theory, which describes the Meissner effect[7]. They assumed that the time derivatives in the equation $\frac{d\mathbf{J}}{dt} = -\left(\frac{ne^2}{m}\right)\frac{d\mathbf{A}}{dt}$ could be neglected, where **J** is the current density, **A** is the magnetic vector, n is the number of electrons, e is the charge of an electron and m is the mass of an electron. This gives the relation:

$$\mu_o \lambda_L^2 \mathbf{J}_s + \mathbf{A} = 0 \qquad (2.13)$$

where λ_L is the London penetration depth, **A** is the magnetic vector potential and $\mathbf{J}_s$ is the surface current density. Taking the curl of both sides of equation 2.13 gives:

$$\mathbf{B} = -\mu_o \lambda_L^2 \nabla \times \mathbf{J}_s \qquad (2.14)$$

This equation describes perfect diamagnetism. The second equation is derived from $\nabla \times \mathbf{E} = -\frac{d\mathbf{B}}{dt}$, by applying the London gauge $\nabla \cdot \mathbf{A} = 0$ and eqn 2.13, to give:

$$\mathbf{E} = \mu_o \lambda_L^2 \frac{\partial \mathbf{J}_s}{\partial t} \tag{2.15}$$

This equation describes perfect electrical conductivity. The London penetration depth λ_L is obtained by comparing the classical current density relation ($\mathbf{J} = \frac{ne^2\tau}{m}\mathbf{E}$) with eqn 2.15 to give:

$$\lambda_L = \left(\frac{m^*}{\mu_o n e^{*2}}\right)^{1/2} \tag{2.16}$$

where m^* is the effective mass of an electron, e^* is the effective change of an electron. The London penetration depth is the distance the magnetic field exponentially decays away from the surface in the Meissner state.

2.6 Ginzburg-Landau equations

2.6.1 Theory

In 1950 Ginzburg and Landau (GL) proposed a phenomenological model to describe the behaviour of superconductors [8, 9]. GL theory describes superconductivity in terms of an order parameter ψ, which characterises the superconducting state near T_c. The order parameter is a function of position (d) and phase (φ), $\psi(d,\varphi) = \psi(d)e^{i\varphi}$. In the normal state ($T > T_c$), ψ is zero, while in the superconducting state ($T < T_c$), ψ is non-zero. Below the critical temperature, ψ increases as the temperature decreases. The superconducting electron density is proportional to $|\psi|^2$.

GL theory assumes that the Gibbs free energy per unit volume (G), near the transition temperature (T_c), can be expanded as a function of the order parameter.

$$G_s(\psi) = G_n + \frac{1}{V}\int d^3\mathbf{r}\left(\begin{array}{l}\frac{1}{2m^*}\left(-i\hbar\nabla + e^*\mathbf{A}\right)\psi^*\left(i\hbar\nabla + e^*\mathbf{A}\right)\psi + \left(\frac{1}{2\mu_o}\right)B^2(\mathbf{r}) + a\psi\psi^* \\ + \frac{1}{2}b\psi\psi^*\psi\psi^* + \cdots\end{array}\right) \tag{2.17}$$

where G_n is the Gibbs free energy in the normal state, $\mathbf{A}$ is the magnetic vector potential and a, b are variables, which only depend on temperature. For a

superconductor in equilibrium, the currents are distributed, so that the total free energy is minimised. Close to T_c the parameters a, b are taken to be:

$$a(T) \approx a_o\left[\frac{T}{T_c} - 1\right] \tag{2.18a}$$

$$b(T) \approx b_o \tag{2.18b}$$

where a_o and b_o are positive constants, so that $a(T)$ is zero at T_c and negative below T_c. The first GL equation is determined, by minimising the Gibbs free energy (eqn 2.17) with respect to the complex conjugate order parameter $\psi(\mathbb{d})^*$, while holding $\psi(\mathbb{d})$ constant. It is then expanded and the London gauge ($\nabla \cdot \mathbb{A} = 0$) applied which gives:

$$\frac{1}{2m^*}\left(\hbar^2\nabla^2\psi - 2i\hbar\mathbb{A}\cdot\nabla\psi - e^{*2}A^2\psi\right) - a\psi - b|\psi|^2\psi = 0 \tag{2.19}$$

The second GL equation is derived, by minimising the free energy (eqn 2.17) with respect to the vector potential $\mathbb{A}$, and $\mathbb{B} = \nabla \times \mathbb{A}$. Maxwell's equation ($\nabla \times \mathbb{B} = \mu_o \mathbb{J}$) is substituted in, to give the equation in terms of the superconductor's supercurrent:

$$\mu_o \mathbb{J} = -\frac{i\hbar e^*}{2m^*}\left(\psi^*\nabla\psi - \psi\nabla\psi^*\right) - \frac{e^{*2}}{m^*}\mathbb{A}|\psi|^2 \tag{2.20}$$

These two-coupled equations are used to determine the properties of the superconducting state. The boundary condition for no current flow through the surface is given by:

$$\left[-i\hbar\nabla\psi + e^*\mathbb{A}\right] = 0 \tag{2.21}$$

2.6.2 GL parameters

The GL equations have a characteristic length known as the coherence length$\left(\xi_{GL}\right)$. The coherence length is the distance into the superconductor from the superconducting-normal interface, for the order parameter to reach ψ_∞. If the first GL equation is written in 1D, assuming no magnetic field is applied ($\mathbb{A} = 0$), it is given by:

$$-\frac{\hbar^2}{2m^*}\frac{d^2\psi(\mathbf{d})}{dx^2} + \left(a + b|\psi|^2\right)\psi(\mathbf{d}) = 0 \tag{2.22}$$

The solution near a superconducting-normal interface is $\psi(\mathbf{d}) = \psi_\infty \tanh\left(\frac{x}{\sqrt{2}\xi_{GL}}\right)$

where $\psi_\infty = \left(\frac{|a|}{b}\right)^{\frac{1}{2}}$, and the coherence length $\xi_{GL} = \left(\frac{\hbar^2}{2m^*|a|}\right)^{\frac{1}{2}}$.

The GL equations also determine the penetration depth λ_{GL}. If one assumes the phase constant $\psi^*\nabla\psi = \psi\nabla\psi^*$, and the magnetic field is along the *z*-direction of the interface. The second GL eqn (eqn 2.20) reduces to:

$$\frac{d^2}{dx^2}A_y(x) = \frac{\mu_o e^{*2}|\psi(x)|^2}{m*}A_y(x) \qquad (2.23)$$

where $A_y(x) = A_o \exp\left(-\frac{x}{\lambda_{GL}}\right)$ which is the vector potential in the y-direction. This is only valid in the bulk of the material when the order parameter has reached ψ_∞. The penetration depth is defined as $\lambda_{GL}^2 = \frac{m^*}{\mu_o e^{*2}|\psi_\infty|^2}$. It is valid as long as $\xi_{GL} << \lambda_{GL}$. The GL penetration depth has the same temperature dependence as the GL coherence length $\left(\lambda_{GL} \propto \left(1-\frac{T}{T_c}\right)^{-\frac{1}{2}}\right)$. Thus at T_c both lengths become infinite, and the magnetic flux penetrates the entire sample. The ratio of λ_{GL} and ξ_{GL} is known as the GL parameter or kappa (κ) and is given by:

$$\kappa = \frac{\lambda_{GL}}{\xi_{GL}} \qquad (2.24)$$

Abrikosov showed that the difference between a Type I and Type II superconductor is $\kappa = 1/\sqrt{2}$. The critical fields of type II superconductors can be derived in terms of the thermodynamic critical field ($B_c(T)$).

The upper critical field, $B_{c2}(T)$ is given by:

$$B_{c2} = \frac{\Phi_o}{2\pi\xi_{GL}^2} = \frac{\lambda_{GL}^2 B_c^2}{\Phi_o} = \sqrt{2}\kappa B_c \qquad (2.25)$$

where the quantised magnetic flux $\Phi_o = \frac{h}{2e}$, and h is Planck's constant. The lower critical field, $B_{c1}(T)$ is given by:

$$B_{c1} = B_c \frac{(\ln\kappa + 0.5)}{\sqrt{2}\kappa} \qquad (2.26)$$

	T_c (K)	$B_{c2}(0)$ (T)	$B_{c1}(0)$ (mT)	κ	λ_{GL} (nm)	ξ_{GL} (nm)
NbTi	9.5	15[10]		40[10]	130.6[11]	4.85[11]
$PbMo_6S_8$	14.8[12]	56[13]	6.4[13]	130[13]	230[13]	2.1[13]
MgB_2	38	3.18 *14.5*[14]	63 *22*[14]	8.1 *37.1*[14]	370 *82*[14]	2.3 *10.2*[14]
$YBa_2Cu_3O_7$	92 [15]	122 *674*[16]	53 *18*[17]	2334 *18*	7000 *145*[18]	3 *16.4*[16]
$Bi_2Sr_2Ca_2Cu_3O_{10}$	110 [15]	39 *1210*[19]	33 *11*[20]	10750 *7*	10,000 *200*[21]	0.93 *29*[19]

Table 2.1. Comparison of the critical parameters for a selection of superconductors. Numbers in normal type are for the c-axis, numbers in *italics* for the *a,b* plane.

There is a third critical field B_{c3} for a superconductor-insulator interface. When a magnetic field is applied parallel to the interface, superconductivity occurs in a surface layer of thickness ξ. It occurs for applied fields up to B_{c3}, which is given by:

$$B_{c3} = 1.69 B_{c2} = 1.695(\sqrt{2}\kappa B_c) \qquad (2.27)$$

Table 2.1 gives a summary of the critical parameters of the most commonly used superconductors. The high T_c superconductors (YBCO & BSCCO) and MgB_2 are anisotropic. The critical parameters for the *c*-axis and the *a,b* plane are given.

2.6.3 Type I & II superconductors

From κ (eqn 2.24), the two different types of superconductors are described. The surface energy (σ) at the superconducting-normal interface has contributions from the positive flux exclusion energy (length scale of λ_{GL}) and the negative condensation energy (eqn 2.12) (length scale ξ_{GL}).

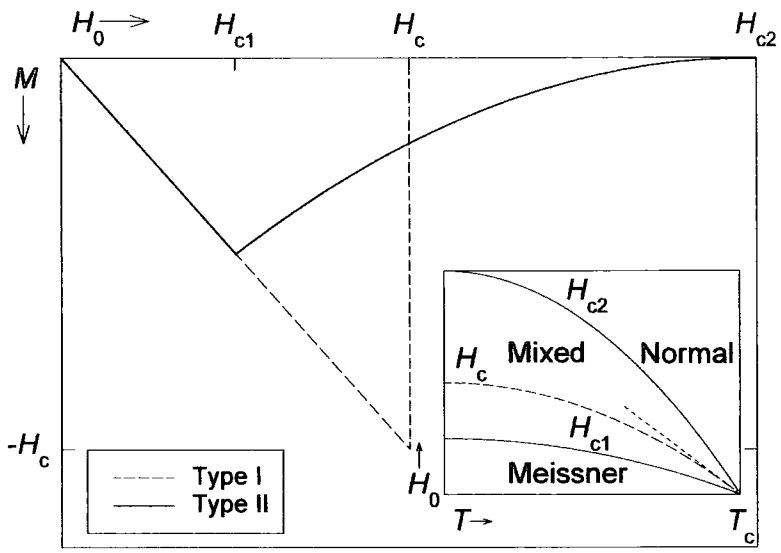

Figure 2.4. The magnetisation (M) of a type I and type II superconductor, with the same H_c as a function of applied magnetic field (H_o). **Inset**: The phase diagrams of type I and type II superconductors.

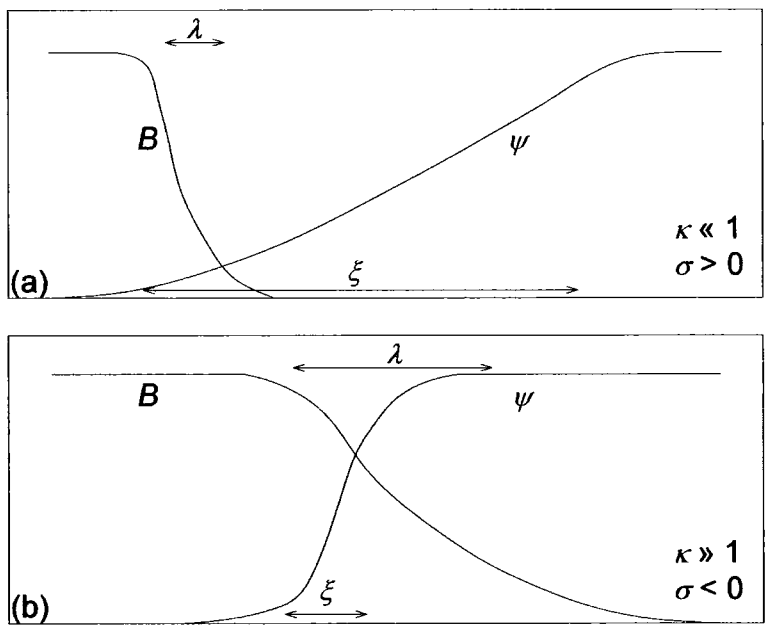

Figure 2.5. The variation in magnetic field (B) and order parameter (ψ) across a superconducting-normal interface for a Type I superconductor (a) and Type II superconductor (b). In (a) $\kappa < 1$ ($\lambda < \xi$) and in (b) $\kappa > 1$ ($\lambda > \xi$).

From fig 2.5a, there is a region where no magnetic field penetrates, but the order parameter has not reached ψ_∞. This region has positive surface energy $(\sigma > 0)$, as all flux is excluded. This describes Type I superconductors (fig 2.4), such as the elements Al, Sn and Mo. From fig. 2.5b, the order parameter reaches ψ_∞ before the magnetic flux has decayed away. The surface energy is negative $(\sigma < 0)$. These boundaries are energetically favourable. They occur at fields greater than B_{c1} (fig. 2.4). These are Type II superconductors, such as 'dirty' elements (Nb), alloys (NbTi), secondary and ternary compounds (Nb_3Sn, $PbMo_6S_8$), and high-temperature superconductors ($Bi_2Sr_2Ca_2Cu_3O_{10}$, $YBa_2Cu_3O_7$).

2.6.4 Abrikosov Lattice

Abrikosov proposed that magnetic flux in the mixed state ($H_{c1} < H < H_{c2}$) is quantised[22]. The magnetic flux penetrates in single vortices $\left(\Phi_0 = \frac{h}{2e}\right)$, rather than continuously. Abrikosov used the first GL equation (eqn 2.18) to determine the vortex formation array. The order parameter is taken to be a superposition of solutions. Abrikosov found that the lowest energy state for the flux-line lattice gave a square lattice[22], with the Abrikosov constant, $\beta_A = 1.18$. This work was corrected by Kleiner[24], who found a triangular lattice for the ground state with $\beta_A = 1.16$.

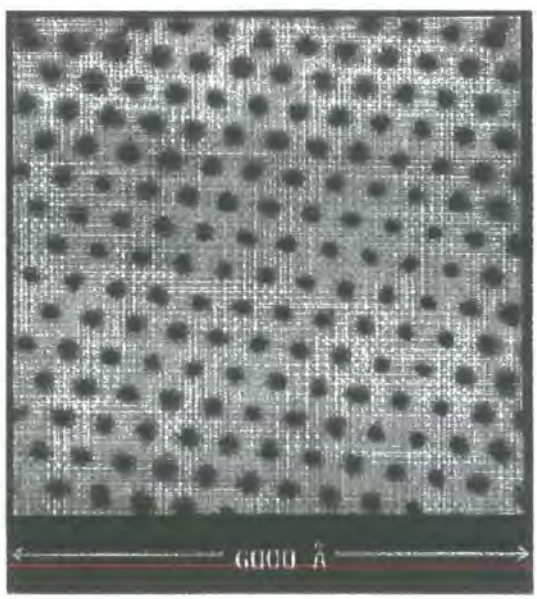

Figure 2.6. The hexagonal Abrikosov flux lattice: Image from a tunnelling electron microscope upon the superconductor $NbSe_2$ (1 T, 1.8 K) from Hess *et al* [23].

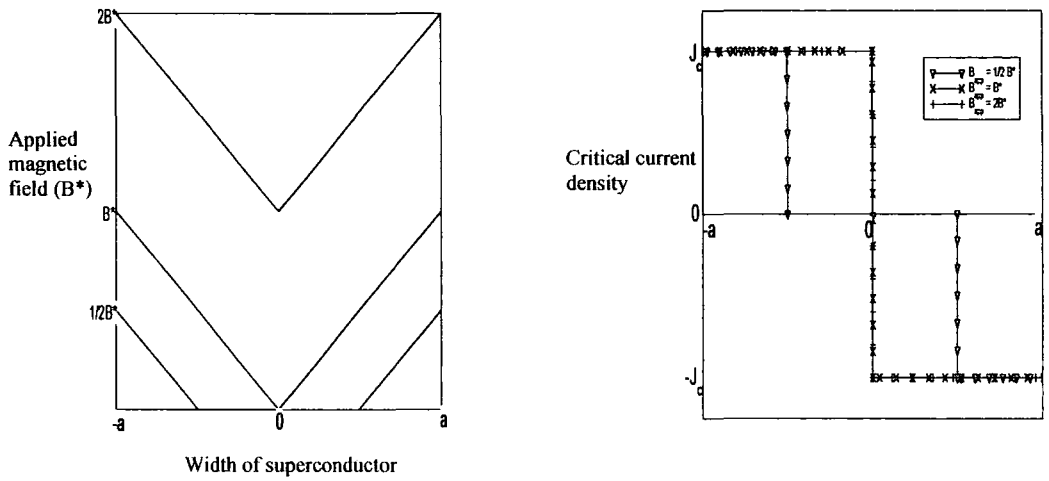

Figure 2.7. (a) The penetration of magnetic flux as a function of distance from the surface and magnetic field. (b) The critical current density across the superconductor, as a function of applied magnetic field. The applied magnetic field is in units of the characteristic field B^*.

Abrikosov determined a relation between the magnetisation (in the reversible region near H_{c2}) and the applied magnetic field, by solving the full GL equations using a perturbative method[25]. The solution is given by:

$$M = -\frac{\left(H_{c2} - H_0\right)}{\beta_A\left(2\kappa^2 - 1\right)} \tag{2.28}$$

2.7 Bean's model and Flux pinning

2.7.1 Bean's Model – Critical state

When an external magnetic field (B_{app}) is applied to the superconductor, magnetic flux enters at the surface. The field decreases with distance from the surface. Critical currents flow in the magnetic field region. This is known as the critical state. There are different models, which describe this state, such as the Bean's model[26], the fixed pinning model[27] and the Kim's model[28]. Bean's model assumes that the critical current density has magnitude J_c in the magnetic flux region and is zero everywhere else.

From figure 2.7a, a slab of superconductor is considered with width $2a$ in the x-direction and infinite in the y- & z- directions and B_{app} is along the z-axis. Using $\nabla \times \mathbf{B} = -\mu_o \mathbf{J}$ the internal magnetic field $B_{in}(x)$is given by:

$$B_{in}(x) = B_{app}\left(\frac{a'+x}{a'-a}\right) \quad -a \le x \le -a'$$

$$B_{in}(x) = 0 \quad -a' \le x \le a' \tag{2.29}$$

$$B_{in}(x) = B_{app}\left(\frac{x-a'}{a-a'}\right) \quad a' \le x \le a$$

where $a`$ is the furthest distance the magnetic field penetrates.

The characteristic field, $B^* = \mu_o J_c a$, is the applied field when the whole sample is penetrated. For $B_{app} > B^*$, the current density is J_c (fig.2.7b), but $B_{in}(x)$ is given by:

$$B_{in}(x) = B_{app} - B^*\left(\frac{a+x}{a}\right) \quad -a \le x \le 0$$

$$B_{in}(x) = B_{app} + B^*\left(\frac{x-a}{a}\right) \quad 0 \le x \le a \tag{2.30}$$

The magnetisation is determined from $B = \mu_o(H + M)$. From Maxwell's boundary conditions, H is continuous across the interface, thus $\mu_o H = B_{app}$. The volume average of the internal magnetic field ($\langle B \rangle$), gives the average magnetisation to be $\mu_o M = \langle B \rangle - B_{app}$.

For the high-field limit $\left(B_{app} >> B^*\right)$, the magnetisation is given by:

$$\begin{aligned} \mu_o M_+ &= \tfrac{1}{2} B^* \\ \mu_o M_- &= -\tfrac{1}{2} B^* \end{aligned} \tag{2.31}$$

where M_+ and M_- are the magnetisation for increasing and decreasing magnetic field. The difference in magnetisation across a high-field hysteresis loop is given by:

$$\mu_o\left(M_+ - M_-\right) = B^* = \mu_o J_c a \tag{2.32}$$

Rearranging eqn 2.31, gives the relation between the measured magnetisation and the critical current density to be:

$$J_c = \frac{\left(M_+ - M_-\right)}{\gamma_{sf}} \tag{2.33}$$

where γ_{sf} is a geometric factor determined from the shape of the superconducting sample, (cf. section 3.7.2). For a parallelepiped the shape factor is $\gamma_{sf} = a\left[1 - \frac{a}{3b}\right]$, where a is the thickness and b is the width of the sample[29].

2.7.2 Flux pinning scaling laws

From section 2.6.4, the flux enters the superconductor in single vortices. The flux vortex experiences a Lorentz volume pinning force:

$$\mathbb{F}_p = \mathbb{J} \times \mathbb{B} \tag{2.34}$$

The force causes the vortices to move. This flux motion increases the resistance, thus decreases the magnitude of the transport current that can be sustained. To increase the transport current, the flux vortices have to be pinned. The flux pinning force fixes the vortices to be stationary. Pinning is caused by any spatial inhomogenities, such as impurities, grain boundaries and voids. For strong pinning, the flux motion is small. It is then assumed to be a perfect conductor.

Fietz and Webb[30] proposed the first scaling law for the flux pinning force. They measured J_c for different NbTi and NbTa samples, over a wide range of fields and temperatures, to give the scaling relation:

$$F_p(B,T) = \alpha_p(T) B_{c2}^n(T) b^p (1-b)^q \tag{2.35}$$

where b is the reduced magnetic field, B/B_{c2}, and α_p, n, p & q are sample dependant constants. Kramer's model[31] also predicts the pinning force density. It predicts p = 1/2 and q = 2. These variables are substituted into eqn 2.35, to give Kramer scaling law $F_p(B,T) = \alpha_p(B_{c2},T) b^{1/2}(1-b)^2$. This equation can be re-arranged to give $J_c^{1/2} B^{1/4} = \alpha_K(B_{c2})(1-B)$. From this relation B_{c2} can be predicted.

2.7.3 Anisotropic Materials

GL theory can be generalised for anisotropic materials. For each axes there is a different effective mass (m_a, m_b, m_c). The coherence length and the penetration depth are mass dependent. From eqns 2.25 & 2.26 the upper and lower critical fields are anisotropic. For a high-T_c superconductor the effective masses in the a,b plane are similar, but differ from the c-axis $(m_a \approx m_b << m_c)$. The upper critical field of anisotropic superconductors, in an applied field, at angle θ to the a,b plane is given by[32]:

$$H_{c2}(\theta) = \frac{H_{c2\|c}}{\left(\cos^2\theta + \gamma_m^2 \sin^2\theta\right)^{\frac{1}{2}}} \tag{2.36}$$

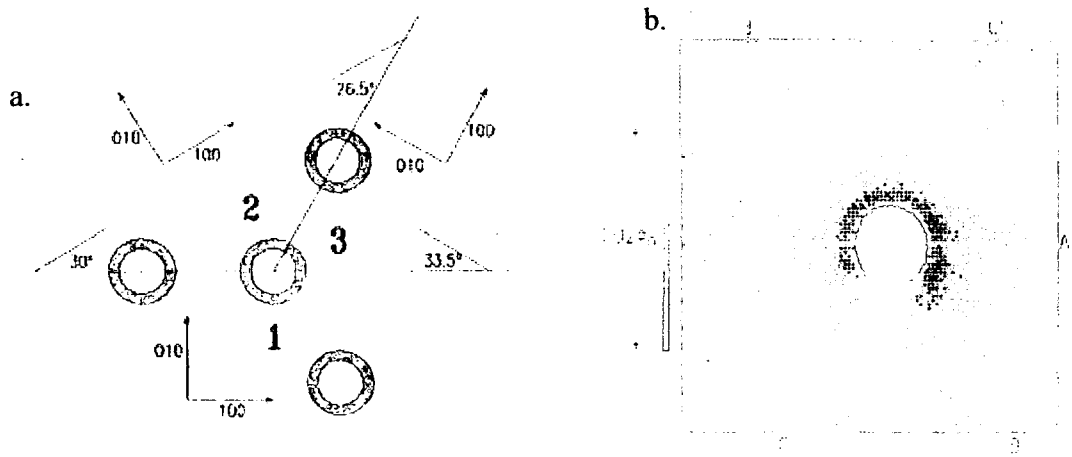

Figure 2.8a. Schematic diagram for the tricrystal (100) $SrTiO_3$ substrate, with four epitaxial $YBa_2Cu_3O_{7-\delta}$ rings. **b.** Scanning SQUID microscope image of the four $YBa_2Cu_3O_{7-\delta}$ rings on the tricrystal. Images were taken by Tsuei[34].

where γ_m is the anisotropic parameter $\gamma_m = \left(\frac{m_c}{m_{ab}}\right)^{\frac{1}{2}} = \frac{\xi_{ab}}{\xi_c} = \frac{\lambda_c}{\lambda_{ab}} = \frac{H_{c2\|ab}}{H_{c2\|c}} = \frac{H_{c1\|c}}{H_{c2\|ab}} > 1.$

For high-T_c superconductors such as $YBa_2Cu_3O_7$ and $Bi_2Sr_2Ca_2Cu_3O_{10}$, $\gamma_m > 5$.

2.8 Ongoing Theory

The theories presented in this chapter describe low temperature superconductors such as NbTi and Chevrel phase. High temperature superconductors such as $YBa_2Cu_3O_7$ and $Bi_2Sr_2Ca_2Cu_3O_{10}$ were discovered 17 years ago[33]. They have critical temperatures of 92 K for $YBa_2Cu_3O_7$[15] and of 110 K for $Bi_2Sr_2Ca_2Cu_3O_{10}$[15]. BCS theory has to be modified to describe High-T_c superconductors. The cuprates are layered superconductors. This means the superconductivity occurs in the CuO_2 planes. Therefore the theory would have to introduce anisotropy.

Another property is they are d-wave superconductors[35]. This means that the energy gap is zero at points on the Fermi surface. This phenomenon can be observed by experiments. Tsuei *et al* demonstrated this by using a tricrystal ring magnetometry, which is sensitive to the order parameter symmetry[35, 34]. In fig. 2.8a, the basic set-up considers of tricrystal $SrTiO_3$ substrate, which has three distinct directions for the (100) plane. Four $YBa_2Cu_3O_{7-\delta}$ rings were deposited on top. The whole set-up was then cooled in a 0.5 μT field. Fig. 2.8b, shows the results when a SQUID microscope

was scanned across the surface. The ring where all 3 junctions meet has π geometry, which means if half-integer flux quantisation is observed, the superconductor is d-wave. Thus high-T_c superconductors are d-wave superconductors, as flux was measured in the centre ring. The mechanism of cuprates is as yet not understood. It is uncertain to whether the electrons pair up due to phonon coupling. This has lead to a number of different models being proposed which describe the some areas of behaviour of High-T_c superconductors. These include nearly antiferromagnetic Fermi liquid model[36], marginal Fermi liquid theory[37], the stripes' model[38] and electron fractionalisation theory[39]. None of these theories completely explain superconductivity in High-T_c superconductors.

References for Chapter 2

1 H. Kamerlingh Onnes, Communications from the physical laboratory of the University of Leiden **124c**, 21 (1911).

2 A. Schilling, M. Cantoni, J. D. Guo, *et al.*, Nature **363**, 56 (1993).

3 C. P. Poole, H. A. Farach, and R. J. Creswick, *Superconductivity* (Academic Press, San Diego, 1995).

4 W. Meissner and R. Ochsenfeld, Die Naturwissenschaften **44**, 787 (1933).

5 L. N. Cooper, Physical Review **104**, 1189 (1956).

6 J. Bardeen, L. N. Cooper, and J. R. Schrieffer, Physical Review **108**, 1175 (1957).

7 F. London and H. London, Pro. Royal Soc. **A149**, 71 (1934).

8 V. L. Ginzburg and L. D. Landau, Zhurnal Eksperimentalnoj i Teoreticheskoj Fisiki **20**, 1064 (1950).

9 V. L. Ginzburg, Soviet Physics JETP **2**, 589 (1956).

10 C. Meingast, P. J. Lee, and D. C. Larbalestier, Journal of Applied Physics **66**, 5962 (1989).

11 D. P. Hampshire, Physica C **296**, 153 (1997).

12 H. Niu, N. A. Morley, and D. P. Hampshire, IEEE transactions on Applied Superconductivity **11**, 3619 (2001).

13 D. N. Zheng, H. D. Ramsbottom, and D. P. Hampshire, Physical Review B **52**, 12931 (1995).

14 M. Zehetmayer, M. Eisterer, J. Jun, *et al.*, Physical Review B **66**, 1 (2002).

15 D. R. Harshman and A. P. Mills, Physical Review B **45**, 10684 (1992).

16 U. Welp, W. K. Kwok, G. W. Crabtree, *et al.*, Physical Review Letters **62**, 1908 (1989).

17 L. Krusin-Elbaum, A. P. Malozemoff, Y. Yeshurun, *et al.*, Physical Review B **39**, 2936 (1989).

18 D. R. Harshman, L. F. Schneemyer, J. V. Waszczak, *et al.*, Physical Review B **39**, 851 (1989).

19 I. Matsubara, H. Tanigawa, T. Ogura, *et al.*, Physical Review B **45**, 7414 (1992).

20 K. Tagaya, K. Senda, T. Yosida, *et al.*, Japan Journal of Applied Physics **31**, L 1170 (1992).

21 M. Cyrot and D. Pavuna, in *Introduction to superconductivity and High-Tc materials*, edited by W. Scientific, 1992), p. 168 .

22 A. A. Abrikosov, Soviet Physics Jetp **5**, 1174 (1957).

23 H. F. Hess, R. B. Robinson, R. C. Dynes, *et al.*, Physical Review Letters **62**, 214 (1989).

24 W. H. Kleiner, L. M. Roth, and S. H. Autler, Physical Review **133**, A1226 (1964).

25 A. A. Abrikosov, J. Phys. Chem. Solids **2**, 199 (1957).

26 C. P. Bean, Reviews of Modern Physics **36**, 31 (1964).

27 L. Ji, R. H. Sohn, G. C. Spalding, *et al.*, Physical Review B **40**, 10 936 (1989).

28 Y. B. Kim, C. F. Hempstead, and A. R. Strnad, Physcial Review Letters **9**, 306 (1962).

29 I. J. Daniel, "The fabrication of Chevrel phase superconductors and the origin of the irreversibility field" *Dept. of Physics*, University of Durham, (1999).

30 W. A. Fietz and W. W. Webb, Physical Review **178**, 657 (1969).

31 E. J. Kramer, Journal of applied physics **44**, 1360 (1972).

32 R. C. Morris, R. V. Colemann, and R. Bhandari, Physical Review B **5**, 895 (1972).

33 J. G. Bednorz and K. A. Muller, Z. Phys.B - Condensed Matter **64**, 189 (1986).

34 C. C. Tsuei, J. R. Kirtley, C. C. Chi, *et al.*, Physical Review Letters **73**, 593 (1994).

35 C. C. Tsuei, J. R. Kirtley, M. Rupp, *et al.*, Physica C **263**, 232 (1996).

36 A. J. Millis, H. Monien, and D. Pines, Physical review B **42**, 167 (1990).

37 A. E. Ruckenstein and C. M. Varma, Physica C **185 -189**, 134 (1991).

38 V. J. Emery, S. A. Kivelson, and O. Zachar, Physical Review B **56**, 6120 (1997).

39 T. Senthil and M. P. A. Fisher, Physical Review B **63**, 134521 (2001).

Chapter 3

Literature review of magnetic techniques

3.1 Introduction

Magnetic measurement techniques are an important analytical tool in experimental physics. They provide a method of measuring magnetic moments in solid state materials. The measurements are generally non-contact. This means that damage to the sample is avoided. They are also useful for measuring the magnetisation and thus the critical current density of superconductors[1]. The magnetic techniques available today are reviewed in section 3.2. The major forms of magnetism are presented in section 3.3. The original method of measuring torque is described in section 3.4. This includes the measurement of NbTi wire, to determine the critical current density. The more recent method of measuring the magnetic moment using cantilever torque magnetometry is reviewed in section 3.5. This includes the different types of cantilever available e.g. piezoresistive and capacitance. A comparison of the cantilevers is also presented. The different experimental results obtained on superconductors are presented in section 3.6. A description of the terminology for the torque magnetometry experiments performed in this thesis is presented in section 3.7.

3.2 Review of magnetic techniques

3.2.1 Vibrating sample magnetometer

The vibrating sample magnetometer (VSM) was developed by Foner in 1956 [2]. Over the last forty-five years, alteration and modifications have been made to the original design[3], [4]. The VSM now works at temperatures below 300 mK [5], fields up to 23 T, and pressures as high as 8 kbar[6].

The VSM consists of a solid rod, which vibrates between two pick-up coils. The sample is fixed to the bottom of the rod. It is aligned in the plane of the DC magnet. The sample is positioned in the centre of the pick-up coils, which are in the centre of the DC magnet. As the sample is vibrating between the pick-up coils the magnetic field is swept. The change in flux produces a voltage in the coils.

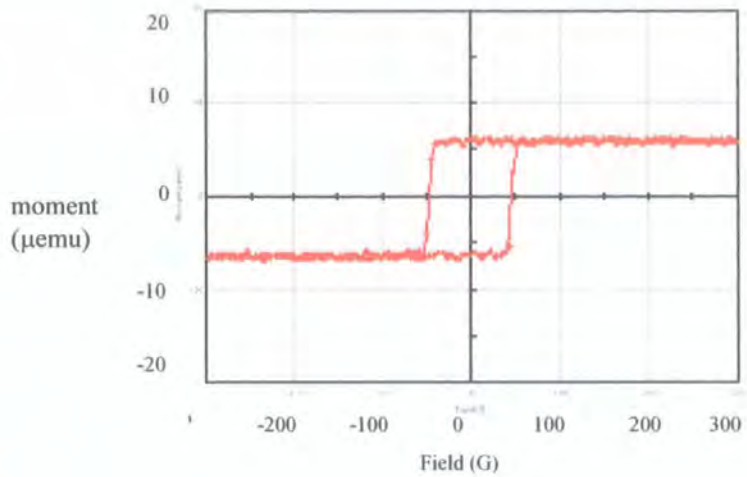

Figure 3.1. Magnetic moment of patterned NiFe film as a function of magnetic field, at 300 K. This is state of the art VSM data, taken by the latest Lakeshore VSM (Model 7400) [7]. The conversion to SI units for magnetic moment is 1 emu = 10^{-3} Am^2 and for magnetic field is 1 G = 10^{-4} T.

This voltage is measured using a lock-in amplifier, which is proportional to the magnetic moment. The sensitivity of a commercial VSM is 1 x 10^{-10} Am^2 (fig 3.1). The advantage of a VSM is they run in fields up to 23 T. They give faster hysteresis loops than SQUIDs. VSMs are easy to use. The sample size is mm, they are therefore used for bulk samples. The disadvantages are that commercial VSMs cannot go below 1.9 K. The vibrating rod causes heating. They are less sensitive than SQUIDs and torque cantilevers. In conclusion VSMs are the most used magnetometer.

3.2.2 SQUIDS

Superconducting quantum interference devices (SQUIDs) are based on Josephson tunnelling and flux quantisation[8]. There are two different types of SQUIDs. The first is the d.c. SQUID. It consists of two Josephson junctions in a superconducting loop. The junctions are damped separately by a resistor. The loop is biased by a current source. The voltage is then read across the parallel junctions. The second type is the RF SQUID. It consists of a superconducting loop with one Josephson junction. The loop is inductively coupled to a resonant LC circuit.

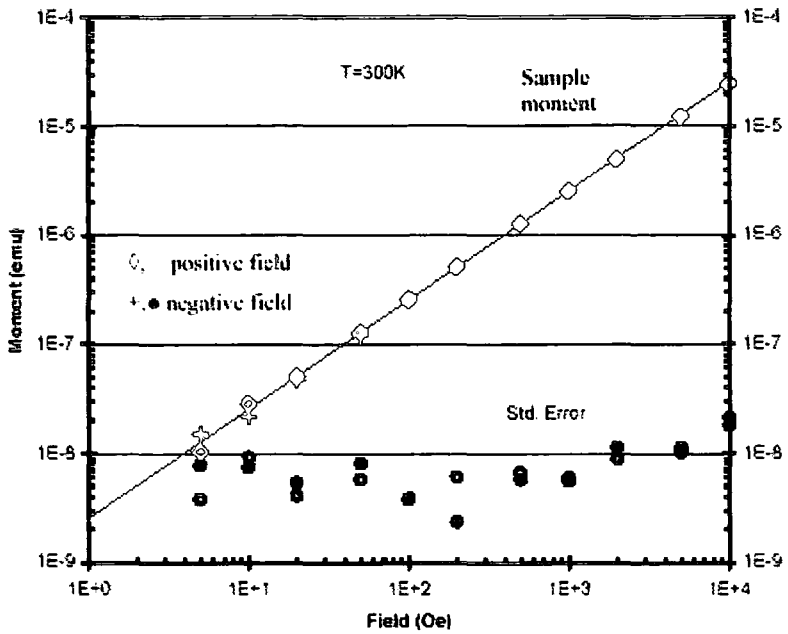

Figure 3.2. The magnetic moment and standard error value, for Er_2O_3 as a function of magnetic field, at 300 K. This is state of the art SQUID data taken by a Quantum Design SQUID[9].

The average voltage is read across the LC circuit. For both SQUIDs the voltage is periodic with the magnetic flux applied. The magnetic flux is applied to the loop, using a superconducting flux transformer loop. It transfers the flux induced into the pick-up coils to the SQUID loop. SQUIDs are made out of both low-T_c and high-T_c superconductors. For magnetic measurements, the sample is lowered through the pick-up coils.

SQUIDS can measure magnetic fields of the order 10^{-14} T and magnetic moments of the order 10^{-12} Am^2 (fig 3.2). Furthermore SQUIDS can work down to 10 mK. They are used to measure small samples. The disadvantage is that the maximum field they work in is 7 T. This is due to the necessity of shielding the Josephson junctions from the magnetic field. The other disadvantage is that the distance the sample is moved is centimetres. As a consequence the sample experiences an inhomogeneous field, which reduces the sensitivity[10].

3.2.3 AC susceptibility

The AC susceptibility experiment consists of a primary coil with two secondary coils, which are wound in opposite directions. The sample is fixed in the centre of one of

the secondary coils. A lockin amplifier is used to provide an ac current in the primary coil. The lockin then measures the difference in voltage across the secondary coils. The coils are balanced with no sample present. The change in flux is measured as the difference in voltage across the secondary coils, which is proportional to the susceptibility.

3.2.4 Faraday force balance

The Faraday balance is based on the force experienced by a magnetic moment in an inhomogeneous magnetic field. The basic design consists of the sample suspended from a rod in the centre of a homogenous field gradient[11]. There are different methods to produce a field gradient. These include adding a set of gradient coils into the centre of a homogenous magnet or having oblique pole faces. The force exerted by the sample is measured on an analytical balance.

Magnetic technique	Moment sensitivity at 1 T (Am^2)	accuracy
VSM[7 12]	1×10^{-10}	0.05 %
SQUID[9]	1×10^{-11}	0.01 %
AC susceptibility[13]	1×10^{-10}	0.1 %
Faraday force balance[14]	1.8×10^{-9}	0.05 %
Durham's Torque Magnetometer	1.2×10^{-8}	5 - 15 %

Table 3.1. Comparison of sensitivity and accuracy of the magnetic techniques used to measure the magnetic moment of isotropic materials. The sensitivity and accuracy are for the state of the art instruments available commercially.

3.3 Magnetic materials

In materials there are five major forms of magnetism. These are diamagnetism, paramagnetism, ferromagnetism, anti-ferromagnetism and ferrimagnetism. They are discussed in turn below.

Diamagnetism occurs in all materials. It is the weak magnetic moment induced by the orbiting electrons, when they experience a magnetic field. Diamagnetism is observed in materials where the atoms have completely paired electrons.

Paramagnetism occurs in materials where the local magnetic moments have no long-range interactions. The magnetisation of a paramagnet is given by:

$$M = Ng_J \mu_B J B_J(y) \tag{3.1}$$

where $B_J(y)$ is the Brillouin function, with $y = \left(g\mu_B J_m B / k_b T\right)$, g_J is the Lande factor, J_m is the angular momentum, μ_B is the Bohr magnetron and N is the number of atoms. The Brillouin function is given by:

$$B_J(y) = \left\{ \left(\frac{2J_m + 1}{2J_m} \right) \coth\left[\frac{(2J_m + 1)}{2J_m} y \right] - \left(\frac{1}{2J_m} \right) \coth\left[\frac{y}{2J_m} \right] \right\} \tag{3.2}$$

For zero magnetic field, the magnetisation is zero. For $B/T \to \infty$, the Brillouin function (eqn 3.2) tends towards one. This leads to the saturated magnetisation $M_{\max} = Ng\mu_B J_m$. Saturation occurs at high magnetic fields, and low temperatures.

For small magnetic fields ($y << 1$), eqn 3.2 is expanded in the form $\coth(y) = \frac{1}{y} + \frac{y}{3}$.

The magnetisation then becomes:

$$M = \frac{Ng_J^2 \mu_B^2 J_m (J_m + 1) B}{3k_b T} \tag{3.3}$$

For the paramagnetic susceptibility, the internal field is $B \approx \mu_o H$, thus the susceptibility is given by:

$$\chi = \frac{\mu_o M}{B} = \frac{\mu_o N g_J^2 \mu_B^2 J_m (J_m + 1)}{3k_b T} = \frac{C}{T} \tag{3.4}$$

where C is Curie's constant.

Ferromagnetism, anti-ferromagnetism and ferrimagnetism are all forms of magnetism, which occur below a material dependant critical temperature. Above this temperature the material is paramagnetic.

Ferromagnetism is the spontaneous alignment of magnetic dipoles in the same direction. It occurs below the Curie temperature (T_c). Ferromagnetism is seen in metals such as iron, cobalt and nickel.

Anti-ferromagnetism is the spontaneous alignment of magnetic dipoles in anti-parallel. This leads to a net magnetisation of zero. The spontaneous magnetisation occurs below the Neél temperature (T_N).

Ferrimagnetism is the spontaneous alignment of different strength magnetic dipoles in anti-parallel. For example, if a set of magnetic dipoles are aligned anti-parallel in a line, with the dipoles pointing upwards having a larger moment than the dipoles points downwards, then the net magnetic moment is in the upwards direction.

3.4 History of Torque magnetometry

Torque magnetometry is an established experiment. John Michell invented the torsion balance in the 1700's. The design consists of two masses attached to a torsion fibre. The masses would rotate due to an external field (magnetic, electric) inducing a torque. The angle of rotation is proportional to the torque. In 1785, Coulomb used a similar torsion balance to determine the force relationship between two electrostatic charges[15]. In 1798 Cavendish used a torsion balance to measure the gravitation constant G[15].

3.4.1 Mathur's torque magnetometry

In 1979, Mathur measured the critical current density of NbTi wire, using a torque torsion balance[16]. The experimental set-up consisted of a cylindrical NbTi sample attached to the bottom of a fixed torsion wire. The sample was fixed perpendicular to the field direction, with the axis along the torque balance axis. A horizontal iron magnet was rotated around the sample at constant speed. The maximum torque was measured.

3.4.1.1 Theory

The torque was measured as a function of angle. Using Friedel's expression[17], the critical current density (J_c) is related to the volume density pinning force (F_p):

$$F_p = BJ_c\mu_o \frac{dH_c(B)}{dB} \tag{3.5}$$

where B is the magnetic field and $H_e(B)$ is the reversible constitutive equation for the material without pinning.

From Wipf's expression, the torque is related to the pinning force per unit length (F_f). The maximum torque is given by:

$$\tau_{\max} = \frac{4F_f vol.RB}{3\pi\phi_o} \tag{3.6}$$

where ϕ_o is one flux quantum. The expression is for a cylinder of volume *vol* and radius R. Thus using the relation between the pinning forces $F_p = \frac{B}{\phi_o}F_f = nF_f$, where n is density of pinning sites. The critical current density with relation to the maximum torque is given by:

$$J_c = \frac{3\pi\tau_{\max}}{4vol.RB} \tag{3.7}$$

3.4.1.2 Experimental Results

Using eqn 3.7, the critical current density was determined for the NbTi wire. It was found to be in excellent agreement with the transport data[16].

3.5 Piezoresistive and capacitance cantilevers

3.5.1 History of piezoresistive cantilevers

In 1990, piezoresistive cantilevers were developed for atomic force microscopy (AFM)[18]. The cantilevers have a sharp point on the end of the platform, which is pulled across the surface of the sample. The change in topography of the surface is measured by the change in position of the cantilever[19]. This is done by a number of different methods. These include measuring the change in resistance across a Wheatstone bridge[19] where the cantilever is one of the resistors in the bridge, measuring the change in position of a laser beam reflected off the chip[20] and measuring the position via capacitance. Piezoresistive cantilevers are also used in conjunction with a SEM[21].

3.5.2 Piezoresistive cantilever design

The original piezoresistive cantilevers used in torque magnetometry were also used in AFM[22]. They are made commercially by Parks Scientific.

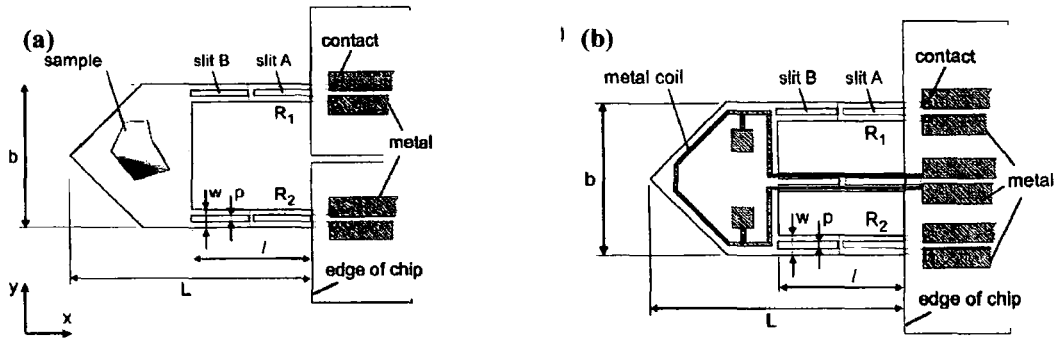

Figure 3.3a. Diagram of the two-leg piezoresistive cantilever, designed for AFM. Diagram taken from the Brugger *et al* paper[23]. **Figure 3.3b**. Diagram of the three-leg piezoresistive cantilever, designed by Brugger for torque magnetometry measurements [23].

Cantilevers were developed to have either two or three legs[23, 24] (fig 3.3). They are made from a single crystal of silicon. The silicon is etched away to leave the platform and legs. The legs are fabricated in the <110> direction. Boron is doped on to the surface of each leg. Boron is an acceptor ion, thus creates a p-type piezoresistor, on each leg. The change in resistance is linear with deflection. In fig. 3.3b, the third leg carries the calibration loop to the platform. The calibration loops provides an absolute way of calibrating the cantilever. It unfortunately decreases the sensitivity of the cantilever, as it adds extra stiffness.

The cantilevers can work in either torsion mode or flexion mode[24]. The torsion mode measures the torque in the x-direction. It measures $\Delta(R_1 - R_2)$, which is the torque about the centre of the lever (fig. 3.3a). The flexion mode measures the torque in the y-direction. It measures $\Delta(R_1 + R_2)$, which is the torque along both of the legs. The cantilevers are used in either the static regime or resonance regime[22]. In the static regime the cantilever is stationary. The change in deflection due to the torque is measured across the Wheatstone bridge arrangement. The resonance regime uses a bimorph to vibrate the cantilever, at an appropriate frequency and amplitude[24]. The cantilever and sample are driven into resonance. A lockin amplifier measures the change in phase or amplitude due to a change in the magnetic field. The advantage with the resonance regime is that it has a higher sensitivity than the static regime.

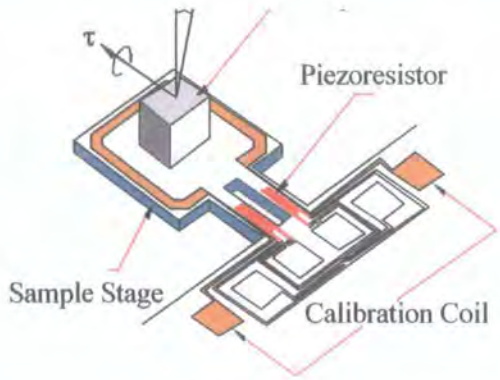

Figure 3.4. Diagram of the Quantum Design piezoresistive torque chip. A protective silicon barrier surrounds the chip's platform[25].

Quantum Design has developed a torque chip[25], which is depicted in fig. 3.4. The chip consists of a 25 μm thick sample stage of area 2 x 2 mm^2. The chip is etched from a silicon (100) wafer, with the legs along the <110> direction. On each of the legs a constantan resistor is patterned. The gravitational force is minimised, by the Wheatstone bridge circuit patterned on the chip. The change in resistance across the Wheatstone bridge is linearly proportional to the torque. The chip is calibrated using the calibration loop on the stage. The thick border of silicon around the stage protects it. It also makes it easier to handle the chip.

3.5.3 Capacitance cantilever design

There are two different designs for capacitance cantilevers. The first design has a fixed base plate. Above the base plate is the top plate, which can only move in the direction of the base plate. This is defined as the *z*-direction[26, 27]. The sample is mounted on top of the top plate. For angular measurements, a horizontal magnet is rotated about the cantilever. The change in capacitance is measured at different angles. It is directly proportional to the applied torque. A variation of this cantilever is the silicon cantilever magnetometer (SCM). It is used in pulsed magnetic fields[28, 29]. The SCM consists of a silicon cantilever plate with a conductive surface, suspended over a fixed conducting plate. The SCM is used down to 20 mK, in pulsed fields up to 36 T.

The second design consists of a torsion beam in the centre of two capacitance plates[30, 31]. The sample is mounted on the end of the beam. The torque from the sample

moves the beam. This changes the capacitance, which is proportional to the torque. The design was miniaturised, by using a microfabricated silicon torsion beam between two electrodes[32]. The sample is glued in the middle of the torsion balance. The whole set-up is placed in a magnetic field. The change in capacitance between the electrodes is linearly proportional to the applied torque[32]. The advantage over the plate design is that the torsion meter is symmetrical. This means it can be mounted on a horizontal axis. This is useful for vertical superconducting magnets.

3.5.4 Advantages and Disadvantages

	Sample	Sensitivity (Nm)	Sensitivity (Am^2)	accuracy	Size (μm^3)
Piezoresistive cantilever – 2 legs	$Tl_2Ba_2CuO_{6+d}$[33] $Bi_2Sr_2CaCu_2O_8$[22]	1.1 x 10^{-14}[22]	~ 10^{-12}[33]	~1 %[22]	200 x 10 x 4[24]
Piezoresistive cantilever – 3 legs	Calibration loop area ~ 1.2 x 10^{-8} m^2[24]	10^{-12} (static)[23] 10^{-14} (dynamic)[24]	1.2 x 10^{-11}	1%[22]	240 x 10 x 4[24]
QD torque magnetometer	$Bi_2Sr_2CaCuO_{8+d}$[25]	2 x 10^{-9}	2 x 10^{-10} at 10 T	1 %	2000 x 2000 x 25
Silicon capacitance cantilever	$YBa_2Cu_3O_7$[28]	2.8 x 10^{-9}[28]	2.5 x 10^{-12}[28]		2000 x 1000 x 5[28]
Torsion beam cantilever[30]	Pb $Nd_{2-x}Ce_xCuO_{4-d}$	2.4 x 10^{-12}	3.4 x 10^{-13}		19000 x 1000 x 29
Silicon torsion beam cantilever	Fe_2O_3 NdFeB[32]	3 x 10^{-13}	3 x 10^{-13}	~ 3 %	5250 x 1500 x 40

Table 3.2. Comparison of torque magnetometers used to measure anisotropic materials, including superconductors.

A summary of the torque magnetometers is presented in table 3.2. The sensitivities for each method are given in torque as well as magnetic moment. The size of each magnetometer is also included.

Piezoresistive cantilevers are small devices (200 x 117 x 5 μm^3). This means the strength of the diamagnetic background is reduced. It also means that small samples such as single crystals can be measured. The cantilevers can be rotated about the horizontal axis, as the capacitance of the leads is unimportant. They are used in solenoid magnets, in fields up to 23 T. They are stand-alone devices. They have been used in dilution fridges[34].

The piezoresistors on the legs of the cantilever are strongly field and temperature dependant. A second cantilever is measured in situ. This cantilever is used as a background reference. The cantilevers are very fragile.

Capacitance cantilevers are temperature and field independent. This means a second cantilever is not required in situ. In addition they are more robust than piezoresistive cantilevers. This is because they are larger in size.

Capacitance cantilevers are hard to miniaturise. This means it is more difficult to obtain the same sensitivity as a piezoresistive cantilever. The cantilevers are sensitive to movement in the twisted pair leads, which produces additional capacitance. They are fixed in position for rotation measurements. The magnet used is a horizontal split magnet with maximum field 8 T. The capacitance bridge required to balance these devices is very expensive.

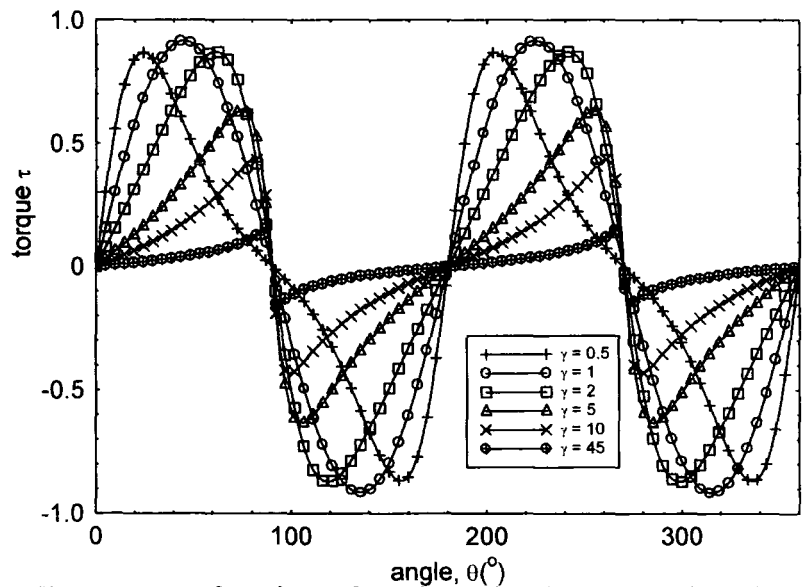

Figure 3.5. Torque as a function of angle and anisotropy, plotted using Kogan's equation[35].

3.5.5 Other applications for cantilevers

Piezoresistive cantilevers have been used for other applications. This is because any external perturbation such as chemical, thermal or magnetic can be converted into a mechanical motion. The cantilevers are useful due to they're small size. They are also stand-alone devices. The applications include measurements of magnetic moments[36] and magnetic anisotropy[37]. They have also been used in measurements of Fermi surfaces by Haas-van Alphen experiments[34, 38].

3.6 Torque cantilever measurements on superconductors

3.6.1 Kogan's equation

In 1988, Kogan derived an equation, which related the torque of a sample in a magnetic field to the anisotropy (γ_m)[35]. The equation is derived from the internal energy of an anisotropic superconductor, as a function of angle (θ), and applied magnetic field (H)[39]. The torque as a function of angle, for constant magnetic field & temperature is given by:

$$\tau(\theta) = \frac{\phi_o H vol}{64\pi^2\lambda^2}\frac{\gamma_m^2 - 1}{\gamma_m^{2/3}}\frac{\sin 2\theta}{\varepsilon(\theta)}\ln\frac{\gamma_m \eta H_{c2}}{H\varepsilon(\theta)} \qquad (3.8)$$

where $\varepsilon(\theta) = \left(\sin^2\theta + \gamma_m^2\cos^2\theta\right)^{1/2}$, *vol* is the volume of the sample, H is the applied magnetic field, ϕ_o is one flux quanta, λ is the penetration depth and $\eta \approx 1$. The dependence of the torque on the anisotropy is shown in fig. 3.5. For $\gamma_m = 1$, the torque has $\sin 2\theta$ dependence.

3.6.2 Measurements of the anisotropy

Piezoresistive cantilevers have been used to measure the anisotropy of superconductors. The temperature and applied magnetic field are held constant, while the sample is rotated in the field. The torque is measured as a function of angle. The anisotropy is determined using Kogan's equation (eqn. 3.8). The temperature and magnetic field are calculated for the superconductor's reversible magnetisation region. The measurement has been carried out on a range of different superconductors including MgB_2[40], $YBa_2Cu_3O_{7-d}$[41, 42], $La_{1.9}Sr_{0.1}CuO_4$[43], $Bi_2Sr_2CaCuO_8$[27] and $Tl_2Ba_2CuO_{6+d}$[33]. At temperatures below T_c, high-T_c superconductors show 2D behaviour, due to their layered structure. At temperatures close to T_c they show 3D

behaviour. By measuring the change in anisotropy as a function of temperature, the 2D – 3D crossover temperature is determined[41].

3.6.3 Irreversibility field and irreversible magnetisation

In the irreversible magnetisation region, the torque data is hysteretic as a function of angle. The angle at which the hysteresis loop starts is the irreversible angle (θ_{irr}). If the anisotropy is large $(\gamma_m > 40)$, the irreversibility field is given by[33]:

$$H_{irr} = H\cos\theta_{irr} \tag{3.9}$$

The irreversible magnetisation is derived from the hysteretic torque as a function of angle[44 45]. The irreversible part of the magnetisation is given by:

$$M_{irr} = \frac{\Delta\tau}{(\mu_o H vol.\sin\theta_{irr})} \tag{3.10}$$

Thus the current density is $J = \frac{M_{irr}}{\gamma_{sf}}$ (eqn 2.33). Eqn 3.10 is valid if it is assumed that the magnetisation component is only in the *c*-direction. Another way of measuring the magnetisation is to apply a magnetic field (H_{app}) along the c-axis, and a second constant field ($H_{\|}$) parallel to the a,b plane[46]. The torque is measured in the *c*-direction, while H_{app} is swept. The magnetisation hysteresis curves are then used to determine the irreversible field (H_{irr}) and the transformation field (H_m).

In the irreversible magnetisation region, the reversible and irreversible torque components as a function of angle can often be calculated from[47]:

$$\begin{aligned} \tau_{rev}(\theta) &= \tfrac{1}{2}\left[\tau_+(\theta) + \tau_-(\theta)\right] \\ \tau_{irr}(\theta) &= \tfrac{1}{2}\left[\tau_+(\theta) - \tau_-(\theta)\right] \end{aligned} \tag{3.11}$$

where τ_+ is the torque for the up field sweep, and τ_- is the torque for the down field sweep. The irreversible torque component is the difference across the hysteresis loop. It is a measure of the effective pinning force[47]. The reversible torque component is the average value of the torque signal. It is proportional to the magnetisation, thus the fundamental superconducting parameters can be calculated[47].

3.6.4 Other measurements in the literature.

The capacitance cantilever was used to measure the re-entrant behaviour of $DyNi_2B_2C$[48], at 0.4 K. For a swept magnetic field, the change in capacitance was

proportional to the applied torque. The different phases of $DyNi_2B_2C$ were determined by the changes in the torque. The capacitance cantilever was used to investigate the flux jump avalanches in $YBa_2Cu_3O_{7-\delta}$[49]. At 5 T, the torque was measured as a function of angle. Between 15 – 30° jumps were observed in the torque hysteresis loop. These jumps were attributed to the crossover from a tilted to a kinked vortex structure.

3.7 Terminology of magnetic torque

3.7.1 Torque theory

In this thesis a field-gradient torque magnetometer was used to measure the critical current density of isotropic superconductors. The following section introduces the theory behind the field-gradient torque magnetometer. It also includes a summary of demagnetisation factors and shape factors.

When a current loop is placed at an angle θ, in a uniform magnetic field (**B**), the torque experienced by the loop is:

$$\tau = IAB\sin\theta\hat{\mathbf{s}} = I\hat{\mathbf{A}}\times\mathbf{B} = \mathbf{m}\times\mathbf{B} \tag{3.12}$$

where the moment is defined as $\mathbf{m} = I\hat{\mathbf{A}}$, and I is the current around the loop of area $\hat{\mathbf{A}}$ and $\hat{\mathbf{s}}$ is an unit vector perpendicular to the area and the magnetic field. In a uniform magnetic field the force experienced by the loop is zero. However when the current loop is placed in a field gradient, it experiences a force and a torque. The torque is the same as in a uniform field $\tau = \mathbf{m}\times\mathbf{B}$. The force is given by:

$$\mathbf{F} = (\mathbf{m}\cdot\nabla)\mathbf{B} \tag{3.13}$$

Therefore in a field gradient the total torque on the current loop is:

$$\tau = \mathbf{l}\times\mathbf{F} + \mathbf{m}\times\mathbf{B} \tag{3.14a}$$

$$\tau = \mathbf{l}\times((\mathbf{m}\cdot\nabla)\mathbf{B}) + \mathbf{m}\times\mathbf{B} \tag{3.14b}$$

where **l** is the distance between the force and the axis of rotation.

3.7.2 Angular dependence of the magnetic moment of an anisotropic reversible superconductor

From Cape *et al* paper[50], when an anisotropic, reversible superconductor is placed in an applied local magnetic field, with the field along one of its symmetry axis, the magnetic moment ($\mathbf{m}_s$) is parallel to the field.

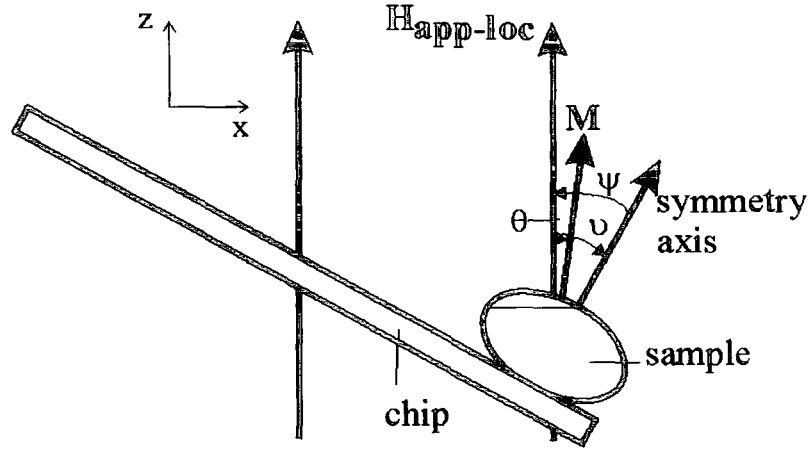

Figure 3.6. Diagram of an anisotropic, reversible superconductor in an applied, local magnetic field ($\mathbf{H_{app\text{-}loc}}$). The field is not aligned with the symmetry axis of the super conductor. The angle ψ is between the symmetry axis and the field, the angle υ is between the reversible magnetisation ($\mathbf{M}$) and the symmetry axis, and the angle θ is between the magnetisation and the field.

When the field is not aligned with the symmetry axis, then the magnetisation is not parallel to the field (fig. 3.6). Thus the sample experiences a torque, which is described by[50 i]:

$$\tau = \mu_o vol\left(M_\perp H_{app-loc\parallel} - M_\parallel H_{app-loc\perp} \right) \tag{3.15}$$

where $\perp$ and $\parallel$ represent the perpendicular and parallel directions in relation to the symmetry axis respectively so that $H_{app-loc\perp}$ is the component of the applied local field perpendicular to the symmetry axis and $H_{app-loc\parallel}$ is the component of the applied local field parallel to the symmetry axis. For a type-II superconductor in the mixed state, the angle between the magnetisation and the symmetry axis is υ, this means the magnetisation components can be expressed as:

$$M_\parallel = M_{rev}\cos\upsilon\,,\quad M_\perp = M_{rev}\sin\upsilon \tag{3.16}$$

where $M_{rev} = \dfrac{(H - H_{c2})}{(2\kappa^2 - 1)\beta_A}$, H_{c2} is the upper critical field, κ is the GL parameter and β_A is the Abrikosov's constant (cf. eqn. 2.28).

---

[i] In the Cape paper[50], the torque experienced by the sample is given by $\tau = \mu_o vol\left(M_\perp H_{app-loc\perp} - M_\parallel H_{app-loc\perp} \right)$, rather than the correct version which is eqn 3.15.

The magnetisation components can also be written in terms of the local field, and the demagnetisation factor ($\bar{N}$) so:

$$M_{\parallel} = \frac{H_{app-loc}\cos\psi - H_{c2}\cos\upsilon}{\gamma + \bar{N}} \;,\; M_{\perp} = \frac{H_{app-loc}\sin\psi - H_{c2}\sin\upsilon}{\gamma + (1-\bar{N})/2} \qquad (3.17)$$

where ψ is the angle between the symmetry axis and the local field, $\gamma = (2\kappa^2 - 1)\beta_A$. The relation between the angles is $\upsilon = \psi + \theta$, where θ is the angle between the magnetisation and the local field. Combining eqn 3.16 and 3.17 gives:

$$\cos\upsilon \equiv \cos(\psi+\theta) = \frac{H_{app-loc}\cos\psi}{(\gamma+\bar{N})M_{rev} + H_{c2}}$$

$$\sin\upsilon \equiv \sin(\psi+\theta) = \frac{H_{app-loc}\sin\psi}{(\gamma+(1-\bar{N})/2)M_{rev} + H_{c2}} \qquad (3.18)$$

Eqn 3.18, $H_{app-loc\parallel} = H_{app-loc}\cos\psi$ and $H_{app-loc\perp} = H_{app-loc}\sin\psi$ are substituted in eqn 3.15, to give the general torque on a superconducting sample:

$$\tau = \mu_o vol.(3\bar{N}-1)\left(\frac{H_{app-loc}^2 \sin 2\psi}{4}\right) \times \frac{M_{rev}^2}{\left[(\gamma+\bar{N})M_{rev} + H_{c2}\right]\left\{\left[\gamma + (\bar{N}-1/2)\right]M_{rev} + H_{c2}\right\}} \qquad (3.19)$$

Thus if the magnetic field is not aligned with a symmetry axis, the magnetisation is not parallel to the field, and a torque experienced by the sample. When the sample is rotated in the field, the angular dependence of the torque is $\sin 2\psi$.

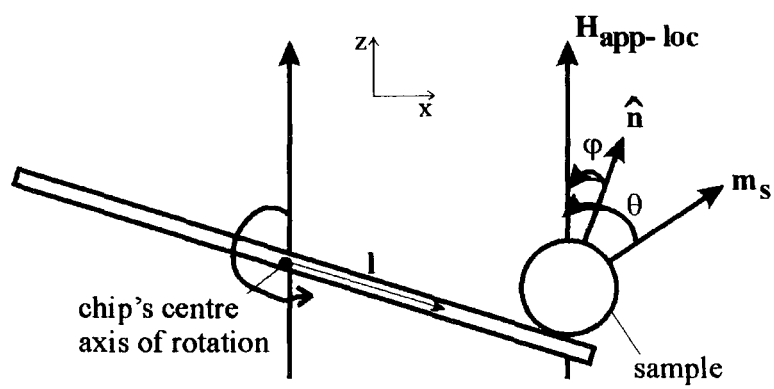

Figure 3.7. Schematic diagram of the experimental set-up of the QD torque chip, in an applied local magnetic field, $\mathbf{H_{app\text{-}loc}}$. In the figure $\hat{\mathbf{n}}$ is normal to the chip, **l** is the distance between the sample and the centre of rotation of the chip and $\mathbf{m_s}$ is the sample moment. The angle θ is between the sample moment and the magnetic field and the angle φ is between the normal to the chip and the magnetic field.

3.7.3 Torque magnetometry in a field gradient for a superconductor with pinning

From fig. 3.7, and eqn 3.14b, the torque for a reversible sample (i.e. with no pinning and neglecting shape and anisotropy effects) is given by:

$$\tau = \mu_o m_z \mathbf{l} \times \frac{d\mathbf{H}_{app-loc}}{dz} \tag{3.20}$$

Eqn 3.20 describes the behaviour of the superconducting moment in the field gradient, when the moment is aligned with the local field. The torque is measured as the change in resistance (ΔR) across a Wheatstone bridge ($\frac{\Delta V}{I} = \Delta R = \alpha_R \tau$), where α_R is the sensitivity of the chip. It is measured as the change in resistance as the Wheatstone bridge is not zero. Thus the change in resistance is given by:

$$\frac{\Delta \boldsymbol{R}}{\alpha_R} = \mu_o |m_s| \cos\theta l \cos\varphi \frac{dH_{app-loc}}{dz} \tag{3.21}$$

If we now consider an isotropic superconductor with pinning, the magnetic moment ($\mathbf{m_s}$) would be parallel to the applied local field ($\mathbf{H_{app\text{-}loc}}$). The angle $\varphi = 0$, and θ changes by 180°. Thus the difference in resistance across the magnetic hysteresis loop $\left(\Delta R_{+-} = \Delta R_{+} - \Delta R_{-}\right)$ is given by:

$$\frac{\Delta R_{+-}}{\alpha_R} = l \left|\Delta m_{s+-}\right| \mu_o \frac{dH_{app-loc}}{dz} \tag{3.22}$$

where $\left|\Delta m_{s+-}\right| = \left|m_{s+}\right| + \left|m_{s-}\right|$, which are the magnitude of the moments for the field sweep up $\left(\left|m_{s+}\right|\right)$ and the field sweep down $\left(\left|m_{s-}\right|\right)$. Rearranging eqn. 3.22 in terms of the moment gives:

$$\left|\Delta m_{s+-}\right| = \frac{1}{\alpha_R l} \frac{d\Delta R_{+-}}{d\left(\mu_o \frac{dH_{app-loc}}{dz}\right)} \tag{3.23}$$

From Bean's model[1], the critical current density is the difference in magnetisation across the hysteresis loop divided by the shape factor (eqn 2.33). The magnetisation of a sample is the magnetic moment divided by the samples' volume. Thus the critical current density is given by:

$$J_c = \frac{\Delta M}{\gamma_{sf}} = \frac{\left|\Delta m_{s+-}\right|}{\gamma_{sf}.vol} = \frac{1}{\alpha_R \gamma_{sf}.vol.l} \frac{d\Delta R_{+-}}{d\left(\mu_o \frac{dH_{app-loc}}{dz}\right)} \tag{3.24}$$

Now consider an anisotropic hysteretic sample, at the reversible angle ($\theta = 0^{o}$), the magnetic moment is aligned with the local field (cf. eqn. 3.14b), but φ need not be zero. Thus the critical current density of an anisotropic superconductor taken at the reversible angle is given by:

$$J_c = \frac{\Delta M}{\gamma_{sf}} = \frac{|\Delta m_{s+-}|}{\gamma_{sf}.vol} = \frac{1}{\alpha_R \gamma_{sf}.vol.l\cos\varphi} \frac{d\Delta R_{+-}}{d\left(\mu_o \frac{dH_{app-loc}}{dz}\right)} \tag{3.25}$$

3.7.4 Demagnetisation factors

The shape of a sample is important when measuring its magnetic moment. The demagnetisation factor relates the internal field (B_{int}) to the external field strength (H_{app}) and the uniform magnetisation (M)[51]. The internal magnetic field (B_{int}) for a magnetic material with uniform magnetisation is given by[52]:

$$\mathbf{B}_{\text{int}} = \mu_o(\mathbf{H} + \mathbf{M}) \tag{3.26}$$

The field strength (**H**) can be written in terms of the applied magnetic field and the demagnetisation field ($\mathbf{H_d}$). It is given by:

$$\mathbf{H} = \mathbf{H}_{app} + \mathbf{H}_d = \mathbf{H}_{app} - \tilde{N}\mathbf{M} \tag{3.27}$$

The demagnetisation factor $\tilde{N}$ has the form of a tensor in eqn 3.28. Thus substituting equation 3.27 into equation 3.26, the internal magnetic field of the material is:

$$\mathbf{B}_{\text{int}} = \mu_o\left(\mathbf{H}_{app} + (1 - \tilde{N})\mathbf{M}\right) \tag{3.28}$$

If the field is taken to be along the c-direction of a sample, where the axis lengths are defined as $a = b \neq c$, the demagnetisation factors for each axis are $N_c = N_{\parallel}$ and $N_a = N_b = N_{\perp}$. The factors are bound by the constraint $N_{\parallel} + 2N_{\perp} = 1$.

The simplest shapes to determine demagnetisation factors for are ellipsoids. They have known demagnetisation factors, which were derived by Osborn [53]. For a prolate ellipsoid[54] ($c > a$), the demagnetisation factor is given by:

$$N_{\parallel} = \frac{1-\varepsilon_d^2}{\varepsilon_d^2}\left[\frac{1}{2\varepsilon_d}\ln\left(\frac{1+\varepsilon_d}{1-\varepsilon_d}\right) - 1\right] \text{ where } \varepsilon_d = \left[1 - \frac{a^2}{c^2}\right]^{1/2} \tag{3.29}$$

and for an oblate ellipsoid[54] ($c < a$):

$$N_{\parallel} = \frac{1}{\varepsilon_d^2} - \frac{\left[1-\varepsilon_d^2\right]^{1/2}}{\varepsilon_d^3}\sin^{-1}\varepsilon_d \text{ where } \varepsilon_d = \left[1 - \frac{c^2}{a^2}\right]^{1/2} \tag{3.30}$$

Eqns 3.29 & 3.30 can be approximated for other shapes. For a long rod ($c > a$)[54], the demagnetisation factors are given by:

$$N_{\parallel} = \frac{a^2}{2c^2}\left[\frac{1}{2}\ln\left(\frac{2c^2}{a^2}\right) - 1\right] \;\&\; N_{\perp} = \frac{1}{2}\left(1 - \frac{a^2}{c^2}\left[\ln\left(\frac{\sqrt{2}c}{a}\right) - 1\right]\right) \qquad (3.31)$$

Equation 3.31 is approximated for a wire ($c>>a$)[54] to be $N_{\parallel} = 0$, $N_{\perp} = \frac{1}{2}$. Eqn 3.30 is approximated for a flat disc ($c << a$)[54] to be $N_{\parallel} \approx 1$, $N_{\perp} \approx 0$.

The Meissner effect in a superconductor is a special case. The internal magnetic field is zero, thus $\mathbf{H}_{app} = -(1-N)\mathbf{M}$. It is assumed that there are no demagnetisation effects, thus is $N_{||} = 0$, and $\mathbf{H}_{app} = -\mathbf{M}$ [54].

3.7.5 Shape Factors

The shape factor (γ_{sf}) is used to determine the critical current density of superconductors. The shape factor differs from the demagnetisation factor as the magnetisation is not uniform. The magnetisation is taken to be a function of the applied magnetic field and the internal magnetic field.

For isotropic superconductors in an applied magnetic field, the critical currents flow in a direction perpendicular to the applied field. The critical current density is proportional to the difference in magnetisation across a hysteresis loop, divided by the shape factor[1]. The shape factor is determined for applied magnetic fields greater than the characteristic field[55] ($B^* = \mu_o J_c l$).

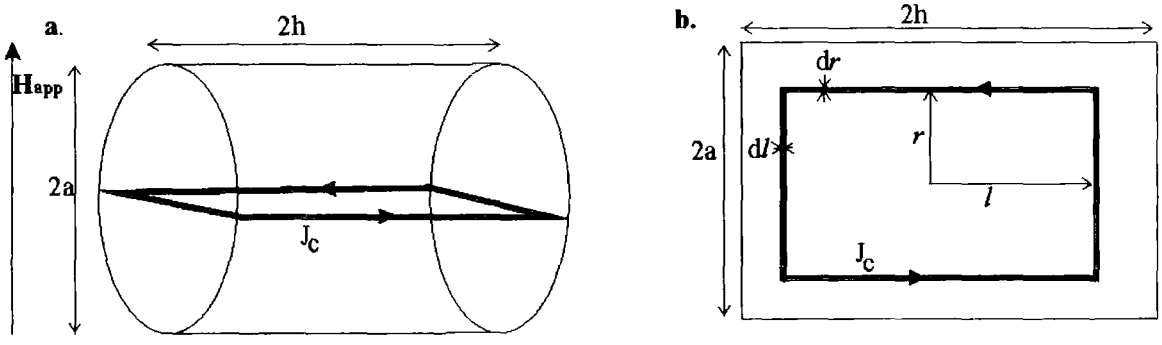

Figure 3.8a. Diagram of a superconducting cylinder with an applied field along the radius. **Figure 3.8b**. A view of a cross-sectional area of the cylinder, with a current loop flowing through it.

From fig. 3.8a the magnetic field is applied perpendicular to the long axis of the cylinder. This means the width and the height of the current loops change with radius. An average radius is determined between 0 and 90 degrees. It is given by:

$$\langle r \rangle = \frac{\frac{\pi}{2}\int_0^a r dr}{\frac{\pi}{2}\int_0^a dr} = \frac{a}{2} \tag{3.32}$$

This means the average height of the whole cylinder in the radial direction is *2a*. The magnetic flux will penetrate the same distance from all sides. This leads to the relation between the radius (*r*) and the length (*l*) being $l - h = r - a$. The critical current density is a constant J_c. From fig. 3.7b, the area enclosed by the loop is *2r2l*. The current flowing around the loop is $I = J_c 2adr$. Therefore the moment of the current loop is $dm = IA = J_c 2a2r2ldr = J_c 8ar(r - a + h)dr$.

The total moment for the cylinder is:

$$\begin{aligned} m &= \int dm = \int_0^a 8J_c ar(r - a + h)dr \\ m &= 4J_c a^3 h\left[1 - \frac{a}{3h}\right] \end{aligned} \tag{3.33}$$

Substituting the volume of the cylinder ($\pi a^2 2h$) into eqn 3.33. The moment for one field direction is $m = 2aJ_c \frac{vol}{\pi}\left[1 - \frac{a}{3h}\right]$. The difference in moment across the hysteresis loop is given by:

$$\Delta m = m_+ - m_- = 4J_c \frac{vol}{\pi} a\left[1 - \frac{a}{3h}\right] \tag{3.34}$$

Rearranging eqn. 3.34, to give the critical current density:

$$J_c = \frac{\Delta m}{4a\frac{vol}{\pi}\left[1 - \frac{a}{3h}\right]} = \frac{\Delta M}{a\left[1 - \frac{a}{3h}\right]} \cdot \frac{\pi}{4} \tag{3.35}$$

This gives the shape factor $\gamma_{sf} = \frac{4a}{\pi}\left[1 - \frac{a}{3h}\right]$. For a wire ($2c >> 2a$), the shape factor is $\gamma_{sf} = \frac{4a}{\pi}$. For a cylinder with radius *a*, with the field along the long axis the shape factor is $\gamma_{sf} = \frac{2a}{3}$. For a rectangular parallelepiped ($vol = 2a \times 2b \times 2c$), with the field along the c-axis, the shape factor is $\gamma_{sf} = a\left[1 - \frac{a}{3b}\right]$[56].

3.8 Conclusions

In superconductivity, magnetic techniques are important as they are used to characterise superconductors. They provide a damage free method of measuring the magnetic moment. The magnetic moment as a function of magnetic field, is used to determine the critical current density, the upper critical field, and the GL parameter (κ). Torque cantilever magnetometry has been used to measure the anisotropy, and magnetisation of superconductors. The advantage it has over commercial VSMs is it is a factor 100 more sensitive. Torque cantilever magnetometers also work in fields up to 23 T and temperatures down to 10 mK. This makes then ideal devices to measure the magnetic properties of superconductors.

References for Chapter 3

1 C. P. Bean, Reviews of Modern Physics **36**, 31 (1964).

2 S. Foner, Review of Scientific Instruments **27**, 548 (1956).

3 S. Foner, Review of Scientific Instruments **46**, 1425 (1975).

4 S. Foner, Review of Scientific Instruments **30**, 548 (1959).

5 N. F. Oliveira and S. Foner, Review of Scientific Instruments **43**, 37 (1972).

6 R. P. Guertin and S. Foner, Review of Scientific Instruments **45**, 863 (1974).

7 B. C. Dodrill, (Lakeshore Cryotronics inc, 2002).

8 J. Flokstra, in *Handbook of applied superconductivity*, edited by B. Seeber (Institute of physics publishing, Bristol and Philadelphia, 1998), Vol. 2, p. 1777 .

9 Quantum Design, (Quantum Design, 2001).

10 I. J. Daniel and D. P. Hampshire, Physical Review B **61** (2000).

11 H. Zijlstra, *Experimental methods in magnetism 2. Measurement of magnetic quantities* (North Holland.

12 D. Dufeu and P. Lethuillier, Review of Scientific Instruments **70**, 3035 (1999).

13 A. Bajpai and A. Banerjee, Review of Scientific Instruments **68**, 4075 (1997).

14 Abbess Instruments, (Abbess Instruments, 2002).

15 Tipler, *Physics for scientists and engineers* (Worth, 1991).

16 M. P. Mathur, D. W. Deis, and M. Ashkin, Journal of Applied Physics **44**, 5116 (1973).

17 J. Friedel, P. G. D. Gennes, and J. Matricon, Applied physics letters **2**, 119 (1963).

18 T. R. Albrecht, S. Akamine, T. E. Carver, *et al.*, Journal of Vacuum Science and Technology **8**, 3386 (1990).

19 M. Tortonese, R. C. Barrett, and C. F. Quate, Applied Physics Letters **62**, 834 (1993).

20 G. Meyer and N. M. Amer, Applied Physics Letters **53**, 1045 (1988).

21 U. Stahl, C. W. Yuan, A. L. d. Lozanne, *et al.*, Applied Physics Letters **65**, 2878 (1994).

22 C. Rossel, P. Bauer, D. Zech, *et al.*, Journal of Applied Physics **79**, 8166 (1996).

23 J. Brugger, M. Despont, C. Rossel, *et al.*, Sensors and Actuators **73**, 235 (1998).

24 M. Willemin, C. Rossel, J. Brugger, *et al.*, Journal of Applied Physics **83**, 1163 (1998).

25 S. Spagna, A. Wilson, M. B. Simmonds, *et al.* (2001).

26 R. Hohne, C. A. Kleint, A. V. Pan, *et al.*, Journal of Magnetism and Magnetic Materials **211**, 271 (2000).

27 H. G. Schnack, R. Griessen, P. Noordeloos, *et al.*, Physic C **266**, 285 (1996).

28 M. J. Naughton, J. P. Ulmet, A. Narjis, *et al.*, Review of Scientific Instruments **68**, 4061 (1997).

29 M. J. Naughton, J. P. Ulmet, A. Narjis, *et al.*, Physica B **246-247**, 125 (1998).

30 M. Qvarford, K. Heeck, J. G. Lensink, *et al.*, Review of Scientific Instruments **63**, 5726 (1992).

31 M. Weber, R. Koch, and K. H. Rieder, Physical Review Letters **73**, 1166 (1994).

32 C. Rossel, M. Willemin, A. Gasser, *et al.*, Review of Scientific Instruments **69**, 3199 (1998).

33 C. Bergemann, A. W. Tyler, A. P. Mackenzie, *et al.*, Physical Review B **57**, 14 387 (1998).

34 C. Lupien, B. Ellman, P. Grutter, *et al.*, Applied Physics Letters **74**, 451 (1999).

35 V. G. Kogan, Physical review B **38**, 7049 (1988).

36 M. Lohndorf, J. Moreland, P. Kabos, *et al.*, Journal of Applied Physics **87**, 5995 (2000).

37 K. Steenbeck and R. Hiergeist, Applied Physics Letters **75**, 1778 (1999).

38 C. Bergemann, S. R. Julian, A. P. Mackenzie, *et al.*, Physica C **317-318**, 444 (1999).

39 L. J. Campbell, M. M. Doria, and V. G. Kogan, Physical Review B **38**, 2439 (1988).

40 M. Angst, R. Puznial, A. Wisniewski, *et al.*, Physical Review Letters **88**, 167004 (2002).

41 D. E. Farrell, J. P. Rice, D. M. Ginsberg, *et al.*, Physical Review Letters **64**, 1573 (1990).

42 C. Ager, F. Y. Ogrin, S. L. Lee, *et al.*, Physical Review B **62**, 3528 (2000).

43 M. Willemin, C. Rossel, J. Hofer, *et al.*, Physical Review B **59**, R717 (1999).

44 R. Hiergeist and R. Hergt, Physical Review B **55**, 3258 (1996).

45 A. Morello, A. G. M. Jansen, R. S. Gonnelli, *et al.*, Physical Review B **61**, 9113 (2000).

46 D. E. Farrell, E. Johnston-Halperin, L. Klein, *et al.*, Physical Review B **53**, 11 807 (1996).

47 D. Zech, C. Rossel, L. Lesne, *et al.*, Physical Review B **54**, 12 535 (1996).

48 K. Winzer, K. Krug, and Z. Q. Peng, Journal of Magnetism and Magnetic Materials **226 - 230**, 321 (2001).

49 A. P. Hope, M. J. Naughton, D. A. Gajewski, *et al.*, Physica C **320**, 147 (1999).

50 J. A. Cape and J. M. Zimmerman, Physical Review **153**, 416 (1966).

51 D. X. Chen, J. A. Brug, and R. B. Goldfarb, IEEE Transactions on Magnetics **27**, 3601 (1991).

52 R. C. O'Handley, *Modern Magnetic Materials* (John Wiley & Sons, Inc, New York, 2000).

53 J. A. Osborn, Physical Review **67**, 351 (1945).

54 C. P. Poole, H. A. Farach, and R. J. Creswick, *Superconductivity* (Academic Press, San Diego, 1995).

55 K. V. Bhagwat and P. Chaddah, Physica C **190**, 444 (1992).

56 I. J. Daniel, "The fabrication of Chervel Phase superconductors and the origin of the irreversibility field" *Dept of Physics*, University of Durham (1999).

Chapter 4

The Superconducting Parameters of $(Pb_{0.75}Eu_{0.25})Mo_6S_8$

4.1 Introduction

Chevrel phase superconductors are one of the next generation of materials that could be used for high field magnets. This chapter reviews the critical and fundamental parameters of Chevrel phase superconductors from the literature in section 4.2. Section 4.3 describes the two different methods which were used to fabricate $(Pb_{1-x}Eu_x)Mo_6S_8$, for $x = 0.0$, 0.25 & 0.5. Both methods finished with hot isostatic pressing (HIP'ing) at 2000 bar, 800 °C, for 8 hours. The different experiments carried out to characterise the samples are described in section 4.4. These include resistivity, ac susceptibility and magnetic moment measurements, as a function of magnetic field and temperature. Specific heat data was also taken by N. Leigh, as a function of magnetic field and temperature. The results from these experiments are presented in section 4.5. These results are analysed to determine the upper critical field ($B_{c2}(0)$), the fundamental parameters ($B_{c1}(0)$, $B_c(0)$, $\lambda(0)$ & $\xi(0)$) and the Sommerfeld constant (γ) of the samples. The temperature dependence of κ is determined from the vibrating sample magnetometer (VSM) measurements, in section 4.6. In section 4.7, the results are discussed and compared for the different measurements. The effect of adding europium ions into $PbMo_6S_8$ is discussed in terms of how the critical and fundamental parameters change. In section 4.8, the conclusion on the characterisation of $(Pb_{1-x}Eu_x)Mo_6S_8$ is presented.

The motivation for this chapter was to investigate the change in the properties of $PbMo_6S_8$, when magnetic europium ions were inserted on to the lead sites. As Eu valence is 2^+, which is the same as lead, the overall electronic structure may not be affected. The inter-relation between magnetisation and superconductivity has been observed in rare earth Chevrel phase superconductors, and in $PbMo_6S_8$ doped with rare earth ions. $(Pb_{1-x}Eu_x)Mo_6S_8$ is a magnetic superconductor, so the interaction between superconducting and magnetic magnetisation can be investigated.

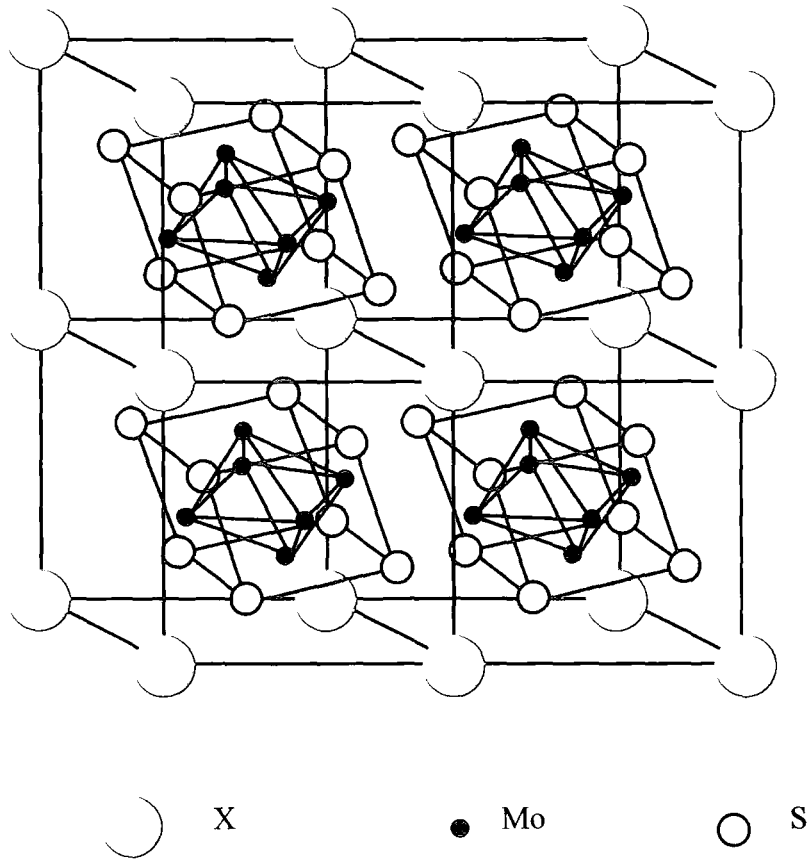

Figure 4.1. Lattice structure of the Chevrel phase superconductors, with the chemical formula XMo_6S_8 where X is a metallic atom.

Also presented in this chapter is a method of determining κ from VSM measurements, in the temperature range 4.2 K to T_c. κ is normally determined for temperatures close to the critical temperature. This is when the superconductor is in the reversible magnetisation region. The method used reduces the irreversible magnetisation, which increases the range of temperatures over which κ can be measured for. The κ value for a magnetic superconductor is difficult to extract from the measured magnetisation. This method is used to determine κ for $(Pb_{1-x}Eu_x)Mo_6S_8$.

4.2 Review of Chevrel Phase materials

Chevrel phase superconductors were discovered in 1971[1]. They are a ternary superconductor with the formula $X_nMo_6S_8$ where X is a metal such as lead, tin or any of the rare earth ions. For large metallic ions e.g. Pb, Sn, n = 1, while for small metallic ions e.g. Cu, Gd n is in the range $1 < n < 2.5$. The critical temperature is

dependant on the metallic ion, e.g. for X = Pb, the T_c is 15 K[2, 3] and for X = Sn the T_c is 14.3 K[4]. While for the rare earth ions the critical temperature tends to be lower, e.g. X = Gd, the T_c is 1.4 K[5]. There is also a relation between the *c/a* ratio and the critical temperature of $PbMo_6S_8$. The larger the *c/a* ratio the higher the critical temperature[6]. Chevrel phase superconductors have high upper critical field, making them suitable for high field applications e.g. for X = Pb the $B_{c2}(0)$ is 56 T[7, 8], and for X = Sn, the $B_{c2}(0)$ is 30 T[4].

Below T_c, magnetism and superconductivity are observed in rare earth Chevrel phase superconductors. The lattice structure (fig. 4.1) suggests there are two independent lattices present. The Mo_6S_8 is in a FCC structure which sits in the body centre of the BCC metal X lattice. Superconductivity occurs in the Mo_6S_8, while the magnetic lattice is the RE ions, in the place of the metal ions. The rare earth Chevrel phase superconductors such as $DyMo_6S_8$ have anti-ferromagnetic ordering in the superconducting phase[9]. Adding rare earth ions into $PbMo_6S_8$ and $SnMo_6S_8$ has also been researched[10, 11, 12, 13]. Zheng added Gd ions into $PbMo_6S_8$[14]. The intrinsic properties such as the critical temperature and the upper critical field increased. The extrinsic properties such as the irreversibility field and the critical current density decreased[14, 15].

4.3 Preparation of materials

Two different methods were used to fabricate the $Pb_{1-x}Eu_xMo_6S_8$ samples, with doping levels of x = 0.0, 0.25 & 0.5. The samples were made from pure elements in powder form, except for the europium, which was in ingot form. The purity of each element was Pb – 99.99 %, Mo – 99.95 %, S – 99.99 % and Eu – 99.9 %. To increase the purity of the molybdenum, it was heat treated at 1000 °C, for 4 hours. The gas flowing through the furnace was Ar – 98 % H_2 – 2 % gas. This removed any oxygen present in the powder. The elements were stoichiometrically added together to make 12.5 g of the final superconductor. Europium in ingot form can not be ground. Thus for the europium to be evenly distributed through the sample, europium sulphide was made. The europium and sulphur were mixed together and placed in a molybdenum crucible. They were reacted together in a tube furnace with the following heat-process:

Room Temperature – 10 °C.hr^{-1} → 80 °C – 3 hr → 80 °C – 33 °C.hr^{-1} → 420 °C – 8 hr → 420 °C - 33 °C.hr^{-1} → 650 °C – 10 hr → 650 °C and switch off furnace

The chemical reaction that took place during the fabrication of $(Pb_{1-x}Eu_x)Mo_6S_8$ was:

$$x\ Eu + x\ S \rightarrow x\ EuS$$

$$(1 - x)\ Pb + x\ EuS + 6\ Mo + (8 - x)\ S \rightarrow Pb_{1-x}Eu_xMo_6S_8$$

The powder elements and EuS were ground together using a pestle and mortar for over forty minutes. They were then pressed into tablets using a hydraulic press. The tablets were put into a molybdenum crucible[16]. The crucible was sealed with a graphite o-ring. A specially designed molybdenum cage[16] was used to hold the lid shut. This was to ensure that sulphur did not leak from the crucible during the reaction.

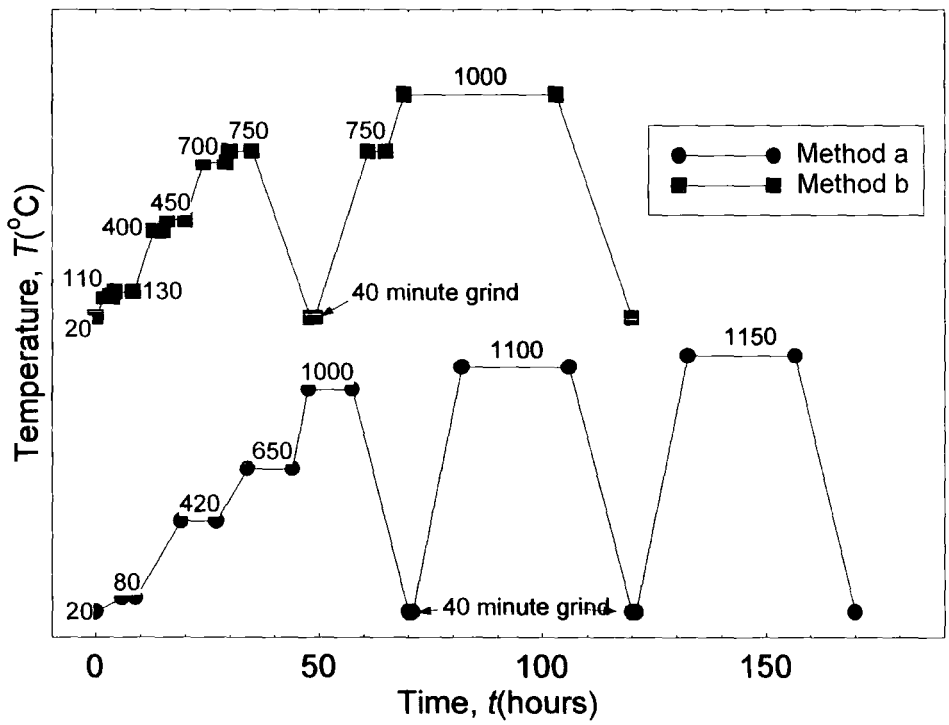

Figure 4.2. The two different heat-sintering methods used to fabricate the samples as a function of time and temperature.

From fig. 4.2, two different heat-sintering methods were used to fabricate the samples. The first was method (a), which was the original method used to fabricate Chevrel phase superconductors. The second was method (b), which was devised by Niu[17]. Method (b) gave higher critical temperatures for $PbMo_6S_8$[17]. It was used to see whether 1000 °C was higher enough to insert Eu ions, as well as increasing the critical temperature. To insert rare earth ions into $PbMo_6S_8$, temperatures above 1000 °C are normally required[18]. A third method was used to fabricate $PbMo_6S_8$. The heat sintering took place at the same temperatures as method (b), but the reaction times were a factor four longer. For all methods, the grinding of the chemicals and sealing of the molybdenum crucible took place in the argon glove box. This ensured no oxygen could contaminate the samples.

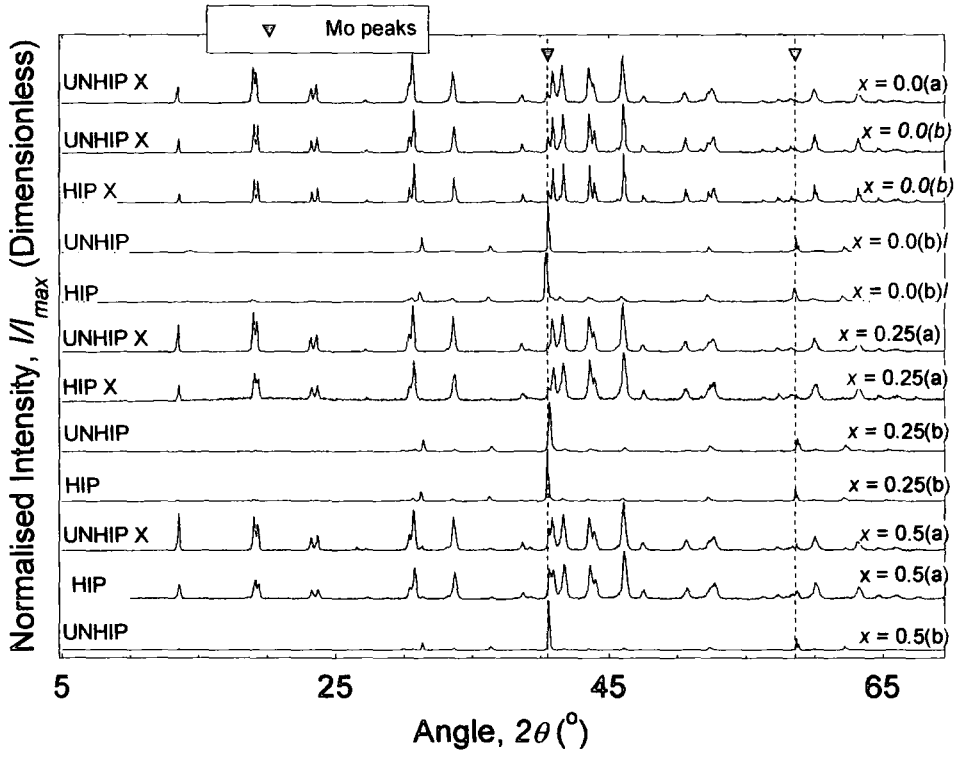

Figure 4.3. X-ray diffraction pattern for the seven unHIP'ed samples and the five HIP'ed samples. The samples were fabricated using either method (a) or (b), as shown in figure 4.2. The label (b)*l* denotes the longer heat-treatment similar to method (b). A cross denotes that the samples' majority phase is Chevrel phase. The dash lines are for the molybdenum peaks.

Oxygen is known to degrade Chevrel phase superconductors[19, 20]. It reduces both the critical temperature and upper critical field[20]. This is because the oxygen replaces the sulphur in the lattice. All precautions were taken to make sure the samples were fabricated without being oxidised. The samples were sintered in a leak tight tube furnace, with argon gas flowing through during the entire reaction process.

Five of the samples fabricated were hot isostatically pressed (HIP'ed), to improve the density of the material[21]. The samples were x = 0.0(b), 0.0(b)*l*, 0.25(a), 0.25(b) and 0.5(a). They were HIP'ed at 800 °C and 2000 bar, for 8 hours.

All the unHIP'ed and HIP'ed samples were X-ray powder diffracted, using a Bruker D5000 powder diffractometer. The wavelength of the x-rays was 1.5409 Å. The X-ray powder diffraction (XRD) was performed by Dr A E Goeta, from the Department of Chemistry at Durham University.

XRD patterns (fig. 4.3) were used to determine whether a sample was single phase or mixed phase. Single phase means there were only Chevrel phase peaks in the XRD pattern. Hence there was less than 5 % impurities in the sample, as this was the resolution of the XRD. Mixed phase means that there were other compounds in the sample. The formation of these second phases was probably a result of sulphur leaking from the crucible, leading to an excess of molybdenum and lead. Mo_2S_3 formed if the fabrication temperature was too low to insert the metal ions into the lattice.

Sample x = 0.0(b)*l*, was still mixed phase after HIP'ing. From the XRD pattern (fig. 4.3), the majority phase was molybdenum. HIP'ing decreased the critical temperature of x = 0.0(b)*l*. The critical temperature and c/a ratio of x = 0.25(b), increased after HIP'ing. This suggests that HIP'ing continued the reaction process, to form $(Pb_{0.75}Eu_{0.25})Mo_6S_8$.

4.4 Experimental set-up

All the unHIP'ed and HIP'ed samples were measured using the resistivity-ac susceptibility (Ressus) probe in a helium dewar. For the resistivity measurement, the sample tablets were dense enough to be cut into blocks of volume 2 x 1 x 4 mm^3. Four wire contacts were made to the top of the sample. Silver paint was used, as it provided a good electrical contact for the wires, but did not permanently damage the sample. The outer two wires were the current leads, and the inner two wires were the voltage taps. The distance between the voltage taps was measured, so the resistivity

could be determined. For the ac susceptibility measurement, a set of coils was used, which are described in section 3.2. The sample was GE-varnished onto a notch in a wooden stick. The notch position was centred in the middle of one of the secondary coils. The Ressus probe was used in a specially designed outer can. The whole can was filled with helium gas when cooled down to 4.2 K in the helium dewar. When the probe had reached 4.2 K the gas was pumped out. The experiment involved ramping the temperature from 4.2 K to above T_c. The resistivity and ac susceptibility voltages were measured on a Stanford lock-in as a function of temperature. This measurement provided the critical temperature of the sample.

For the magnetic field measurements, the Oxford Instrument variable temperature insert (VTI) was used in the Oxford Instrument superconducting 15 T magnet. In the VTI, the resistivity, ac susceptibility and specific heat measurements were carried out on the HIP'ed samples. The Ressus probe was used to measure the resistivity and ac susceptibility, while the VTI controlled the temperature of the probe. The magnetic field was held constant, and the temperature was swept from 4.2 K to above T_c. The resistivity and ac susceptibility voltages were measured as a function of temperature. The magnetic fields used in the experiment were 0, 3, 6, 9, 12 & 15 T. This measurement gave the critical temperature as a function of magnetic field.

The vibrating sample magnetometer (VSM) in Birmingham was used to measure the magnetic moment of the HIP'ed x = 0.0(b) and x = 0.25(a) samples. These samples were measured as they were both single phase and had the highest critical temperatures, for each fabricated superconductor. The magnetic moments were measured at fixed temperatures, from 4.2 K to above T_c, as a function of magnetic field. The magnetic field was swept from –0.5 T to 12 T, and then back to 0 T. The sweep rate was 150 Oemin^{-1}.

The samples x = 0.0(b), 0.0(b)*l* & 0.25(b), were powders before HIP'ing. They were only measured using ac susceptibility. The resistivity, ac susceptibility and VSM measurements were made on bulk samples. They were cut from the large HIP'ed tablets. The VSM bulk samples were then ground up into a powder, which was glued together with GE-varnish to form the powder sample. This ensured the same sample was measured, and any inhomogeneities in the large HIP'ed tablet, were not measured.

Criterion used for T_c	$0.5\rho_N$ (K)	$0.5\chi'$ (K)	χ''(peak) (K)	c/a ratio
Eu content				
$x = 0.0$ (a)	12.73	12.16	12.24	1.2453
$x = 0.0$ (b)	-	14.4	14.26	1.2503
$x = 0.0$ (b)*l*	-	14.06	13.95	-
$x = 0.25$ (a)	11.89	10.84	10.98	1.2478
$x = 0.25$ (b)	-	9.26	8.39	1.2558
$x = 0.5$ (a)	< 6	< 6	< 6	1.2508
$x = 0.5$ (b)	< 6	< 6	< 6	1.2538

Table 4.1. The critical temperature and c/a ratios for all the unHIP'ed samples. The critical temperatures were all measured in zero field, in a helium dewar.

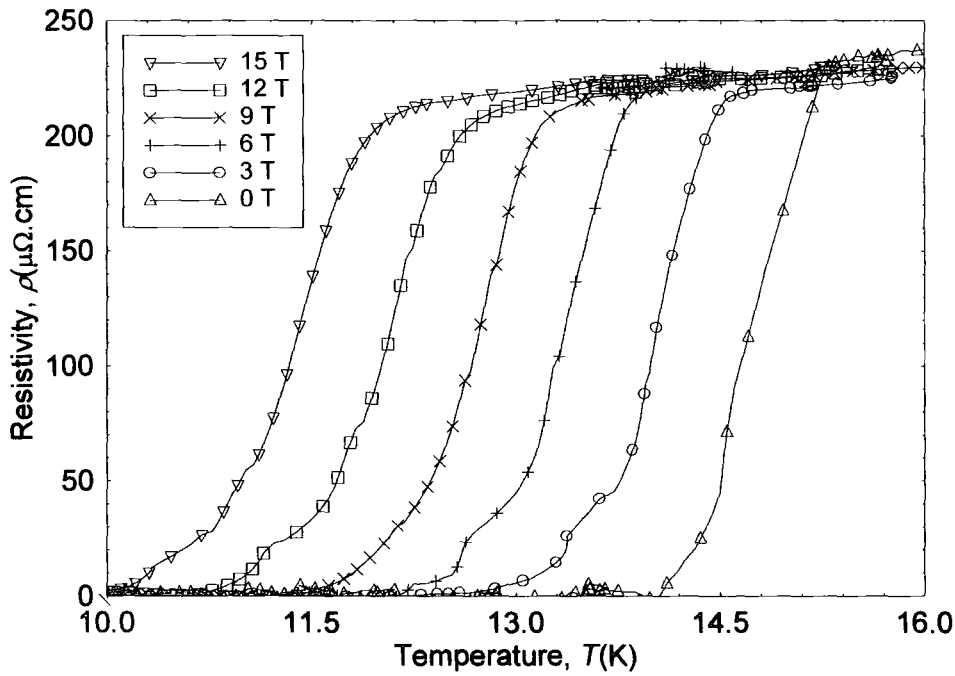

Figure 4.4. Resistivity of $PbMo_6S_8$ as a function of temperature and applied magnetic fields. The material was produced using method (b).

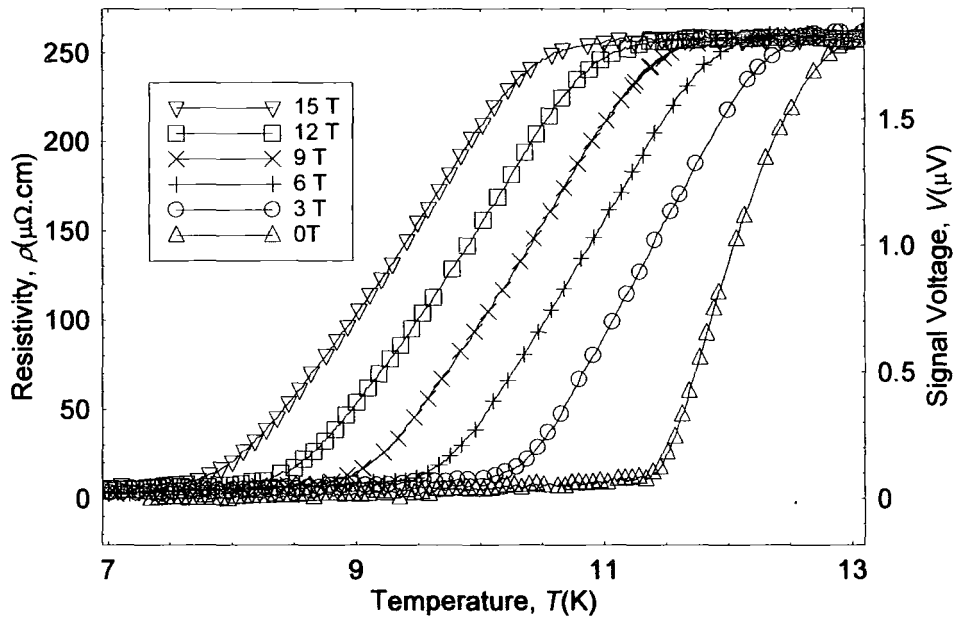

Figure 4.5a. Resistivity of $(Pb_{0.75}Eu_{0.25})Mo_6S_8$ as a function of temperature and applied magnetic field. The material was produced using method (a).

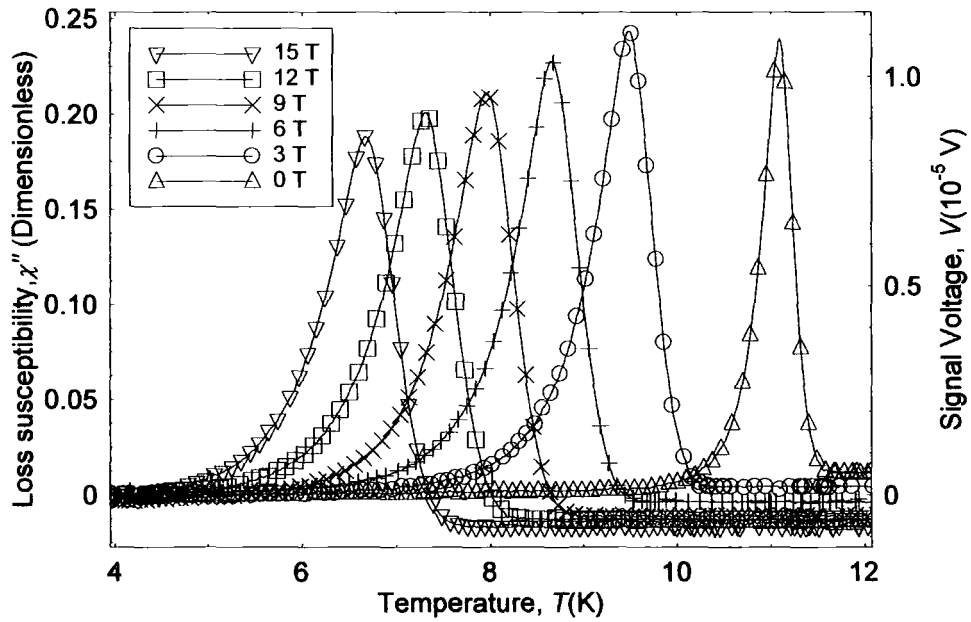

Figure 4.5b. Loss ac susceptibility of $(Pb_{0.75}Eu_{0.25})Mo_6S_8$ as a function of temperature and applied magnetic field. The material was produced using method (a).

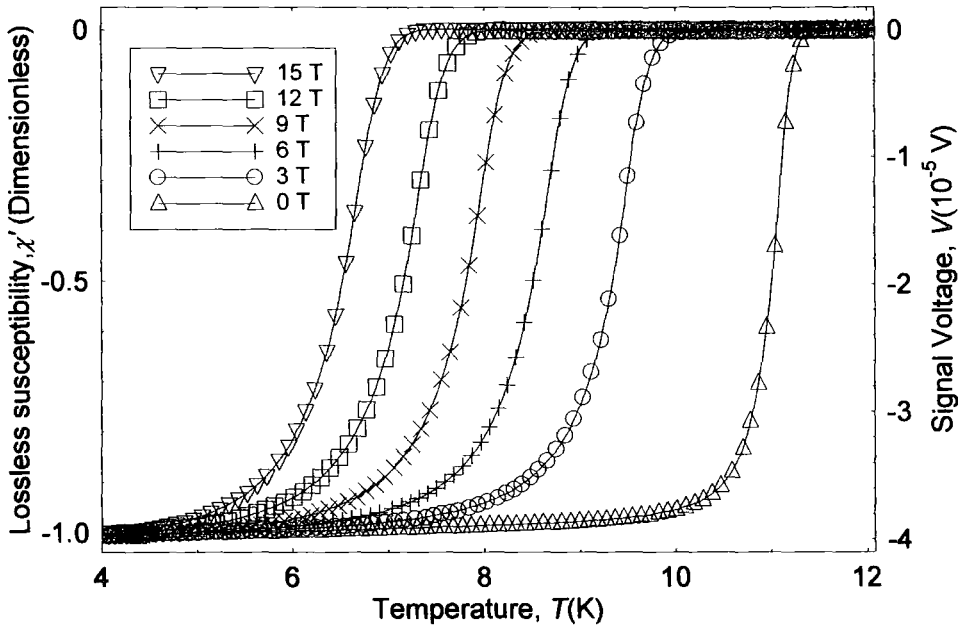

Figure 4.5c. Lossless ac susceptibility of $(Pb_{0.75}Eu_{0.25})Mo_6S_8$ as a function of temperature and applied magnetic field. The material was produced using method (a).

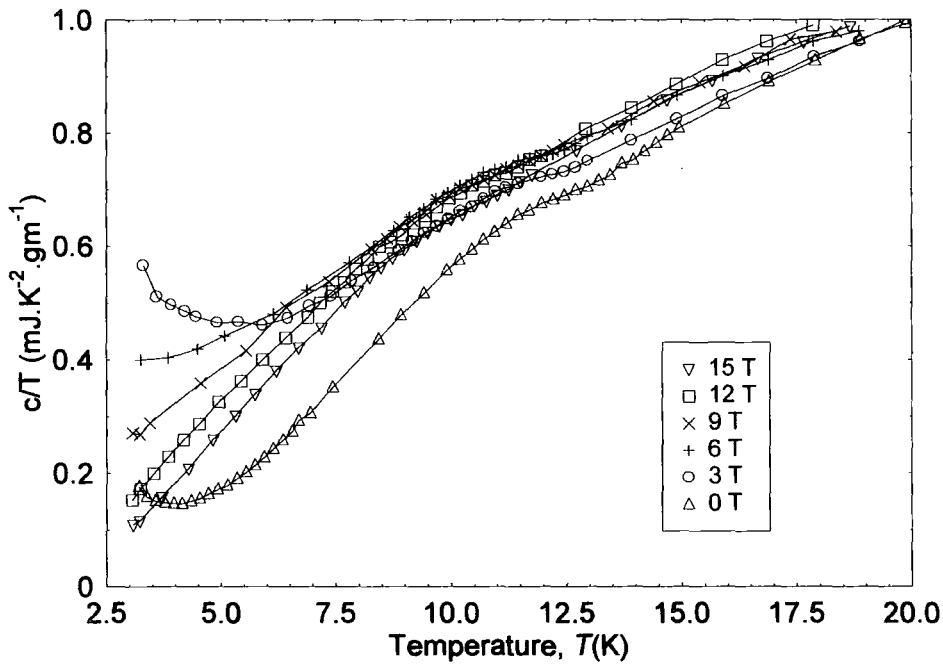

Figure 4.6. Specific heat divided by temperature of $(Pb_{0.75}Eu_{0.25})Mo_6S_8$ as a function of temperature and applied magnetic field. (Data taken by N. Leigh[22])

4.5 Results

4.5.1 Resistivity, ac susceptibility & specific heat measurements

The unHIP'ed samples were measured in zero field to determine their critical temperature. The *c/a* ratios were determined from the XRD (fig. 4.3). From table 4.1, the *c/a* ratio increased as europium was added in to the $PbMo_6S_8$. The critical temperature decreased as Eu ions were added.

From fig. 4.4, x = 0.0(b) had one of the highest critical temperatures (15.16 K) measured for a Chevrel phase superconductor[17] (cf. Table 4.2). From table 4.2, the highest T_c in the literature was measured by Mühlratzer, thus the T_c of x = 0.0(b) is a good sample. The critical temperature of x = 0.25(a) decreased, due to the doped europium ions (fig 4.5). The specific heat data taken by N. Leigh, shows that magnetism and superconductivity occurred simultaneously in x = 0.25(a) (fig.4.6). This is seen as the increase in c/T at temperatures below 5 K.

The criterion for determining the critical temperatures were 90 % and 50 % of the normal resistivity transition, the peak of the loss susceptibility (χ''), and 50 % of the lossless susceptibility transition (χ'). All critical temperatures are for the zero field measurements. The width of the lossless susceptibility ($\Delta\chi'$) gave a measure of the homogeneity of the samples.

Criterion used for T_c	$0.9\rho_N$ (K)	$0.5\rho_N$ (K)	$0.5\chi'$ (K)	$\Delta\chi'$ (K)	χ''(peak) (K)	*c/a* ratio
x = 0.0 (b)	15.16	14.72	14.17	0.9	14.32	1.2495
x = 0.0 (b)*l*	13.70	13.32	13.14	0.4	13.20	1.2394
x = 0.25 (a)	12.62	11.99	11.00	0.7	11.09	1.2479
x = 0.25 (b)	12.82	10.00	-	-	10.90	1.2577
x = 0.5 (a)	5.37	2.17	-	-	-	1.2541
Mühlratzer $x = 0.0$[2]	-	14.7	-	-	-	1.25

Table 4.2. The critical temperatures & *c/a* ratios for the HIP'ed Chevrel phase samples. The critical temperatures were all measured in the 15 T magnet at zero field.

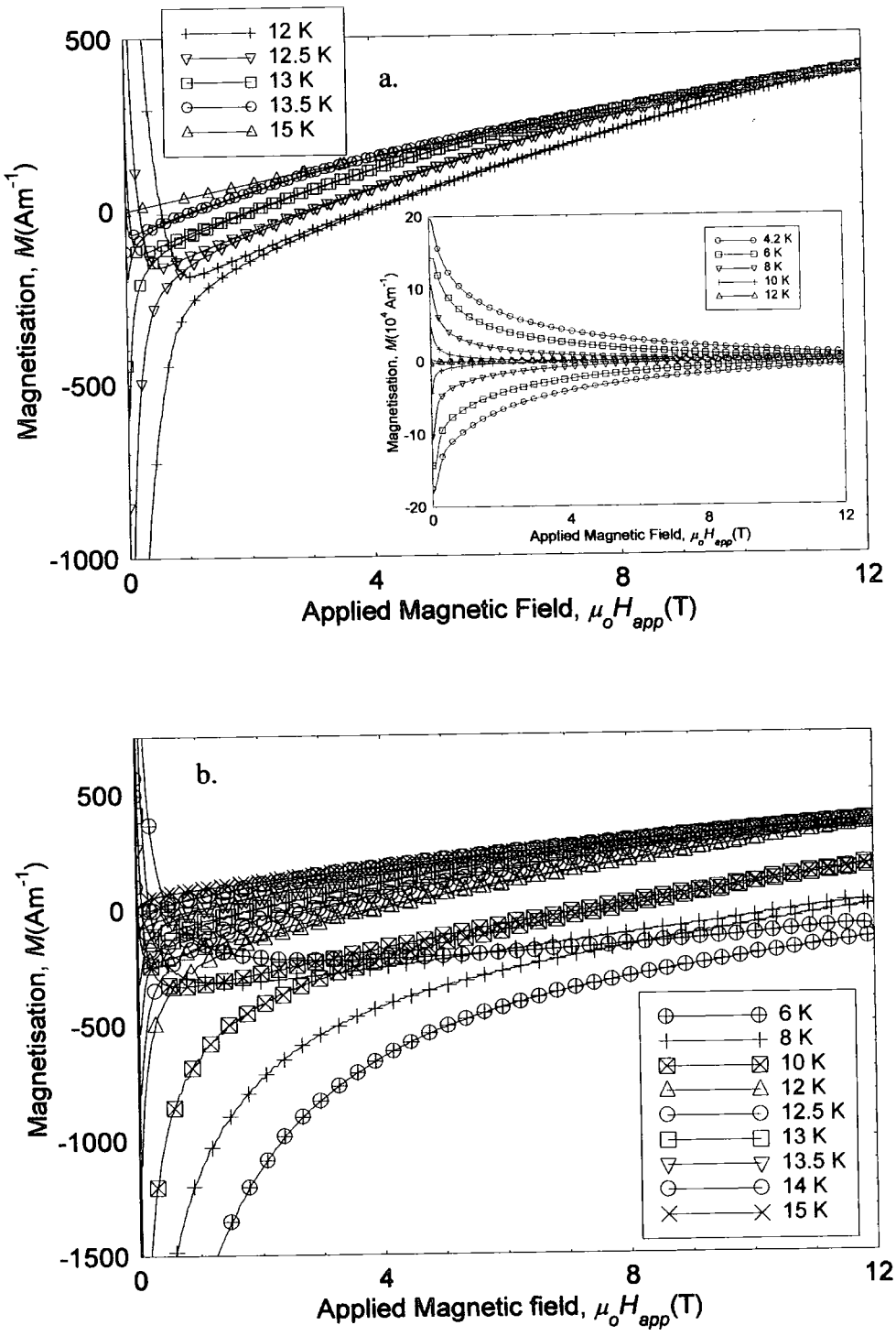

Figure 4.7a & b. Magnetisation of $PbMo_6S_8$ as a function of applied magnetic field and temperature, for (a) bulk and (b) powder samples. **Inset (a):** The low temperature magnetisation for $x = 0.0$(b), as a function of magnetic field and temperature.

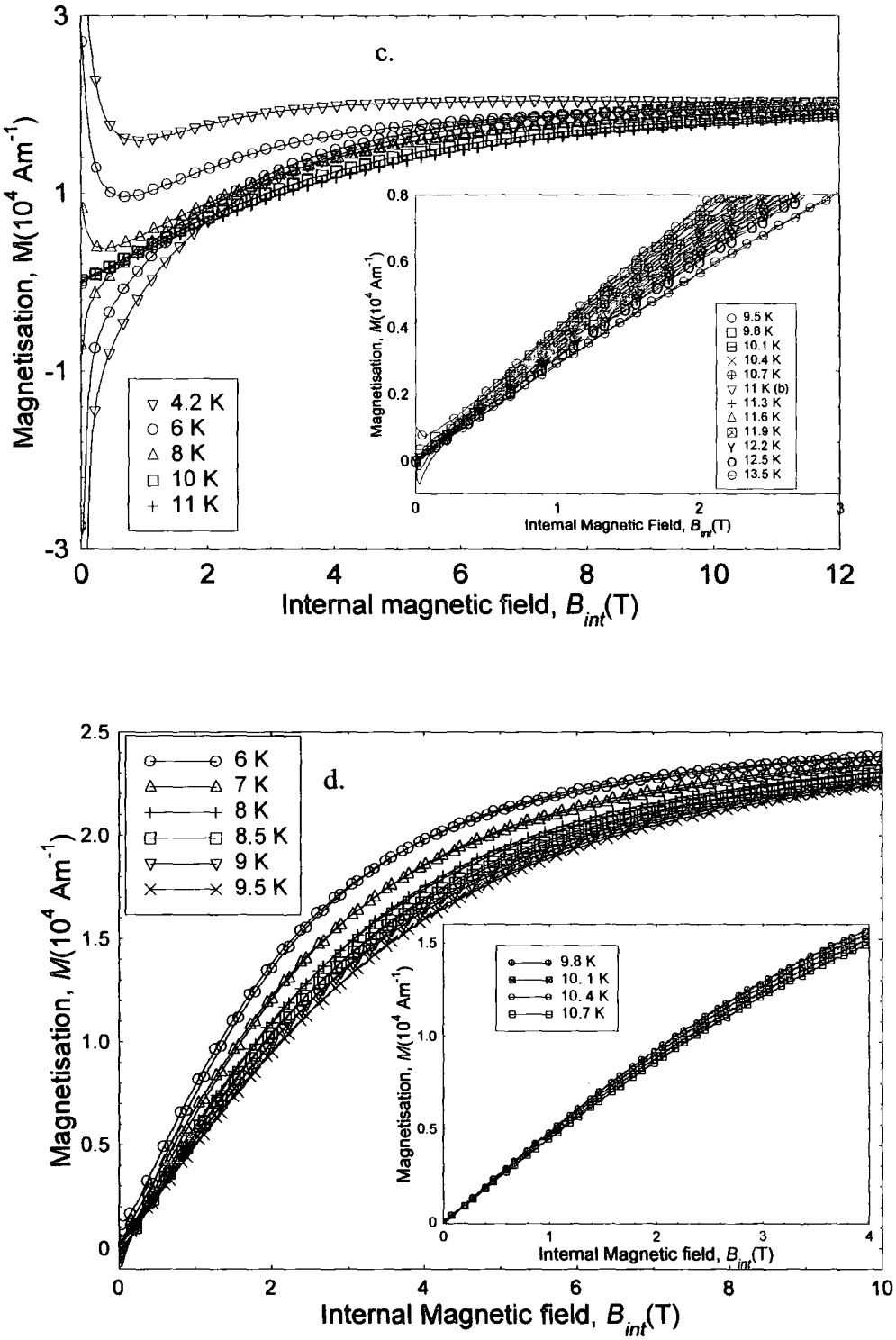

Figure 4.7c & d. Magnetisation of $(Pb_{0.75}Eu_{0.25})Mo_6S_8$ as a function of internal magnetic field and temperature, for (c) bulk and (d) powder samples. **Insets (c) & (d):** The high temperature magnetisation for x = 0.25(a), as a function of magnetic field and temperature.

Table 4.2 gives a summary of the critical temperatures and *c/a* ratios for the HIP'ed samples. Method (b) gave higher *c/a* ratio than method (a). This means the lattice was strained more, thus less isotropic. The width of the transitions for x = 0.0(b) and x = 0.25(a) were less than 1 K. HIP'ing did not change the critical temperature of the single phase samples. The critical temperature decreased as the percentage of Eu ions was increased.

4.5.2 VSM Measurements

The magnetic moments were measured for the single phase HIP'ed x = 0.0(b) and x = 0.25(a) samples. They were measured in bulk and powder forms. The magnetisation (M) for the bulk x = 0.0(b) was calculated by dividing the magnetic moment (m) by the samples' volume (vol) $\left(M = \frac{m}{vol}\right)$. The bulk x = 0.25(a) magnetisation was calculated by dividing the magnetic moment by the volume minus the porosity of the sample. The x = 0.0(b) and x = 0.25(a) powder magnetisations were calculated by determining the overall volume of the sample, which was then divided into the measured magnetic moment.

The x = 0.25(a) magnetisation is plotted as a function of internal magnetic field, $\left(\mathbb{B}_{in}\right)$. This was determined from the expression $\mathbb{B}_{in} = \mu_o(\mathbb{H} + \mathbb{M}) = \mu_o\left(\mathbb{H}_{app} + \left(1 - \tilde{N}\right)\mathbb{M}\right)$, where $\tilde{N}$ is the demagnetisation tensor. From section 3.7.2, the demagnetisation factors for the bulk x = 0.25(a) were $N_{\parallel} = 0.76$ & $N_{\perp} = 0.12$. For the powder, the grains were assumed to be spherical, thus the demagnetisation factors were $N_{\parallel} = N_{\perp} = \frac{1}{3}$.

The bulk x = 0.0(b) magnetisation has symmetric half hysteresis loops, at low temperatures (fig. 4.7a). The powder magnetisation has asymmetric hysteresis loop, at all temperatures (fig. 4.7b). The bulk and powder x = 0.25(a) magnetisation has hysteresis due to the superconducting contribution, as well as the reversible paramagnetic contribution (fig. 4.7c & d). The hysteresis is reduced in the x = 0.25(a) powder sample compared to the bulk sample, which makes it almost reversible. For the high temperature x = 0.0(b) data (fig. 4.7a), the background magnetisation (15 K data) is subtracted away before any analysis is carried out.

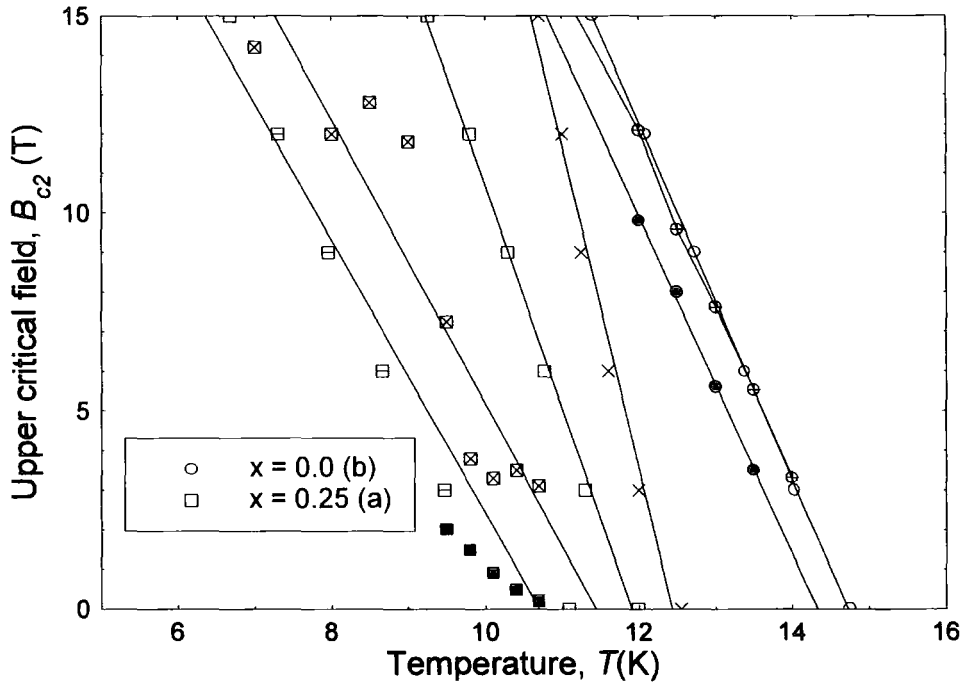

Figure 4.8. The upper critical field of $(Pb_{1-x}Eu_x)Mo_6S_8$ with $x = 0.0$ and $x = 0.25$, as a function of temperature and applied magnetic field. The open shapes denote the resistivity data, the closed shapes denote the VSM bulk data, the shapes with crosses inside denote the VSM powder data, and the crosses denote the specific heat data. The squares with a line inside denote the ac susceptibility lossless data. The x = 0.25(a) VSM values were determined from Arrott plots. The solid lines are the straight-line fits through the data. The samples were produced using one of the different methods denoted (a) or (b).

Eu Content	T_c ($0.9\rho_N$) (K)	ρ_N(16 K) (μΩ.cm)	RRR	$-\frac{dB_{c2}}{dT}\Big\|_{T=T_c}$ ($0.9\rho_N$) ($T.K^{-1}$)	$-\frac{dB_{c2}}{dT}\Big\|_{T=T_c}$ (VSM) ($T.K^{-1}$)	$B_{c2}(0)$ ($0.9\rho_N$) (T)	$B_{c2}(0)$ (VSM) (T)
$x = 0.0$ (b)	15.16	240	3.7	4.83	4.4	51.2	50
$x = 0.25$ (a)	12.62	260	4.3	6.41	3.34	56.8	30

Table 4.3. T_c, ρ_N, RRR, $-dB_{c2}/dT$ (at T_c) and $B_{c2}(0)$, for transport and magnetic measurements of the HIP'ed x = 0.0(b) and x = 0.25(a). RRR is the ratio of the resistivity at 16 K and 300 K. The VSM data is for the powder samples.

4.6 Analysis

4.6.1 Upper critical field, $B_{c2}(0)$

The resistivity, ac susceptibility and specific heat measurements were taken at fixed magnetic field, whilst the temperature was ramped. The critical temperatures were found by using the criterion in section 4.5.1 and plotted against the fixed field. For the VSM magnetisation data there were two possible methods for determining $B_{c2}(T)$. Method *i* involved drawing a straight line through the reversible magnetisation data and determining $B_{c2}(T)$ by extrapolating to $M = 0$. The equation of the line is given by Abrikosov's magnetisation equation[23]:

$$\mu_o M = \frac{(B_{c2} - B)}{\beta_A(2\kappa^2 - 1)} \tag{4.1}$$

where β_A is Abrikosov's constant. For method *ii*, $B_{c2}(T)$ was the field at which the magnetisation became zero on fig. 4.7a. For the powder data, the method *i* was used to calculate $B_{c2}(T)$ at all temperatures.

From Werthamer, Helfand and Hohenberg (WHH) theory[24] the upper critical field at 0 K, $B_{c2}(0)$, for type II superconductors is given by:

$$B_{c2}(0) = -0.7T_c \left.\frac{dB_{c2}}{dT}\right|_{T=T_c} \tag{4.2}$$

where $-\left.\frac{dB_{c2}}{dT}\right|_{T=T_c}$ is the solid straight line through the data on the fig. 4.8 and T_c is the temperature where $B_{c2}(0) = 0$ T. From fig. 4.8, $-\left.\frac{dB_{c2}}{dT}\right|_{T=T_c}$ of $x = 0.0$(b) were consistent for the different experiments. For $x = 0.25$(a), $-\left.\frac{dB_{c2}}{dT}\right|_{T=T_c}$ had a wide range of values from 1.54 for the bulk magnetic data to 8.17 for the specific heat data. The RRR for each of the HIP'ed samples was determined from $RRR = \frac{\rho_N(300K)}{\rho_N(16K)}$, the normal resistivity (ρ_N) was measured above T_c at 16 K. The resistivity at 16 K, for $x = 0.0$(b) & $x = 0.25$(a) was almost the same (table 4.3).

From table 4.3, the resistivity $B_{c2}^{0.9\rho_N}(0)$ of $x = 0.25$(a) is 6 T larger than $x = 0.0$(b), while the VSM $B_{c2}^{M\to 0}(0)$ of $x = 0.25$(a) is 20 T smaller. Also $-\left.\frac{dB_{c2}}{dT}\right|_{T=T_c}$ decreases by a factor 2 between the resistivity and the VSM powder data for $x = 0.25$(a). The $x = 0.0$(b) resistivity ($0.9\rho_N$) and the VSM powder upper critical fields and $-\left.\frac{dB_{c2}}{dT}\right|_{T=T_c}$ are in good agreement (fig.4.8).

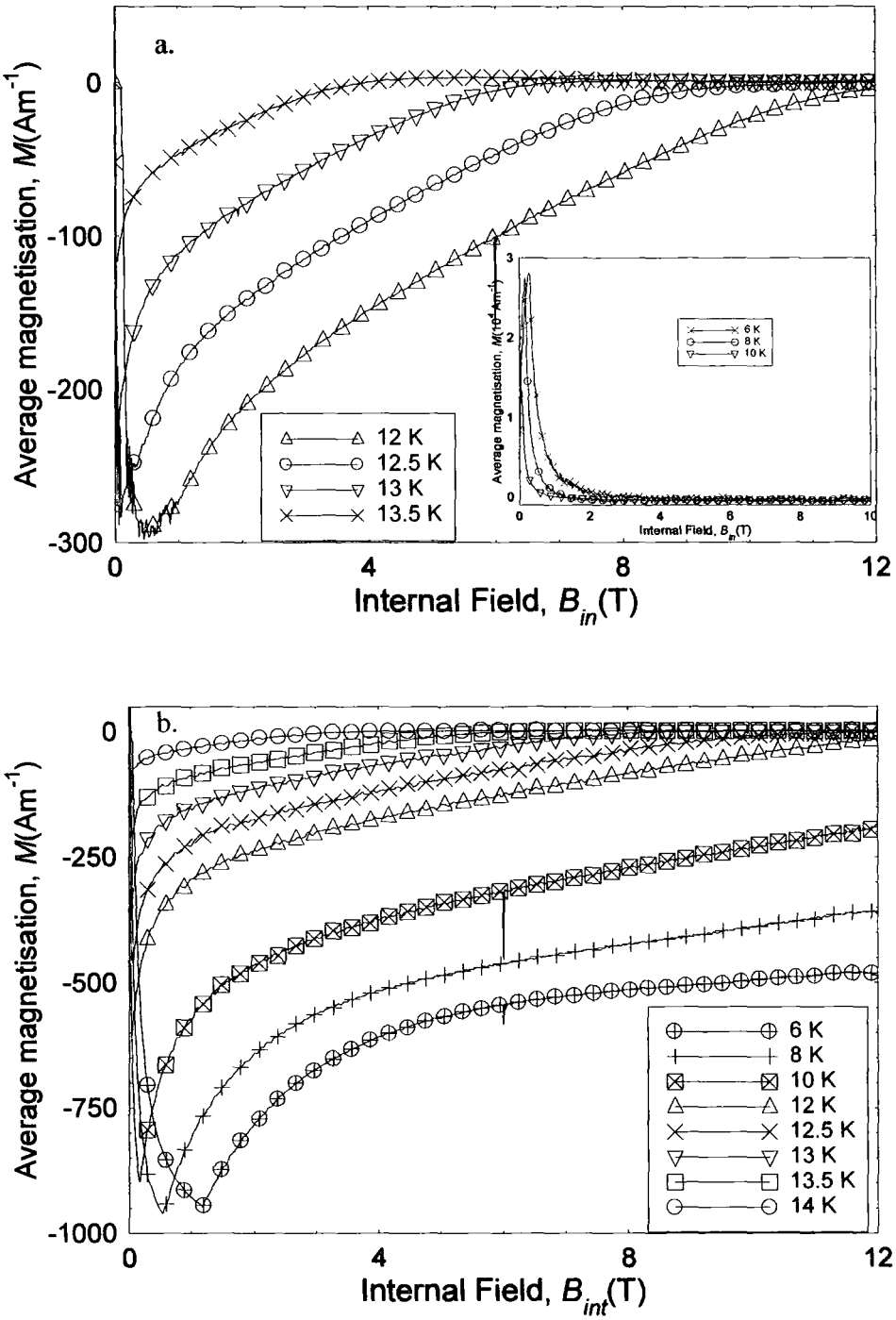

Figure 4.9a & b. Average magnetisation of $PbMo_6S_8$ as a function of internal magnetic field and temperature for the (a) bulk and (b) powder samples. **Inset (a):** Low temperature average magnetisation as a function of internal magnetic field and temperature.

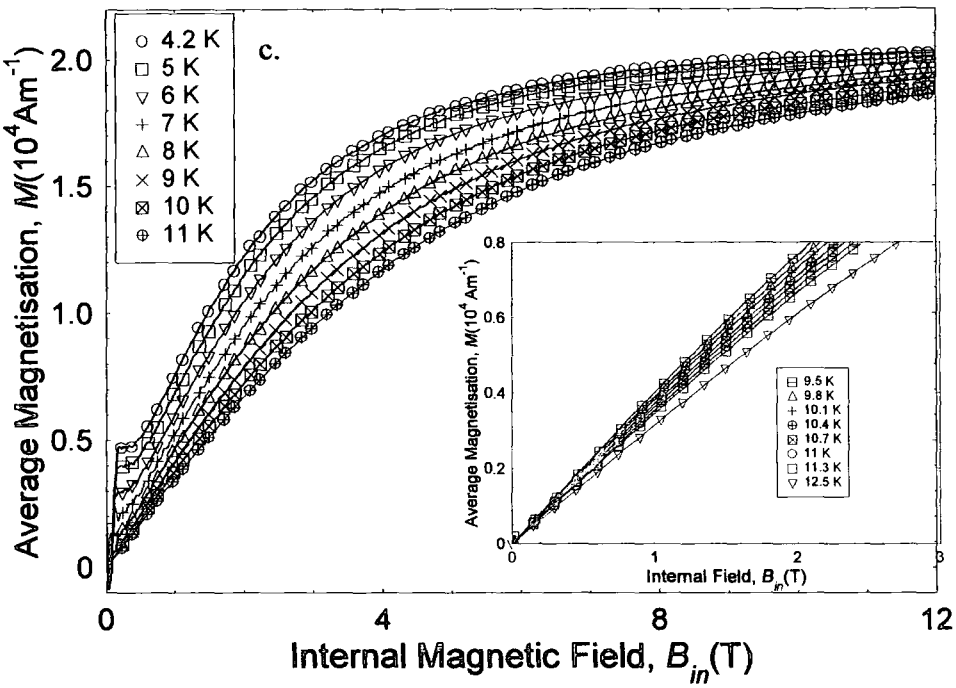

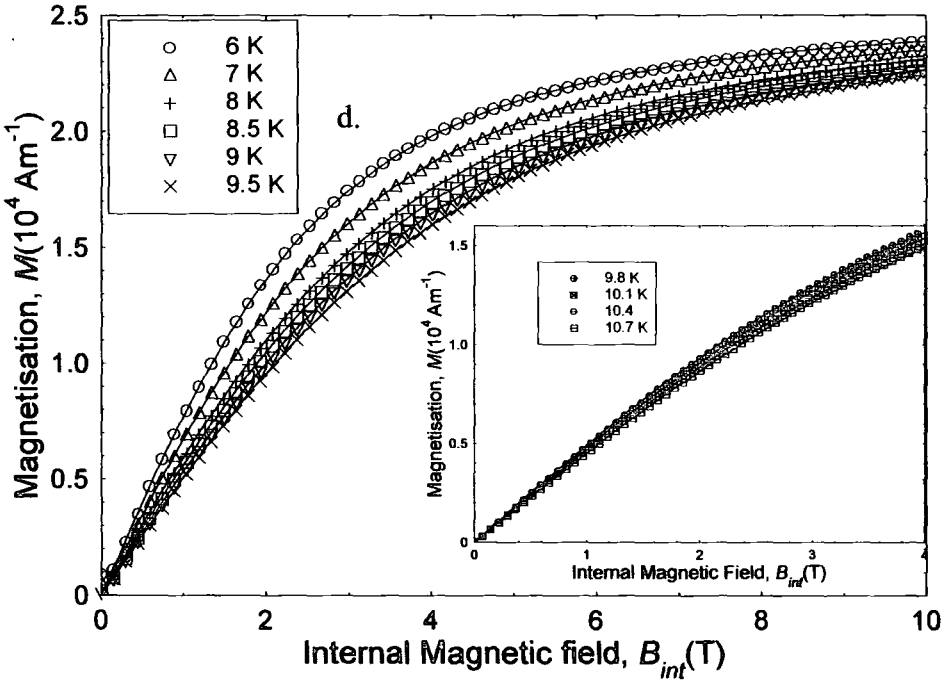

Figure 4.9c & d. Average magnetisation of $(Pb_{0.75}Eu_{0.25})Mo_6S_8$ as a function of internal field and temperature for the (c) bulk and (d) powder samples. **Inset (c) & (d):** High temperature average magnetisation as a function of internal field and temperature.

4.6.2 Average magnetisation & critical parameters

At temperatures above 12 K, the average magnetisation, ($M_{av} = M_+ + M_-$ where M_+ & M_- are the magnetisation for the upwards and downwards field sweep respectively) for the bulk and powder x = 0.0(b) samples were similar (fig. 4.9a & b). For all temperatures, the x = 0.0(b) powder average magnetisation had similar curve shape. At temperatures above 8 K, the average magnetisation for the x = 0.25(a) bulk sample showed paramagnetism (fig. 4.9c). At these temperatures, the sample was in the reversible magnetisation region. The x = 0.25(a) powder sample magnetisation was almost reversible at all temperatures, and paramagnetism was observed at all fields. The low temperature bulk data for x = 0.0(b) and x = 0.25(a) have peaks at 0.25 T.

κ and the fundamental parameters, for x = 0.0(b) were determined from the high temperature bulk average magnetisation (fig. 4.13a), and from all the temperature powder average magnetisation (fig. 4.9b). The low temperature average magnetisation for the bulk sample gave a non-physical negative gradient. κ was determined by fitting a straight line to the linear reversible region, close to T_c. The gradient $\frac{dM}{dB}$ was substituted into eqn 4.1. From section 2.6.2, the fundamental parameters ($B_{c1}(0)$, $B_c(0)$, $\lambda(0)$ & $\xi(0)$) were derived from the Ginsburg-Landau equations. The parameters are obtained using the following expressions. For the thermodynamic critical field, $B_c(T)$ the relation with the upper critical field is:

$$B_{c2}^{T\approx T_c}(T) = \sqrt{2}\kappa B_c^{T\approx T_c}(T) \tag{4.3}$$

where the superscript means the equation is valid for temperatures close to T_c. For all other temperatures the equation $\frac{dB_{c2}(T)}{dT} = \sqrt{2}\kappa \frac{dB_c(T)}{dT}$ is used. This is because $B_{c2}(T)$ and $B_c(T)$ have different temperature dependencies away from T_c. The temperature dependence of $B_c(T)$ is given by the microscopic expression[25]:

$$B_c^{T\approx T_c}(T) = 1.74 B_c(0)\left(1 - \frac{T}{T_c}\right) \tag{4.4}$$

The lower critical field, $B_{c1}(0)$ from the GL equations for temperatures close to T_c, is given by:

$$B_{c1}^{T\approx T_c}(T) = \frac{B_c^{T\approx T_c}(T)(\ln\kappa + 0.5)}{\sqrt{2}\kappa} \tag{4.5}$$

The temperature dependence is given by:

$$B_{c1}^{T\approx T_c}(T) = B_{c1}(0)\left(1-\left(\frac{T}{T_c}\right)^2\right) \tag{4.6}$$

The coherence length, $\xi(0)$ in terms of the upper critical field is given by:

$$B_{c2}(T) = \frac{\Phi_o}{[2\pi\xi^2(T)]} \tag{4.7}$$

and the temperature dependence close to T_c is $\xi^{T\approx T_c}(T) = \xi(0)\left(1-\frac{T}{T_c}\right)^{-\frac{1}{2}}$, thus the relation between the upper critical field and the zero field coherence length is:

$$B_{c2}^{T\approx T_c}(T) = \frac{\Phi_o}{2\pi\xi^2(0)}\left(1-\frac{T}{T_c}\right) \tag{4.8}$$

This expression is only true for temperatures close to the critical temperature[25].

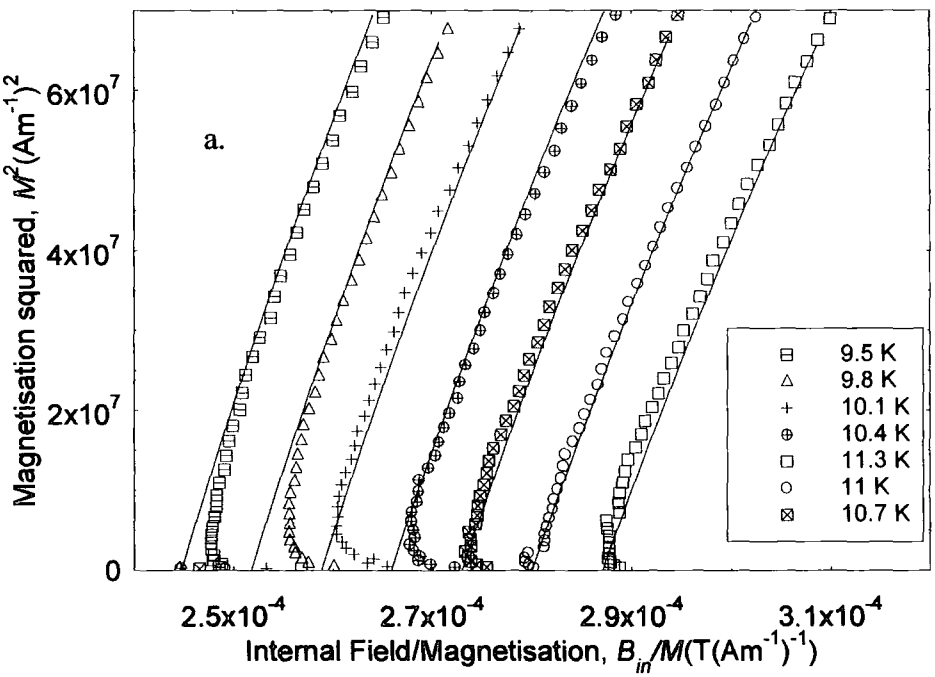

Figure 4.10a. Average magnetisation squared of the bulk $(Pb_{0.75}Eu_{0.25})Mo_6S_8$, as a function of internal magnetic field divided by the average magnetisation, and temperature. The solid lines are the best-fit calculated paramagnetic magnetisation for above $B_{c2}(T)$.

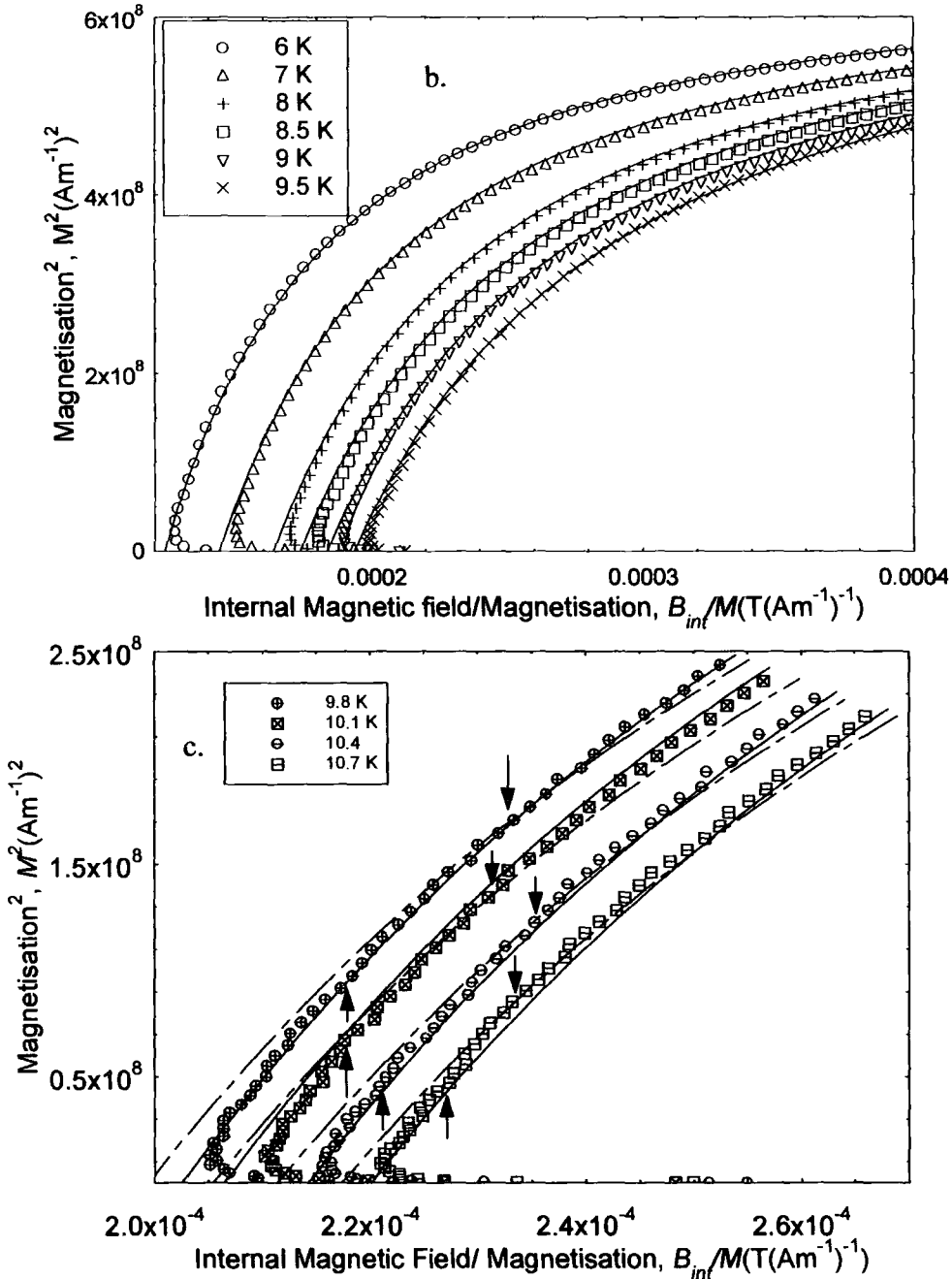

Figure 4.10b & c. Average magnetisation squared of powder $(Pb_{0.75}Eu_{0.25})Mo_6S_8$, as a function of internal magnetic field divided by the average magnetisation, and temperature, for (b) low temperature data and (c) high temperature data. In (b) the solid lines are the best-fit calculated magnetisation for all the temperatures. In (c) the dashed lines are the best-fit calculated magnetisation for all temperatures with N = 3.77 x 10^{26} m^{-3}, and the solid lines are the best-fit calculated magnetisation for the high temperatures only, with N = 3.87 x 10^{26} m^{-3}. The best-fit curves were fitted to the data above $B_{c2}(T)$. The upwards arrows denote the $B_{c2}(T)$ for the high temperature fit lines, and the downwards arrows denote $B_{c2}(T)$ for the all temperature fit lines. These are graphs are known as Arrott plots[26].

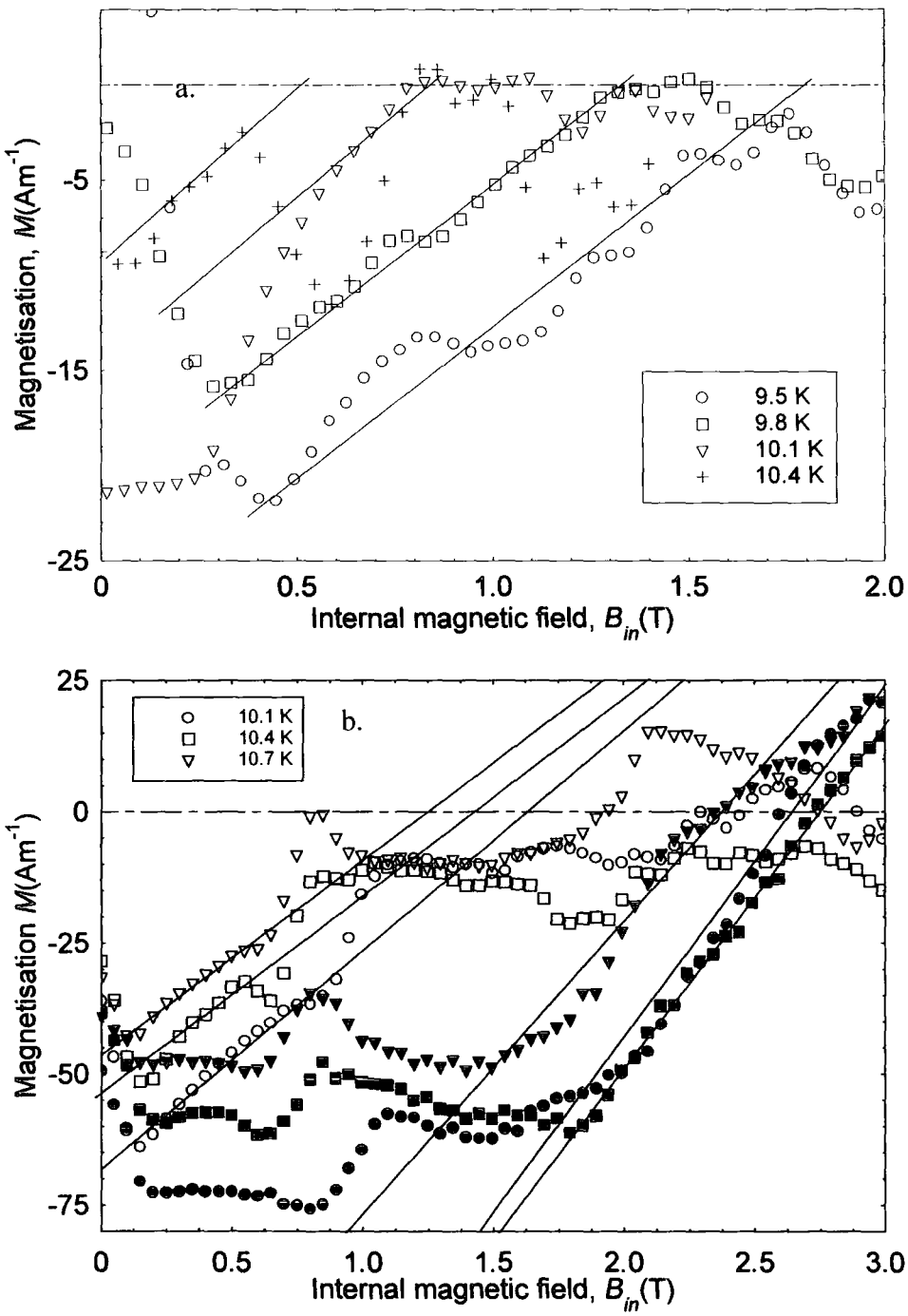

Figure 4.11a & b. Superconducting magnetisation of $(Pb_{0.75}Eu_{0.25})Mo_6S_8$ as a function of temperature and internal magnetic field for (a) bulk and (b) powder samples. The solid lines in both figures are the best-fit lines through the linear part of the data. The dashed line in both figures is $y = 0$. In (b) the open shapes denote the superconducting magnetisation determined from the best-fit magnetisation to the high temperatures only, and the closed shapes denote the best-fit magnetisation to all the temperatures.

x = 0.25(a) showed magnetic as well as superconducting contributions, due to the europium ions (fig. 4.9c & d). The magnetisation shows paramagnetic behaviour described by the Brillouin function, which is given by:

$$B_J(y) = \left\{ \left(\frac{2J+1}{2J} \right) \coth\left[\frac{(2J+1)}{2J} y \right] - \left(\frac{1}{2J} \right) \coth\left[\frac{y}{2J} \right] \right\} \qquad (4.9)$$

where $y = \left(g_J \mu_B J_m B / k_b T \right)$, g_J is the Lande number, J_m is the angular momentum and μ_B is the Bohr magneton. B is a function of internal field and magnetisation, described by $B = B_{in} + \lambda_\chi M$. λ_χ is a fraction of the overall susceptibility, and is related to the ordering temperature (T_θ), by $\lambda_\chi = \frac{C}{T_\theta}$, where C is Curies' constant (eqn 3.4). The magnetisation, for a paramagnetic material is given by:

$$M = N_M g_J \mu_B J_m B_J(y) \qquad (4.10)$$

where N_M is the number density of magnetic ions. Equation 4.10 was fitted to the average magnetisation for the bulk (fig. 4.9c) and the powder (fig. 4.9d) samples, at a field above the upper critical field for each temperature. The fitting was carried out in excel using the solver programme. For eqn 4.10, the Eu ions were assumed to be free ions 2+ state with J_m = 3.5 and g_J = 2.016, thus the variables N_M and λ_χ were determined. The theoretical paramagnetic magnetisation was calculated using Maple. The best-fit paramagnetic magnetisation was plotted against the VSM data, in M^2 vs. B_{in}/M space[26]. The superconducting contribution is seen in the Arrott plots, as the deviation between the data and the theory (fig. 4.10a, b & c). The best-fit calculated paramagnetism was subtracted from the total average magnetisation, leaving the average superconducting magnetisation.

From fig. 4.11a & b the temperature dependant κ and $B_{c2}(T)$ were determined for the bulk and powder x = 0.25(a) data. A straight line was put through the linear part of the data, at each temperature and substituted into eqn 4.1. The fundamental parameters ($B_{c1}(0)$, $B_c(0)$, $\xi(0)$ & $\lambda(0)$) were calculated using equations 4.3 – 4.8, using the $B_{c2}(0)$ (fig. 4.8) and κ determined from the Arrott plots. From figs. 4.11a & b, a linear $\frac{dM}{dB_{in}}$ is observed at low fields, but as the field increases the error bars increase because the superconducting magnetisation is the result of subtracting away two numbers, which are two orders of magnitude larger than the result.

	J_m	g_J	N_M (m^{-3})	λ_χ	T_θ (K)
$x = 0.25$ bulk	3.5	2.016	3.20×10^{26}	-17	-0.003 ± 0.002
$x = 0.25$ powder	3.5	2.016	3.77×10^{26} *3.87×10^{26}*	-3.1 *-9.9*	-0.02 ± 0.004 *-0.006 ± 0.003*
$x = 0.25$ Cp data[22]	3.5	2.0	9.0×10^{26}	-	- 0.35

Table 4.4. Summary of the J_m the total angular momentum, g_J the Lande parameter, N_M the number density, and T_θ the ordering temperature of $(Pb_{0.75}Eu_{0.25})Mo_6S_8$, for the different measurements. The specific heat magnetic variables were determined by Leigh[22]. The powder data variables in normal type are for the best-fit magnetisation to all temperatures, and the variables in italics are the high-temperature data fit.

4.6.3 Magnetic parameters of $x = 0.25$

The magnetic parameters (J_m, g_J, N_M & λ_χ) of the europium ions were determined from the best-fit paramagnetic magnetisation (eqn 4.10), which was fitted to the $x = 0.25$(a) data above the upper critical field at each temperature.

In figure 4.11a & b, the data lines have oscillations in, which were caused by the noise and thermal oscillations occurring when using the VSM. This added errors into the determination of $B_{c2}(T)$ and κ.

Another problem was the temperature control of the VSM. The temperature during the experiment oscillated about the set temperature by ± 0.1 K. This caused problems for the higher temperature data, as the fitting was done to the accuracy of 0.1 K, hence oscillations were seen in the data from the temperature instability.

From table 4.4, there was a difference in the value of N_M determined from the VSM and specific heat experiments. The ordering temperatures (T_θ) for the three measurements were negative, and were within 0.5 K of each other. The ordering temperatures for the bulk data and the powder high temperature data agree within errors.

Temperature (K)	$N_M = 3.77\times10^{26}$ m^{-3} $\lambda_\chi = -3.1$ K		$N_M = 3.87\times10^{26}$ m^{-3} $\lambda_\chi = -9.6$ K		$N_M = 3.77\times10^{26}$ m^{-3} $\lambda_\chi = -3.4$ K	
	$B_{c2}(T)$ (T)	κ	$B_{c2}(T)$ (T)	κ	$B_{c2}(T)$ (T)	κ
10.1	3.3	98	1.63	91	2.7	90
10.4	3.5	82	1.3	88	2.5	74
10.7	3	94	1.24	96	2.1	65

Table 4.5. $B_{c2}(T)$ and κ for the different values of N_M (m^{-3}) & λ_χ in the paramagnetic magnetisation (eqn 4.12). $B_{c2}(T)$ and κ were determined using equation 4.1.

There are two different methods of determining the errors for the VSM magnetic variables. One method was to use the standard error analysis for fitting parameters. From fitting the Brillouin function to the average magnetisation of the powder data the error for N_M is $\pm 1.4\times10^{24}$ m^{-3} and the error for T_θ was $\pm$ 0.006 K, while the errors for the bulk data variables are $\pm 1\times10^{25}$ m^{-3} for N_M and $\pm$ 0.002 K for T_θ.

From fig. 4.10c, two different best-fit magnetisation were plotted with the VSM average magnetisation data for x = 0.25(a). The $N_M = 3.87\times10^{26}$ m^{-3} is for the best-fit magnetisation to the high temperature data, and $N_M = 3.77\times10^{26}$ m^{-3} is for the best-fit magnetisation to all the temperature data. The two different superconducting contributions due to the two best-fit magnetisations are shown in fig. 4.11b. The difference in changing N_M by 1 % is observed in the different shapes of the superconducting magnetisation curves.

Using eqn 4.1, $B_{c2}^{M\to0}(0)$ and κ were determined for the different superconducting magnetisations in fig. 4.11b, and presented in table 4.5. The difference in $B_{c2}^{M\to0}(0)$, for the two different N_M values is about 50 %, while the difference in κ is about 7 %. When λ_χ was changed by 10%, κ changed by less than 10 % compared to the other κ values in table 4.5, while $B_{c2}^{M\to0}(0)$ was about a third smaller than the contribution for the same N_M. The major error in the best-fit magnetisation calculation is on the value of N_M. Thus the error on $B_{c2}^{M\to0}(0)$ for x = 0.25(a) is $\pm$ 5 T, and the error on κ is $\pm$ 10.

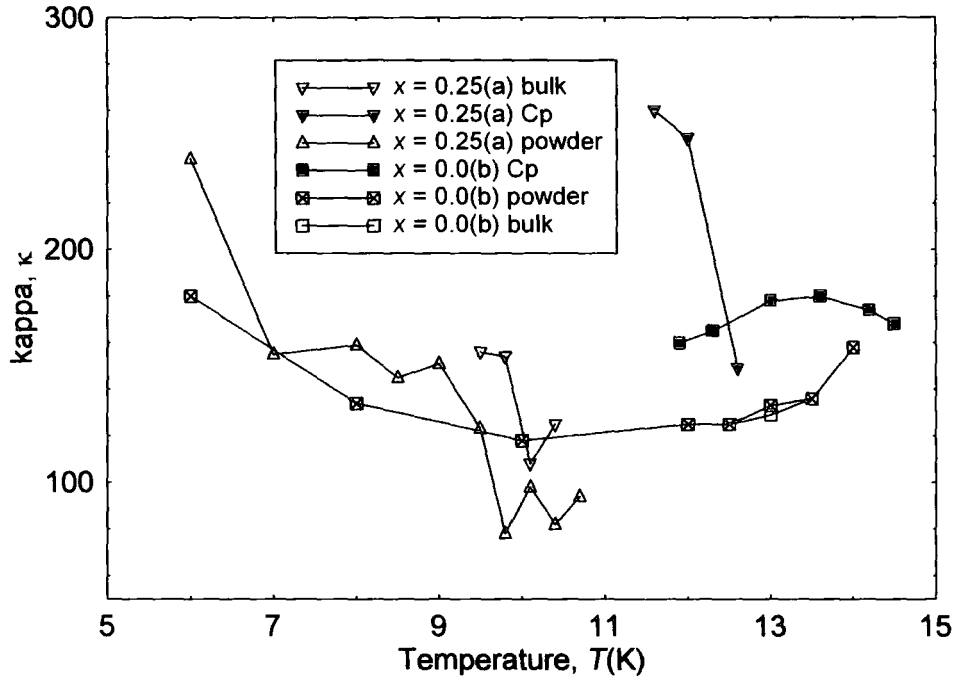

Figure 4.12. The GL parameter (κ), of x = 0.0(b) and x = 0.25(a) as a function of temperature. The open shapes denote the VSM data and the closed shapes denote the specific heat data. The specific heat data taken by N. Leigh[22]. The x = 0.25(a) κ were determined from Arrott plots.

4.6.4 GL parameter

From the specific heat data taken by N. Leigh (fig. 4.6), the discontinuity in the specific heat $\left(\frac{\Delta c}{T_c}\right)$ is used to determine κ from the thermodynamic equation:

$$\left.\frac{\Delta c}{T_c}\right|_B = \frac{\left(\frac{dB_{c2}}{dT}\right)^2}{1.16\mu_o\left(2\kappa^2 - 1\right)} \tag{4.11}$$

where $\frac{dB_{c2}}{dT}$ is taken from fig. 4.8. Thus at each magnetic field the specific heat κ was determined as a function of critical temperature, for x = 0.0 and x = 0.25(a). The specific heat data measured the x = 0.0 sample fabricated by D N Zheng.

From fig. 4.12, the powder x = 0.0(b) and x = 0.25(a) κ values increases as the temperature decreases. The x = 0.0 specific heat κ has the same temperature dependence as the VSM data. The x = 0.25(a) specific heat data κ at 0 T, is the same order of magnitude as the bulk and powder κ values.

4.6.5 Sommerfeld constant, γ

The Sommerfeld constant γ is the electronic contribution to the heat capacity. It can be determined from specific heat measurements, and magnetic measurements.

For the specific heat data, the ratio of the superconducting to the normal state electronic contribution is given by the modified BCS relation[27], which is:

$$\frac{\Delta c}{\gamma_{cp} T_c} = 1.43\left[1+53\left(\frac{T_c}{\omega_{ln}}\right)^2 \ln\left(\frac{\omega_{ln}}{3T_c}\right)\right] \qquad (4.12)$$

where ω_{ln} is a weighted average phonon frequency and γ_{cp} denotes the Sommerfeld constant has been determined from the discontinuity in the specific heat. ω_{ln} is determined from eqn 4.12, when γ and $\frac{\Delta c}{T_c}$ are known for the superconductor. In the weak coupling limit $\omega_{ln} = \infty$[28], thus $\frac{\Delta c}{\gamma_{cp} T_c} = 1.43$. In the strong coupling limit ω_{ln} is finite, thus is characterised by $\left(\frac{T_c}{\omega_{ln}}\right)$. From the literature, Leigh[22] determined the ω_{ln} value for $PbMo_6S_8$, using equation 4.14. The range of values include $\omega_{ln} = \infty$[28] in the weak limit to ω_{ln} = 181 K[29] and 185 K[30], in the strong coupling limit. For x = 0.0(b), the ratio $\frac{\Delta c}{\gamma_{cp} T_c}$ has the value 2.15, if ω_{ln} = 183 K[22], in the strong coupling limit.

Another method is to use the modified BCS relation[27, 31, 25] in terms of the thermodynamic critical field, the critical temperature and the weight average phonon frequency. The relation is given by:

$$\frac{\gamma_{\omega_{ln}} T_c^2}{\mu_o H_c^2(0)} = 2.11\left[1-12.2\left(\frac{T_c}{\omega_{ln}}\right)^2 \ln\left(\frac{\omega_{ln}}{3T_c}\right)\right] \qquad (4.13)$$

where $\gamma_{\omega_{ln}}$ denotes the Sommerfeld constant was determined using the weighted average phonon frequency and the thermodynamic critical field. Therefore substituting $B_{c2}(0) = \sqrt{2}\kappa B_c(0)$ (eqn 4.3) into the above equation, gives:

$$\gamma_{\omega_{ln}} = \frac{B_{c2}^2(0)}{2\mu_o T_c^2 \kappa^2} 2.11\left[1-12.2\left(\frac{T_c}{\omega_{ln}}\right)^2 \ln\left(\frac{\omega_{ln}}{3T_c}\right)\right] \qquad (4.14)$$

This means in the weak coupling limit where $\omega_{ln} = \infty$, the Sommerfeld constant is $\gamma_{\omega_{ln}} = \frac{2.11B_{c2}^2(0)}{2\mu_o\kappa^2T_c^2}$. While in the strong coupling limit, taking $\omega_{ln} = 183$ K[22] for x = 0.0(b), the Sommerfeld constant is $\gamma_{\omega_{ln}} = \frac{1.86B_{c2}^2(0)}{2\mu_o\kappa^2T_c^2}$.

The third method uses the thermodynamic relation, involving the thermodynamic critical field, in the weak coupling limit:

$$B_c(0) = 7.65\times10^{-4}\gamma^{1/2}T_c \tag{4.15}$$

Thus substituting equation 4.3 into the above equation gives:

$$B_{c2}(0) = 1.08\times10^{-3}\kappa\gamma^{1/2}T_c \tag{4.16}$$

where $B_{c2}(0)$ and T_c, can be from either the resistivity or the magnetic measurements. In the strong coupling limit, equation 4.15 becomes:

$$B_c(0) = \frac{7.65\times10^{-4}\gamma_\Delta^{1/2}T_c}{\left[1-\frac{1}{5}\left(\frac{2\Delta}{k_bT_c}-\frac{7}{2}\right)\right]^{1/2}} \tag{4.17}$$

where Δ is the energy gap and γ_Δ denotes the Sommerfeld constant determined from the energy gap and the thermodynamic critical field. Substituting eqn 4.3 into eqn 4.17 gives:

$$B_{c2}(0) = \frac{1.08\times10^{-3}\kappa\gamma_\Delta^{1/2}T_c}{\left[1-\frac{1}{5}\left(\frac{2\Delta}{k_bT_c}-\frac{7}{2}\right)\right]^{1/2}} \tag{4.18}$$

From literature the energy gap of $PbMo_6S_8$ is 2.4 meV[32]. The energy gap of $Gd_{0.1}Pb_{0.9}Mo_6S_8$ is 5.2 meV[33], thus introducing magnetic ions to $PbMo_6S_8$ increases the energy gap. It therefore was not possible to assume a value of Δ for the x = 0.25(a) sample, so the Sommerfeld constant was only determined for eqn 4.18, in the weak coupling limit.

These three different methods were used to determine the Sommerfeld constant of x = 0.0(b) and x = 0.25(a). For x = 0.0(b), the Sommerfeld constant was determined from eqns 4.14 & 4.18 in both the strong and the weak coupling limit. The Sommerfeld constant was also determined for the 90% resistivity $B_{c2}(0)$ and T_c values as well as the powder magnetic measurement values (cf. table 4.3). The κ value was taken to be 129. For eqn 4.14, ω_{ln} = 183 K, while for eqn 4.18, Δ = 2.4 meV.

	γ_{cp} ($JK^{-1}m^{-3}$) $\left(\frac{\Delta c}{T_c}\right)$	$\gamma_{\omega_{ln}}^{0.9\rho_N}$ ($JK^{-1}m^{-3}$)		$\gamma_{\omega_{ln}}^{M\to 0}$ ($JK^{-1}m^{-3}$)		$\gamma_{\Delta}^{0.9\rho_N}$ ($JK^{-1}m^{-3}$)		$\gamma_{\Delta}^{M\to 0}$ ($JK^{-1}m^{-3}$)	
		w	*s*	*w*	*s*	*w*	*s*	*w*	*s*
$x = 0.0$ (b)	-	575	507	576	508	575	541	575	541
$x = 0.25$ (a)	251	823	-	276	-	823	-	276	-

Table 4.6. The Sommerfeld constant γ, determined from equations 4.12, 4.14 & 4.18. In the table *w* stands for the weak coupling limit (with $\omega_{ln} = \infty$) and *s* stands for the strong coupling limit (with $\omega_{ln} = 183$). γ_{cp} represents the Sommerfeld constant calculated from the discontinuity in the specific heat data (eqn 4.12), determined in the weak limit. $\gamma_{\omega_{ln}}$ represents the Sommerfeld constant calculated from the modified BCS theory, using the weighted average phonon frequency (eqn 4.14). γ_{Δ} represents the Sommerfeld constant calculated from BCS theory, using the energy gap of the superconductor (eqn 4.18). $\gamma^{0.9\rho_N}$ denotes the Sommerfeld constants determined from the 90 % resistivity values of $B_{c2}^{0.9\rho_N}(0)$ and T_c while $\gamma^{M\to 0}$ denotes the Sommerfeld constants determined from the powder VSM values of $B_{c2}^{M\to 0}(0)$ and T_c.

For $x = 0.25$(a), ω_{ln} & Δ were unknown, thus γ could only be determined for the weak coupling case in equations 4.12, 4.14 and 4.18. In the weak coupling limit eqns 4.14 and 4.18 are the same. The κ value taken was 144, and the powder $B_{c2}^{M\to 0}(0)$ and T_c were used.

From table 4.6, the Sommerfeld constants ($\gamma_{\omega_{ln}}^{M\to 0}$ & $\gamma_{\Delta}^{M\to 0}$) for x = 0.25(a) are a factor 2 smaller than the x = 0.0(b) values for eqns 4.14 & 4.18 in the weak coupling limit. For x = 0.25(a), the specific heat γ_{cp} is the same order of magnitude as $\gamma_{\omega_{ln}}^{M\to 0}$ & $\gamma_{\Delta}^{M\to 0}$. For x = 0.0(b), the Sommerfeld constants agree for the resistivity and VSM values, for each different equation.

Eu content	$-\frac{dB_{c2}}{dT}\Big\|_{T=T_c}$ ($T.K^{-1}$)	$B_{c2}(0)$ (T)	$B_{c1}(0)$ (mT)	$B_c(0)$ (mT)	κ	$\xi(0)$ (nm)	$\lambda(0)$ (nm)
$x = 0.0$(b) bulk VSM *method ii*	5.3	54	4.5	196	132	2.1	277
$x = 0.0$(b) bulk VSM *method i*	4.8	48	6.9	224	129	2.1	282
$x = 0.0$(b) powder VSM *method i*	4.4	50	6.8	205	129	2.3	291
$x = 0.25$(a) bulk VSM	1.54	12	0.9	39	160	4.4	739
$x = 0.25$ (a) powder VSM	3.34	30	1.6	78	144	2.13	307
$x = 0.25$ (a) Specific heat	5.0	73.8	0.9	35	148	2.11	313

Table 4.7. The fundamental parameters ($B_{c1}(0)$, $B_c(0)$, $B_{c2}(0)$, $\xi(0)$ & $\lambda(0)$) for $x = 0.0$(b) and $x = 0.25$(a), determined from the VSM magnetisation data and the specific heat data taken by N. Leigh. For $x = 0.0$(b) and $x = 0.25$(a), the VSM bulk and powder data is presented. For method i, $B_{c2}(T)$ was determined using $\mu_o M = aB - B_{c2}$ through the average magnetisation data. For method ii, $B_{c2}(T)$ was determined from the average magnetisation graphs for $M = 0$. The difference values of $B_{c2}(T)$ were then used to determine the fundamental parameters. The κ values were determined from eqn 4.3, for temperatures close to T_c. The specific heat values of $B_{c1}(0)$, $B_c(0)$, $\xi(0)$ & $\lambda(0)$ were determined using the $B_{c2}(0)$ and κ from Leigh's data.

4.6.6 Summary

A summary of the fundamental parameters, critical fields and κ are presented in table 4.7, for the bulk and powder, $x = 0.0$(b) & $x = 0.25$(a) VSM data. The specific heat data was taken by N. Leigh for the $x = 0.25$(a) sample. From table 4.7, for $x = 0.0$(b) bulk and powder samples, the $B_{c2}(T)$ and κ agree. The addition of Eu ions in to $x = 0.25$(a) has reduced $B_{c1}(0)$ and $B_c(0)$, but κ is the same order of magnitude the $x = 0.0$(b) values.

4.7 Discussion

4.7.1 Materials Properties

The properties of $PbMo_6S_8$ and $EuMo_6S_8$ are well known[34]. Decroux measured the properties of $EuMo_6S_8$, and found that it was not superconducting at ambient pressure[35, 36], and only became superconducting at pressures above 13 kbar[36]. In this chapter, the properties of $(Pb_{1-x}Eu_x)Mo_6S_8$ for $x = 0.0$ and 0.25, were investigated. Therefore a decrease in critical temperature for an increase in Eu ions was expected. The critical temperature of $PbMo_6S_8$ was 15.16 K compared with 12.6 K for $(Pb_{0.75}Eu_{0.25})Mo_6S_8$, hence the critical temperature of $(Pb_{1-x}Eu_x)Mo_6S_8$ does decrease as the value of x is increased.

The fabrication process of Chevrel phase superconductors is important, as it affects the superconducting parameters of the material[4, 37]. It is known that temperatures higher than 1000 °C are required to insert rare earth ions into the Chevrel phase lattice[18, 13]. Two different fabrication methods were used to fabricate $(Pb_{1-x}Eu_x)Mo_6S_8$. For method (a), the highest temperature was 1150 °C. From the XRD patterns, $x = 0.25$ and $x = 0.5$ were both single phase samples. For method (b), the highest temperature was 1000 °C. The method was tried as it produced higher critical temperatures in $PbMo_6S_8$. The samples $x = 0.25$ and $x = 0.5$ were not pure Chevrel phase and had lower critical temperatures compared to method (a), which confirms temperatures above 1000 °C were required to insert the Eu ions into $PbMo_6S_8$. The c/a ratio increased as the concentration of Eu ions increased. The values are broadly consistent with a linear increase between the two ternary end compounds. The change is due to the Eu ions having smaller radii than the Pb ions, this changes the strain on the lattice.

The superconducting properties of Chevrel phase materials are degraded at the surface of the grains, and across the grain boundaries[37]. The degradation is caused by second phase materials forming[38], which leads to a different value of $B_{c2}(T)$ in the grains compared to in the grain boundaries, hence gives a distribution in $B_{c2}(T)$ over the whole sample. Thus the upper critical field ($B_{c2}(0)$) will differ in value for each of the measurements. For magnetic measurements, the distribution in $B_{c2}(T)$ changes the gradient of the average magnetisation close to $B_{c2}(T)$, as the different parts of the superconductor become normal. For eqn 4.1, $\frac{dM}{dB}$ was measured in the reversible magnetisation region between B_{irr} and $B_{c2}(T)$ (fig. 4.9a). In this region the superconductor was still superconducting, but no critical current was flowing. Thus the field gradient $\frac{dM}{dB}$ was measured below the magnetic field where the gradient changed, so the calculated values of κ and $B_{c2}^{M\to 0}(T)$ were not affected by the $B_{c2}(T)$ distribution. For specific heat measurements, a distribution in $B_{c2}(T)$ reduces the height and sharpness of the discontinuity, which made it difficult to determine the size of the discontinuity and the critical temperature. Hence the accuracy of the measured parameters decreased. For the resistivity measurement, the percolative path through the superconductor was measured. A distribution in $B_{c2}(T)$, will broaden the transition width, as the grain boundaries will become normal before the grains. The critical temperature at $0.9\rho_N$ remains unchanged as it is the T_c of the grains, while the $0.5\rho_N$ will change depending on the distribution of $B_{c2}(T)$ in the sample. The distribution in $B_{c2}(T)$ for the $x = 0.25$(a) sample was observed in the resistivity and ac susceptibility data, as the data taken at field have a wider transition width compared to the zero field transition. Therefore the specific heat critical temperatures and upper critical field $\left(B_{c2}^{cp}(0)\right)$ are expected to be higher than the magnetic measurements $\left(B_{c2}^{M\to 0}(0)\right)$. For the $(Pb_{0.75}Eu_{0.25})Mo_6S_8$ sample the specific heat measurement $B_{c2}^{cp}(0)$ had the highest value of 71 T, compared to the lowest value of 12 T for the bulk VSM measurement of $B_{c2}^{M\to 0}(0)$.

4.7.2 Upper critical field, $B_{c2}(0)$

There are three factors, which control the upper critical field ($B_{c2}(0)$) in magnetic superconductors. They are the compensation effect, the normal state resistivity (ρ_N),

and the electronic contribution to the specific heat (γ). The compensation effect is due to the magnetic nature of the Eu ions opposing the paramagnetic limiting, which causes $B_{c2}(T)$ to be higher in a magnetic superconductor, than in a non-magnetic superconductor[39].

From GL theory, the upper critical field, ($B_{c2}(0)$), is described in terms of the normal state resistivity and the electronic contribution to the specific heat. It is given by:

$$B_{c2}(0) = 3.0 \times 10^3 \gamma \rho_N T_c \qquad (4.19)$$

where γ is the Sommerfeld constant, which is the electronic contribution to the specific heat. The normal resistivity of the samples fabricated was ~ 250 μΩ.cm. From eqn 4.19, the upper critical field ($B_{c2}(0)$) will increase if the normal resistivity is increased. From table 4.3, at 16 K, x = 0.25(a) has a larger resistivity than x = 0.0(b). The $B_{c2}(0)$ of x = 0.25(a) for the resistivity measurement was 6 T higher than the $B_{c2}(0)$ determined for x = 0.0(b).

The Sommerfeld constant was determined for x = 0.0(b) from the BCS equations (eqn 4.14 & 4.18). From table 4.6, for x = 0.0(b), for eqn 4.14 in the strong limit the $\gamma_{\omega_{ln}}^{0.9\rho_N}$ = 507 $JK^{-1}m^{-3}$ and $\gamma_{\omega_{ln}}^{M\to 0}$ = 508 $JK^{-1}m^{-3}$. Similarly for eqn 4.18 in the strong limit $\gamma_{\Delta}^{0.9\rho_N} = \gamma_{\Delta}^{M\to 0_N}$ = 541 $JK^{-1}m^{-3}$. Thus the Sommerfeld constants for each equation agree for the resistivity and VSM data, which suggest the distribution in $B_{c2}(T)$ across the sample is negligible. Leigh determined the Sommerfeld constant of $PbMo_6S_8$ from the discontinuities in the specific heat measurements and equation 4.12[22]. In the weak coupling limit he determined $\gamma_{cp} = 498$ $JK^{-1}m^{-3}$ and for the strong coupling limit $\gamma_{cp} = 339$ $JK^{-1}m^{-3}$. The weak coupling limit Sommerfeld constant is in agreement with the measured values from the BCS equations in this work. The strong coupling limit Sommerfeld constant is a third smaller for the specific heat compared with a tenth smaller for the BCS equations. This was expected from the modified BCS equations (eqns 4.12 & 4.13), as the strong coupling limit parts were different functions of $\left(\frac{\omega_{ln}}{T_c}\right)$. The literature suggests $PbMo_6S_8$ is a strongly coupled superconductor[33].

The Sommerfeld constant of x = 0.25(a), in the weak coupling limit, determined from the discontinuity in the specific heat (eqn 4.12) was γ_{cp} = 251 $JK^{-1}m^{-3}$ and from the BCS equations in terms of the thermodynamic critical field (eqns 4.14 & 4.18) were

$\gamma_{\omega_{\ln}}^{M\to 0} = \gamma_{\Delta}^{M\to 0} = 276$ JK^{-1}m^{-3}. They are the same order of magnitude (table 4.6). Hence the addition of europium ions to $PbMo_6S_8$ has decreased the Sommerfeld constant. From table 4.6, the values determined from the resistivity data, (eqn 4.14 & 4.18) were $\gamma_{\omega_{\ln}}^{0.9\rho_N} = \gamma_{\Delta}^{0.9\rho_N} = 823$ JK^{-1}m^{-3}, which are 4 times larger than the $\gamma^{M\to 0}$ values, due to the upper critical field of the resistivity data $\left(B_{c2}^{0.9\rho_N}(0)\right)$ being a factor two greater than the VSM $B_{c2}^{M\to 0}(0)$. The T_c of $x = 0.25$(a) changed by less than 1 K between the different measurements. The change in γ between the different measurements was due to the grains and grain boundaries having different $B_{c2}(T)$ values, which lead to a distribution in $B_{c2}(T)$. The magnetic measurement of $B_{c2}^{M\to 0}(0)$ was unchanged by the distribution, as the VSM measured the properties of the grains. From XRD (fig. 4.3) the grains were single phase $(Pb_{0.75}Eu_{0.25})Mo_6S_8$. The specific heat discontinuity at 0 T γ_{cp} has the same order of magnitude Sommerfeld constants determined from the VSM data, which suggests the distribution in $B_{c2}(T)$ did not affect the discontinuity in the specific heat measurement at 0 T, but only affected the discontinuities in the specific heat data taken in an applied magnetic field. For $x = 0.25$(a), the VSM $B_{c2}^{M\to 0}(0)$ decreased as the critical temperature and Sommerfeld constant decreased in comparison with the $x = 0.0$(b) values (eqn 4.19). The resistivity measurements were dependent on the properties of the grains and grain boundaries. The resistivity values of $B_{c2}^{0.9\rho_N}(0)$ and $\gamma^{0.9\rho_N}$ increased for $x = 0.25$(a), compared with the VSM values, hence the sample had impurities in the grain boundaries. This means the normal resistivity of the boundaries was greater than the grains, thus $B_{c2}^{0.9\rho_N}(0)$ of $x = 0.25$(a), was higher than the $x = 0.0$(b) value. This increase in normal resistivity across the grain boundaries compensated for the decrease in $\gamma^{0.9\rho_N}$ and T_c for $x = 0.25$(a).

4.7.3 Average Magnetisation and critical parameters

The difference in the shape of magnetisation loops measured for the bulk samples and the powder samples was due to different pinning mechanisms. The bulk $x = 0.0$(b) symmetric magnetisation loops were characteristic of flux being pinned at pinning centres. The pinning centres for bulk polycrystalline materials are at the grain boundaries[40]. The powder $x = 0.0$(b) magnetisation (fig. 4.7b) shows the

characteristic asymmetric shape of the Bean-Livingston surface barrier[41], as in grinding up the sample, the grain boundaries were destroyed, thus the pinning centres no longer existed. Above 12 K, the average magnetisation of the bulk and powder x = 0.0(b) samples had the same magnitude. Also for all temperatures, the powder x = 0.0(b) average magnetisation had the same curve shape, therefore it was assumed that the surface pinning did not affect the average magnetisation. Thus equation 4.1 was fitted to the linear region of the powder average magnetisation at all temperatures. For x = 0.0(b) and x = 0.25(a), the bulk data were used to determine the critical current density. The powder data were used to find the temperature dependant upper critical field, $B_{c2}^{M\to 0}(T)$ and κ, over the temperature range 4.2 K to T_c.

The equations used to determine the fundamental parameters ($B_c(0)$, $B_{c1}(0)$, $\lambda(0)$ and $\xi(0)$) were derived from the GL equations[42] (eqn 4.3 – 4.8), and are valid for temperatures close to T_c. The bulk and powder values of $B_{c2}^{M\to 0}(0)$ and κ were used to determine these parameters for x = 0.0(b) and x = 0.25(a). From table 4.7, two different methods were used to determine $B_{c2}^{M\to 0}(0)$ for x = 0.0(b). The first method determined $B_{c2}^{M\to 0}(0)$ by fitting a straight line through the reversible data (fig 4.9), and solving for $M = 0$, while the second method took $B_{c2}^{M\to 0}(0)$ to be the field on fig 4.9, where $M = 0$. For method *i* $B_{c2}^{M\to 0}(0)$ = 48 T and for method *ii* $B_{c2}^{M\to 0}(0)$ = 54 T, the difference is due to the distribution in $B_{c2}(T)$ in the sample changing the average magnetisation gradient below $B_{c2}^{M\to 0}(T)$.

From table 4.7, the coherence length $\xi(0)$ and penetration depth $\lambda(0)$ of the x = 0.25(a) bulk sample were a factor 2 larger than the bulk x = 0.0(b) sample. While $\xi(0)$ and $\lambda(0)$ of the powder sample were unchanged by the addition of Eu ions. For both the bulk and powder x = 0.25(a) samples, the $B_{c1}(0)$ and the $B_c(0)$ decreased compared with the x = 0.0(b) values, which suggests the Eu ions produced an internal magnetic field in the superconductor, which opposed the critical fields.

4.7.4 Magnetic parameters of x = 0.25(a)

The magnetic parameters (N_M and λ_χ) were determined from the best-fit paramagnetic magnetisation (eqn 4.8) to the x = 0.25(a) VSM data. The parameters are presented in table 4.4, including the parameters determined from the specific heat data by Leigh.

For all three measurements, the J_m and g_J were assumed to be the free Eu ion values. The number density of magnetic ions (N_M) calculated for the bulk sample was 3.2×10^{26} m^{-3}. For the powder data there were two different paramagnetic contributions. For the high temperature data (above 9.8 K) N_M = 3.87 x 10^{26} m^{-3} and λ_χ = - 9.6 K, while for the low temperature data (below 9.5 K) N_M = 3.79 x 10^{26} m^{-3} and λ_χ = -9.9 K. The difference occurred between the two different sensitivities of the VSM amplifier. Then fitting to all the data gave N_M = 3.77 x 10^{26} m^{-3} and λ_χ = - 3.1 K. The difference in N_M between the bulk and the powder data is about 15 %, and is probably due to errors in the analysis and the determination of the different volumes of the samples. The specific heat calculation assumed $N_M = 9 \times 10^{26}$ m^{-3} [22], which is the N_M value, which gives 25 % Eu ions from the lattice parameters. The VSM bulk and powder magnetisation data seemed to have only measured a third of the total number of Eu ions present in the sample. One reason for this is the sample only contained x = 0.08 ions rather than 0.25, which is unlikely as the XRD data contained no europium peaks nor any other second phase materials (fig 4.3). Another reason could be the Eu ions were clustered within the large HIP'ed sample. At the moment the reason for the reduction in N_M for the magnetisation calculations is unknown.

From table 4.4, T_θ varied by two orders of magnitude between the different measurements. The T_θ values of the bulk data and the high temperature powder data were in good agreement.

4.7.5 GL parameter, κ

From GL theory, the parameter κ is independent of temperature close to T_c. Maki[43] introduced two κ parameters, $\kappa_1(T)$ and $\kappa_2(T)$, which have different temperature dependencies away from T_c. $\kappa_1(T)$ is related to the upper critical field, and $\kappa_2(T)$ is related to the magnetisation. From experiment it was discovered that $\kappa_1(T)$ and $\kappa_2(T)$ increased as the temperature was decreased[44, 45]. In the clean limit $\kappa_2(T)$ is greater than $\kappa_1(T)$, while in the dirty limit $\kappa_1(T) \approx \kappa_2(T)$ [45]. Using Abrikosov equation (eqn. 4.1), $\kappa_2(T)$ is determined from the VSM. For the specific heat measurements eqn 4.11 was used to determine $\kappa_2(T)$. A rough approximation of the temperature dependence is $\kappa \propto \left(1 + \frac{T}{T_c}\right)^{-1}$ [46], therefore $\kappa(T)$ can be taken to be slowly varying with temperature.

From fig. 4.12 the $\kappa(T)$ values determined from the powder magnetic data, increased with decreasing temperature for x = 0.0(b) and x = 0.25(a), so are consistent with the literature.

From fig. 4.12, for x = 0.0(b) the bulk κ = 129 ± 2 and the powder κ = 133 ± 2, at 13 K. The κ values agree within the errors. The specific heat and magnetic measurements of κ have similar temperature dependence for $PbMo_6S_8$ (fig. 4.12). The specific heat data is 1.3 larger than the magnetisation data. For x = 0.25(a), although N varied between the bulk and the powder data, the κ values were consistent for the two samples. For the bulk sample κ = 108 ± 10 and the powder sample κ = 98 ± 10 at 10.1 K (fig. 4.12). For the specific heat measurement at 0 T, κ was 148. From table 4.7, the powder VSM κ was 144, and the bulk κ was 160 hence κ was consistent for all three measurements. As the distribution in $B_{c2}(T)$ affected the specific heat measurements in fields, it was expected that κ measured in magnetic fields would be higher. From fig. 4.12, the specific heat κ increased more rapidly with decreasing temperature than the magnetic κ. At 11.6 K, the specific heat κ = 260, which is a factor 2 larger than the powder κ at 7 K. Thus the specific heat $\kappa(0\ T)$ value and the VSM κ values for x = 0.0(b) and x = 0.25(a) are in agreement. The method of measuring the magnetisation of powder samples provides a way of determining κ for a wider temperature range.

4.8 Conclusion

The Chevrel phase superconductors $PbMo_6S_8$ and $(Pb_{0.75}Eu_{0.25})Mo_6S_8$ were fabricated and characterised. To add Eu ions onto the lead sites of the Chevrel phase lattice, the samples have to be fabricated at temperatures higher than 1000 °C. The addition of Eu ions increases the resistivity upper critical field ($B_{c2}(0)$) and the c/a ratio. The $B_{c2}(0)$ determined from the resistivity experiments increased by 6 T from 51 T to 57 T, by doping with Eu ions. The $(Pb_{0.75}Eu_{0.25})Mo_6S_8$ critical temperature was 12 K compared to 15.16 K for $PbMo_6S_8$, which is equal to the highest reported critical temperatures of a single phase $PbMo_6S_8$ sample. The Sommerfeld constant for x = 0.0(b) was $\gamma_{\omega_{tn}}^{M\to 0}$ = 508 $JK^{-1}m^{-3}$ in the strong coupling limit. The addition of Eu ions reduced the constant to $\gamma_{\omega_{tn}}^{M\to 0}$ = 276 $JK^{-1}m^{-3}$. Thus the increase in $B_{c2}^{0.9\rho_N}(0)$ was due to the increase in the resistivity across the grain boundaries in x = 0.25(a).

$(Pb_{0.75}Eu_{0.25})Mo_6S_8$ is a magnetic superconductor. Its fundamental parameters were $B_{c1}(0)$ = 1.6 mT, $B_c(0)$ = 78 mT, $\xi(0)$ = 2.13 nm and $\lambda(0)$ = 307 nm.

For $PbMo_6S_8$, κ was determined for bulk and powder samples from the VSM measurements in the temperature range 6 K to T_c. At 13 K the bulk $\kappa = 129 \pm 2$ and the powder $\kappa = 133 \pm 2$, thus are the same within errors. For x = 0.0(b) the powder $\kappa = 133$ at 13 K, and increases to $\kappa = 153$ at 6 K. The specific heat data taken by Leigh had a similar temperature dependence to the magnetic data, but κ was a factor 1.3 higher. For x = 0.25(a) κ was determined from Arrott plots for the bulk and the powder samples. At 10.1 K, the bulk $\kappa = 108 \pm 10$ compared to the powder $\kappa = 98 \pm 10$. Although N_M changed between the samples the κ values were within errors. Similarly κ increased as the temperature was decreased, for the powder sample $\kappa = 92$ at 10.4 K, which increases to $\kappa = 180$ at 8 K. From the specific heat data taken by N. Leigh the x = 0.25(a) data κ increased more rapidly as the temperature was decreased compared to the VSM powder κ value. For x = 0.25(a), the specific heat zero field κ was 148, which is in good agreement with the VSM powder κ of 144 and the bulk κ of 160.

For x = 0.25(a), the measured magnetisation was the sum of the magnetic contribution and the superconducting contribution. The magnetic contribution was determined for both the powder and the bulk samples, by fitting a Brillouin function to the average magnetisation, which gave the magnetic parameters for x = 0.25(a) powder samples to be g_J = 2.016, J_m = 3.5, $N_M = 3.77 \times 10^{26}\ m^{-3}$ and order temperature = -0.02 K. The average magnetisation of the powder samples was used to determine the fundamental parameters and κ in the temperature range 4.2 K to T_c.

References for Chapter 4

1 R. Chevrel, M. Sergent, and J. Prigent, J. Sol. State. Chem **3**, 515 (1971).

2 A. Muhlratzer, J. J. Nickl, B. Seeber, et al., Solid State Communications **19**, 239 (1976).

3 H. Niu, *Private Communication,* University of Durham, (2000)

4 L. A. Bonney, T. C. Willis, and D. C. Larbalestier, Journal of Applied Physics **77**, 6377 (1995).

5 M. Ishikawa and J. Muller, Solid State Communications **27**, 761 (1978).

6 F. S. Delk and M. J. Sienko, Solid State Communications **31**, 699 (1979).

7 D. N. Zheng, H. D. Ramsbottom, and D. P. Hampshire, Physical Review B **52**, 12931 (1995).

8 O. Fischer, H. Jones, G. Bongi, et al., J.Phys. C: Solid State Phys. **7**, L450 (1974).

9 K. Rogacki, E. Tjukanoff, and S. Jaakkola, Physical Review B **64**, 1 (2001).

10 D. N. Zheng and D. P. Hampshire, Inst. Phys. Conf. ser. **148**, 255 (1995).

11 P. Fumagalli and J. Schoenes, Physical Review B **44**, 2246 (1991).

12 D. W. Harrison, K. C. Lim, J. D. Thompson, et al., Physical Review Letters **46**, 280 (1981).

13 N. R. Leigh, I. J. Daniel, D. N. Zheng, et al., Inst. Phys. Conf. No 167, 175 (1999).

14 D. N. Zheng, S. Ali, H. A. Hamid, et al., Physica C: Superconductivity **291**, 49 (1997).

15 D. N. Zheng, A. B. Sneary, and D. P. Hampshire, Inst. Phys. Conf. ser **158**, 1005 (1997).

16 I. J. Daniel, "The fabrication of Chevrel phase superconductors and the origin of the irreversibility field" *Dept of Physics*, University of Durham, 1999.

17 H. Niu, N. A. Morley, and D. P. Hampshire, IEEE transactions on Applied Superconductivity **11**, 3619 (2001).

18 R. Baillif, A. Junod, B. Lachal, et al., Solid State Communications **40**, 603 (1981).

19 D. W. Capone, R. P. Guertin, S. Foner, et al., Physical Review B **29**, 6375 (1984).

20 S. Foner, E. J. McNiff, and D. G. Hinks, Physical Review B **31**, 6108 (1985).

[21] N. J. C. Ingle, T. C. Willis, D. C. Larbalestier, et al., Physica C **308**, 191 (1998).

[22] N. R. Leigh, "Specific heat measurements on Chevrel phase materials exhibiting coexistence of superconductivity and magnetism" *Dept. of Physics*, University of Durham, 2001.

[23] A. A. Abrikosov, Soviet Physics Jetp **5**, 1174 (1957).

[24] N. R. Werthamer, E. Helfand, and P. C. Hohenberg, Physical Review **147**, 295 (1966).

[25] J. R. Waldram, *Superconductivity of metals and cuprates* (Institue of physics publishing, Bristol and Philadelphia, 1996).

[26] A. Arrott, Physical Review **108**, 1394 (1957).

[27] F. Marsiglio and J. P. Carbotte, Physical Review B **33**, 6141 (1986).

[28] N. E. Alekseevskii, G. Wolf, C. Hohlfeld, et al., Journal of Low Temperature Physics **40**, 479 (1980).

[29] F. Y. Fradlin, G. S. Knapp, S. D. Bader, et al., in *Superconductivity in d- and f- band metals*, edited by D. H. Douglass, 1976), p. 297

[30] H. P. v. e. Meulen, J. A. J. A. J. Perenboom, T. T. J. M. Berendschot, et al., Physica B **211**, 269 (1995).

[31] H. Okamoto and Y. Ishihara, Physical Review B **48**, 3927 (1993).

[32] C. P. Poole, *Handbook of superconductivity* (Academic press, 2000).

[33] R. Odermatt and M. Hardiman, Solid state communications **32**, 1227 (1979).

[34] D. P. Hampshire, in *Handbook of Superconducting Materials*, 2000).

[35] M. Decroux, M. S. Torikachvili, M. B. Maple, et al., Physical Review B **28**, 6270 (1983).

[36] M. Decroux, S. E. Lambert, M. S. Torikachvili, et al., Physical Review Letters **52**, 1563 (1984).

[37] P. Selvam, D. Cattani, J. Cors, et al., Journal of Applied Physics **72**, 4232 (1992).

[38] S. Even-Boudjada, V. Tranchant, R. Chevrel, et al., Materials Letters **38**, 90 (1999).

[39] O. Fischer, M. Decroux, S. Roth, et al., Phys C: Solid State Phys **8**, L474 (1975).

[40] R. Wordenweber, Rep. Prog. Phys. **62**, 187 (1998).

[41] C. P. Bean and J. D. Livingston, Physical Review Letters **12**, 14 (1964).

[42] V. L. Ginzburg and L. D. Landau, Zhurnal Eksperimentalnoj i Teoreticheskoj Fisiki **20**, 1064 (1950).

[43] K. Maki, Physical Review **148**, 362 (1966).

[44] W. A. Fietz and W. W. Webb, Physical Review **178**, 657 (1969).

[45] M. Decroux, P. Selvam, J. Cors, et al., IEEE Transactions on Applied Superconductivity **3**, 1502 (1993).

[46] M. Tinkham, *Introduction to superconductivity* (McGraw-Hill International, 1996).

Chapter 5

Design and calibration of the field-gradient torque magnetometer

5.1 Introduction

Magnetic measurements are used to determine the critical current density of superconductors[1]. A new method of measuring the magnetic moment of anisotropic superconductors is torque magnetometry using silicon cantilevers[2, 3]. This chapter covers the design, construction and calibration of the field-gradient torque magnetometer, which measures the magnetic moment of isotropic superconductors in magnetic field gradients. Commercial vibrating sample magnetometers (VSMs) measure magnetic moments in the temperature range 4.2 K to 300 K, in fields up to 12 T[4]. The torque magnetometer was designed to measure magnetic moments in the temperature range 300 mK to 100 K, in fields up to 15 T. The torque is measured using a Quantum Design (QD) silicon torque chip[5]. The field-gradient torque magnetometer fits on to the base of the helium-3 pot of the Oxford Instruments Heliox probe. This means for temperatures above 2 K, the temperature control is better than ± 50 mK, and below 2 K, it is better than ± 10 mK. The whole torque chip can be rotated about the horizontal axis through 360°.

Section 5.2, describes the experimental procedure for using the Heliox probe. The section also includes the problems that can arise when using the Heliox. The final design, including the external circuitry for the torque magnetometer is presented in section 5.3. The alterations that were made and the problems that arose are included. The calibration of the torque magnetometer components including the QD torque chips, the Hall chip and the RuO_2 thermometer are presented in section 5.4. In section 5.5, the calibration of the field-gradient torque magnetometer using NbTi wire is described. For the field-gradient torque magnetometer, the change in voltage across the Wheatstone bridge on the QD chip was measured as the magnetic field was swept. The voltage was then plotted as a function of magnetic field, to give the voltage vs. field sweep loop. In section 5.6, the results from measuring the NbTi wire sample (filament dimensions: 1 mm x 28 μm ∅) on the torque magnetometer and the VSM are presented.

The NbTi wire sample was measured on two different chips as the first chip broke. The calibration constant of chip 3 was an order of magnitude larger than chip 4. The measurements on chip 3 were taken in liquid helium. The first set of measurements was taken at the field centre. The change in magnitude of the hysteresis of the voltage loops was measured as a function of angle. The second set of measurements was taken at the four angles where the voltage loops were reversible at the field centre. The voltage vs. field sweep loops was measured as a function of local magnetic field and magnetic field gradient.

On chip 4 the measurements were taken in liquid helium and in vacuum. In liquid helium, the first measurements were taken at the field centre, and measured the change in magnitude of the hysteresis in the voltage loops as a function of angle. At 0^{o} the change in magnitude of the hysteresis in the voltage loops as a function of magnetic field and magnetic field gradient were measured. In vacuum, the sample was fixed at 180^{o}, using a stationary holder. The change in magnitude of the hysteresis in the voltage loops as a function of local magnetic field and field gradient were measured in the temperature range 300 mK to 10 K. A second set of voltage loops was measured as a function of magnetic field, field gradient and temperature, in vacuum. For this data set, at each field gradient, the voltage loops were measured for every temperature, before the probe was moved to the next field gradient.

From the voltage loops measured as a function of local magnetic field and field gradient, the critical current density for the NbTi wire sample are determined in section 5.7. The critical current densities from the VSM data are also presented. The errors for the critical current densities measured are discussed. In section 5.8, the comparison between the field-gradient torque magnetometer and the VSM is discussed, including the advantages and disadvantages of both magnetometers. The overall performance of the torque magnetometer is presented in section 5.9.

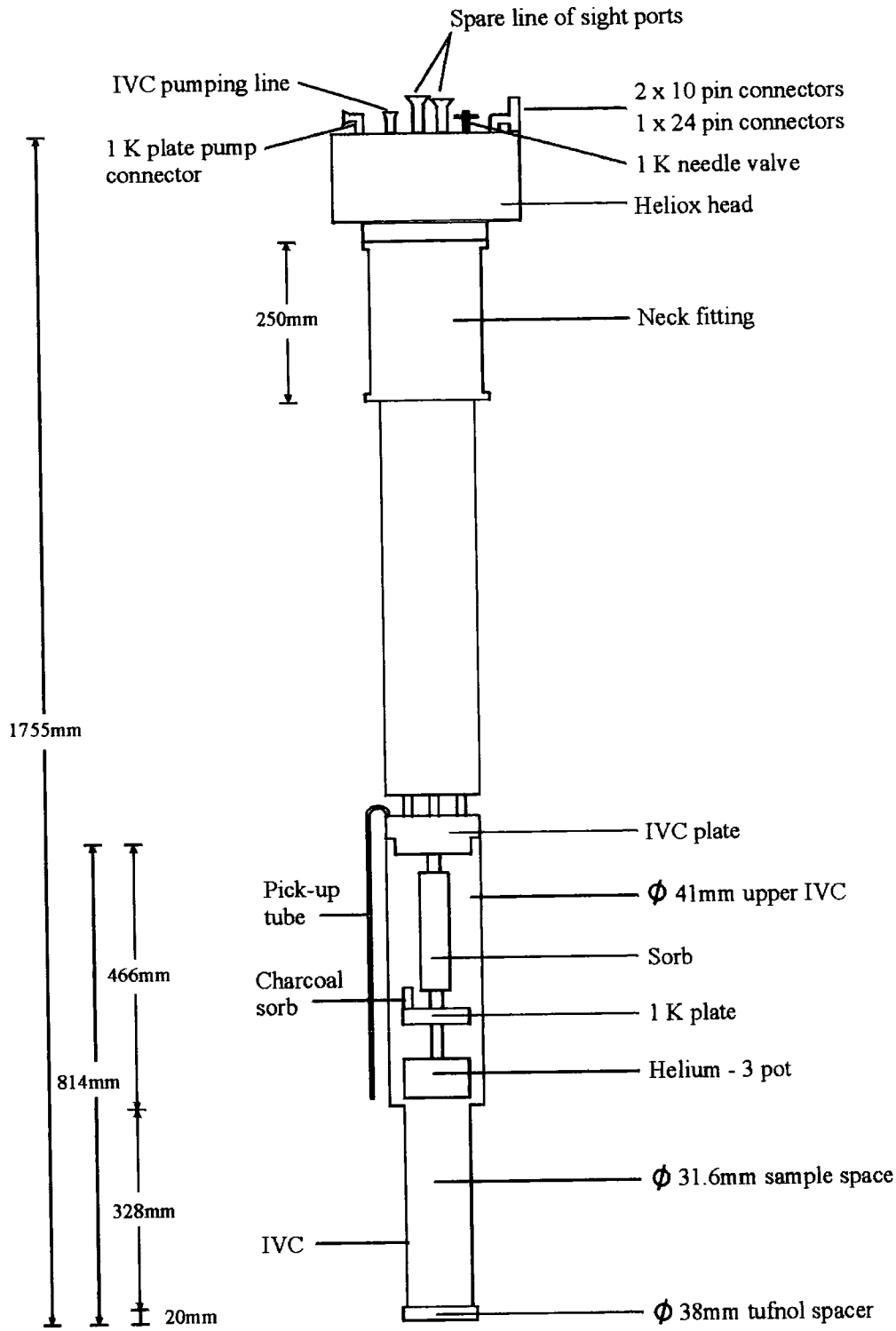

Figure 5.1. Schematic diagram of the Oxford Instruments Heliox probe.

5.2 Heliox probe

The field-gradient torque magnetometer was designed to attach to the bottom of the helium-3 pot of an Oxford Instruments Heliox probe. The Heliox was used to control the temperature of the whole experiment. The temperature range of the Heliox was 250 mK to 100 K. It was designed to work in the Oxford Instruments 15 T magnet. The Heliox used liquid helium-3, to reach temperatures below 2 K. The helium-3 gas was sealed in a self-contained vessel, so none of the gas could escape.

The lower part of the probe was covered with a brass vacuum can (IVC) (see fig. 5.1). To prepare the probe for cool down, a few preliminary checks were made. All the wires were either glued or tied down, the charcoal sorb was checked and all the old vacuum grease was removed. This was to make sure there were no touches to the IVC.

The IVC was connected to the IVC plate (fig. 5.1) using silicon vacuum grease. The IVC plate and IVC opening were sandpapered to remove any scratches. The IVC plate was thickly covered in vacuum grease, to create a good seal. The IVC opening was lightly smeared with grease. The IVC was gently and carefully slid over the lower part of the probe, so no vacuum grease touched the probe. The IVC was pushed hard on to the IVC plate. The IVC was then pumped out to a rough vacuum for 15 minutes, or until it did not move when pulled. The 1 K plate pick-up tube was taped down onto the IVC. This meant it was secure and would not hit the baffles when lowered into the magnet. Helium gas was blown through the pick-up tube via the 1 K plate connector for 10 - 20 minutes. This removed any water in the tube, and checked it was not blocked. The helium gas was kept connected to the pick-up tube during the cool down. This meant the pick-up tube was under positive pressure, so a blockage was less likely to form.

The whole probe was slowly lowered into the magnet. The helium boil off was kept low. In the magnet the Heliox head rested on the neck fitting. The whole probe could be lifted up in the magnet. A clamp was used above the neck fitting to hold the probe in position. As the IVC was under a rough vacuum, it was left overnight to cool down. If the vacuum was too strong, a small amount of helium gas was added to help the cool down. At 4.2 K, the charcoal sorb on the 1 K plate absorbed the helium gas in the IVC, which created a vacuum.

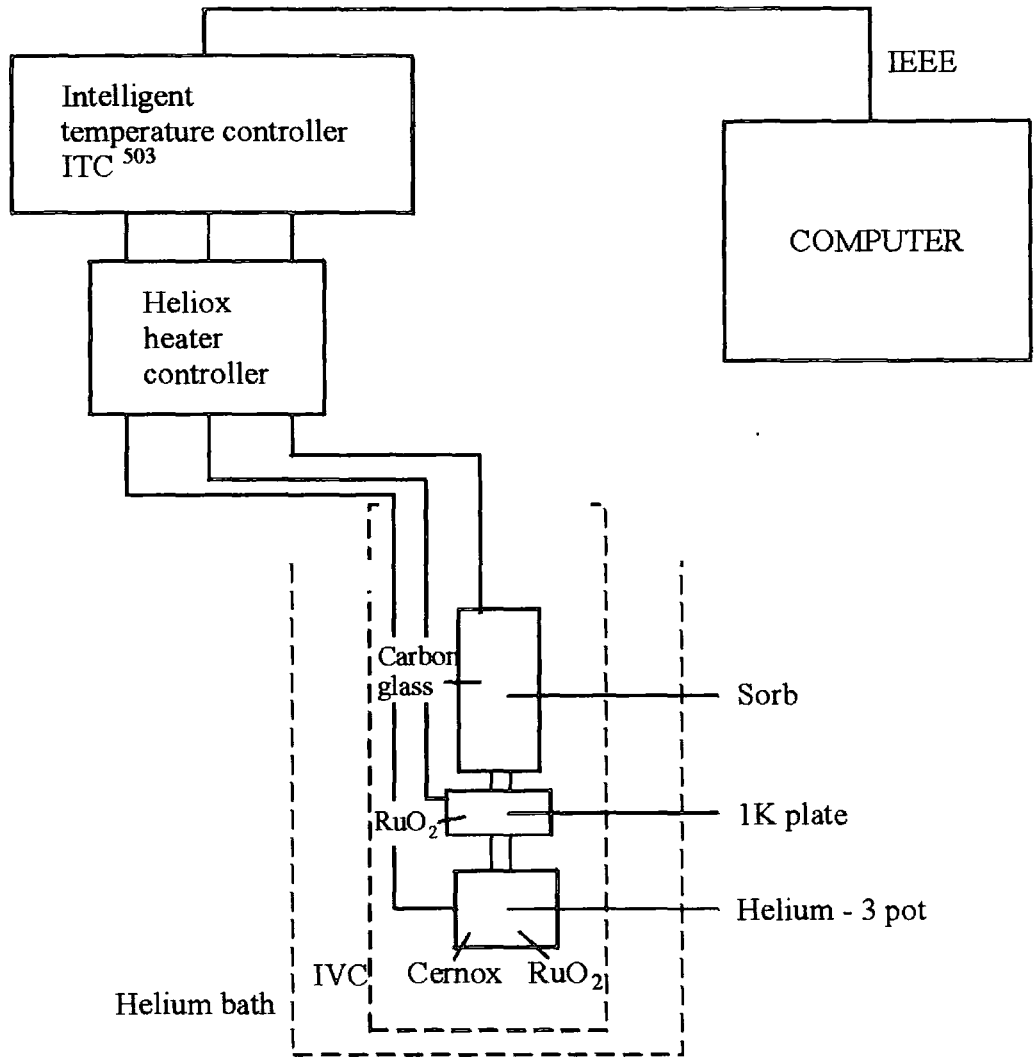

Figure 5.2. Schematic diagram of the external circuitry of the Oxford Instruments Heliox probe.

At 4.2 K, the probe could be cooled down to 250 mK. The vacuum pump was attached to the 1 K plate connector and the 1 K plate needle valve was opened. The vacuum pump pulled liquid helium through the pick-up tube and around the 1 K plate. This cooled the 1 K plate down to 1.6 K. The reading on the vacuum pump pressure controller was 2 mbar. The sorb was then heated to 30 K. This released the helium-3 gas stored in the sorb. The boiling point of helium-3 is 3.2 K. This meant the helium-3 gas was condensed by the 1 K plate. The liquid ran down into the helium-3 pot. The helium-3 pot temperature was the same as the 1 K plate. The probe was left for half an hour for all the helium-3 gas to condense. The sorb temperature was then reduced to 2 K. At temperatures below 30 K, it absorbed the helium-3 vapour, which reduced the pressure above the liquid helium-3. The temperature of the liquid and thus

the helium-3 pot temperature decreased down to the base temperature of 250 mK. The base temperature was held for 3 – 6 hours.

The temperature of the helium-3 pot was controlled using the Oxford Instruments Intelligent Temperature Controller (ITC). The ITC read the four thermometers and controlled the two heaters on the Heliox. On the sorb was a carbon resistor, which was thermometer 1 on the ITC. Its temperature was controlled by heater 1. The 1 K plate temperature was read by a RuO_2 thermometer, which was thermometer 2 on the ITC. The helium-3 pot had a cernox thermometer for temperatures above 2 K, and a RuO_2 thermometer for temperatures below 2 K. On the ITC the cernox was thermometer 3, and the RuO_2 was thermometer 2. The two RuO_2 thermometers had different connectors. During the condensation process the 1 K plate RuO_2 thermometer was connected to the heater controller (fig. 5.2). During the experiments, the heater controller read the helium-3 pot RuO_2 thermometer. For temperatures above 2 K, the temperature of the helium-3 pot was controlled by heater 3, which was sunk into the pot. For temperatures below 2 K, the temperature was controlled by heater 1. This controlled the temperature of the sorb, and thus the vapour pressure above the liquid helium-3. The PIDs for the experiment were P = 15 %, I = 2.0 s and D = 0.1 s, and were used at all temperatures.

Before the probe was removed from the magnet, the speedivalves on the vacuum pump and the 1 K plate were closed. The vacuum pump was removed. The 1 K plate needle-valve was then closed. A rubber bladder was put on to the IVC relief valve, and the valve opened. This meant any liquid which evaporated, would not build up pressure in the IVC. The probe was then removed slowly from the magnet. It was left under vacuum to warm up. When the IVC was opened to atmosphere, the air was let in slowly, to avoid damaging the chip. The IVC was removed from the bottom of the probe using a sliding hammer.

A few problems occurred when using the Heliox. One of the main problems was a touch to the IVC from the helium-3 pot. When a touch occurred, the cool down to 4.2 K took less than an hour. As the IVC was in the liquid helium bath, it was at 4.2 K. When there was a touch the IVC acted as a heat link, so the helium-3 pot was at 4.2 K. The helium-3 pot temperature would not decrease down to 1.6 K nor increase when heater 3 was applied. To remove the touch, the probe was warmed to room temperature and the IVC removed. The touch was generally a wire, which was not tied down.

When there was too much helium gas in the IVC, the temperature of the 1 K plate was not stable at 1.6 K, when the sorb temperature was increased to 30 K. The 1 K plate temperature increased, as the sorb heated the helium gas. The gas moved the heat around the IVC. It was not possible to condense the helium-3 gas, as the temperature of the 1 K plate was above 3.2 K, but the helium-3 pot temperature could be increased above 4.2 K. The helium gas was removed by vacuum pumping the IVC out for 2 – 3 hours. The sorb was held at 30 K, during the pumping, to evaporate some of the excess liquid helium. If after three hours of pumping, there was still gas in the IVC, the vacuum seal had probably broken. This meant the probe had to be warmed up to room temperature, and the seal remade.

Another problem was blockages in the pick-up tube. The blockages were caused by water or vacuum grease freezing in the tube. When a blockage occurred, the 1 K plate stayed at 4.2 K, and was under vacuum. This was because the liquid helium could not be drawn through the pick-up tube, by the vacuum pump. If the blockage was small, it was pulled through the system by the vacuum pump. For large blockages the probe had to be warmed up. At room temperature the blockage was removed by putting high pressure helium gas through the pick-up tube for an hour.

The end of the pick-up tube was about 5 cm above the top of the magnet. For the Heliox to operate, the end of the pick-up tube had to be in liquid helium. If the pick-up tube's end was not in the liquid helium, the temperature of the helium-3 pot was not stable. The base temperature of the helium-3 pot was dependent on the temperature of the 1 K plate and the mass of the material attached to it. The lower the 1 K plate temperature, the lower the base temperature. For the field-gradient torque magnetometer, the mass of copper attached to the helium-3 pot, meant the base temperature was stable for three hours before slowly rising. This meant that recondensation of the helium-3 occurred at least twice in the experiment.

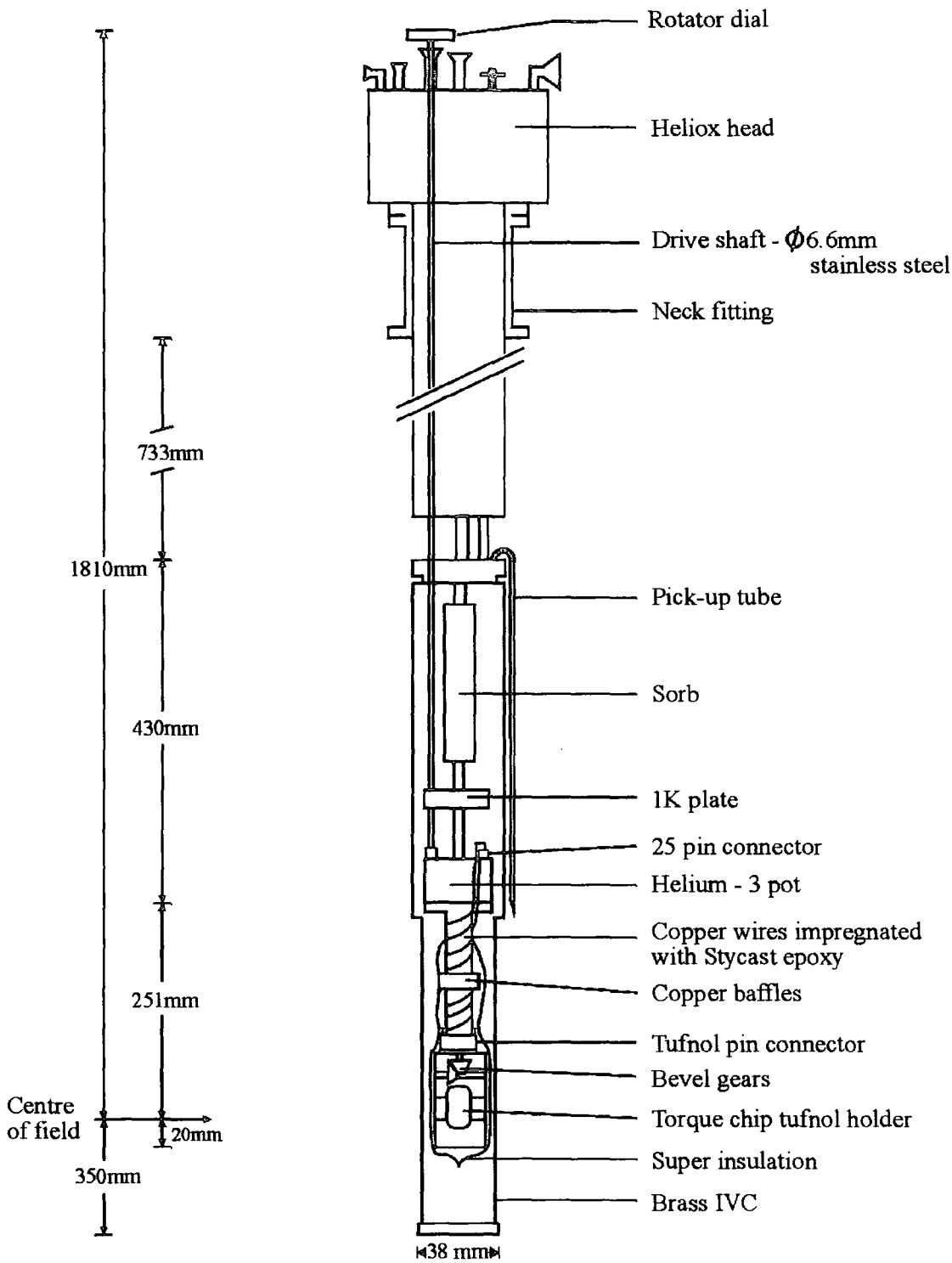

Figure 5.3. Schematic diagram of the final design of the field-gradient torque magnetometer.

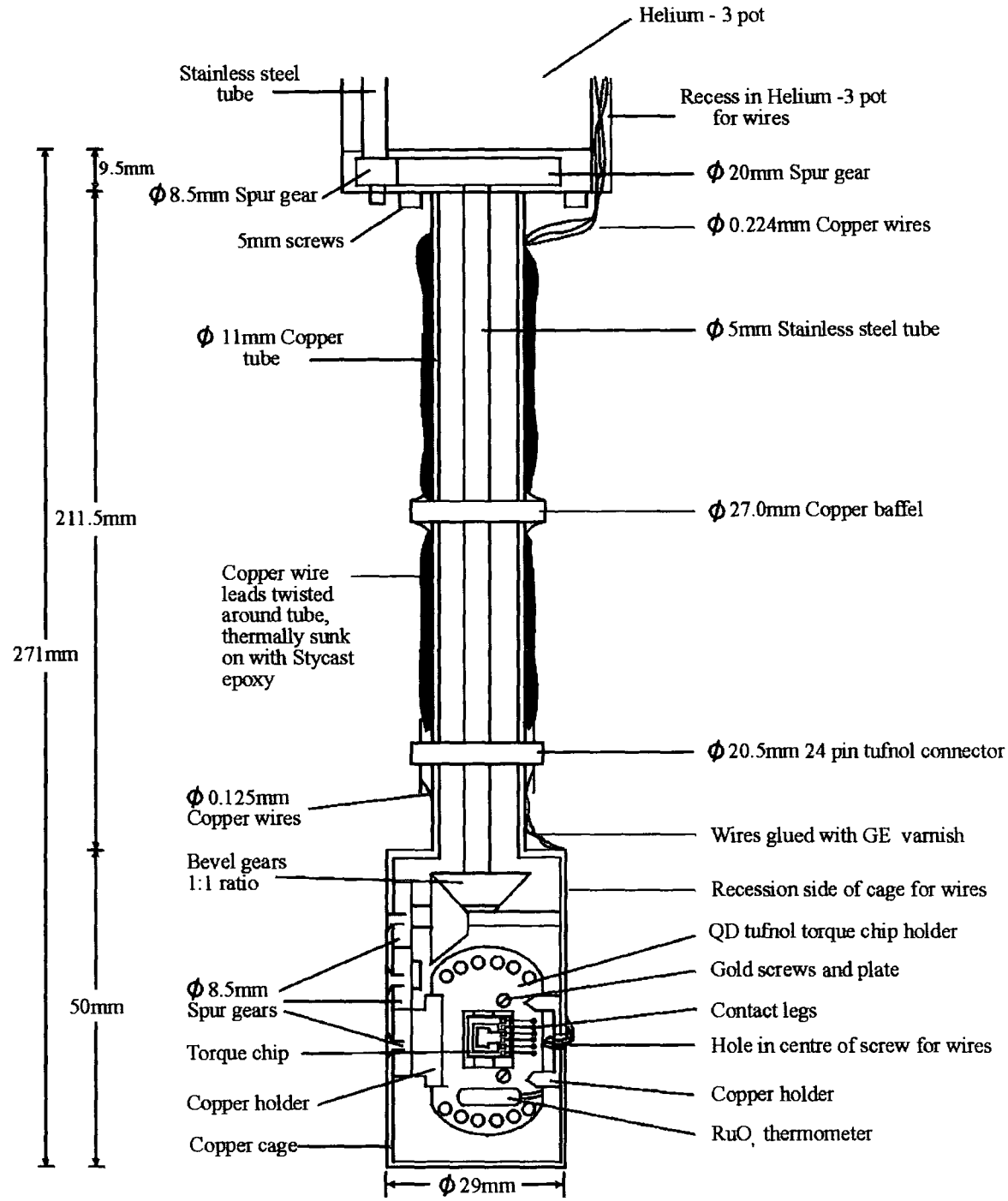

Figure 5.4. Schematic diagram of the field-gradient torque magnetometer, from below the helium-3 pot. The diagram includes the rotation set-up and the QD torque chip.

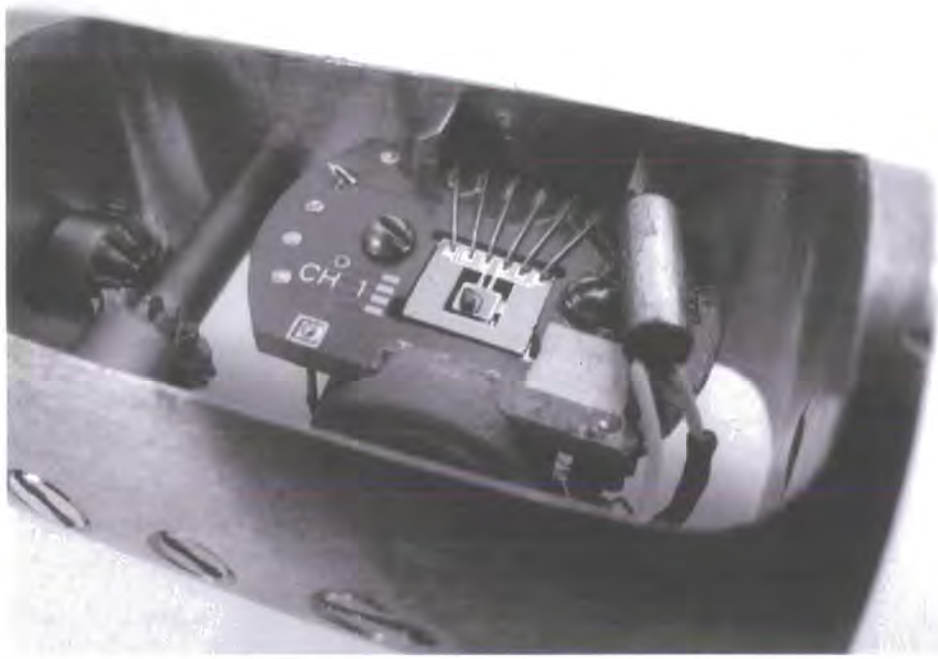

Figure 5.5. Photograph of the field-gradient torque magnetometer copper cage end piece, with the rotational set-up inside. The QD torque chip is in the centre of the tufnol chip holder. The sample on the platform is $Pb_{0.75}Eu_{0.25}Mo_6S_8$, and is glued on using GE varnish.

5.3 Design of the field-gradient torque magnetometer

5.3.1 Final design of the field-gradient torque magnetometer

Figures 5.3 & 5.4 show the final design of the field-gradient torque magnetometer. The field-gradient torque magnetometer was designed to be a separate unit, from the Heliox. It attached onto the bottom of the helium-3 pot. All the wiring for the torque chip and components were connected into a male 25 pin connector. On top of the helium-3 pot was the corresponding female connector. This meant the torque magnetometer could be removed, without taking apart any of the commercially built Heliox.

The torque magnetometer main structure was made from copper (figs. 5.4 & 5.5). Copper was used as it has a thermal conductivity of 5 $W(cm\ K)^{-1}$, at 4.2 K. The torque magnetometer consisted of a 29 mm diameter cage, where the tufnol chip holder was fixed, a 211 mm long copper tube of diameter 11 mm, which was attached to a copper pot of diameter 31.5 mm. The copper pot was tightly bolted onto the

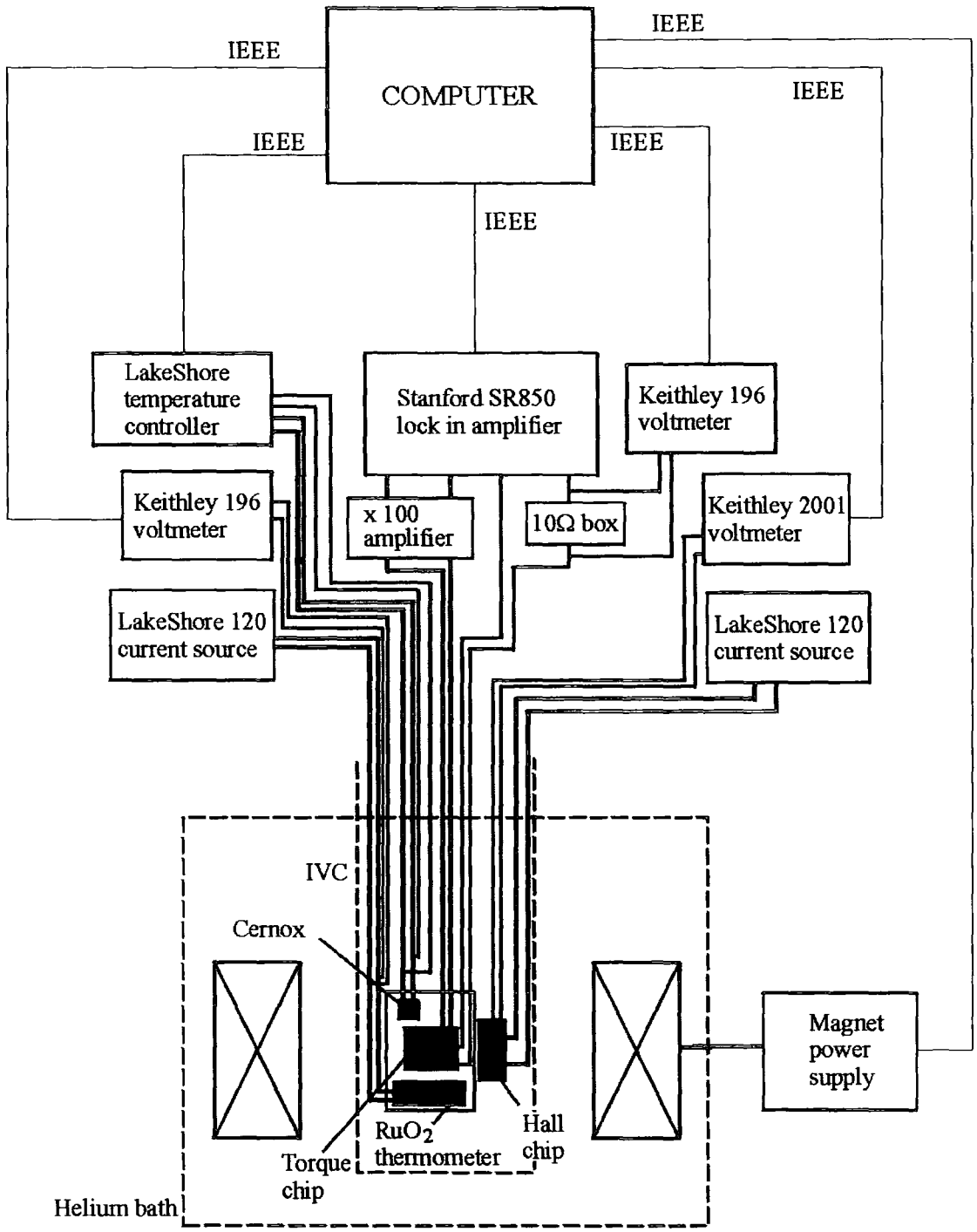

Figure 5.6. Schematic diagram of the external circuitry of the field-gradient torque magnetometer. The thick lines represent the current leads, the thin lines represent the IEEE cables and the medium thick lines represent the voltage leads.

helium-3 pot using five 5 mm screws, ensuring there was good contact between them. Inside the top of the copper pot was a 20 mm spur gear attached to a stainless steel rod. The rod was inside the copper tube, and went to a bevel gear. The bevel gears moved the rotation from the vertical axis to the horizontal axis. The bevel gears had a ratio of 1:1. Attached to the second bevel gear was an 8.5 mm diameter spur gear. The spur gear was one of three along the side of the cage. Attached to the last spur gear was a copper holder. On the other side of the cage was a second copper holder. The copper holders were designed to hold the QD tufnol torque chip holder in the cage. They also rotated the tufnol chip holder through 360 degrees. The wires for the experiments entered the cage through the centre of the screw attached to the second copper holder. This reduced the rotation of the wires, in the magnetic field. It also meant the wires did not get wrapped around the tufnol chip holder.

At the top of the Heliox was the rotator dial piece, which was attached to a line of sight port. The dial was connected to the drive shaft. The dial could be rotated in both directions. The drive shaft went to the bottom of the probe through the line of sight port, to just below the helium-3 pot. The drive shaft was made from a 6.5 mm diameter seamless stainless steel tube. At the bottom it was connected to an 8.5 mm spur gear, which met with the larger spur gear. These two gears were required to change the rotation from the side of the probe to the centre. The line of sight ports went from the top to the helium-3 pot. They did not go to the centre of the sample space. The ratio of the rotation from the rotator dial to the tufnol chip holder was 2.7:1.

The field-gradient torque magnetometer was used under two different configurations. These were in liquid helium and in vacuum. For the liquid helium measurement, a specially designed brass can was used. The can was screwed on to the IVC plate. The bottom of the can had holes in, so when in the magnet, the whole of the lower part of the probe was in liquid helium. For the measurements in vacuum the set-up and procedure is described in section 5.2.

The external circuitry of the field-gradient torque magnetometer is shown in fig. 5.6. The temperature of the sample was measured by two thermometers, which were glued on to the tufnol chip holder. The zero field temperature was determined from the RuO_2 thermometer, as the resistance of the RuO_2 thermometer changed with magnetic field. A cernox thermometer was used to measure the temperature when in field. The RuO_2 thermometer and the cernox were both measured using four terminal resistance

measurements. For the RuO_2 thermometer, a Lakeshore current source provided a 1 μA dc current, and a Keithley 196 voltmeter measured the voltage. For the cernox, a Lakeshore temperature controller measured the resistance.

The angle between chip and the applied magnetic field was measured using a Hall chip. The Hall chip was attached to the copper holder. A Lakeshore current source provided a 10 μA dc current, and the voltage was measured by a Keithley 196 voltmeter.

The torque chip had a Wheatstone bridge patterned on it (cf. fig. 3.4). A Stanford SR850 DSP lock-in amplifier was used to provide an ac current through the bridge. The lock-in read the corresponding voltage across the bridge. The ac current went through a 10 Ω resistor box. This was used to phase the lock-in at the beginning of the experiment. The voltage across the 10 Ω resistor box was read by a Keithley 2001 voltmeter. This meant the current through the Wheatstone bridge could be determined. The measured voltages were amplified by a Stanford x 100 amplifier. To increase the sensitivity of the experiment, a variable resistor was put in parallel with one of the resistors in the Wheatstone bridge. The resistance of the variable resistor was set so the voltage across the Wheatstone bridge was zero.

The whole experiment was controlled by a LABview program, which was run from a computer. The voltages of the components were recorded on the computer.

The QD torque chip was placed in the tufnol chip holder using tweezers. It was held in the holder by a gold plate underneath it, and the contact legs on top. The samples measured on the field-gradient torque magnetometer were cylindrical. They were glued on the 2 x 2 mm^2 platform of the torque chip with GE-varnish (fig. 5.5). The long axis of the sample was parallel to the side edge of the platform. The sample was positioned a distance l from the centre of rotation of the platform.

5.3.2 Problem solving and trouble shooting

The original design of the magnetometer had to be altered due to problems arising from the cool down process and the experimental procedure. The problems that arose included thermal heating, mounting the sample and movement of the sample in the magnetic field. All these problems are discussed.

5.3.2.1 Thermal Heating

One of the main concerns was the heat transfer during the experiment. The Heliox was designed so the helium-3 pot at temperatures below 1.5 K was isolated from the rest of the probe. Any heat that entered the IVC would warm up the helium-3 pot and the sample. The three ways heat could have entered the IVC were convection, conduction and radiation. The heating effects were most noticeable below 1 K. Originally the helium-3 pot would reach 300 mK, while the platform would be at 350 – 400 mK. To reduce the temperature difference, the isolation of the helium-3 pot and torque magnetometer was improved.

To reduce the radiation reaching the chip, superinsulation was used. It was wrapped tightly around the torque magnetometer, seven or eight times. It covered from just below the helium-3 pot to beyond the bottom of the copper cage. This made sure it did not touch the IVC, but as much radiation as possible was reflected. This reduced the temperature of the platform by ~ 20 mK.

If there was helium gas in the IVC, convection occurred between the IVC and the helium-3 pot. The gas caused instability in the temperatures above 4.2 K, which reduced the accuracy of the measurement. The temperature of the helium-3 pot would not decrease below 4.2 K. The charcoal sorb could only absorb a small amount of helium; thus the excess gas was pumped out. The IVC was kept in vacuum to reduce convection.

Conduction occurred through the drive shaft and the copper wires. To reduce the heat conduction, the wires were heat sunk to the helium-3 pot. The wires were then epoxied onto the copper tube with stycast epoxy. On the copper cage, they were glued down with GE-varnish. As the wires were heat sunk, they were at the same temperature as the helium-3 pot. This meant when cooling down below 1 K, the heat was removed from the platform via the copper wires. This reduced the temperature of the platform ~ 30 mK.

The drive shaft conducted the most heat into the IVC. It was connected from the rotator dial to the spur gear just below the helium-3 pot (fig. 5.4). It went through the helium-3 pot and the 1 K plate. This meant it had a temperature gradient from 300 K to 300 mK over 1.5 m. The drive shaft also had to be rigid enough to transmit the rotational motion from the dial, to the spur gear. Originally the drive shaft was made from a stainless steel rod of 5 mm diameter, which had a 20 cm tufnol section just above the helium-3 pot. The tufnol section was a thermal break, which reduced the

heat reaching the helium-3 pot. Tufnol is an insulator, with a thermal conductivity of 0.1 mW(cm K)$^{-1}$ at 4.2 K, which is a factor 30 smaller than stainless steel. The stainless steel rod and tufnol piece were rigid enough to transmit the rotation. The base temperature of the helium-3 pot with this drive shaft was 300 mK, while the platform was 350 mK. This was 50 mK higher than the base temperature without the drive shaft. The second thermal break was a plastic tube, which had a lower thermal conductivity than the tufnol. The problem with the plastic tube was it bent under rotation. The final drive shaft was made from thin walled stainless tube of outer diameter 6.5 mm, with a connector above the helium-3 pot. The tube was rigid to transmit the rotational motion, when connected. The heat conducted down the tube was a factor 1.25 less than down the rod. For the measurements below 1 K, the rotator dial and drive shaft were lifted up 2 cm, breaking the connection, thus leaving the helium-3 pot and the torque magnetometer in isolation. The lowest helium-3 pot temperature reached with this drive shaft was 275 mK with the platform at 300 mK.

5.3.2.2 Mounting the sample

There were problems with mounting the sample on the chip's platform. The whole process was viewed down a microscope. The QD chip was tightened into the tufnol chip holder, which was in the copper cage. This provided a secure position for the chip. Initially the sample was placed on the platform by hand using tweezers, but this method proved unreliable. The sample would either not be vertical or the platform would break as too much force was applied by the tweezers. To solve this problem a micro-manipulator was built. The micro-manipulator consisted of a pair of tweezers mounted on a platform at a 45 degree angle. The platform could move in all three directions using vernier gauges. The sample was held in the end of the tweezers, by having one leg fixed, and tightening a screw against the other. A syringe was used to place the GE-varnish onto the platform. The consistency of the GE-varnish was thick enough so it did not run over the platform, but was not too thick to stay attached to the syringe. If any GE-varnish ran onto the legs, it was soaked off using isopropanol. If the GE-varnish was left on the legs, during the cool down, it would freeze. GE-varnish contracts at a different rate to the silicon. This put stress on the legs, which caused them to break. If the GE-varnish was too thick it would stick to the platform and the syringe. This meant it was difficult to remove the syringe without pulling the platform up, which added extra stress to the legs. Once the GE-varnish was on the

platform, the micro-manipulator was moved, so that the sample was at the correct angle. The tweezers were then lowered down slowly. When on the platform the tweezers were opened and the sample positioned. The tweezers were then lifted away from the platform. The GE-varnish was left for 12 hrs to dry.

5.3.2.3 Sample movement in the magnetic field

Another problem was the sample moving in the magnetic field. The movement could have been caused by the tufnol holder, the chip or the sample. The movement was observed as discontinuities in the voltage vs. field sweep loops. These were either in the form of a peak, which decayed back to the voltage loop or as a jump where voltage moved from one value to another. The discontinuities degraded the data.

To ensure the sample did not move on the platform, the GE-varnish was left overnight to dry. The torque chip was held tightly in the tufnol chip holder by a gold plate underneath it, and the six contact legs on top. There was about a 1 mm gap between the chip and the holder. To stop the chip moving, vacuum grease was put in the gap. When the grease froze, the chip was fixed in place. The tufnol chip holder was glued into the copper holders with GE-varnish, to stop any movement.

The backlash of the gears caused the tufnol chip holder to move. When on the bench, the tufnol holder was set at 90^{o}, if the edge of the holder was touched, it moved about five degrees. This movement was due to the gears not being perfectly interlocked, and was a major problem. For the rotational holder, a grub screw was put into the cage. It was tightened up against the lowest spur gear, thus holding the spur gear in position, reducing its movement. The only problem was the Heliox had to be warmed up and the IVC removed, for the grub screw to be tightened. The tufnol holder could then be rotated against the grub screw, which also reduced the movement. To stop all movement of the tufnol holder, a stationary copper holder was made, which fitted into the copper cage. It screwed into the existing holes on the side of the cage. The stationary holder held the tufnol holder and thus the chip at 180 degrees.

5.4 Calibrations

Some of the components used on the field-gradient torque magnetometer were calibrated, before the main experiments were carried out. These include the RuO_2 thermometer, the Hall chip and the Quantum Design torque chips.

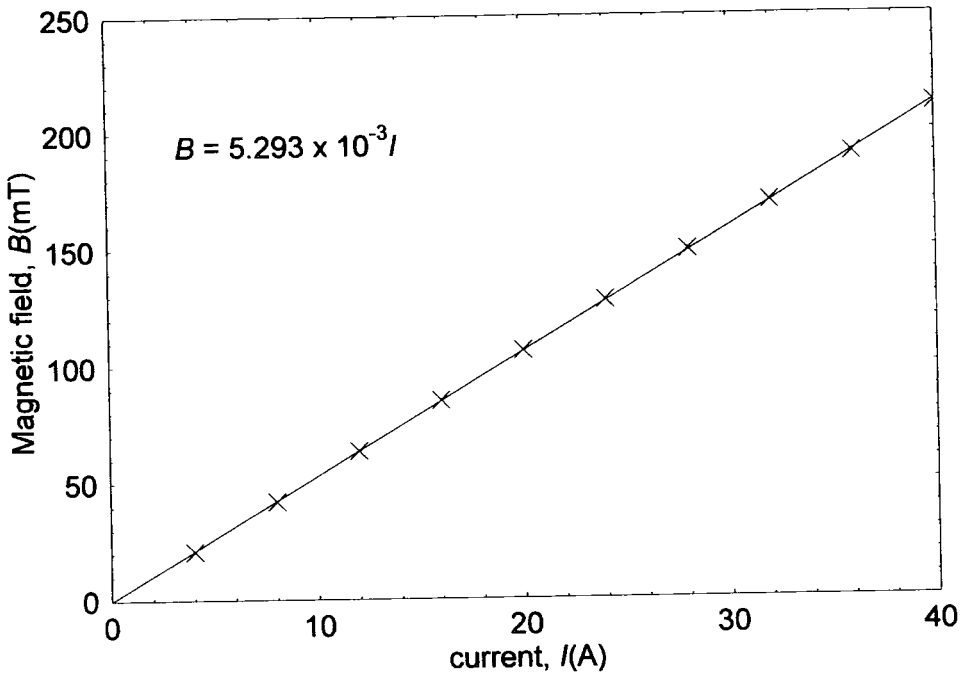

Figure. 5.7. The magnetic field at the centre of the copper solenoid as a function of the applied current. The equation gives the relation between the magnetic field (in T) and the current (in A).

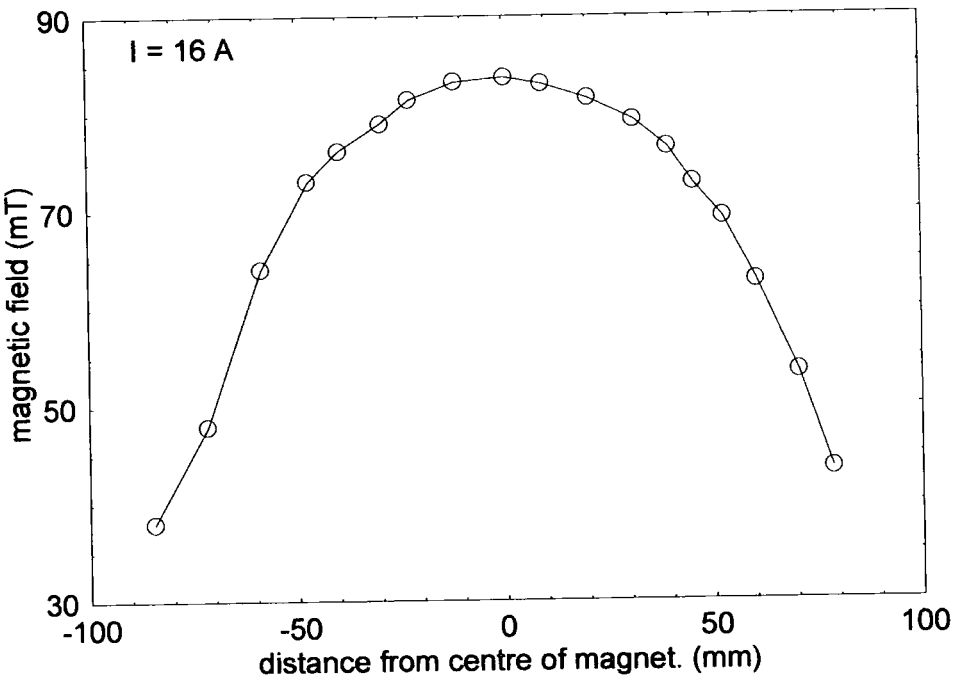

Figure. 5.8. The magnetic field profile in the copper solenoid magnet as a function of distance from the magnet centre, with 16 A flowing through the magnet.

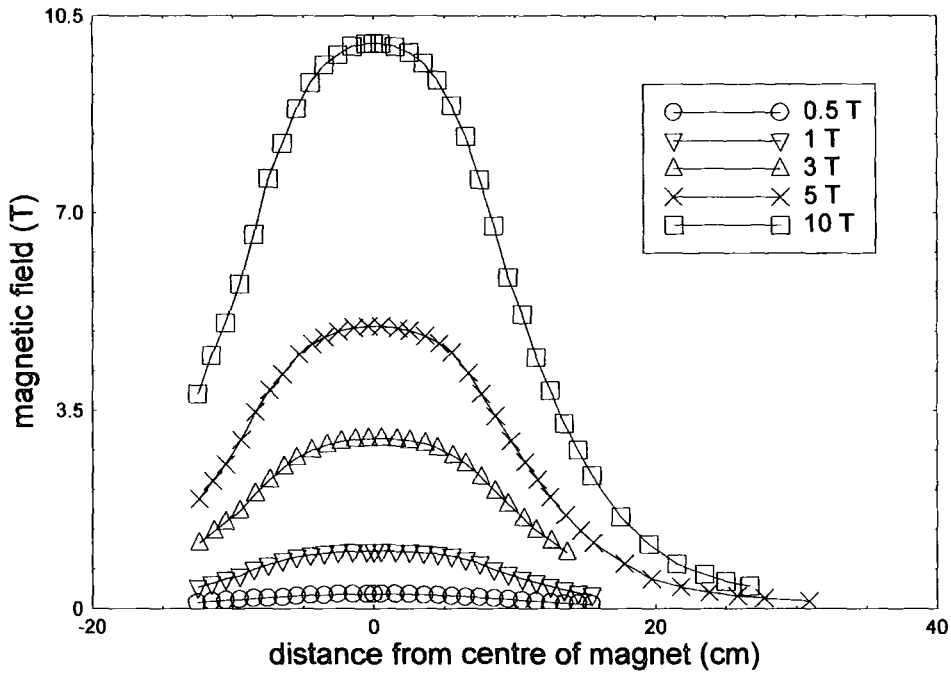

Figure 5.9. The magnetic field profile in the 15 T superconducting magnet, as a function of magnetic field and distance from the centre of the magnet. The field was measured every 2 cm, using a Hall probe.

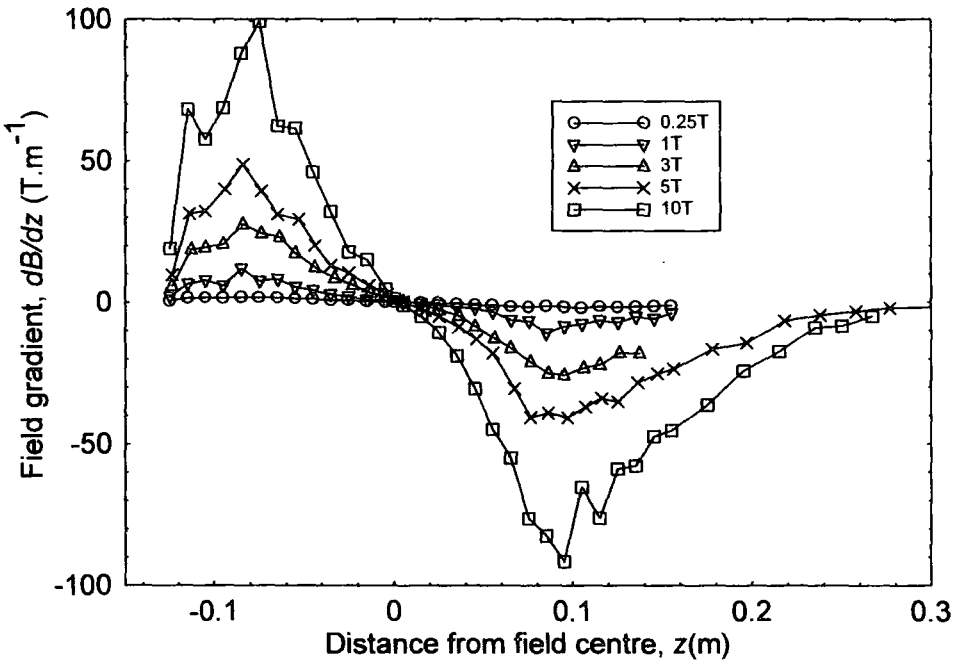

Figure. 5.10. Magnetic field gradient $\frac{dB}{dz}$ of the superconducting 15 T magnet, as a function of magnetic field, and distance from the centre of the magnet.

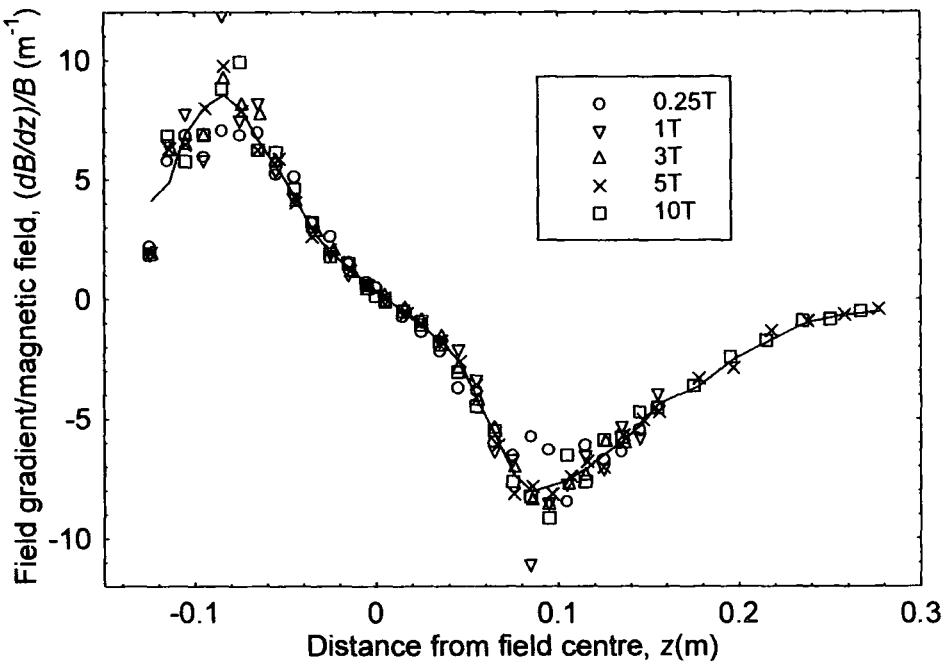

Figure 5.11. Magnetic field gradient divided by magnetic field for the 15 T magnet as a function of distance from the field centre and magnetic field. The solid line is a smoothed line through the 5 T data, and is used as a guide for the eye.

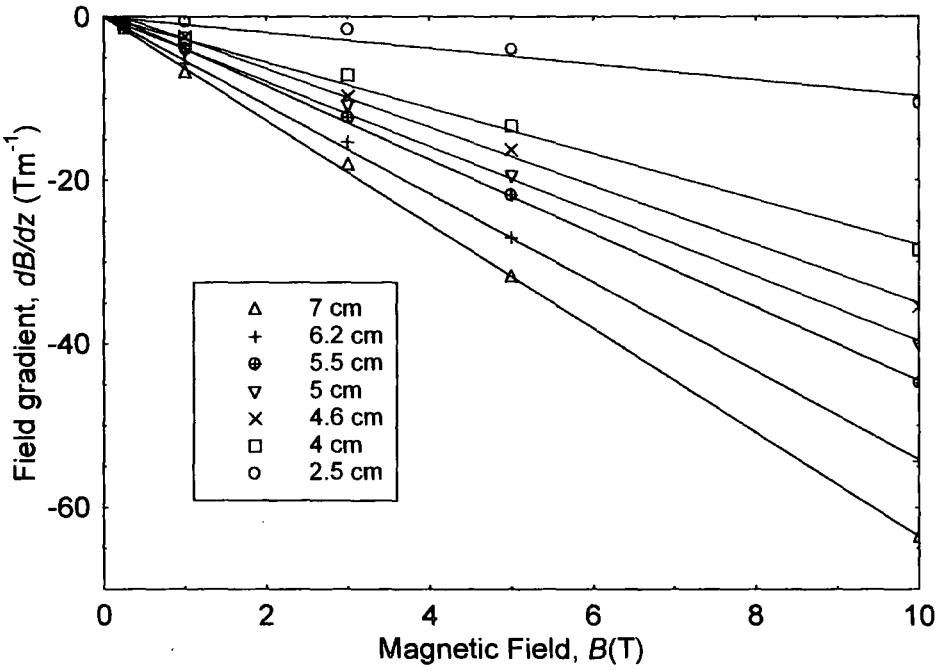

Figure 5.12. Magnetic field gradient $\frac{dB}{dz}$, of the 15 T magnet as a function of magnetic field and distance from the centre of the magnet (z). The solid lines are the best-fit straight lines through each data set. The equation of these lines gives the relation between the field gradient and the magnetic field at each height z.

5.4.1 Copper solenoid magnet and superconducting magnet

Two solenoid magnets were used in this work. The first magnet was a copper solenoid magnet, which was used submersed in liquid nitrogen. It was used for preliminary calibration measurements of the QD torque chips. The Oxford Instruments power supply (IPS 120-10) provided the current through the magnet. The magnet was calibrated by measuring the magnetic field at the centre, for different currents through the coil. The magnetic field was measured using a Hall probe. The magnetic field was then plotted as a function of current.

From figure 5.7, the calibration equation for the copper solenoid magnet is:

$$B = 5.29 \times 10^{-3} I \qquad (5.1)$$

where I is the current through the magnet and B is the magnetic field in the centre. The field profile of the copper magnet was also measured. The magnetic field for I = 16 A was measured using the Hall probe as a function of distance from the centre of the magnet. Figure 5.8 shows that the magnetic field was almost homogenous about the magnet centre.

The second magnet was an Oxford Instruments 15 T superconducting magnet. It was also controlled by the Oxford Instruments IPS. The field profile at five different fields was measured using a Hall chip. The magnetic field was measured every two cm from the top of the magnet. The local magnetic field at a distance z from the field centre was determined from fig. 5.9. This was the magnetic field experienced by the sample at height z. The field gradients were calculated by taking the gradient of the field in fig. 5.9, and plotting them against z. The field gradients for each of the magnetic fields as a function of height z are in fig. 5.10. The maximum change in gradient occurs between 5 cm to 8 cm. From fig. 5.11, the form of the field gradient at each field is the same as a function of distance z. For the torque magnetometry experiment, the field gradients as a function as magnetic fields, for constant height z are required. Fig. 5.12 shows the relation between the field gradient and the magnetic field at height z is linear as expected.

5.4.2 RuO_2 Thermometer

The ruthenium oxide resistor was used to measure the temperature of the sample between 250 mK and 15 K. The RuO_2 resistor was bought from Lakeshore Cryotronics Ltd, and arrived uncalibrated. The RuO_2 thermometer was calibrated on

the Heliox, using a copper holder. The holder consisted of a thick walled copper tube, the outer diameter of which was 7 mm and the inner diameter was 3.5 mm. The RuO_2 thermometer was held in the tube with vacuum grease. The holder was screwed into the base of the helium-3 pot. The wires were glued onto the holder using stycast epoxy and on to the helium-3 pot using GE-varnish. Hence the RuO_2 resistor was in good thermal contact with the helium-3 pot. The resistance of the RuO_2 resistor was measured using a four terminal measurement. A dc current of 1 μA was applied by a Lakeshore current source. The voltage was measured by a Keithley 196 voltmeter. The voltage was measured for both directions of the current. The resistance was determined using Ohm's law. The RuO_2 thermometer was calibrated against the thermometers on the helium-3 pot.

The Heliox was cooled down to 250 mK, as described in section 5.2. The resistance was measured at every 20 mK from 250 mK up to 500 mK, then every 50 mK between 500 mK and 1 K. Between 1 K and 4 K, the resistance was measured every 250 mK, then every 500 mK between 4 K and 15 K. For each temperature the average resistance from both current directions was calculated. The calibration equation for a RuO_2 thermometer is given by:

$$\ln\left(\frac{1}{T}\right) = \sum_{i=0}^{4} a_i \left[\ln\left(R - R_o\right)\right]^i \qquad (5.2)$$

where R_o is the resistance of the RuO_2 thermometer at room temperature. The constants a_i were determined for the RuO_2 thermometer by plotting equation 5.2, and applying a fourth order polynomial to the data.

A calibration LABview programme was written for the RuO_2 thermometer. The programme measured the resistance, subtracted R_o, then used the variables a_i and equation 5.2, to calculate the temperature of the resistor. The calibration of the RuO_2 thermometer was checked a year later. It was found that the RuO_2 thermometer still had the same a_i variables. The RuO_2 thermometer was also strongly field dependent, hence the cernox thermometer was used to measure the temperature of the sample during the field sweeps. The problem with the cernox was the leads had to be silver epoxied on each time, which could change the measured resistance. Thus the temperature of the cernox read by the Lakeshore did not always agree with the RuO_2 resistor. Therefore the RuO_2 thermometer was used to determine the zero field temperature, while the cernox was used to check the temperature did not increase during the field sweep.

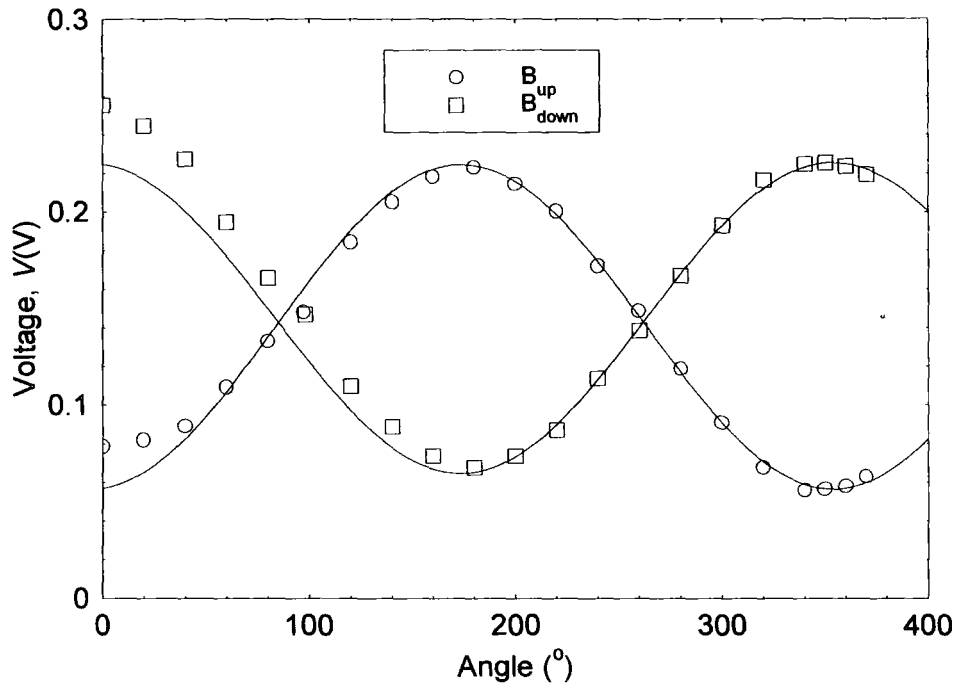

Figure 5.13. Voltage induced by the rate of change of magnetic flux through the loop, as a function of angle, and magnetic field direction. The solid lines are sine curves through the data. The angle was determined from the rotator dial at the top of the Heliox probe. The sweep rate of the magnetic field was 1.5 $Tmin^{-1}$.

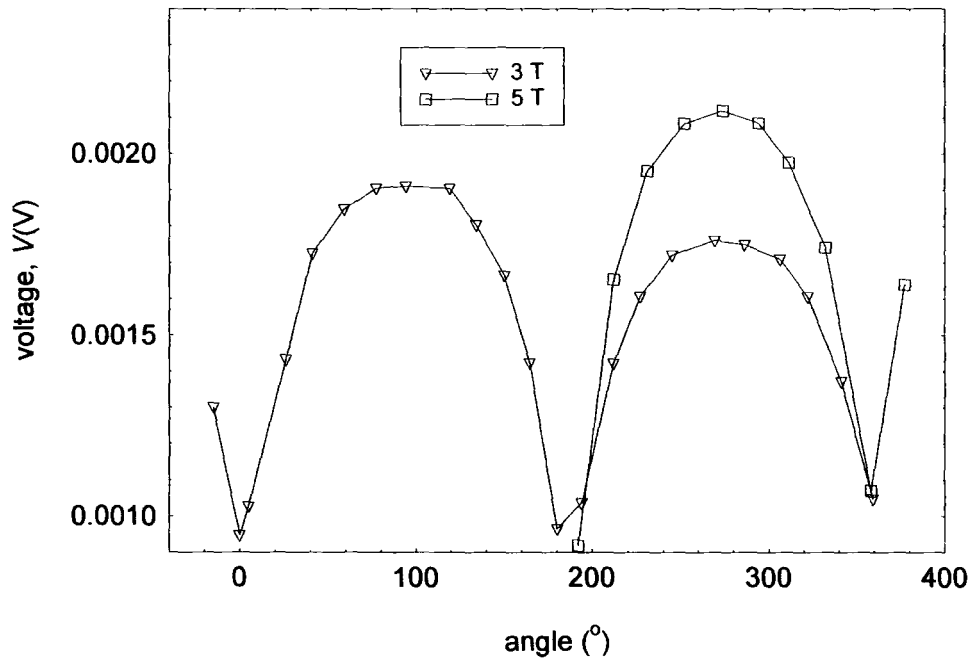

Figure 5.14. The measured Hall voltage as a function of angle, at 3 T & 5 T, at 4.2 K. The angle was determined from the sine curves in figure 5.13.

5.4.3 Hall Chip

The Hall chip was used to measure the angle between the chip and magnetic field. It was fabricated by Prof. Robin Nicholas at Oxford University. It was calibrated as a function of angle, at 4.2 K, 3 T using the rotation set-up, on the torque magnetometer. A single loop of copper wire of area 14 x 22 mm^2 was glued around the edge of the tufnol chip holder. The Hall chip was glued on to one of the copper holders. The brass can with holes in was screwed on to the IVC plate. The Heliox was cooled down in liquid helium, thus the Hall chip and wire loop were immersed. The magnet was swept at a faster sweep rate, as any eddy heating, which occurred, was removed by the liquid helium. The sweep rate was 1.5 $Tmin^{-1}$. The magnetic field was swept up to 5 T and back down to zero. The voltage induced in the loop (i.e. $V = -\frac{\partial \phi}{\partial t}$) was measured on a Keithley 2001 voltmeter. The induced voltage was amplified by a DC nanovolt amplifier, with amplification x 50000. The voltage across the Hall chip was measured as a function of magnetic field. The tufnol chip holder was initially positioned at 0 degrees. The measurement was repeated every 20°, over 360 degrees. The angle of the tufnol chip holder was roughly determined from the rotator dial.

Fig. 5.13 shows the sine dependence of the flux through the loop. The solid lines are $\sin\theta$ curves plotted through the data. At each of the measured angles, the angle of the tufnol chip holder was taken from the sine curve. The Hall voltage was then plotted as a function of this angle. Fig. 5.14 is the calibration curve of the Hall chip, at 3 T, 4.2 K. The Hall chip does not have sine dependence with angle. The Hall chip was more sensitive to angles at low resistances. It was mounted on the copper holder, so at 0° & 180°, the lowest resistances were measured. This meant the Hall chip was most sensitive to the change in angle around 0° & 180°, thus this improved the accuracy of determining the reversible angle. The Hall voltage was also used to determine whether the platform had moved. The voltage was measured as a function of magnetic field. If the platform moved the Hall voltage would change, due to the change in angle. The disadvantage was at fields below 2 T, the voltage was the same at all angles.

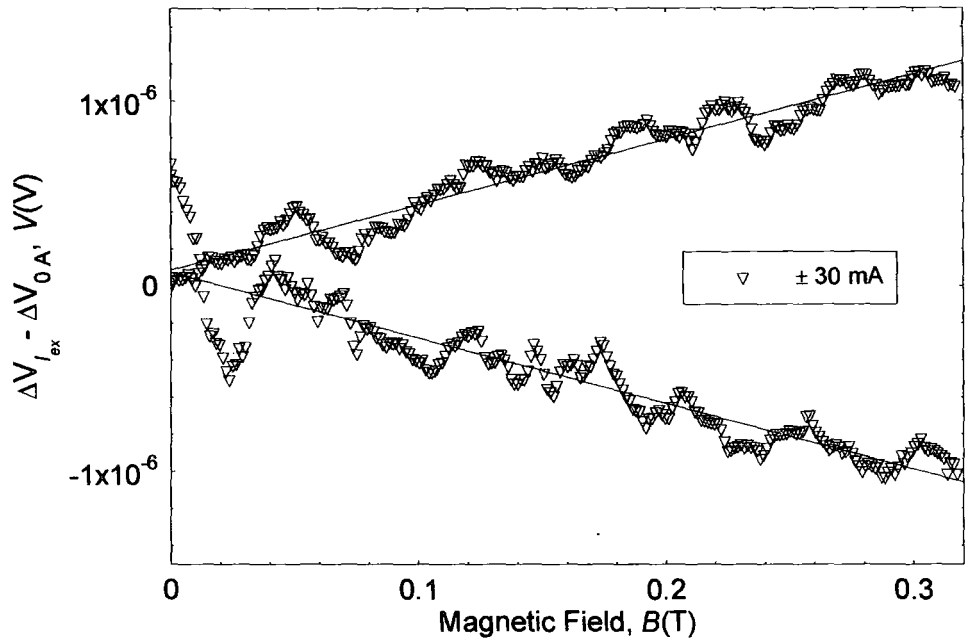

Figure 5.15. The calibration graph of a QD torque chip, in liquid nitrogen. The change in voltage $\Delta V_{I_{ex}}$ for $I_{ex} = \pm$ 30 mA as a function of applied magnetic field, at 90° and 77 K. The background change in voltage (ΔV_{0A}) has been subtracted away. The solid lines are the best-fit lines through the data. The gradient of each line is used to determine α_V. The calibration constant α_V, for the chip is 45 V(Nm)$^{-1}$.

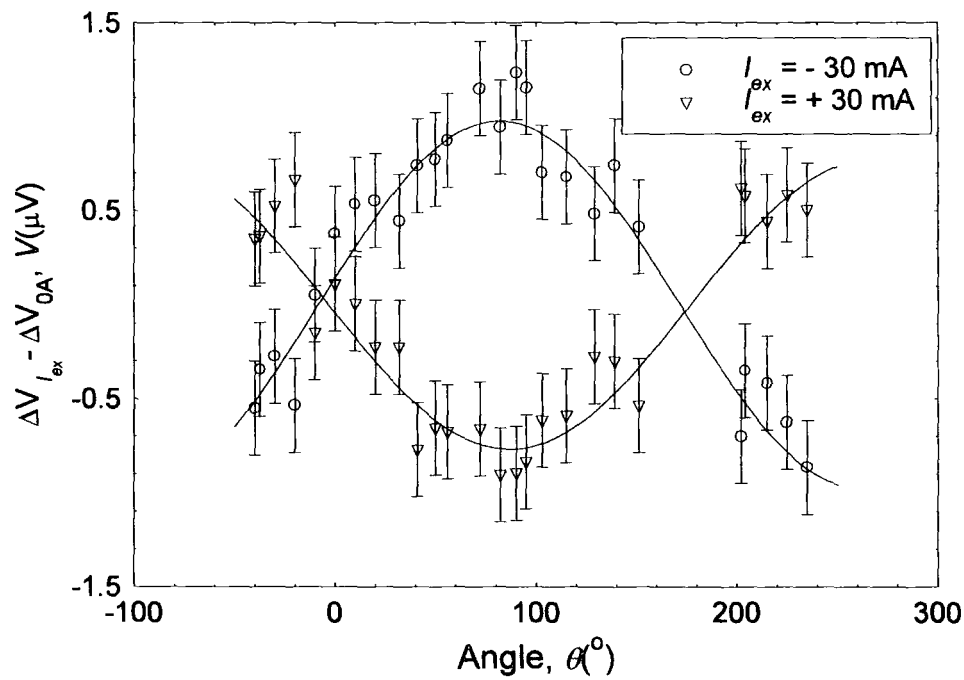

Figure 5.16. The difference in $\Delta V_{I_{ex}}$, as a function of angle and applied excitation current, at 77 K and 300 mT. The solid lines show the sinθ dependence of the applied torque.

5.4.4 Quantum Design silicon torque chips

The piezoresistive torque chips used in this experiment were brought from Quantum Design (cf. section 3.5.2). To calibrate the QD chips, two separate experiments were carried out. The first calibration was a preliminary measurement to ensure that the chip was not broken or faulty. The second calibration was the full calibration of the QD chip.

From torque theory (cf. section 3.7), when a current flows around a loop, a magnetic moment is produced perpendicular to the area (**A**) of the loop. For both experiments the chip was calibrated by putting an excitation current (I_{ex}) through the loop around the edge of its platform. The chip's platform was parallel to the applied magnetic field. From section 3.7, the torque on the current loop was:

$$\tau = \mathbf{m}_I \times \mathbf{B} = I_{ex}\mathbf{A} \times \mathbf{B} = I_{ex}AB\sin\theta\hat{\mathbf{s}} \qquad (5.3)$$

where $\mathbf{m_I}$ is the magnetic moment due to the excitation current and $\hat{\mathbf{s}}$ is a unit vector perpendicular to the platform. This meant the maximum torque was measured. The magnetic field was swept up to a set field and then back down to zero. The change in voltage across the Wheatstone bridge was measured as a function of the applied field (ΔV). The Wheatstone bridge was unbalanced at the start, so there was an initial voltage across it. For each applied excitation current the change in voltage is denoted by $\Delta V_{I_{ex}}$.

The first calibration used the copper solenoid magnet in liquid nitrogen. The torque chip was fastened into the tufnol chip holder. The brass can with holes in was screwed on to the IVC plate. The probe was then slowly lowered in to the liquid nitrogen.

The chip was positioned in the centre of the magnet. The magnetic field was swept up to 0.32T.

For no current through the loop (I_{ex} = 0 mA), the change in voltage measured was taken to be the background voltage of the Wheatstone bridge. The experiment was repeated for I_{ex} = ± 30 mA. The measured background ΔV_{0A} was subtracted away from the excitation current $\Delta V_{I_{ex}}$. This gave the calibration of the chip as a function of magnetic field. The change in voltage $\Delta V_{I_{ex}}$ - ΔV_{0A}, is linearly proportional to the applied magnetic field (fig. 5.15). The equation relating the applied torque to the change in voltage, and thus the change in resistance is a function of the excitation current $\left(\Delta R_{I_{ex}}\right)$ is given by:

$$\tau = \frac{\Delta V_{I_{ex}}}{\alpha_V} = \frac{\Delta R_{I_{ex}}}{\alpha_R} \tag{5.4}$$

where α_V is the voltage calibration constant $(V(Nm)^{-1})$ and α_R is the resistance calibration constant $(\Omega(Nm)^{-1})$.

Comparing equations 5.3 and 5.4, the calibration constant α_R is proportional to the gradient of the lines in the figure 5.15. It is given by:

$$\alpha_R = \frac{\left(\frac{d(\Delta R_{I_{ex}} - \Delta R_{0A})}{dB}\right)}{m_I} \tag{5.5}$$

The calibration constant α_R is also a measure of the sensitivity of the measurement. This first calibration gave the order of magnitude of α_R, and checked the chip had a linear response to an applied torque.

From eqn. 5.3, the applied torque has sine dependence with angle. This was investigated by measuring the change in voltage across the Wheatstone bridge as a function of angle, for $I_{ex} = 0, \pm 30$ mA.

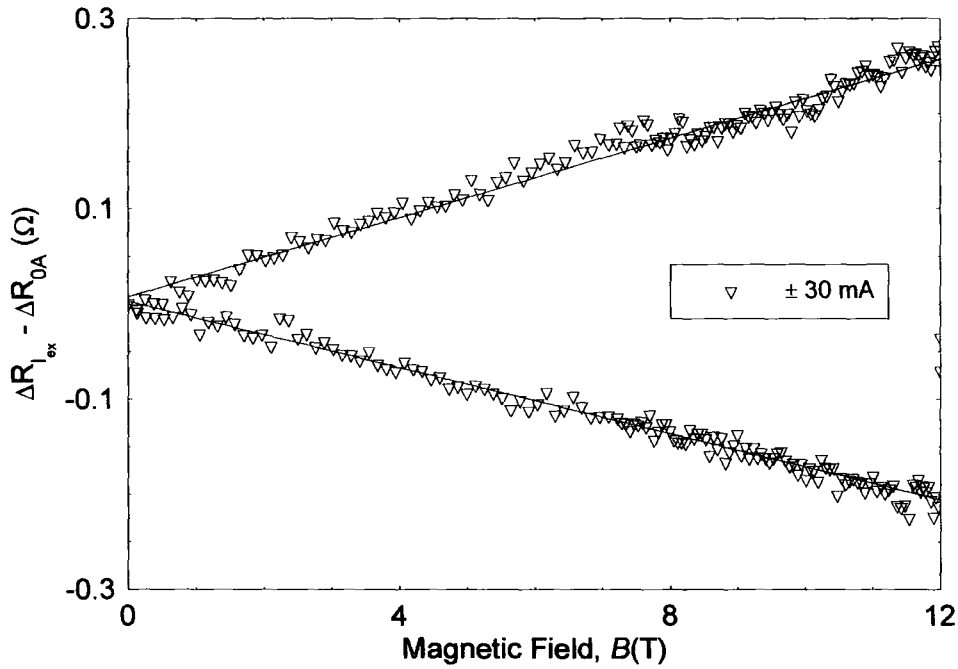

Figure 5.17. The calibration graph of a QD torque chip, in liquid helium. Change in resistance $\Delta R_{I_{ex}}$, for $I_{ex} = \pm 30$ mA as a function of applied magnetic field, at 4.2 K and 90 degrees. The background change in resistance has been subtracted away from the data. The solid lines are the best-fit straight lines through the data. The gradient of the lines is used to determine α_R. The calibration constant α_R for this chip is 2.22 x 10^4 $\Omega(Nm)^{-1}$

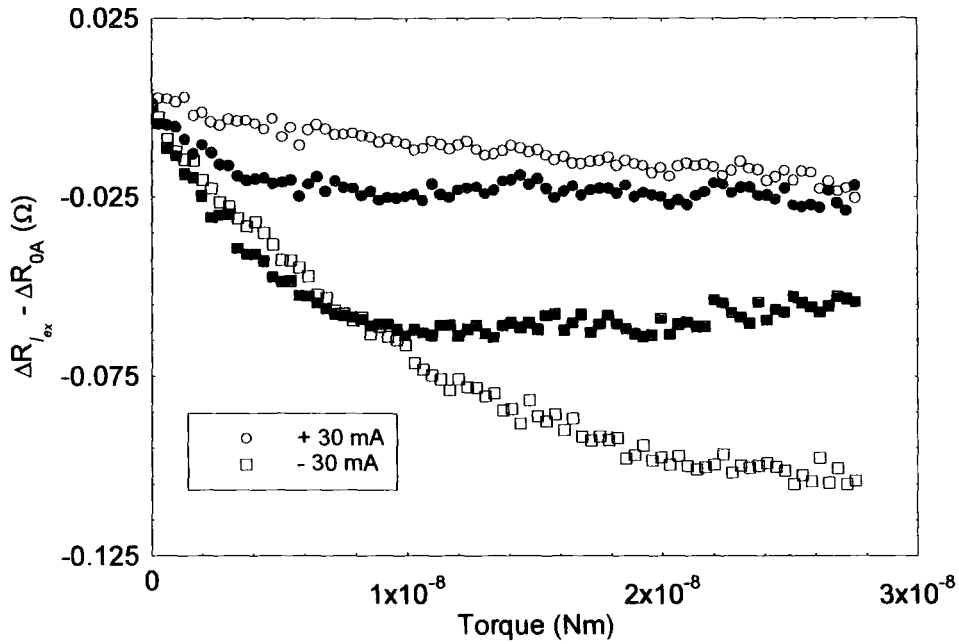

Figure 5.18a. Change in resistance $\Delta R_{I_{ex}}$, for $I_{ex} = \pm$ 30 mA as a function of torque at 77 K. The calibration was repeated twice, the open shapes denote the first set of measurements, the closed shapes denote the second set of measurements. The calibration constant was not repeatable between the measurements. The background resistance ΔR_{0A} was subtracted away from the data.

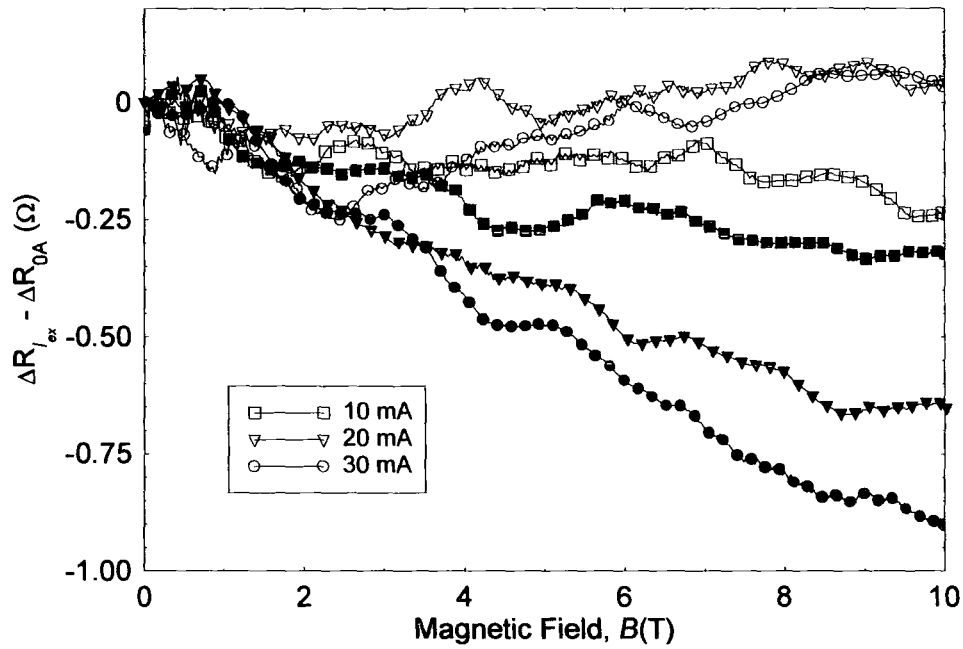

Figure 5.18b. Change in resistance $\Delta R_{I_{ex}}$ as a function of field and excitation current at 4.2 K. The open shapes represent the positive I_{ex}, the closed shapes represent the negative I_{ex}. The background resistance ΔR_{0A} was subtracted away from the data.

In fig. 5.16, the sine dependence of the torque is observed. Thus the chip was not faulty as it obeyed equation 5.3, when an excitation current flowed through the calibration loop.

For the second calibration, the chip was immersed in liquid helium, at the centre of the 15 T superconducting magnet. The procedure was the same as for the liquid nitrogen calibration. The calibration took place in liquid helium, rather than in vacuum as the resistance of the calibration loop was 10 Ω. At 4.2 K, for an excitation current of 30 mA, the power dissipated was 9 mW. This was enough to increase the temperature of the chip by 20 K. Thus the calibration was carried out in liquid, so any heat dissipated from the current through the loop was removed. This meant the temperature was constant through the whole calibration. The magnetic field swept was swept to 12 T. The excitation currents were 0, ± 30 mA.

As shown in figure 5.17, the chip had a linear response to the torque up to 12 T. The calibration constants α_R and α_V were determined from the gradient of the lines and eqn 5.5. In liquid nitrogen α_V = 45 V(Nm)$^{-1}$, while in liquid helium the calibration constant was α_V = 20 V(Nm)$^{-1}$, thus the calibration constants were about a factor 2 smaller at 4.2 K compared to 77 K.

5.4.5 Faulty QD torque chips

As the torque chips were bought from Quantum Design, there was no control over the manufacture process, the size or the linearity of the calibration constant. This meant there were often problems with the chips. These problems included an imbalance in the Wheatstone bridge resistors. This occurred when one of the resistors was either larger or smaller by at least 100 ohms compared with the other three. This introduced a large background resistance to the measurement. Thus the relationship between the applied torque and the difference in $\Delta R_{I_{ex}}$ was not linear. The imbalance in the resistance leads to unrepeatable calibration constants (fig. 5.18(a)). Another problem was the voltage calibration constant (α_V) having a value less than 20 V(Nm)$^{-1}$, which reduced the sensitivity of the measurement. The signal to noise ratio of the chip was about 1. If the chip was not manufactured correctly, there was excess silicon attached to the platform. This increased the noise on the voltage, and reduced the signal to noise ratio. Another problem was the chip having a different calibration constant

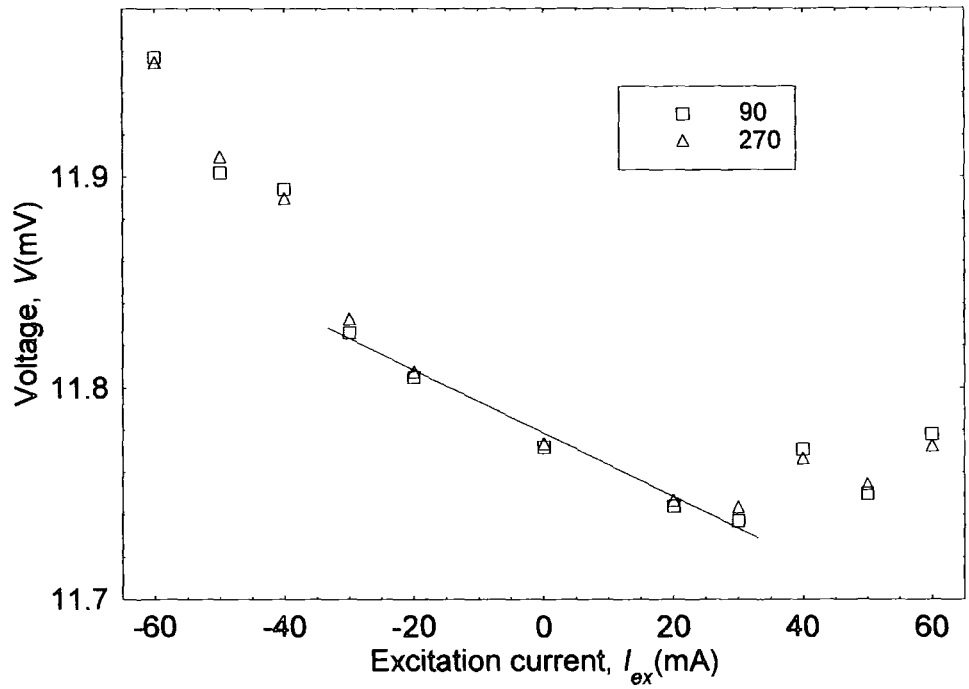

Figure 5.19. Voltage across the Wheatstone bridge, as a function of excitation current and angle to the magnetic field, at 5 T, 4.2 K and $z = 0$ cm. The solid line is a linear-fit through the data between – 30 mA and + 30 mA.

for each torque directions (fig. 5.18b). Any of the above problems meant the QD chip was unusable for the experiment.

Problems were experienced when removing the sample from the chip. The sample and chip were originally soaked in acetone. After the third soaking, the acetone damaged the silicon and constantan on the chip. The damage to the resistors affected the resistance of the Wheatstone bridge, which caused a non-linear response to the torque. The problem was solved by soaking the chips in isopropanol, which was a less strong solvent than acetone.

5.5 Experimental Set-up

5.5.1 Field-gradient torque magnetometer

The excitation current (I_{ex}) chosen to calibrate the QD torque chips was ± 30 mA. This was because the change in voltage across the Wheatstone bridge due to the applied torque was large enough to be measured on the lock-in amplifier, but not too large for the response of the chip to be non-linear. From fig. 5.19, for excitation currents between – 30 mA and + 30 mA, the change in voltage across the Wheatstone

bridge with respect to the 0 mA voltage was linear. For excitation currents greater than ± 30 mA, the change in voltage across the Wheatstone bridge with respect to the 0 mA voltage was non-linear.

For the measurements in liquid helium the sweep rate of the superconducting magnet was 1 $Tmin^{-1}$. For the measurements in vacuum the sweep rate of the 15 T magnet was 0.45 $Tmin^{-1}$. These were the highest sweep rates for each condition that could be used before the thermometers on the platform increased in temperature, due to Eddy heating occurring.

The magnetic field gradients and thus the height from the magnet centre were chosen from fig 5.11. They were chosen so the increment between the field gradients were the same. The temperatures were chosen so they were evenly spaced between the base temperature (300 mK) and the critical temperature of the superconductor. The number of temperatures and field gradients were chosen so a complete data set could be taken in the time available. The length of time for the whole experiment was dependent on the amount of liquid helium available for the superconducting magnet.

The superconducting samples on the torque magnetometer were cylindrical in shape. The samples were glued onto the chip's platform with the long axis of the cylinder parallel to the edge of the platform. This meant through 360 degrees the magnetic field was always along the radial direction of the sample. The volume of the samples was measured using digital micrometer callipers.

The voltage applied by the lock-in across the Wheatstone bridge was 0.01 V. This was the highest voltage, which could be applied without heating occurring. The current through the Wheatstone bridge was measured. This was to ensure the current did not change during the measurement. It also meant the change in resistance across the Wheatstone bridge was determined, which is proportional to the applied torque.

The procedure of the experiment for the torque magnetometer involved finding the angle where the voltage loops measured at field centre were reversible. To do this the sample was rotated about the 0 or 180 degrees position. At every 2 degrees, the magnetic field was swept up to 5 T and then back to zero. The change in voltage across the Wheatstone bridge on the torque chip was measured. The change in voltage (ΔV) was then plotted against the applied magnetic field, the loops obtained were the voltage vs. field sweep loops. The angle where the voltage loops at field centre were reversible was the reversible angle.

At the reversible angle, the voltage vs. field sweep loops were measured at each field gradient. This involved sweeping the magnetic field up to a set field, and then back down to zero. The first loop was measured at $z = 0$ cm, the Heliox was then lifted out of the magnet to the furthest height, and the voltage vs. field sweep loops measured at every field gradient, back down to $z = 0$ cm. The loop at $z = 0$ cm was re-measured to check that the platform had not moved during the measurements. This procedure was repeated for every temperature. The heights were the same for each temperature, as height markers were used, which fitted between the neck fitting and the Heliox head (fig. 5.1). The voltage vs. field sweep loops measured as a function of field gradient and magnetic field, were plotted as a function of the local magnetic field. This is the field experienced by the sample, at the height z from the magnet centre. The local fields are determined from fig. 5.8.

The superconductor measured was a NbTi wire sample, which consisted of three 1 mm lengths of wire, which were glued together with GE-varnish, in a pyramid shape. The NbTi wire consisted of 61 filaments in a copper matrix. Each filament radius was 14 μm. The ends of the wires were sandpapered, to ensure they were flat. NbTi wire was measured as it has known superconducting parameters.

5.5.2 Vibrating sample magnetometer (VSM)

For a good comparison between the field-gradient torque magnetometer and the VSM, the same NbTi sample was measured on both.

The critical current densities of the NbTi wire sample was measured on the VSM in Birmingham. The magnetic moment was measured as a function of the magnetic fields up to 12 T and temperatures at 4.2 K, 6 K, 8 K and 10 K.

The NbTi wire sample measured on the VSM was still attached to the platform of the torque chip. This meant it was easier to align on the vibrating rod. The sample was measured with the field perpendicular and parallel to its long axis. The sample was held onto the sample rod using double-sided sticky tape, with PTFE tape wrapped around on top to secure the sample.

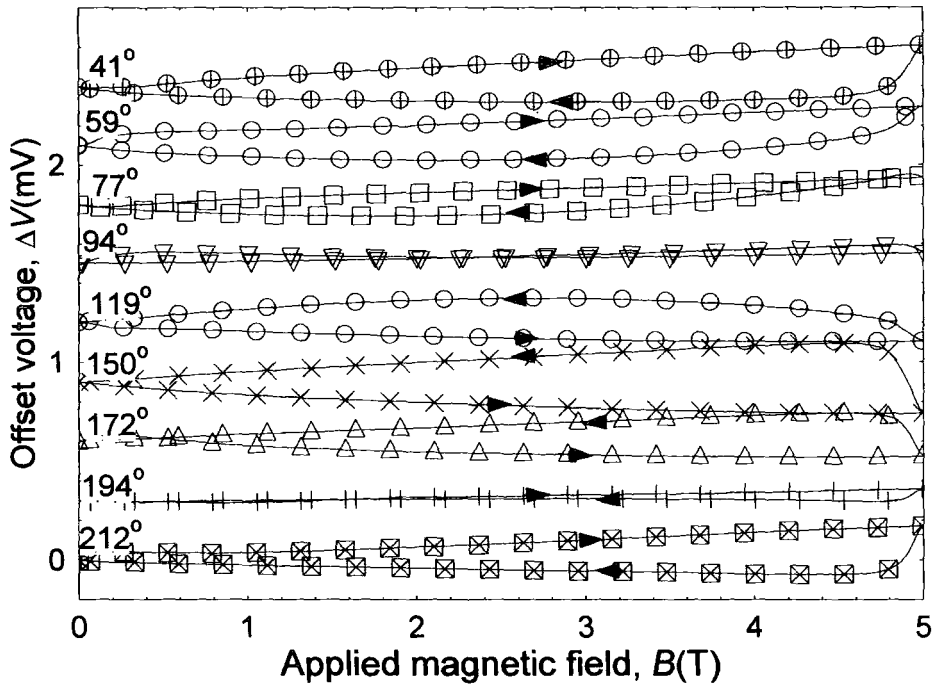

Figure 5.20. Voltage vs. field sweep loops for NbTi wire as a function of magnetic field, and angle, at 4.2 K & z = 0 cm, taken on chip 3 (α_V = 200 V(Nm)$^{-1}$). The loops were offset along the y-axis, so the change in the magnitude of the voltage hysteresis was observed. The arrows indicate the increasing or decreasing magnetic field.

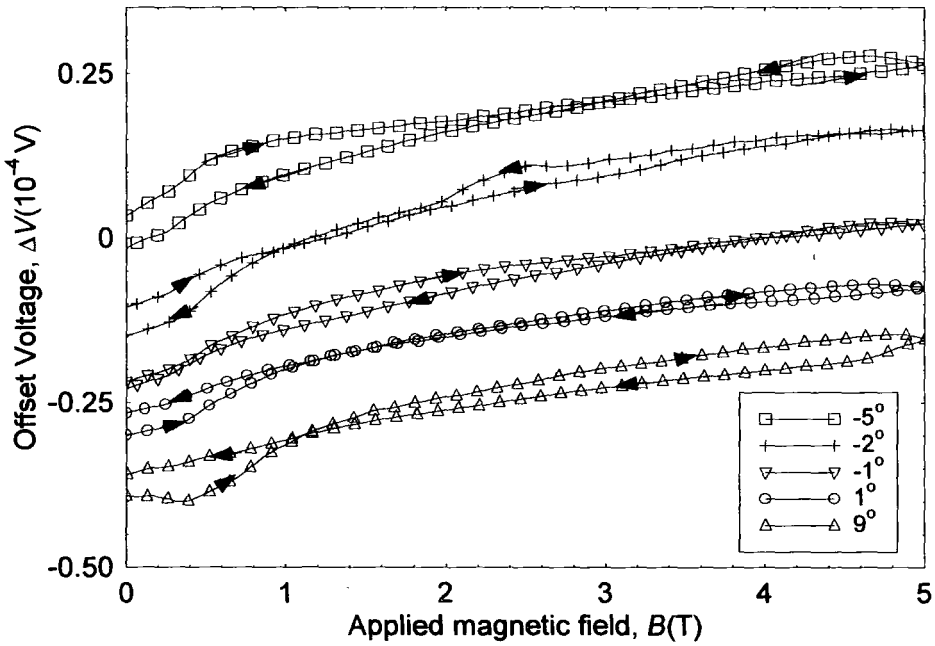

Figure 5.21. Voltage vs. field sweep loops (ΔV) for NbTi wire as a function of magnetic field and angle, at 4.2 K & z = 0 cm, taken on chip 4 (α_V = 20 V(Nm)$^{-1}$). The loops were offset along the y-axis, so the change in the voltage hysteresis was observed. The arrows indicate the increasing or decreasing magnetic field.

5.6 Experimental results - NbTi wire

5.6.1 Change in the voltage vs. field sweep loops as a function of angle

The first set of measurements on NbTi wire were taken in liquid helium. The voltage calibration constant of chip 3 was α_V = 200 V(Nm)$^{-1}$, thus the resistance calibration constant was α_R = 2.28 x 10^5 Ω(Nm)$^{-1}$. The sample was rotated through 360 degrees, at the field centre, to investigate the change in magnitude of the hysteresis in the voltage loops with angle. At every 20 degrees, a voltage vs. field sweep loop was measured (fig. 5.20). The magnetic field was swept up to 5 T and back down to 0 T at a sweep rate of 1 Tmin^{-1}. Fig. 5.20 shows the change in magnitude of the hysteresis in the voltage vs. field sweep loop over 180°. At 90° and 180° the voltage loops were almost reversible. The voltage vs. field sweep loops for angles below the reversible angle were in the opposite direction to the loops at angles above the reversible angle. An equivalent data set was measured about 0°.

The second set of NbTi wire measurements were carried out in liquid helium using chip 4, with voltage calibration constant of α_V = 20 V(Nm)$^{-1}$, thus the resistance calibration constant was α_R = 2.22 x 10^4 Ω(Nm)$^{-1}$ (fig. 5.17).

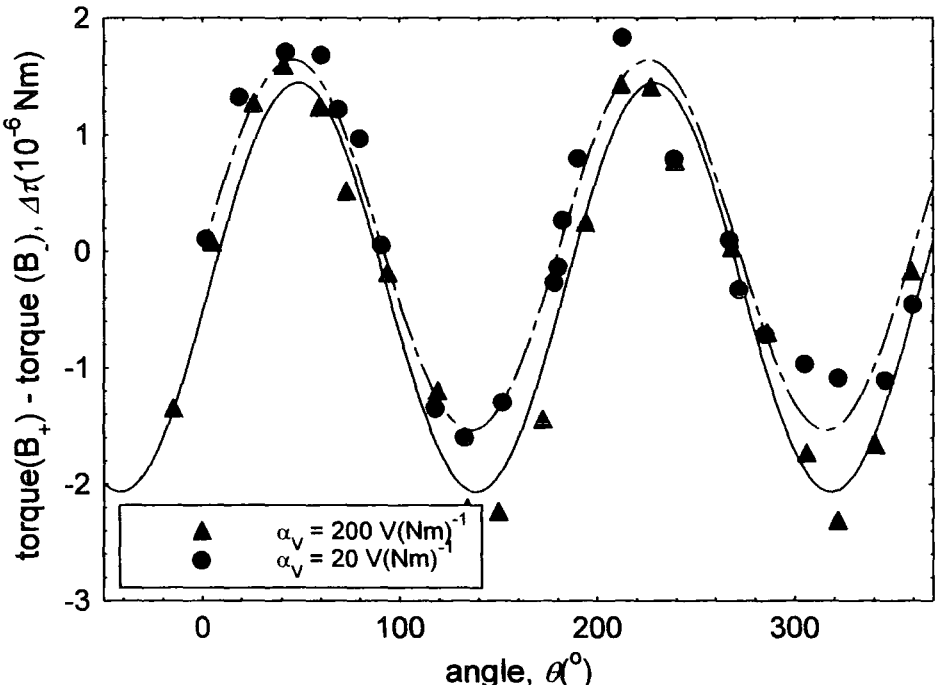

Figure 5.22. Difference in torque across the field sweep loops as a function of angle, and QD chip, at 4.2 K, 4 T and z = 0 cm. The solid line is through the α_V = 200 V(Nm)$^{-1}$ data, and the dashed line is through the α_V = 20 V(Nm)$^{-1}$data. The sample on chip 3 was 30° from the platform edge, and the sample on chip 4 was parallel to the platform edge.

The change in magnitude of the hysteresis in the voltage vs. field sweep loops was measured as a function of angle over 360°. The data were taken every 20°, for fields up to 5 T. Around the reversible angles the loops were measured every 2° to determine the reversible angle (fig. 5.21).

The difference in voltage across the voltage vs. field sweep loop $\left(\Delta V_{+-} = \Delta V_{+} - \Delta V_{-}\right)$ was determined for the data taken on chip 3 and 4 (fig. 5.20 & 5.21). This difference in voltage $\left(\Delta V_{+-}\right)$ is converted into the difference in torque $\Delta\tau = \tau_{+} - \tau_{-}$ across the loops from the eqn:

$$\Delta\tau = \frac{\Delta V_{+-}}{\alpha_{V}} = \frac{\Delta R_{+-}}{\alpha_{R}} \tag{5.6}$$

where α_V and α_R are the chip's calibration constants. From fig. 5.22, the difference in torque across the field sweep loops as a function of angle has sin2θ dependence. The $\Delta\tau$ reversible angles occur at 0, 90, 180 and 270 degrees. The difference in torque across the field sweep loops at z = 0 cm was independent of the QD chip.

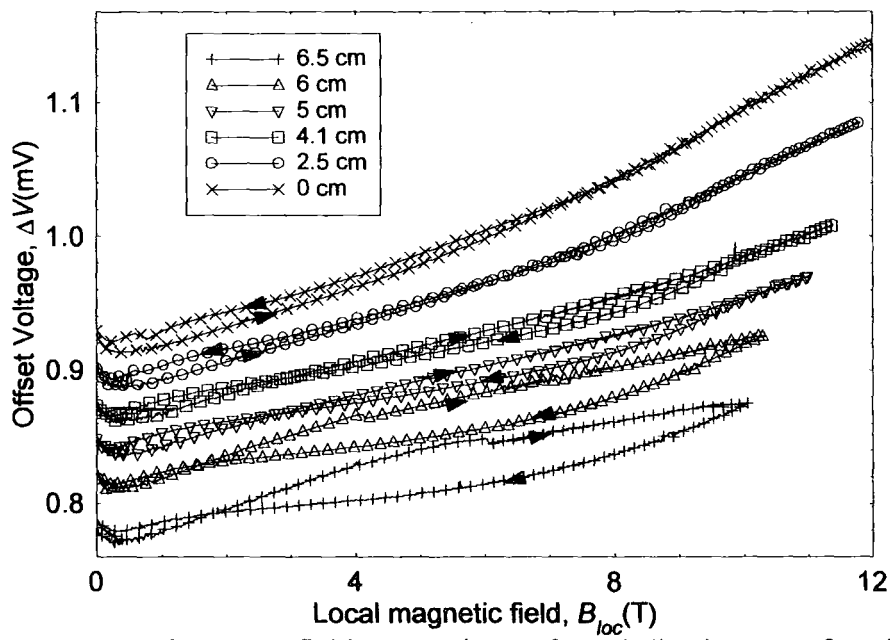

Figure 5.23. Voltage vs. field sweep loops for NbTi wire as a function of local magnetic field and height from the magnet centre at 4.2 K, 0°, taken on chip 3 (α_V = 200 V(Nm)$^{-1}$). The loops were offset along the y-axis, so the change in the magnitude of the voltage hysteresis was observed. The arrows on the data indicate the increasing or decreasing magnetic field, during the measurement.

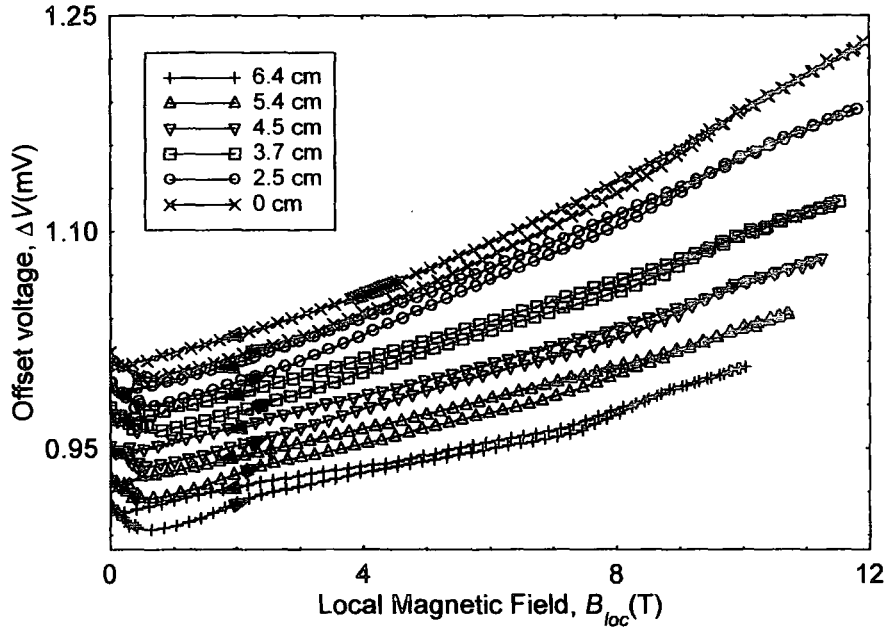

Figure 5.24. Voltage vs. field sweep loops for NbTi wire as a function of local magnetic field and height from the magnet centre at 4.2 K, 180°, taken on chip 3 (α_V = 200 V(Nm)$^{-1}$). The loops were offset along the y-axis, so the change in the magnitude of the voltage hysteresis was observed. The arrows indicate the increasing or decreasing magnetic field.

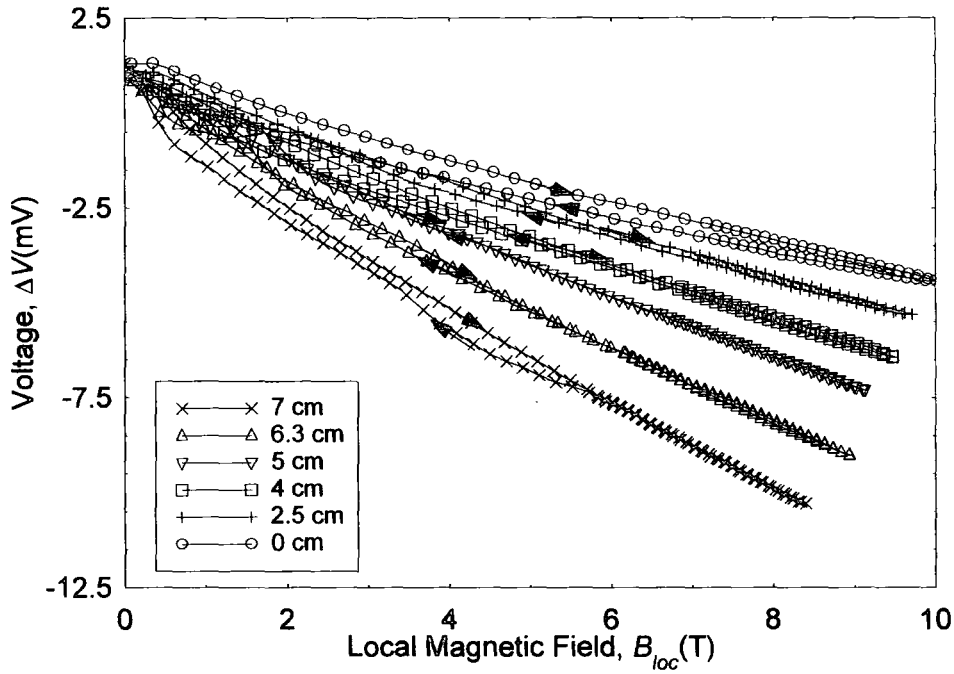

Figure 5.25. Voltage vs. field sweep loops (ΔV) for NbTi wire as a function of local magnetic field and height from the magnet centre at 4.2 K and 270 degrees, taken on chip 3 (α_V = 200 V(Nm)$^{-1}$). The arrows on the data indicate the increasing or decreasing magnetic field, during the measurement.

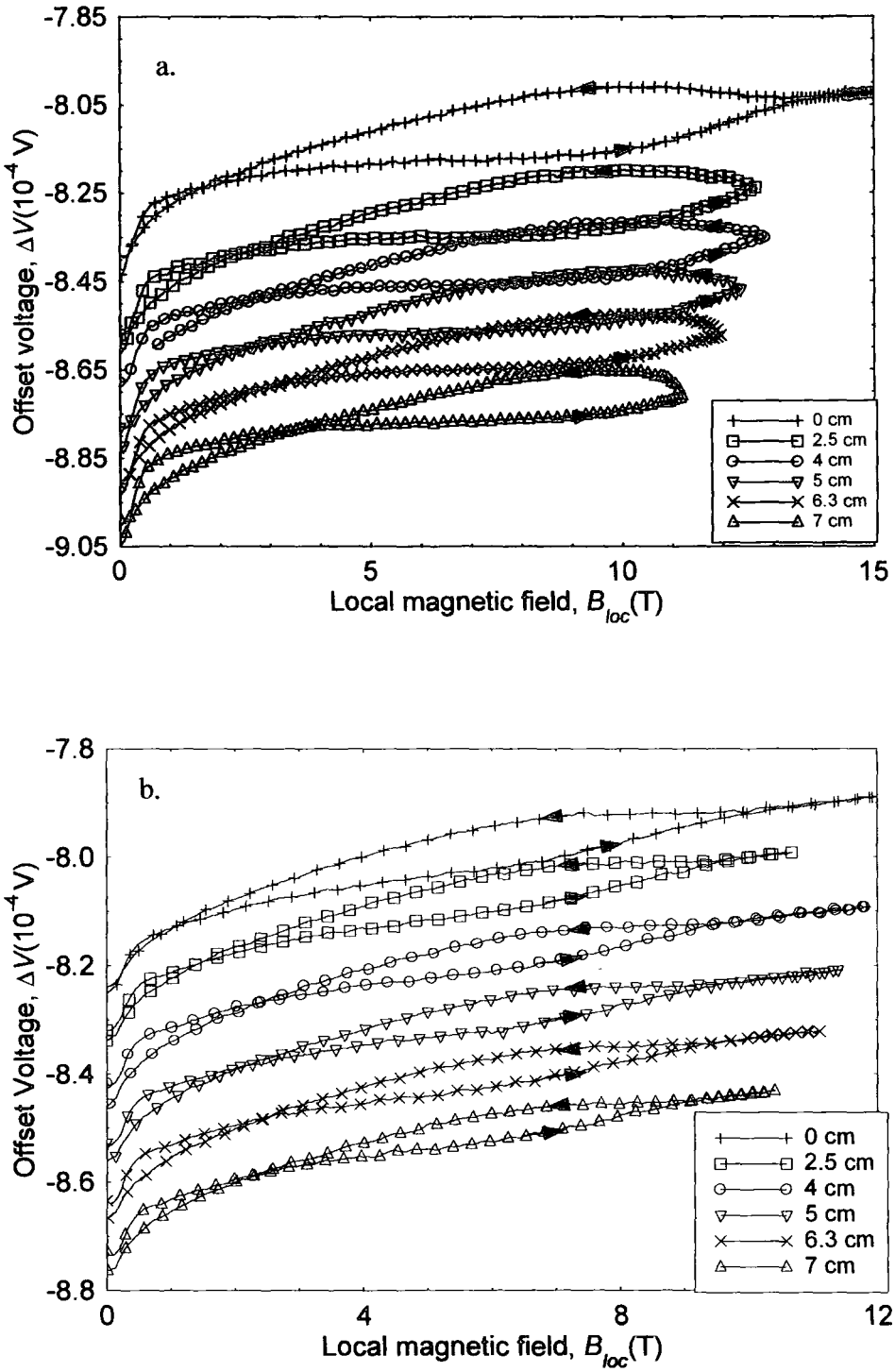

Figure 5.26. Voltage vs. field sweep loops (ΔV) for NbTi wire as a function of local magnetic and height from the magnet centre, fixed at 180 degrees and (a) 300 mK and (b) 4.2 K, taken on chip 4 (α_V = 20 V(Nm)$^{-1}$). The loops were offset along the y-axis, so the change in magnitude of the hysteresis was observed. The arrows on the data indicate the increasing or decreasing magnetic field, during the measurement.

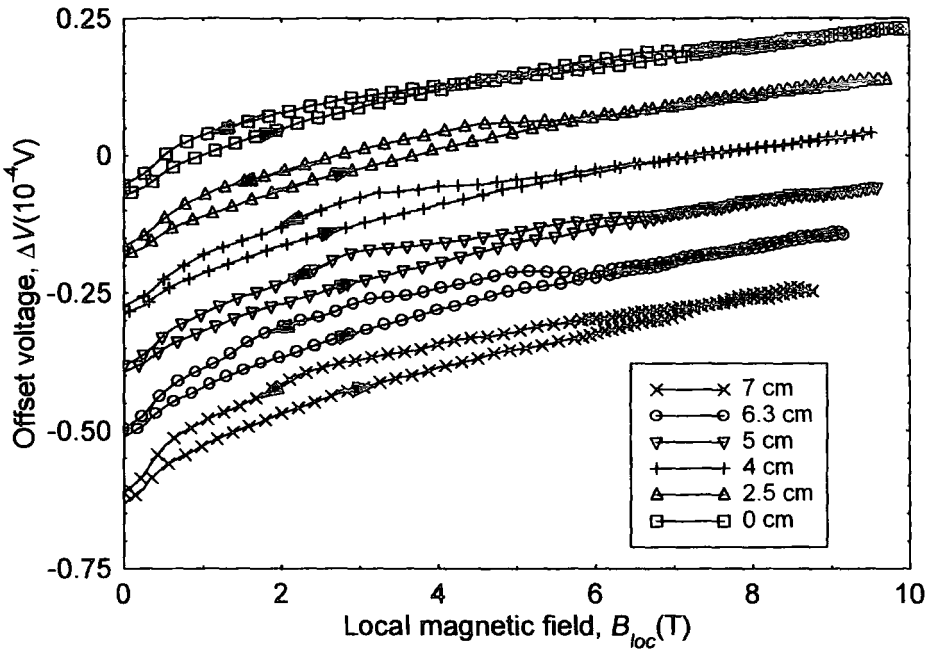

Figure 5.27. Voltage vs. field sweep loops (ΔV) for NbTi wire as a function of local magnetic field and height from the magnet centre at 4.2 K and 0°, taken on chip 4 (α_V = 20 V(Nm)$^{-1}$). The loops were offset along the y-axis, so the change in magnitude of the hysteresis was observed. The arrows on the data indicate the increasing or decreasing magnetic field, during the measurement.

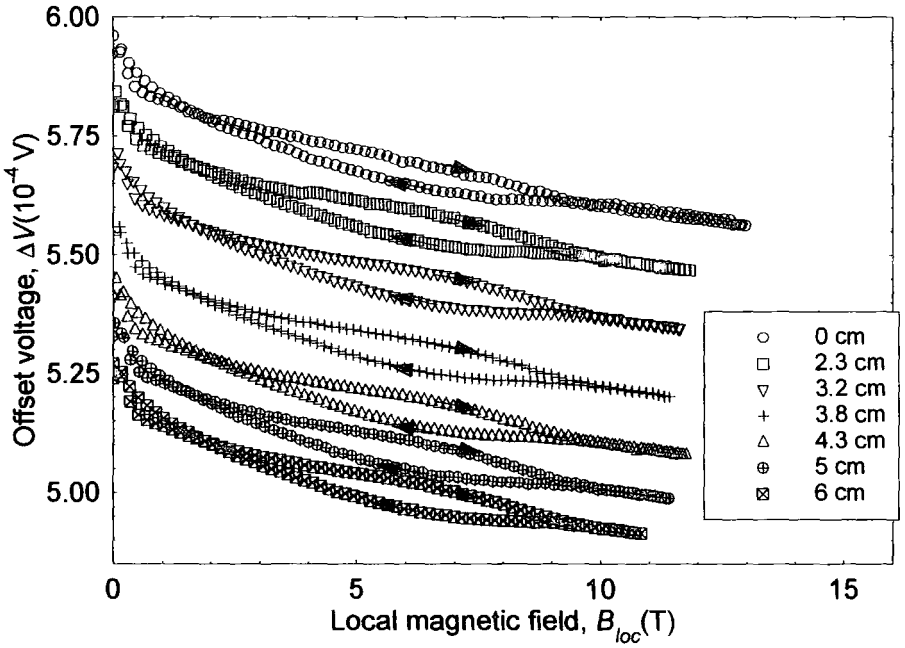

Figure 5.28. Voltage vs. field sweep loops (ΔV) for NbTi wire as a function of local magnetic and height from the magnet centre at 4.2 K, fixed at 180°, taken on chip 4 (α_V = 20 V(Nm)$^{-1}$). At each field gradient, all the voltage loops were measured for each temperature, before the sample was moved to the next height. The loops were offset along the y-axis, so the change in magnitude of the hysteresis was observed.

5.6.2 Change in the voltage vs. field sweep loops as a function of field gradient

For the NbTi wire sample on chip 3, the voltage vs. field sweep loops were measured at the angles where the loops were reversible at the field centre (0, 90, 180 & 270 degrees (fig. 5.22)). At each of the six field gradients, the magnetic field was swept up to 12 T and back down to 0 T (fig. 5.23). The NbTi wire sample was positioned at about 30 degrees to the platform edge. For figs. 5.23 & 5.24, the voltage vs. field sweep loops were offset from each other along the y-axis. This meant the change in magnitude of the voltage hysteresis with field gradient could be observed. For the loops taken at 0 degrees, the magnitude of the voltage hysteresis increased as the field gradient was increased (figs. 5.23), while at 180 degrees the magnitude of the hysteresis in the voltage vs. field sweep loops decreased as the field gradient increased (fig. 5.24). From fig. 5.25, the 270 degrees voltage vs. field sweep loops had almost no change in the voltage hysteresis as the field gradient was increased. A similar data set was measured at 90 degrees.

The NbTi wire on chip 4 was measured in vacuum at 180 degrees using the stationary holder (figs 5.26) and in liquid helium at 0^{o} (fig. 5.27). The voltage vs. field sweep loops were measured at eight gradients, which were at the following heights from the magnet centre 0, 2.5, 4, 4.5, 5, 5.5, 6.2 and 7 cm. In vacuum the temperatures measured at were 300 mK, 2 K, 4.2 K, 6 K, 8 K and 10 K. The voltage vs. field sweep loops for 300 mK and 4.2 K are presented in fig 5.26a & b. For the other temperatures, similar voltage vs. field sweep loops were measured, as a function of local magnetic field and field gradient. At 180^{o}, the magnitude of the voltage hysteresis in the loops decreased as the height from the magnetic field centre increased (fig. 5.26a), while at 0^{o}, the magnitude of the hysteresis in the voltage vs. field sweep loops increased, as the height from the magnet centre increased (fig 5.27). In vacuum, the voltage loops measured using the stationary holder were non-reversible at the field centre (fig. 5.26). At 4.2 K and 4 T, the difference in the voltage across the loop $\left(\Delta V_{+-}\right)$ at the field centre was converted into $\Delta\tau$ (eqn. 5.6). From the $\Delta\tau$ vs. angle graph (fig. 5.22), the sample was at an angle about 2^{o} away from the reversible angle. The stationary arrangement held the tufnol chip holder and QD chip at 180^{o}, which suggests the chip platform was not parallel with the outside edge of the chip. Hence the sample was not at 180 degrees to the field, thus the voltage vs. field sweep loop was non-reversible at $z = 0$ cm.

The NbTi wire on chip 4 was then measured in vacuum on the stationary holder again. For this measurement instead of measuring all the field gradients at constant temperature, the voltage loops were measured at every temperature at one field gradient, before the probe was moved to the next height. This procedure was repeated at every field gradient. For each loop, the sample was left for twenty minutes for the temperature to stabilise. The temperatures measured at were 300 mK, 2 K, 4.2 K (fig. 5.28), 6 K, 8 K and 10 K, at each of the following heights (z) from the magnet centre 0, 2.5, 3.2, 4, 4.5, 5, 5.5, & 6.2 cm. In fig. 5.28, the change in magnitude of the hysteresis between consecutive voltage vs. field sweep loops was difficult to observe, at 4.2 K. Only the 4.2 K data are presented, the other temperatures have similar voltage vs. field sweep loops as a function of local magnetic field and field gradient. The NbTi sample on chip 4 was parallel to the edge of the chips' platform.

5.6.3 VSM

The magnetic moment of the NbTi wire with the magnetic field perpendicular to the long axis has different field dependence to the magnetic moment when the field was applied perpendicular to the long axis (fig. 5.29). The data at 4.2 K shows oscillations due to the liquid-gas transition of helium in the VSM.

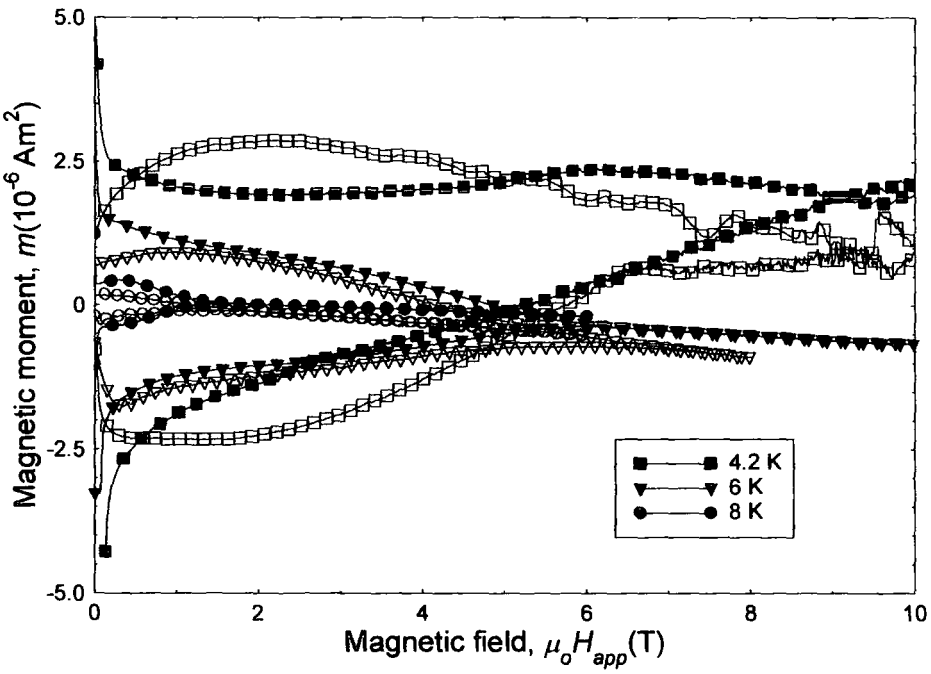

Figure 5.29. Magnetic moment of NbTi wire as a function of magnetic field and temperature measured on the VSM. The open shapes denote the field parallel to the long axis, and the closed shapes denote the field perpendicular to the long axis.

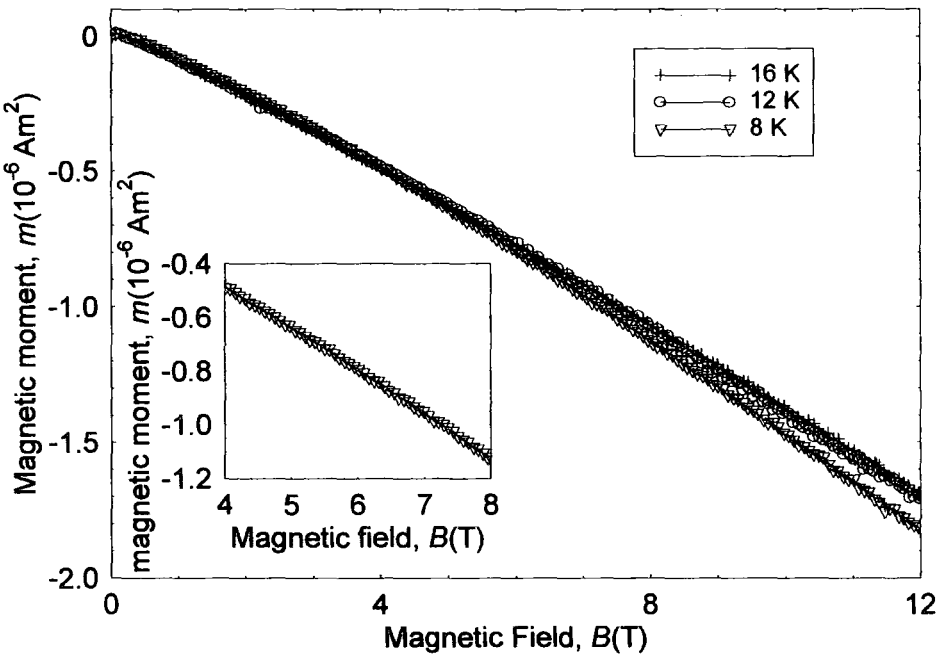

Figure 5.30. Background magnetic moment of the VSM as a function of magnetic field and temperature. The measured background included the sample holder, PFTE tape and double-sided sticky tape. **Inset**: Magnification of the 8 K data.

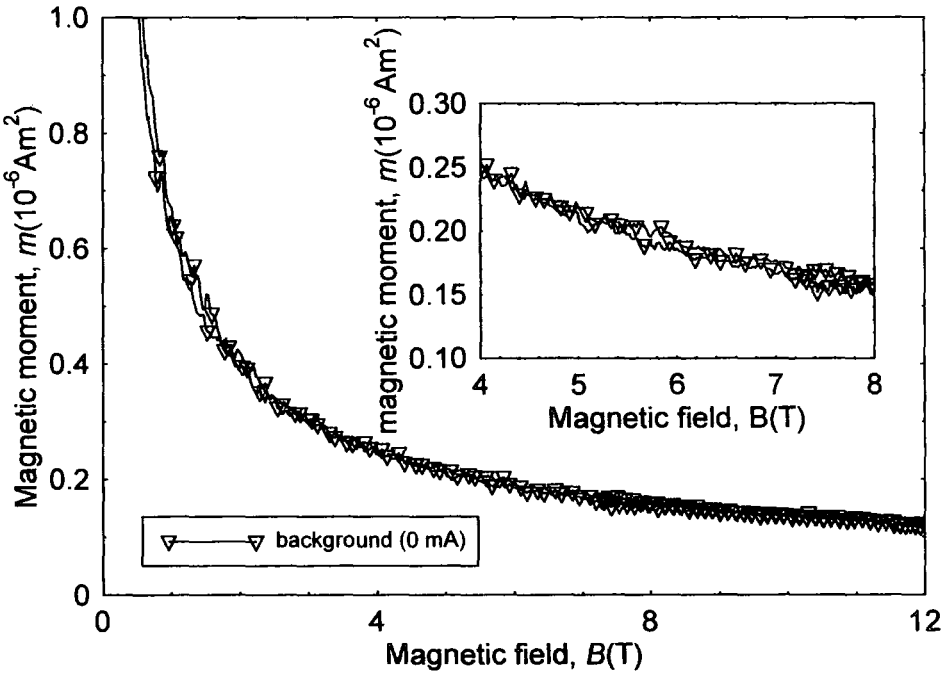

Figure 5.31. Background magnetic moment of chip 4 with no sample attached, as a function of magnetic field, at 4.2 K and field centre. The calibration constant was 20 $V(Nm)^{-1}$. **Inset:** Magnification of the magnetic moment between 4 T and 8 T.

	Background Sensitivity at 5 T (Am^2)	Sample	Signal to Noise Ratio 4.2 K, 5T (*8 K*)	Field Range (T)	Temp. Range (K)
Vibrating sample magnetometer	2.64×10^{-8}	NbTi	217 (*136*)	0 - 12	4.2 - 300
Field-gradient torque magnetometer	2×10^{-8}	NbTi	12 (*1*)	0 - 15	0.25 - 20

Table 5.1. The sensitivity, signal to noise ratio (SNR), field and temperature range of the VSM and the field-gradient torque magnetometer. The background sensitivity is double the noise of the data taken with no sample attached to the magnetometer. The sensitivity for the torque magnetometer is for chip 4, at the field centre. The field and temperature ranges are for the Oxford Instruments VSM in Birmingham University. For the torque magnetometer, the NbTi wire was measured on chip 4 (α_V = 20 $V(Nm)^{-1}$). The SNR in italics is for the data taken at 8 K.

5.6.4 Signal to noise ratio

For the torque magnetometer the signal to noise ratio (SNR) and the sensitivity depended on the calibration constant (α_V) of the QD torque chip and the applied field. The background sensitivity of the torque magnetometer was determined from the measured voltage across the Wheatstone bridge for chip 4, for no sample attached to the platform, at 4.2 K. The moment was then determined from the torque equation (eqn 5.3). The sensitivity of the torque magnetometer decreases as the magnetic field decreases (fig. 5.31).

The VSM background moment has a linear dependence with field (fig. 5.30). The background measured for the VSM was the sample holder, PTFE tape and double-sided sticky tape. The sensitivity for each magnetometer was taken to be double the background noise at 5 T from figs. 5.30 and 5.31. The torque magnetometer moment sensitivity is the same order of magnitude as the VSM moment sensitivity (table 5.1). The SNR for each magnetometer were determined from the data measured for the sample. The SNR for the torque magnetometer is dependent on the noise of the

background, and the noise from the sample. For the NbTi wire at 4.2 K, chip 4's calibration constant was α_V = 20 V(Nm)$^{-1}$, and the SNR at 5 T was 12 (fig. 5.27), while for chip 3 α_V = 200 V(Nm)$^{-1}$, and the SNR at 5 T was 70 (fig. 5.23). Hence as α_V increases, the SNR increases, so the sensitivity of the measurement improves. As the sensitivity of the torque magnetometer depends on the applied field (fig. 5.31), the SNR will also depend on the applied field. At 0 T the signal to noise ratio is zero.

5.7 Critical current density Analysis

5.7.1 Determination of the critical current density

The critical current density of an anisotropic superconductor measured at the reversible angle (θ = 0), is given by eqn 3.24. In the equation, the local applied field gradient, $\mu_o\left(\frac{dH_{app-loc}}{dz}\right)$, at each height z was determined from fig. 5.11. The difference in resistance across the field sweep loops $\left(\Delta R_{+-}\right)$, as a function of magnetic field gradient is plotted for each magnetic field, as the gradient of each line is proportional to the difference in magnetic moment $\left(\left|\Delta m_{+-}\right|\right)$ for that field (eqn 3.24). The magnetic moment was determined using two LABview programs (appendix 3). For each height z, the local magnetic field, the field gradient and ΔR_{+-} were put into a data file. The LABview program (jccal.vi) read the data file, for each magnetic field. The program put the field gradient and ΔR_{+-} into a new data file, for that field. This procedure was repeated for each height z. At the end of the programme, each field had a file, which contained eight field gradients and the corresponding ΔR_{+-}. The gradcal.vi program then read each field data file and put a straight line fit through the points. The gradient of the line and the magnetic field were then written to another file. This process was repeated for every field data file, until the end file contained all the fields and corresponding gradients. The last data file was then plotted in Easyplot. The critical current density was determined by dividing the data by the variables in eqn 3.24, which were the same for all temperatures.

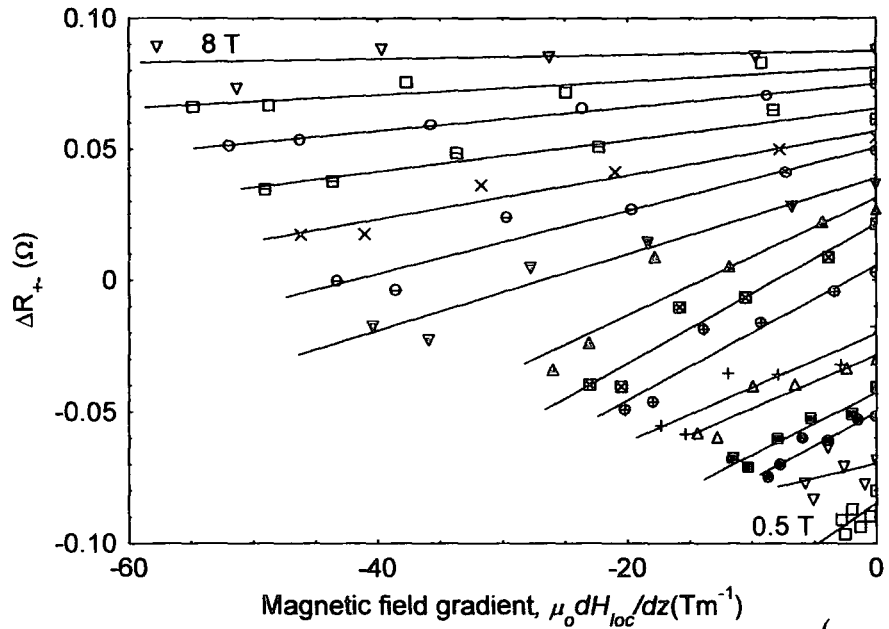

Figure 5.32. Difference in resistance across the field sweep loops (ΔR_{+-}) for NbTi wire as a function of field gradient and local magnetic field, at 4.2 K, 0°, taken on chip 3 (α_V = 200 V(Nm)$^{-1}$). The lines are offset by $\Delta R_{+-} = (0.02B)$, where B is the magnetic field for the line. The solid lines are the best-fit lines through the data.

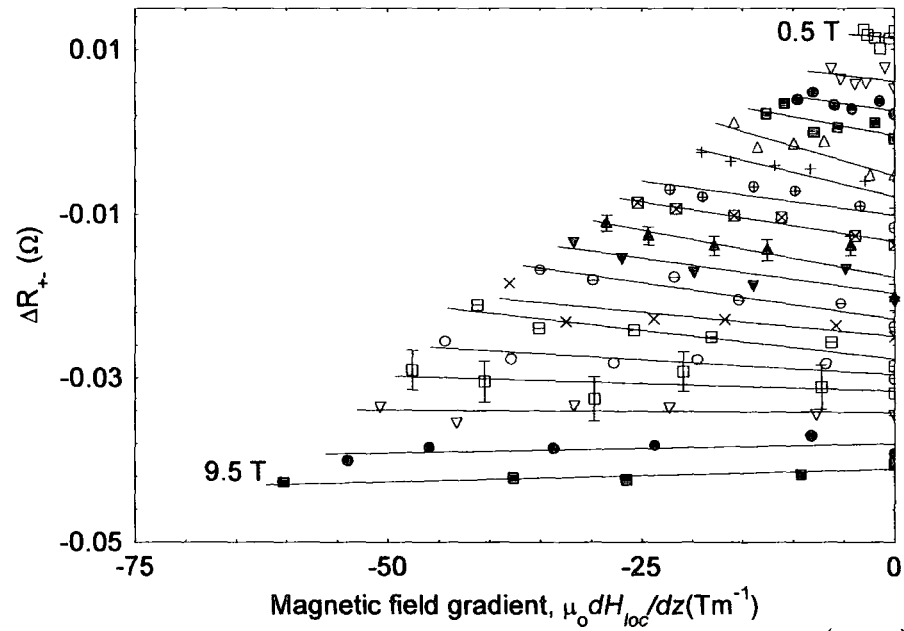

Figure 5.33. Difference in resistance across the field sweep loops (ΔR_{+-}) for NbTi wire as a function of field gradient and local magnetic field, at 4.2 K and 0°, taken on chip 4 (α_V = 20 V(Nm)$^{-1}$) in liquid helium. The lines are offset by $\Delta R_{+-} = (0.005B)$, where B is the magnetic field for the line. The solid lines are the best-fit lines through the data. The error bars were determined from the SNR (12).

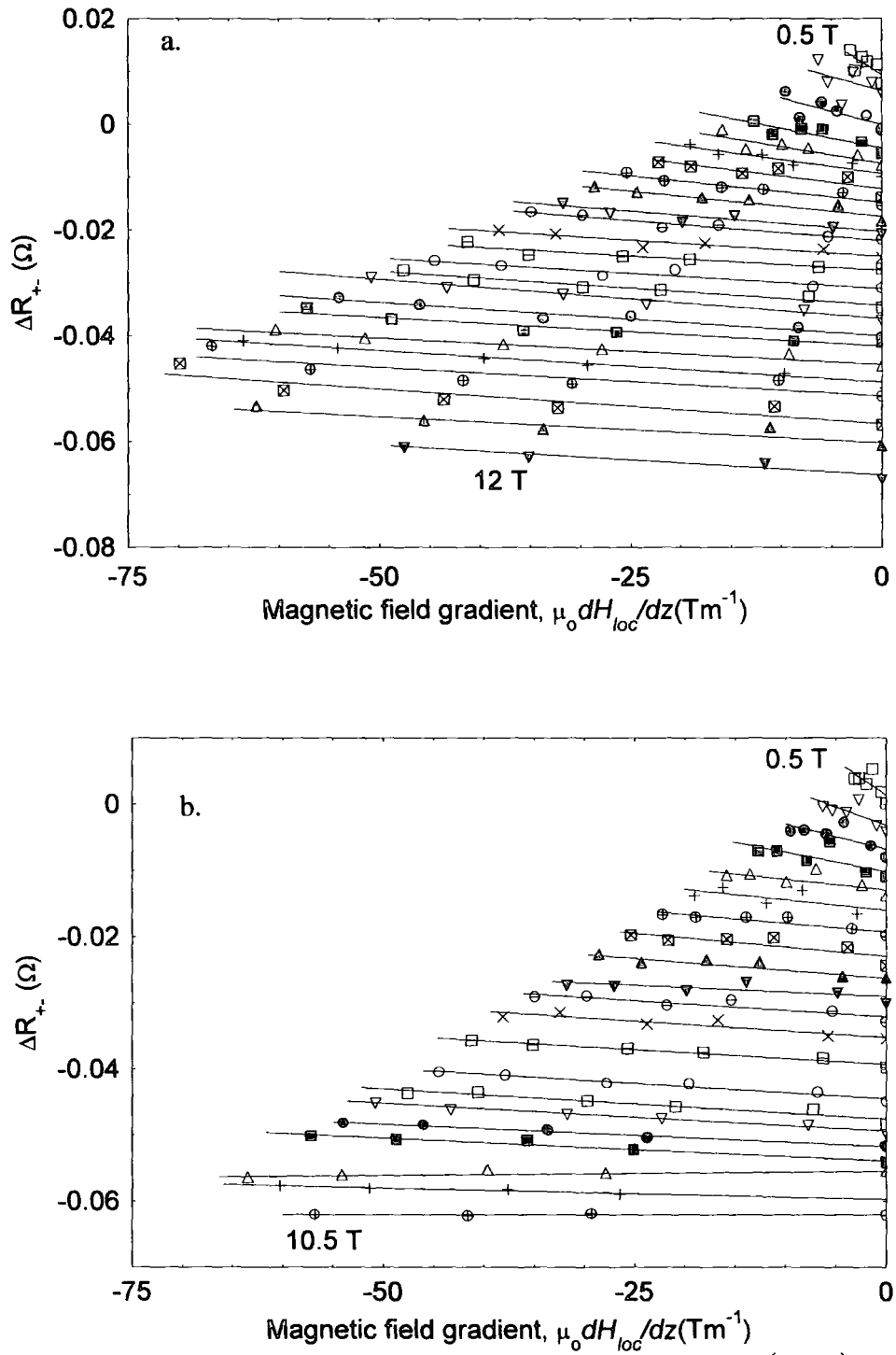

Figure 5.34. Difference in resistance across the field sweep loops (ΔR_{+-}) for NbTi wire as a function of field gradient and local magnetic field, at (a) 300 mK and (b) 4.2 K and 180°, taken on chip 4 (α_V = 20 V(Nm)$^{-1}$) in vacuum. The lines are offset by $\Delta R_{+-} = (0.005B)$, where B is the magnetic field for the line. The solid lines are the best-fit lines through the data.

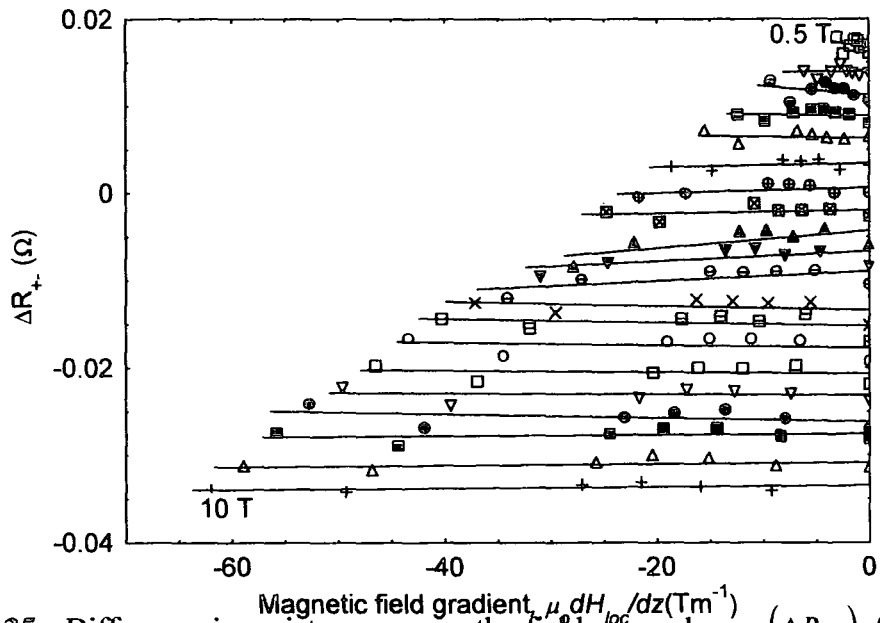

Figure 5.35. Difference in resistance across the field sweep loops (ΔR_{+-}) for NbTi wire as a function of magnetic field gradient and local magnetic field, at 4.2 K, 180°, taken on chip 4 (α_V = 20 V(Nm)$^{-1}$). At each field gradient, the voltage loops were measured for every temperature, before the Heliox was lifted to the next height. The lines are offset by $\Delta R_{+-} = (0.005B)$, where B is the magnetic field for the line.

The analysis to determine the critical current density (J_c) removes any systematic errors, such as gravity and the torque due to the field not being along a symmetry axis of the sample, as they were the same at each field gradient. The only torques, which contributed to the critical current density were those that changed with magnetic field gradient.

The critical current densities of the VSM data were determined from the equation 2.33, with the same γ_{sf} for the field perpendicular to the long axis and $\gamma_{sf} = \frac{2a}{3}$, for the field parallel to the long axis.

In figs. 5.32 – 5.35, the lines were offset along the ΔR_{+-} axis, so they did not overlap with each other, hence the spreading out of the lines was observed as the magnetic field increases.

At 0°, the data lines for chip 3 (fig. 5.32) are decreasing in the opposite direction to the data lines for chip 4 (fig. 5.33). The direction in which the gradients decrease depends on whether the lower or upper part of the voltage vs. field sweep loop was measured for the increasing field sweep. For the chip 3 data, the lower leg of the

loops were measured as the field increased, while for the chip 4 data, the upper leg of the loops were measured as the field was swept to the max values. This gives the difference in resistance across the loops to be either negative (chip 3) or positive (chip 4), thus the direction the gradients decrease will be different. The modulus of the gradient is taken, when determining the critical current density.

The error bars on the data taken in liquid helium on chip 4 were determined from the SNR of the voltage loops in fig. 5.31. For the data taken on chip 4 in vacuum (figs. 5.34a & b), the gradients decrease in the same direction as the chip 4 gradients taken in liquid helium, but the lower leg of the voltage loops were measured as the magnetic field increased (fig. 5.26). This is because the change in the magnitude of the hysteresis in the voltage loops decreased with increasing field gradient for the data taken at 180°, while at 0° the change in magnitude of the hysteresis in the voltage loops increased with increasing field gradient.

For the measurements on chip 4, where the loops were measured at every temperature, before the field gradient was changed, the gradients of the solid lines through the data above 6 T are almost the same value (fig. 5.35).

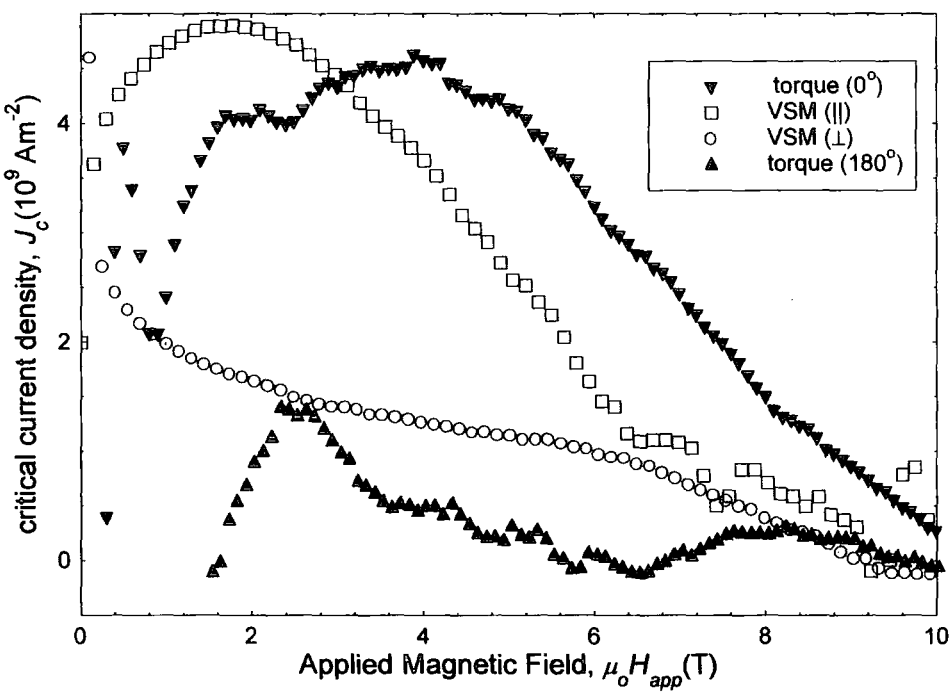

Figure 5.36. Critical current density of NbTi wire as a function of magnetic field and experiment at 4.2 K. The circles denote the VSM data for the sample perpendicular to the long axis and the squares denote the VSM data for the field parallel. The torque data was taken on chip 3 in liquid helium.

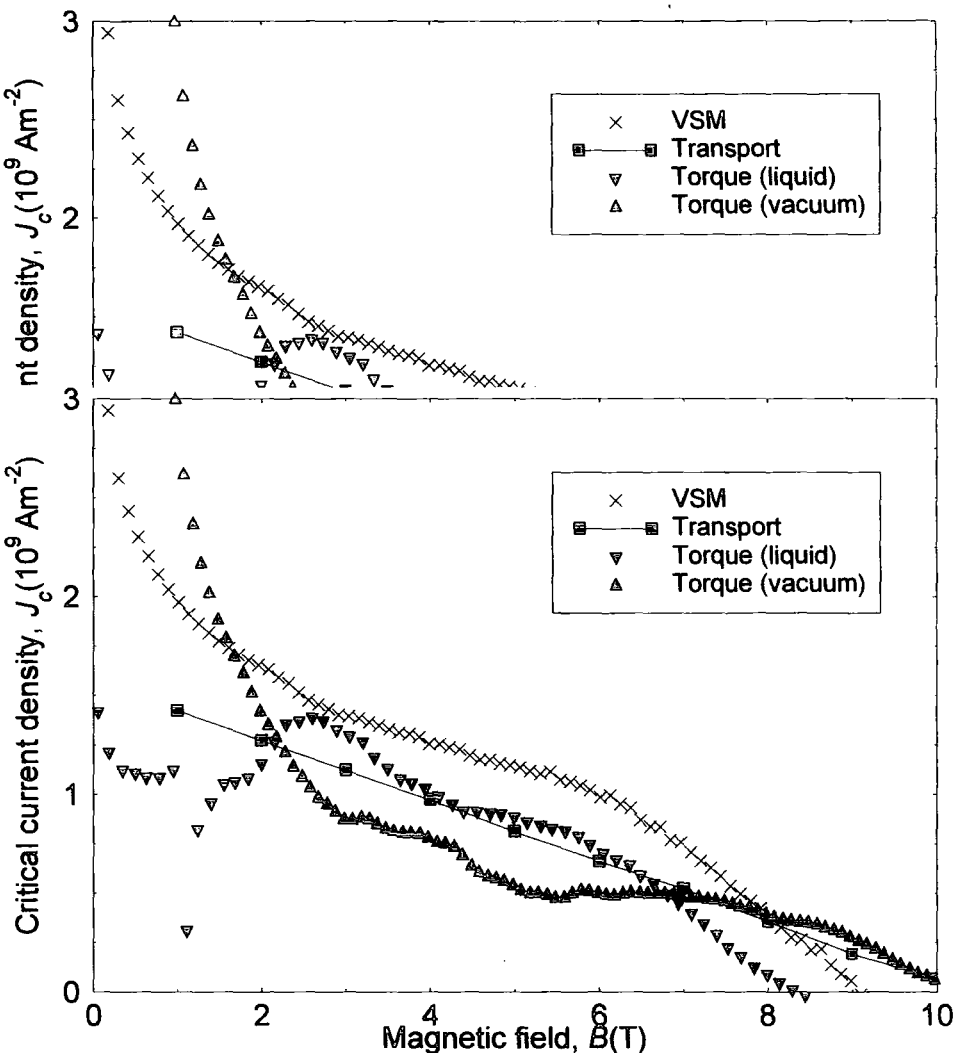

Figure 5.37. Critical current density of NbTi wire as a function of magnetic field, at 4.2 K. The VSM data is for the magnetic field perpendicular to the long axis. Both torque measurements were taken on chip 4. The transport data was taken by C Friend[6].

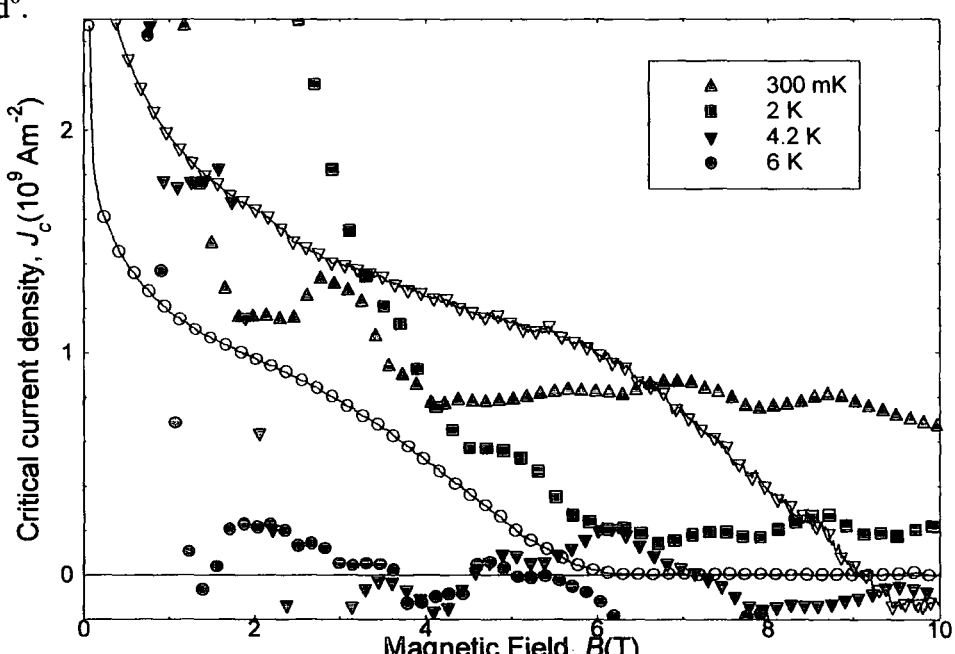

Figure 5.38. The critical current density of NbTi wire as a function of magnetic field and temperature. For these data, at each field gradient, the voltage vs. field sweep loops were measured for every temperature, before the Heliox was lifted to the next height from the magnet centre. The closed shapes are the torque data, and the open shapes are the VSM data. The sample was on chip 4.

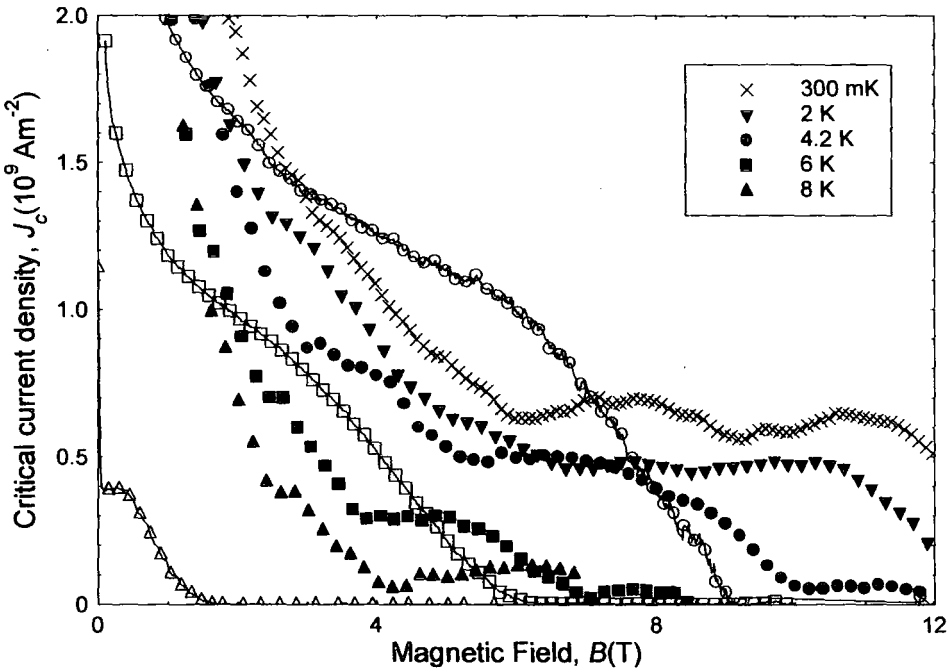

Figure 5.39. Critical current density of NbTi wire as a function of magnetic field and temperature. The closed shapes and the crosses are the torque data, and the open shapes are the VSM data. The sample was on chip 4.

5.7.2 Critical current density

For the measurement of NbTi wire on chip 3, the torque critical current density taken at 0° has the same order of magnitude and similar curve shape to the VSM critical current density, with the field parallel to the long axis (fig. 5.36). The critical current density $\left(J_c^{\tau}\right)$ measured at 180° has a similar curve shape to the parallel J_c^{VSM}, but is an order of magnitude smaller. Both J_c^{τ} were offset by 2 T along the x-axis, compared to the J_c^{VSM}. Also both J_c^{τ} have a peak at about 3.5 T. Jungst investigated the change in critical current density of NbTi wire as a function of magnetic field, and the angle ϕ between the long axis of the sample and the magnetic field[7]. He found the shape of the J_c curve was dependent on the angle between the field and the long axis. For $\phi = 90$ (perpendicular to long axis), the critical current density has the same shape as the J_c^{VSM} perpendicular data (fig. 5.37), while for $\phi = 0$ (parallel to long axis), the critical current density peaked at low fields and then decreased to zero as the field was increased, which is consistent with the J_c^{VSM} parallel data (fig. 5.36). As ϕ decreased towards 0°, the peak appeared in the J_c data, at low fields (< 2 T). The

shape of the J_c^r curves at 0° & 180° were consistent with angle between the field and the long axis of the sample not being 90°[7]. In this case the sample on chip 3 was at roughly 30 degrees to the platform edge, hence the angle of the NbTi sample to the edge of the platform affected the shape of the J_c^r curve. The change in J_c shape with angle is due to the anisotropy of the pinning centres in NbTi wire[8].

For the measurements on chip 4, the J_c^r taken in liquid helium and the J_c^r in vacuum are the same order of magnitude as the J_c^{VSM} with the field perpendicular to the long axis (fig. 5.37). The vacuum J_c^r has different field dependence and is 65 % of the magnitude of J_c^r measured in liquid helium (fig. 5.37), which is assumed to be due to Eddy currents induced in the copper matrix. In liquid helium any heat that occurred was removed from the sample by the liquid, while in vacuum, the heat was removed from the sample via the copper leads and the annealed copper wire fixed to the chip. Hence it would have taken longer time to remove heat from the sample. From fig. 5.39, the torque critical current density of NbTi wire has similar field dependence for all temperatures, thus heating occurred at all temperatures. The 10 K voltage vs. field sweep loops were reversible for all temperatures, thus no background was subtracted away from the NbTi J_c^r.

For the measurement where the voltage loops were measured at every temperature before the field gradient was changed, the torque critical current densities are the same order of magnitude as the VSM critical current densities, but at all temperatures J_c^r had a different field dependence (fig. 5.38). These loops were measured to try and remove one of the errors from the experiment, hence the probe was only moved eight times, rather than the 40 times it was moved in a normal measurement. This should have reduced the error on the calculated field gradient, thus improve the accuracy of the critical current density measured. The magnitude of J_c^r at 4.2 K, 5 T was 8.4 % of the J_c^{VSM}, and the J_c^r for temperatures above 4.2 K went negative at 2 T, and then returned positive at higher fields. The reason for the different magnitude and field dependence of J_c^r was because the change in magnitude of the hysteresis in the voltage vs. field sweep loops was not linear with field gradient (cf. fig. 5.35). Hence the difference in resistance across the field sweep loops changed randomly between the different heights. Thus the best fit lines through the data were almost

constant for all magnetic fields above 6 T. The irregular change in the voltage hysteresis may have been due to the temperature of the sample being unstable at each field gradient.

5.7.3 Errors for the critical current density

When using the field-gradient torque magnetometer to determine J_c of an isotropic superconductor, a number of errors have to be included. These are discussed below.

The first error is the height of the sample from the centre of the magnet (z). It is important in determining the field gradient experienced by the sample (fig. 5.9). The height was measured externally from the Heliox head to the magnet neck fitting. The probe was designed so the sample was in the magnet centre when the Heliox head rested on top of the magnet neck fitting (fig. 5.1). The height was kept fixed for each field sweep loop by using a height marker. These markers were made to fit between the Heliox head and the neck fitting. They reduced the error on the measured height. Therefore the error for the measured height of the sample (z) is $\pm$ 1 mm.

The second error occurred from the temperature control of the whole experiment. The magnetic moment of a superconductor is temperature dependent, so large changes in the temperature will affect the measurement. The temperature control is better than $\pm$ 10 mK at temperatures below 2 K, and $\pm$ 50 mK for temperatures above 2 K. This means that if the probe is working correctly, i.e. the pick-up tube is in the liquid helium, the temperature stability of the experiment should not pose a problem.

The third error is the position of the sample on the torque chip. The distance between the centre of the sample and the middle of the torque chip platform (l) is difficult to measure. It was found by photographing the whole chip platform down a microscope, hence digital micrometer callipers were not placed near the chip, which reduced the risk of breaking the platform. From the photograph of the platform the enlargement factor is known, as the width of the platform is 2 mm. The enlarged l is measured using a ruler off the photograph. The scaling factor is then used to determine the actual l, and the error for it. The error for l is $\pm$ 0.05 mm.

The fourth error is the angle between the chip and the magnetic field measured using the Hall chip. The error for the Hall voltage depends on the angle between the Hall chip and the field. At angles close to 0 degrees, the change in Hall voltage at 3 T, for a change of 1 degree in angle is $\pm$ 2 x 10^{-5} V. From fig. 5.12, this is where the Hall

chip is the most sensitive to a change in angle. For angles close to 90 degrees, the change in Hall voltage, for a change of 1 degree in angle is $\pm$ 3.6 x 10^{-7} V. Around 90 degrees the Hall chip is the least sensitive to a change in angle, which means the sensitivity of the angle is reduced by two orders of magnitude over 90 degrees. Therefore the error on the angle increases as the angle increases towards 90 degrees. The angle between the sample and the applied field is taken to be 0 or 180 degrees, when the measured voltage vs. field sweep loop at $z = 0$ cm is reversible.

Material	Sample & Experiment	Critical current density J_c(4.2 K, 5T) (Am^{-2})
NbTi wire	1 mm length VSM	$1.232 \pm 0.01 \times 10^9$
	Transport	8.05×10^8
	Torque (liquid)	$8.79 \pm 0.8 \times 10^8$
	Torque (vacuum)	$5.375 \pm 0.5 \times 10^8$

Table 5.2. Comparison of the critical current densities of NbTi wire for the different experiments. The errors for the torque magnetometer data and the VSM data were determined using standard error analysis. The NbTi wire transport data was taken by C Friend[6].

The error for J_c is determined from standard error analysis. For equation 5.7, the error for J_c^{τ} for the torque magnetometer data is given by:

$$\left(\frac{\varepsilon(J_c^{\tau})}{J_c^{\tau}}\right)^2 = \left(\frac{\varepsilon(\alpha_R)}{\alpha_R}\right)^2 + \left(\frac{\varepsilon(l)}{l}\right)^2 + \left(\frac{\varepsilon(vol)}{vol}\right)^2 + \left(\frac{\varepsilon(\gamma)}{\gamma}\right)^2 + \left(\frac{\varepsilon\left(\frac{dR_{+-}}{d\frac{d\mu_0 H_{loc}}{dz}}\right)}{\frac{dR_{+-}}{d\frac{d\mu_0 H_{loc}}{dz}}}\right)^2 \qquad (5.7)$$

where $\varepsilon(x)$ is the error for the variable x. The error for α_R was found from the calibration graph (fig. 5.17). The error for l was determined from the method described above. The errors for the volume $(\varepsilon(vol))$ and the shape factor $(\varepsilon(\gamma))$ were determined from the error for the lengths of the samples.

From the experiment, the error for any dimension of a sample was $\pm$ 0.02 mm. This was because the samples were fragile, so care had to be taken when measuring them

with the digital micrometer callipers. The error for $\frac{dR_{+-}}{d\frac{d\mu_o H_{loc}}{dz}}$ was taken from the signal to noise ratio of the corresponding voltage vs. field sweep loops. The error for the angle φ was negligible compared to the other errors, as the data were taken at the reversible angle, so φ was either 0^o or 180^o. These angles are where the Hall voltage was most sensitive to the change in angle. A similar equation was used to determine the error for the VSM data.

The errors for the J_c^r are determined at 5 T. For the torque magnetometer the errors are field dependent, which means at 0 T, the error on the data is infinite, as the SNR is zero. Hence for fields lower than 2 T, the critical current densities determined from the torque magnetometer data, were either an order of magnitude larger than the J_c above 2 T or negative (fig. 5.37), due to the voltage vs. field sweep loops for all field gradients being either reversible or having the same voltage up to 2 T.

When determining the error for J_c^r, using standard error analysis (eqn. 5.7), the largest error was for the gradient $\frac{d\Delta R_{+-}}{d\left(\frac{d\mu_o H_{loc}}{dz}\right)}$. This is because the calibration constant of the chip limits the sensitivity, and thus the SNR. The error bars on the ΔR_{+-} vs. field gradient graph for NbTi wire in liquid helium (fig. 5.34) were determined from the SNR of the NbTi wire voltage vs. field sweep loops measured (fig. 5.26). The error bars show how much the gradient could change due to the noise on the signal. This error could be reduced, by measuring more voltage vs. field sweep loops at different field gradients or by using a QD chip with a calibration constant $\left(\alpha_V\right)$ greater than 100 $V(Nm)^{-1}$. The next largest error was for the dimensions of the sample. This meant the overall error for the NbTi wire J_c^r was larger than the SNR of the measured voltage data. For the VSM J_c^{VSM}, the uncertainties in the dimensions of the samples were the largest contributing errors.

For the NbTi wire measured on chip 4 in liquid helium, at 5 T $J_c^r = 8.79 \pm 0.8 \times 10^8\,Am^{-2}$ compared to $J_c^{VSM} = 1.232 \pm 0.01 \times 10^9\,Am^{-2}$ for the VSM data taken with the magnetic field perpendicular to the long axis (fig. 5.37). For the torque magnetometer, the SNR at 5 T was 12 (fig. 5.27), hence the largest contribution to the

error for J_c^r was from $\frac{d\Delta R_{+-}}{d\left(\frac{d\mu_o H_{loc}}{dz}\right)}$ (fig. 5.33). For the same sample and chip measured in vacuum at 5 T, 4.2 K, $J_c^r = 5.375 \pm 0.5 \times 10^8\ \mathrm{Am}^{-2}$ (fig. 5.37). Again the largest contributing error was from $\frac{d\Delta R_{+-}}{d\left(\frac{d\mu_o H_{loc}}{dz}\right)}$, due to the small SNR of the voltage vs. field sweep loops (fig. 5.26).

5.8 Discussion

5.8.1 Change in voltage vs. field sweep loop area with angle

From Bean's model[1], if an isotropic superconductor is placed in a uniform magnetic field, with the field along one the symmetry axes, the magnetic moment is in the same direction as the field. Therefore at the field centre (z = 0 cm), for a cylinder when the field is applied along the radial direction, the field should be along a symmetry axis, thus there should be no torque. The superconducting samples were all nominally cylindrical shapes. They were glued onto the chip's platform parallel to the edge of the platform (fig. 5.5). This meant the local magnetic field $\mu_o H_{loc}$, should have been perpendicular to the long axis, thus parallel to the radial axes, for every angle during the rotation. Therefore at the field centre, the loops should have been reversible, as the sample was rotated through 360 degrees.

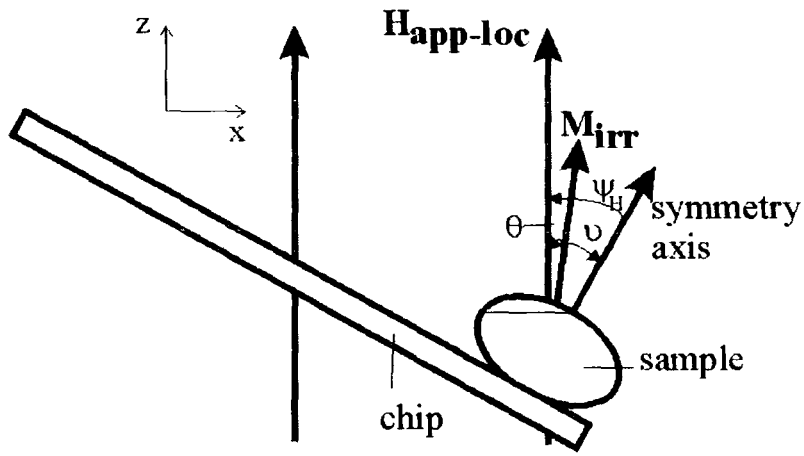

Figure 5.40. Diagram of an anisotropic, irreversible superconductor in an applied local magnetic field ($\mathbf{H_{app\text{-}loc}}$), when the field is not aligned with a symmetry axis of the sample. The angle between the symmetry axis and the local field is ψ_H, the angle between the irreversible magnetisation ($\mathbf{M_{irr}}$) and the symmetry axis is υ, and the angle between the magnetisation and the field is θ.

From the NbTi wire voltage vs. field sweep loops the change in $\Delta\tau$ over 360° was determined to be $\sin 2\theta$ (fig. 5.22), with reversible angles at 0°, 90°, 180° and 270°. From fig. 5.40, the torque experienced by an anisotropic, irreversible superconductor when the applied local field is not aligned with the symmetry axis is:

$$\tau = \mu_o vol\left(M_{irr\perp} H_{app-loc\parallel} - M_{irr\parallel} H_{app-loc\perp}\right) \tag{5.8}$$

where $M_{irr\parallel}$ is the component of the irreversible magnetisation parallel to the symmetry axis, and $M_{irr\perp}$ is the component of the irreversible magnetisation perpendicular to the symmetry axis. The components of the applied local field are $H_{app-loc\parallel} = H_{app-loc}\cos\psi_H$ and $H_{app-loc\perp} = H_{app-loc}\sin\psi_H$, where ψ_H is the angle between the symmetry axis and the local field. The magnetisation components are $M_{irr\parallel} = M_{irr}\cos\upsilon$ and $M_{irr\perp} = M_{irr}\sin\upsilon$, where υ is the angle between the magnetisation and the symmetry axis. The relation between the angles is $\psi_H = \upsilon + \theta$, where θ is the angle between the magnetisation and the local field. If there are two symmetry axes perpendicular to each other, then the magnetisation can lie along either of them, depending on the angle ψ_H. Thus the measured torque will have $\sin 2\psi_H$ dependence rather than $\sin\psi_H$ dependence, and is given by:

$$\tau = \mu_o vol M_{irr} H_{app-loc} \sin 2\psi_H \tag{5.9}$$

The change in torque across the field sweep loops is $\Delta\tau = \tau_+ - \tau_-$. In eqn 5.9, the irreversible magnetisation depends on the field direction. Therefore the change in torque across the field sweep loops as a function of angle is:

$$\Delta\tau = \mu_o vol H_{app-loc} \Delta M_{irr} \sin 2\psi_H \tag{5.10}$$

where ΔM_{irr} is the change in irreversible magnetisation across the field sweep loop. This suggests the samples behaved as parallelepipeds rather than cylinders during the experiment. This is because there were two distinct symmetry axes in the radial directions, as the angular dependence of the change in torque was $\sin 2\psi_H$ (fig. 5.22). When the platform was at 0 or 180 degrees, the distance l was perpendicular to the local field. If the reversible angle coincided, then at the field centre $\Delta\tau$ was zero, and the voltage loop was reversible (fig. 5.23). When the platform was at 90 or 270 degrees, the distance l is a parallel to the magnetic field, hence at field gradients to the first order, there is no contribution from $\mathbb{l} \times m_z \mu_o \dfrac{d\mathbf{H}_{app-loc}}{dz}$, where m_z is the magnetic

moment in the z-direction. Thus the voltage vs. field sweep loops are almost reversible at every field gradient consistent with fig. 5.25.

The change in $\Delta\tau$ across the NbTi wire field sweep loops, as a function of angle (fig. 5.22) is independent of the QD chip, and the angle between the long axis of the sample and the platform edge. The angle between the long axis of NbTi wire measured on chip 3 and the platform edge was 30 degrees compared with the angle between the sample on chip 4 and the platform edge, which was less than 10 degrees.

5.8.2 Advantages and disadvantages of the field-gradient torque magnetometer and the VSM

The field-gradient torque magnetometer has many advantages. These include having a base temperature of 300 mK and operating in fields up to 15 T. The torque magnetometer also has a temperature stability of ± 10 mK for temperatures below 2 K, and ± 50 mK for temperatures above 2 K. This is because it is fixed to the base of the helium-3 pot of the Heliox probe. The Heliox operates in vacuum, which increases the temperature stability of the experiment. The background sensitivity of the torque magnetometer is 2 x 10^{-8} Am^2 at 5 T and field centre. The sensitivity is field dependent, and decreases with decreasing magnetic field (fig. 5.31). The torque magnetometer measures isotropic superconductors. The sample can be rotated horizontally through 360°, in the magnetic field. The torque magnetometer can be used to determine the anisotropy of a superconductor, the critical current density and the upper critical field ($B_{c2}(T)$). The size of the QD chip platform means it could be used to measure single crystals.

The disadvantages of the torque magnetometer are that samples, which are heavier than 10 mg or have a magnetic moment greater than 1 x 10^{-5} Am^2 (1 T), cannot be measured. This is because the QD chips' 25 μm thick legs are very fragile. This limits the torque, which can be applied before the legs break or the elastic limit of silicon is reached. The noise on the data is dependent on the calibration constant (α_V) of the QD chip and the superconducting sample. The noise on the measured voltage increases, as the value of α_V decreases. The SNR also limits the accuracy of the J_c measured. Another disadvantage is changing a sample on the chip's platform takes at least 48 hours. This means the torque magnetometer is useful for measuring

one sample at many temperatures, rather than measuring a series of samples at only a couple of temperatures.

The vibrating sample magnetometer (VSM) is a reliable technique for measuring magnetic moments[4]. It is easy to use. The sample change over time is about 2 hours. This means it is convenient for measuring a series of samples, and hardly any helium is wasted, as the measurements are almost continuous. The VSM can be used to measure samples, which are heavier than 10 mg, and moments as large as 3×10^{-3} Am^2. The noise on the data is normally at least two orders of magnitude smaller than the signal. VSMs will work in fields up to 17 T[9] and in the temperature range 4.2 K – 300 K[10].

The VSM has the disadvantage that the base temperature is 1.8 K. This is because the vibrating rod and sample are cooled by helium gas. At 4.2 K the gas-liquid transition for helium occurs, which causes instabilities in the temperature. This is seen as periodic oscillations in the magnetic moments measured (fig. 5.29), which makes the data unreliable. The temperature control of a VSM is ± 0.1 K. This is a large enough change in temperature to affect the measurement of the magnetic moment. Another disadvantage is the ac-field, which penetrates into the sample, due to the vibrating of the sample in a magnetic field gradient[11]. The VSM measurements of J_c and B_{irr} become inaccurate for small samples, and at high magnetic fields.

The VSM background magnetic moment (fig. 5.30) affects measurements taken on the highest amplification. The measured background has a linear dependence with magnetic field, and is only weakly temperature dependent. At 8 K, 5 T the background moment of the VSM is -6.7×10^{-7} Am^2, hence any magnetic moment smaller than 1×10^{-6} Am^2, will have the background moment superimposed on top. The background has to be subtracted away from the measured moment, before any calculations are carried out, which increases the noise on the measured moment. Thus the moments measured on the highest amplification at high fields have lower SNR than the moments at low fields.

5.8.3 Specifications of the VSM and the torque magnetometer

For the VSM, magnetic moments can be measured in the range 3×10^{-3} to 3×10^{-8} Am^2. The background noise is 3×10^{-8} Am^2 (fig. 5.30). The moment sensitivity is independent of the applied magnetic field.

For anisotropic superconductors, the Quantum Design PPMS Torque Magnetometer can be used to measure the magnetic moment. The QD chips used are the same chips as used for the field-gradient torque magnetometer. The magnetic moment is determined from $\tau = \mathbb{m} \times \mathbb{B}$. The dimensions of the maximum sample that can be measured are 1.5 x 1.5 x 0.5 mm^3. The maximum weight of the sample is 10 mg. The moment sensitivity of the instrument is dependent on the applied field. At 5 T, the range of moments that can be measured is from 2 x 10^{-10} Am^2 to 2 x 10^{-6} Am^2. The background noise is 2 x 10^{-10} Am^2. The sensitivity of the moment increases as the field increases. At 0 T, no moment can be measured on the instrument.

For isotropic superconductors, the field-gradient torque magnetometer is used to measure the magnetic moment. The QD chips are used to measure the torque. The maximum sample size is 1.5 x 0.5 x 0.5 mm^2, and the maximum weight is 10 mg. From eqn 3.14b $\left(\tau = \mathbb{l} \times (\mathbb{m} \cdot \nabla)\mathbb{B} + \mathbb{m} \times \mathbb{B}\right)$ the ideal moment sensitivity of the torque magnetometer can be calculated for our experimental arrangement assuming optimum noise. In an ideal set-up, l = 0.5 mm and $\mathbb{m} \times \mathbb{B} = 0$. From fig. 5.10, the field gradient at 5 T, 6 cm is ~ 25 Tm^{-1}. Taking torque limits to be the maximum applied torque (1 x 10^{-5} Nm) and the minimum applied torque (1 x 10^{-9} Nm) from the QD chip specification. At 5 T, the moment ideal range is from 8 x 10^{-8} Am^2 to 8 x 10^{-4} Am^2. The achieved specifications of the torque magnetometer were determined from the error on the critical current densities and the eqn 5.7. For NbTi wire the sensitivity was 1 x 10^{-7} Am^2 at 5 T. The sensitivity of the field-gradient torque magnetometer is field dependent (eqn 3.14b). Thus as the applied local field is increased the sensitivity increases. As the field is decreased to zero (below 2 T), the error for the data increases towards infinity.

5.9 Conclusions

A field-gradient torque magnetometer has been designed and constructed, which uses a QD torque chip to measure the magnetic moment of isotropic superconductors. The magnetometer works in the temperature range 300 mK to 20 K and in fields up to 15 T.

If the local field is not along one of the symmetry axes of a superconductor, then the sample's moment is not parallel to the field, and the sample experiences a torque. The angular dependence of the torque for an almost isotropic superconductor is $\sin 2\psi_H$,

where ψ_H is the angle between the symmetry axis and the field. For NbTi wire on the torque magnetometer, the angular dependence of the change in torque across the loop was $\sin 2\psi_H$. This means the cylindrical samples had two distinct symmetry axes in the radial direction. It was found that the $\sin 2\psi_H$ dependence was independent of the QD chip and the angle between the long axis of the sample and the platform edge.

The critical current density of NbTi wire was determined using the field-gradient torque magnetometer, for the voltage vs. field sweep loops measured at the reversible angle. The critical current densities were compared with VSM measurements made on the same sample. It was found that the calibration constant of the QD chip determined the sensitivity, SNR and accuracy of the data taken on the magnetometer. The SNR was also dependent on the sample being measured and the applied field.

For the NbTi wire measured on chip 4 in liquid helium $J_c^\tau = 8.79 \pm 0.8 \times 10^8\ \mathrm{Am}^{-2}$ and in vacuum $J_c^\tau = 5.375 \pm 0.5 \times 10^8\ \mathrm{Am}^{-2}$. The difference in the magnitude of the J_c^τ was due to heating occurring during the vacuum measurement. For the same NbTi wire sample $J_c^{VSM} = 1.232 \pm 0.01 \times 10^9\ \mathrm{Am}^{-2}$ for the VSM data taken with the magnetic field perpendicular to the long axis. The difference in J_c between the VSM and the torque data, was due to the difference in the SNR of each measurement. The SNR of the VSM at 5 T was 217, compared to 12 for the torque data. The decrease in the SNR of the torque magnetometer meant the error for the J_c^τ increased.

For the VSM, magnetic moments can be measured in the range 3 x 10^{-8} to 3 x 10^{-3} Am^2. The field-gradient torque magnetometer ideally should measure magnetic moments in the range 8 x 10^{-8} to 8 x 10^{-4} Am^2, at 5 T. From the error for the J_c^τ of NbTi wire, the measured sensitivity is 1 x 10^{-7} Am^2 at 5 T.

References for Chapter 5

1 C. P. Bean, Reviews of Modern Physics **36**, 31 (1964).

2 M. Willemin, C. Rossel, J. Brugger, et al., Journal of Applied Physics **83**, 1163 (1998).

3 M. Tortonese, R. C. Barrett, and C. F. Quate, Applied Physics Letters **62**, 834 (1993).

4 S. Foner, Journal of Applied Physics **79**, 4740 (1996).

5 S. Spagna, A. Wilson, M. B. Simmonds, et al., (2001).

6 C. M. Friend, "Transport critical current density measurements on high and low temperature superconductors in magnetic fields up to 15 T" *Dept. of Physics*, University of Durham, 1994.

7 K.-P. Jungst, IEEE transactions on Magnetics **11**, 340 (1975).

8 H. Kuepfer and T. Matsushita, Journal of Applied Physics **63**, 5060 (1988).

9 N. F. Oliveira and S. Foner, Review of Scientific Instruments **43**, 37 (1972).

10 B. C. Dodrill, (Lakeshore Cryotronics inc, 2002).

11 I. J. Daniel and D. P. Hampshire, Physical Review B **61** (2000).

Chapter 6

Critical current density of $PbMo_6S_8$, $Pb_{0.75}Eu_{0.25}Mo_6S_8$ and NbTi wire in the temperature range 300 mK to T_c

6.1 Introduction

This chapter details the use of a field-gradient torque magnetometer to measure the magnetic moment of a 1 mm length $PbMo_6S_8$ sample, a 1 mm length NbTi wire sample and a 1 mm length $Pb_{0.75}Eu_{0.25}Mo_6S_8$ sample, from 300 mK to T_c, in fields up to 15 T. From the torque data the critical current density (J_c) and the upper critical field ($B_{c2}(0)$) are determined.

A vibrating sample magnetometer (VSM) was also used to measure the magnetic moments of the 1 mm length samples. The magnetic moments of 3 other lengths NbTi wire samples (2 mm, 3.83 mm & 5 mm), and 4 mm length $PbMo_6S_8$ and $Pb_{0.75}Eu_{0.25}Mo_6S_8$ samples were measured using the VSM. For the torque samples measured using the VSM, the magnetic moments were measured with the field parallel to and perpendicular to the long axis.

In section 6.2, the experimental procedures for measuring the upper critical field, using the torque magnetometer, VSM and resistivity are described. In section 6.3 are presented the results from measuring the NbTi wire samples, the $PbMo_6S_8$ samples and the $Pb_{0.75}Eu_{0.25}Mo_6S_8$ samples by both magnetometers. For the torque magnetometer measurements, the voltage vs. field sweep loops were measured at the reversible angle as a function of magnetic field, field gradient and temperature. Using the VSM, the magnetic moment of each sample was measured as a function of magnetic field and temperature. The resistivity of the NbTi wire was measured on the Heliox probe from 300 mK to 10 K as a function of magnetic field.

In section 6.4, the critical current densities of the 1 mm length $PbMo_6S_8$ sample, 1 mm length $Pb_{0.75}Eu_{0.25}Mo_6S_8$ sample and the 1 mm length NbTi wire sample were determined from the torque magnetometer data. Similarly the critical current densities for both field directions of all the samples were obtained from the VSM data. The critical current densities and the irreversibility fields from the VSM data for the 4 mm bulk samples of $PbMo_6S_8$ and $Pb_{0.75}Eu_{0.25}Mo_6S_8$ are compared. For the NbTi wire samples, and the $PbMo_6S_8$ samples, the flux pinning forces were determined

from the VSM and the torque data. The flux pinning forces for the 4 mm length $Pb_{0.75}Eu_{0.25}Mo_6S_8$ sample were calculated. The upper critical fields of $PbMo_6S_8$ and NbTi wire were determined from the torque magnetometer, VSM and resistivity measurements. In section 6.5, the critical current densities of NbTi wire, $PbMo_6S_8$ and $Pb_{0.75}Eu_{0.25}Mo_6S_8$ are discussed. For the NbTi samples and the $PbMo_6S_8$ samples, the anisotropy between the critical current densities for the field parallel to and perpendicular to the long axis are discussed. The flux pinning force of NbTi wire is discussed in terms of the different mechanism, as a function of temperature and reduced magnetic field, and are compared with the literature. The 4 mm length $PbMo_6S_8$ and $Pb_{0.75}Eu_{0.25}Mo_6S_8$ samples critical current densities and flux pinning forces are compared. The upper critical field at 0 T of NbTi wire is presented, and compared with the literature. The conclusions are presented in section 6.6.

6.2 Experimental Procedure

6.2.1 Field-gradient torque magnetometer

For the field-gradient torque magnetometer, the voltage vs. field sweep loops were measured as a function of local magnetic field, field gradient and temperature, at the reversible angle, as described in section 5.5.

The same samples were measured on the torque magnetometer and VSM. The bulk $PbMo_6S_8$ sample had dimensions of 0.32 x 0.4 x 1 mm^3, and was roughly cylindrical. Similarly for $Pb_{0.75}Eu_{0.25}Mo_6S_8$ the sample was cylindrical with dimensions 0.15 x 0.15 x 1 mm^3. For the NbTi wire sample, three 1 mm lengths of wire were glued together with GE-varnish, to form a pyramid. The end of the each wire was sandpapered to obtain a flat surface.

6.2.2 Vibrating sample magnetometer (VSM)

The VSM measured the magnetic moments of the samples as a function of magnetic field and temperature (section 4.4). Each of the cylindrical samples measured on the torque magnetometer was measured with the magnetic field parallel and perpendicular to the long axis. The $Pb_{0.75}Eu_{0.25}Mo_6S_8$ sample measured on the torque magnetometer was on the limit of the VSM resolution hence a second cylindrical sample was measured with dimensions 0.3 x 0.3 x 1 mm^3. Four different NbTi wire samples were measured using the VSM. They were all made from three pieces of NbTi wire,

which were glued together with GE-varnish, in a pyramid arrangement. The different lengths were 1 mm, 2 mm, 3.83 mm, and 5 mm.

6.2.3 Resistivity

The Heliox probe was used to measure the resistivity of the NbTi wire. A standard four terminal resistance measurement was conducted. The voltage taps were a distance 12 mm apart. All the wires were GE varnished and tied down with dental tape to the torque magnetometer copper cage. This ensured they were thermally sunk to the helium-3 pot. To determine the critical temperature at zero field, the Heliox was used in a helium dewar. The Heliox temperature was swept from 6 K to 12 K. The Stanford lock-in provided the applied ac voltage (V_{ac} = 0.1 V) across the wire, and measured the resistivity voltage.

In the Oxford Instruments superconducting magnet, the resistivity of the NbTi wire was measured as a function of magnetic field and temperature. The magnetic field was applied perpendicular to the long axis of the wire. At each temperature (300 mK, 1 K, 1.5 K, 2 K, 4 K 6 K, 8 K and 10 K), the magnetic field was swept through the superconducting transition. The Stanford lock-in was used to provide the two different applied voltages across the wire. The voltages were 0.1 V and 0.01 V. This was to check for heating effects.

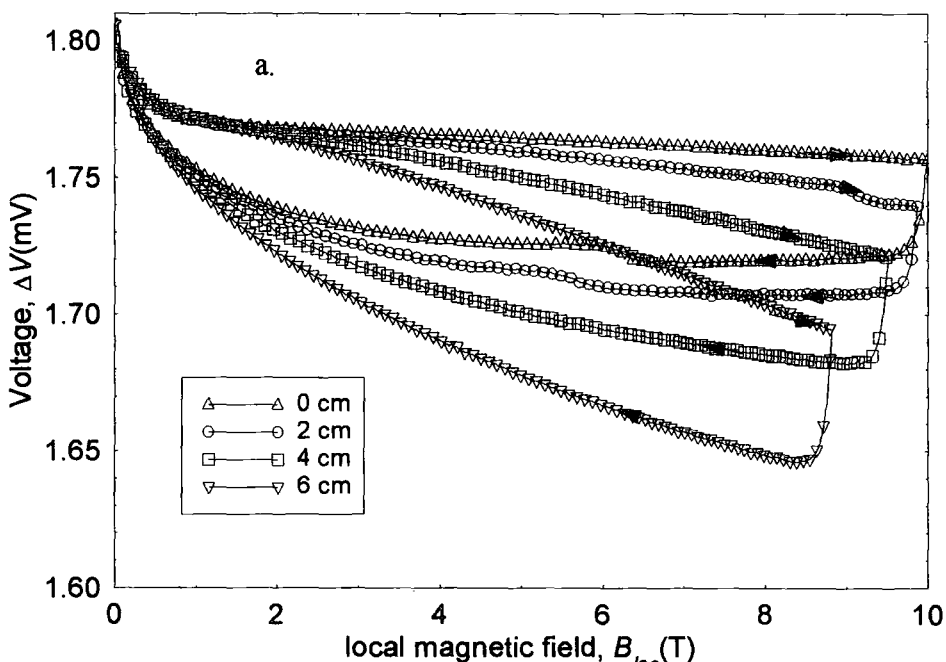

Figure 6.1a. Voltage vs. field sweep loops (ΔV) for $Pb_{0.75}Eu_{0.25}Mo_6S_8$ as a function of local magnetic field and height from the magnet centre at 0° and 5 K. The arrows indicate the increasing or decreasing magnetic field, during the measurement.

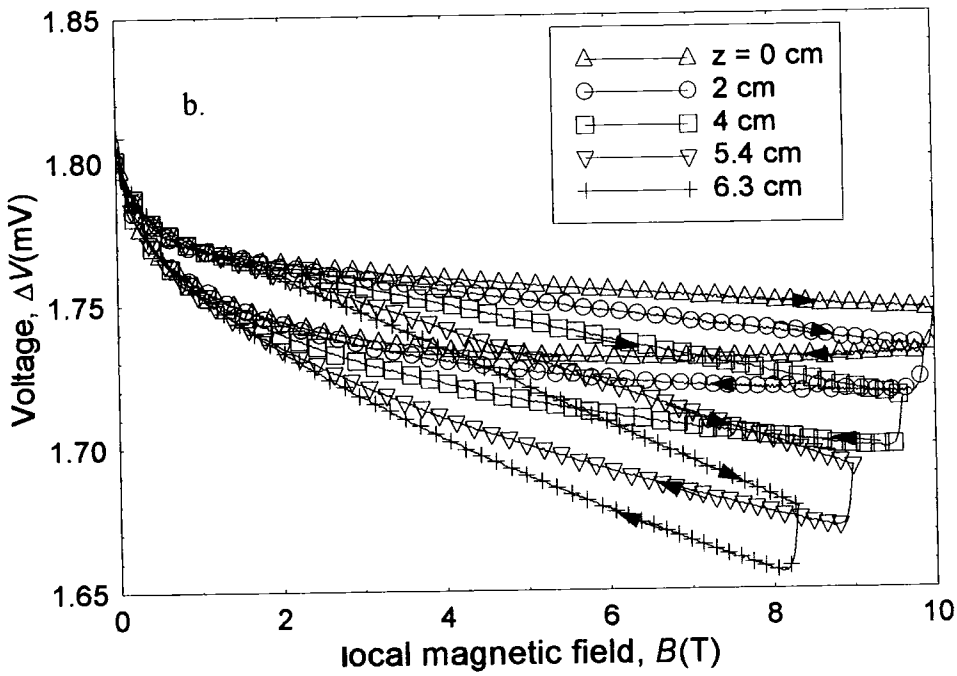

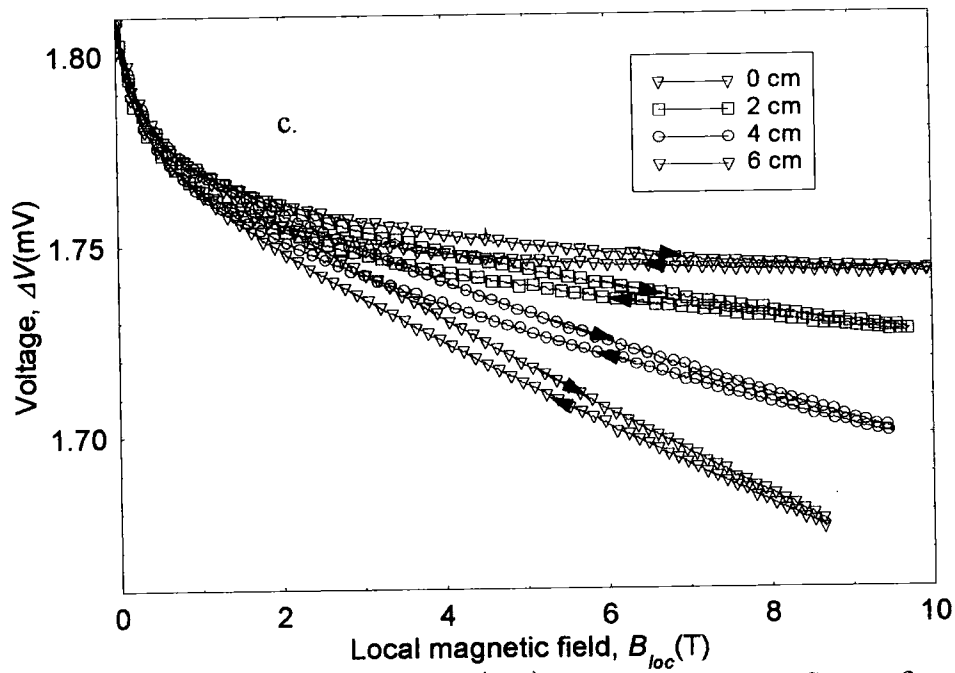

Figure 6.1. Voltage vs. field sweep loops (ΔV) for $Pb_{0.75}Eu_{0.25}Mo_6S_8$ as a function of local magnetic field and height from the magnet centre at 0 degrees and (b) 6 K & (c) 8 K. The arrows on the data indicate the increasing or decreasing magnetic field, during the measurement.

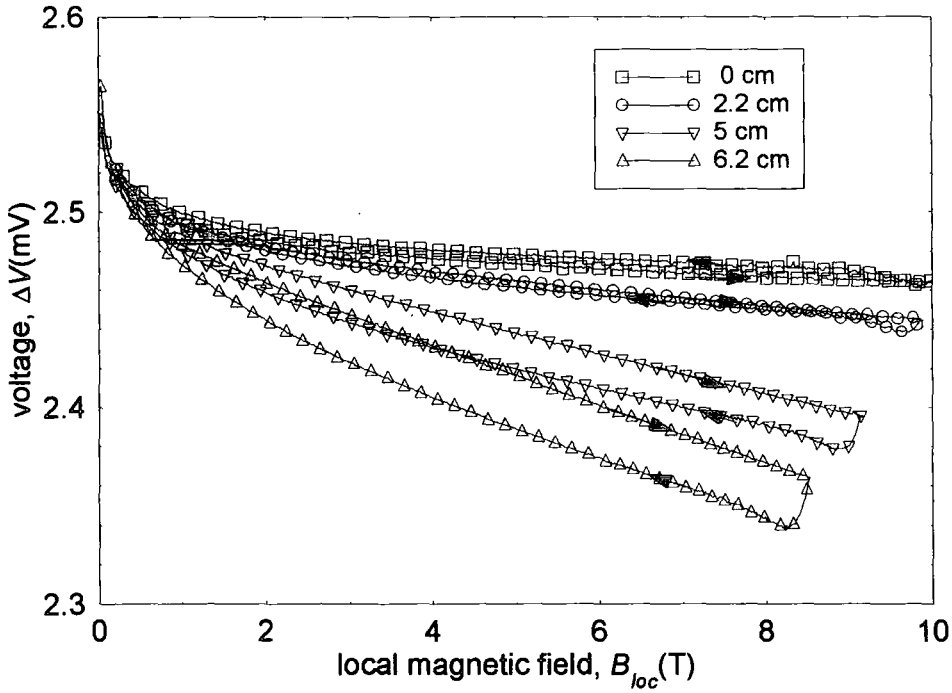

Figure 6.1d. Voltage vs. field sweep loops (ΔV) of $Pb_{0.75}Eu_{0.25}Mo_6S_8$ as a function of local magnetic field and height from the magnet centre, at 4.2 K, and the reversible angle. The arrows on the data indicate the increasing or decreasing magnetic field, during the measurement.

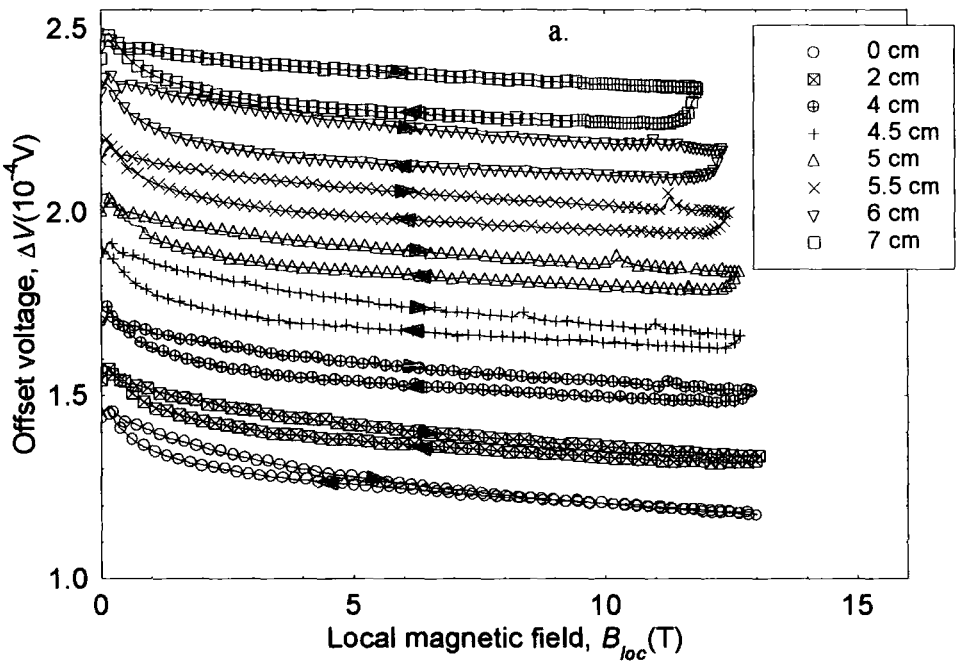

Figure 6.2a. Voltage vs. field sweep loops for $PbMo_6S_8$ as a function of local magnetic field and height from the magnet centre at 0°, 300 mK. The loops are offset by $\Delta V = -(0.05 \times 10^{-4} z)$, where z is the height from the magnet centre. The arrows indicate the increasing or decreasing magnetic field, during the measurement.

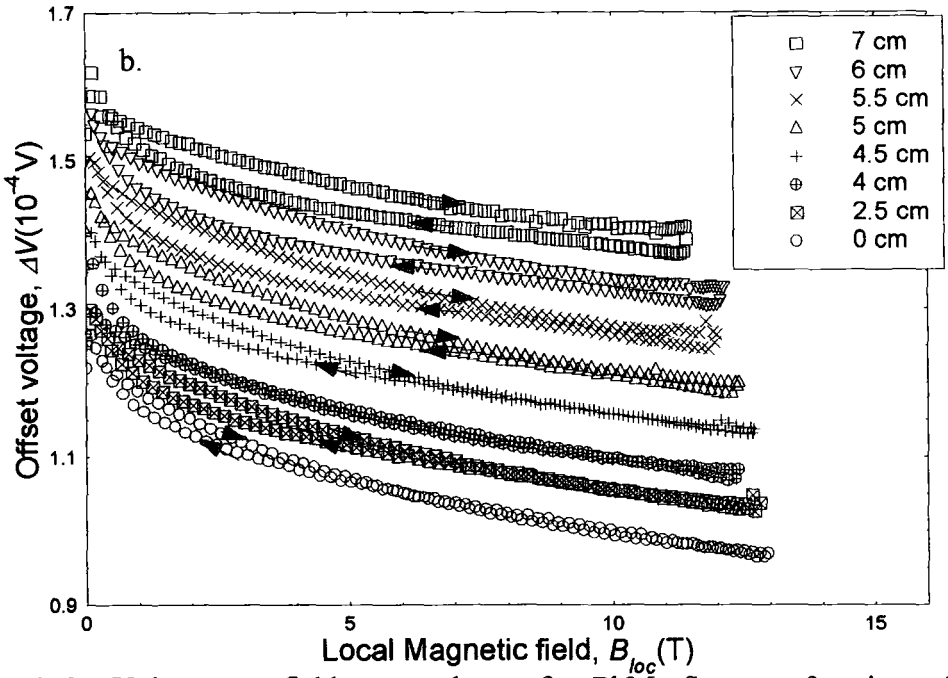

Figure 6.2b. Voltage vs. field sweep loops for $PbMo_6S_8$ as a function of local magnetic field and height from the magnet centre at 0°, 4.2 K. The loops are offset by $\Delta V = -(0.05 \times 10^{-4} z)$, where z is the height from the magnet centre. The arrows indicate the increasing or decreasing magnetic field, during the measurement.

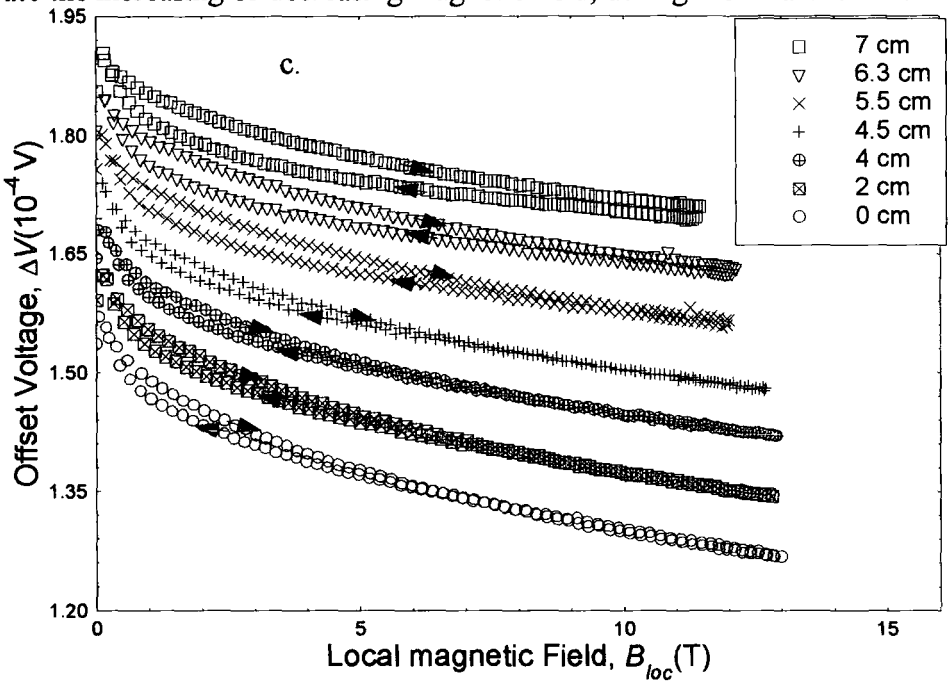

Figure 6.2c. Voltage vs. field sweep loops for $PbMo_6S_8$ as a function of local magnetic field and height from the magnet centre at 0°, 6 K. The loops are offset by $\Delta V = -(0.05 \times 10^{-4} z)$, where z is the height from the magnet centre. The arrows indicate the increasing or decreasing magnetic field, during the measurement.

6.3 Results

6.3.1 Field-gradient torque magnetometer

In figs. 6.2, the voltage vs. field sweep loops are offset along the y-axis, so they do not overlap. This means the change in the magnitude of the hysteresis in the voltage vs. field sweep loops between the different heights could be observed.

The initial measurements were carried out on $Pb_{0.75}Eu_{0.25}Mo_6S_8$. For the first measurement the calibration constant α_V of the torque chip 1 was not measured. This was because the method of calibrating a torque chip had not yet been determined. From the magnitude of the hysteresis in the voltage vs. field sweep loops and the magnitude of the VSM critical current density for $Pb_{0.75}Eu_{0.25}Mo_6S_8$, the voltage calibration constant was taken to be $\alpha_V \approx 200$ V(Nm)$^{-1}$. The experiment took place in vacuum, with the tufnol chip holder fixed at 0° using the grub screw. The voltage vs. field sweep loops were measured at 5 K, 6 K and 8 K, and at four magnetic field gradients (figs. 6.1). From figs. 6.1a, b & c, the data measured at 0°, were not reversible at $z = 0$ cm. The magnitude of the hysteresis in the voltage vs. field sweep loops decreased as the temperature was increased, which is observed between the data at 5 K (fig. 6.1a) and the data at 8 K (fig. 6.1c).

For the second measurement on $Pb_{0.75}Eu_{0.25}Mo_6S_8$, the torque chip 2 was calibrated using the method described in section 5.4.4. The voltage calibration constant was α_V = 160 V(Nm)$^{-1}$. This measurement also took place in vacuum, but at the angle where the voltage loop at $z = 0$ cm was reversible. The voltage vs. field sweep loops were measured at 4.2 K (fig. 6.1d) and 10 K, at four magnetic field gradients. From fig. 6.1d, the magnitude of the hysteresis in the voltage vs. field sweep loops increased as the height from the magnet centre increased. At 10 K, the voltage vs. field sweep loops were reversible at all field gradients. For both measurements the sample was aligned within 10 degrees of the platform edge.

The $PbMo_6S_8$ sample was measured at 300 mK, 2 K, 4.2 K, 6 K, 8 K and 12 K at the reversible angle, with the platform at 0°. The voltage vs. field sweep loops for 2 K, 8 K and 12 K are similar to the other temperatures' data (figs 6.2). For the $PbMo_6S_8$ the magnitude of the hysteresis in the voltage vs. field sweep loops increased as the field gradient increased (fig 6.2a). The voltage vs. field sweep loops for the 1 mm length NbTi wire sample are in section 5.6 (figs 5.28). The calibration constant for the chip which measured the $PbMo_6S_8$ and the NbTi wire samples was 2.22 x 10^4 Ω(Nm)$^{-1}$.

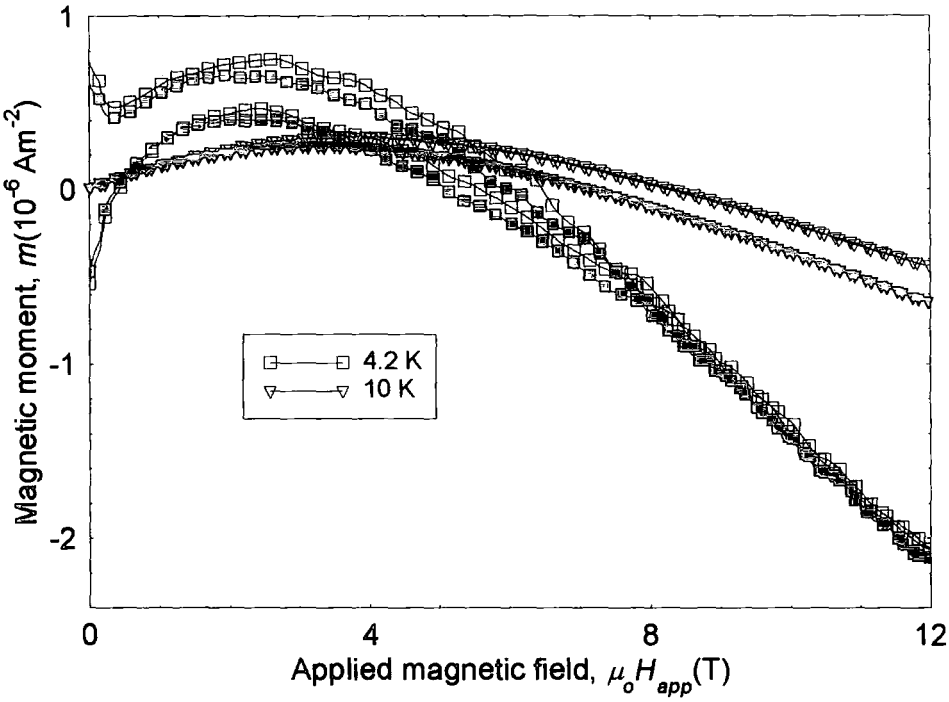

Figure 6.3. Magnetic moment of the 150 μm ∅ $Pb_{0.75}Eu_{0.25}Mo_6S_8$ sample as a function of magnetic field $(\mu_o H_{app})$ and temperature measured on the VSM. The open shapes denote the magnetic field parallel to the long axis, and the closed shapes denote the magnetic field perpendicular to the long axis.

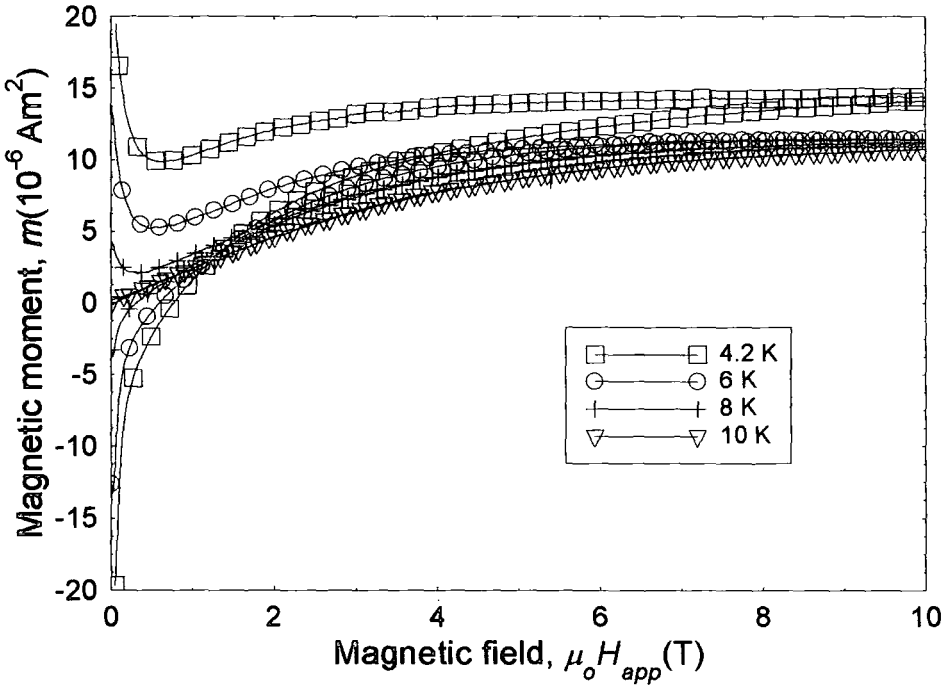

Figure 6.4. Magnetic moment of the 300 μm ∅ $Pb_{0.75}Eu_{0.25}Mo_6S_8$ sample as a function of magnetic field $(\mu_o H_{app})$ and temperature measured on the VSM. The magnetic field was perpendicular to the long axis.

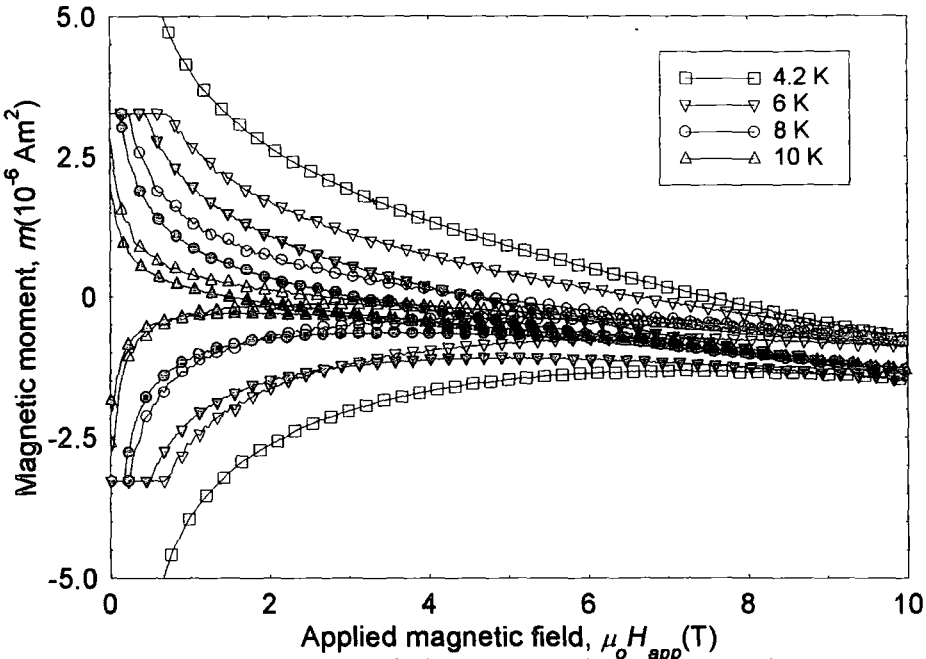

Figure 6.5. Magnetic moment of the 1 mm $PbMo_6S_8$ sample, as a function of magnetic field $\left(\mu_o H_{app}\right)$ and temperature. The open shapes represent the field parallel to the long axis, and the closed shapes represent the field perpendicular to the long axis. The 4.2 K perpendicular moment data are not plotted on the figure.

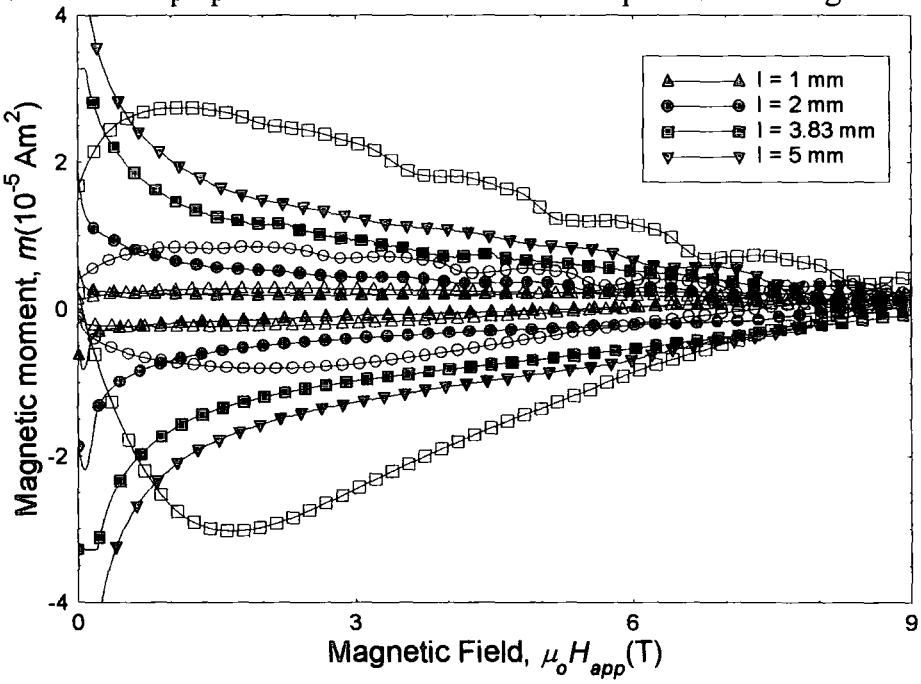

Figure 6.6. Magnetic moment of NbTi wire as a function of magnetic field, at 4.2 K, measured using the VSM. The samples lengths were 1 mm (upwards triangle), 2 mm (circle), 3.83 mm (square), and 5 mm (downwards triangle). The open shapes represent the field parallel to the long axis, and the closed shapes represent the field perpendicular to the long axis.

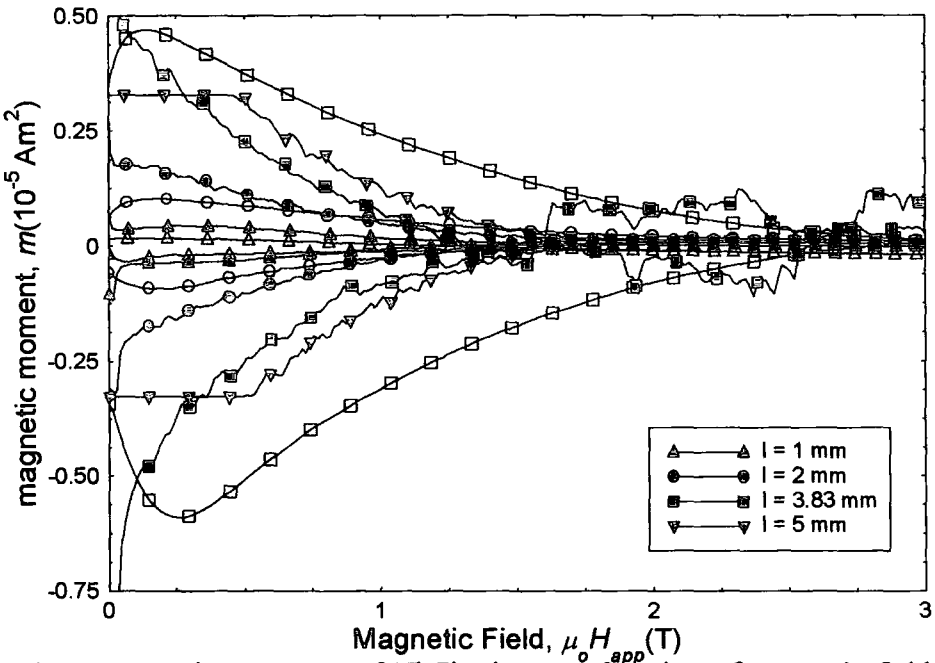

Figure 6.7. Magnetic moments of NbTi wire as a function of magnetic field at 8 K, measured using the VSM. The samples measured were 1 mm length (upwards triangle), 2 mm length (circle), 3.83 mm length (square), and 5 mm length (downwards triangle). The open shapes represent the field parallel to the long axis, and the closed shapes represent the field perpendicular to the long axis.

6.3.2 Vibrating sample magnetometer (VSM)

Using the VSM, the magnetic moments as a function of magnetic field $\left(\mu_o H_{app}\right)$ and temperature for $Pb_{0.75}Eu_{0.25}Mo_6S_8$, $PbMo_6S_8$, and NbTi wire were measured.

Three $Pb_{0.75}Eu_{0.25}Mo_6S_8$ samples were measured on the VSM. The 4 mm length sample (dimensions 2 x 1 x 4 mm^3) data are found in chapter 4, the 300 μm ∅ sample was only measured on the VSM (fig 6.4), while the 150 μm ∅ sample (fig 6.3) was also measured on the torque magnetometer. The magnetic moment of the 150 μm ∅ sample has the background moment of the VSM superimposed on top of the superconducting magnetic moment. For the 4 mm length $PbMo_6S_8$ sample, the results are found in chapter 4, (fig. 4.7). The 1 mm length $PbMo_6S_8$ sample was measured at 4.2 K, 6 K, 8 K and 10 K. For both field directions, the magnetic moments were almost symmetric about the *x*-axis (fig. 6.5). The drop below the *x*-axis at the higher fields was due to the background of the VSM (fig. 5.30). The 4.2 K perpendicular data were not plotted as the background changed during the measurement.

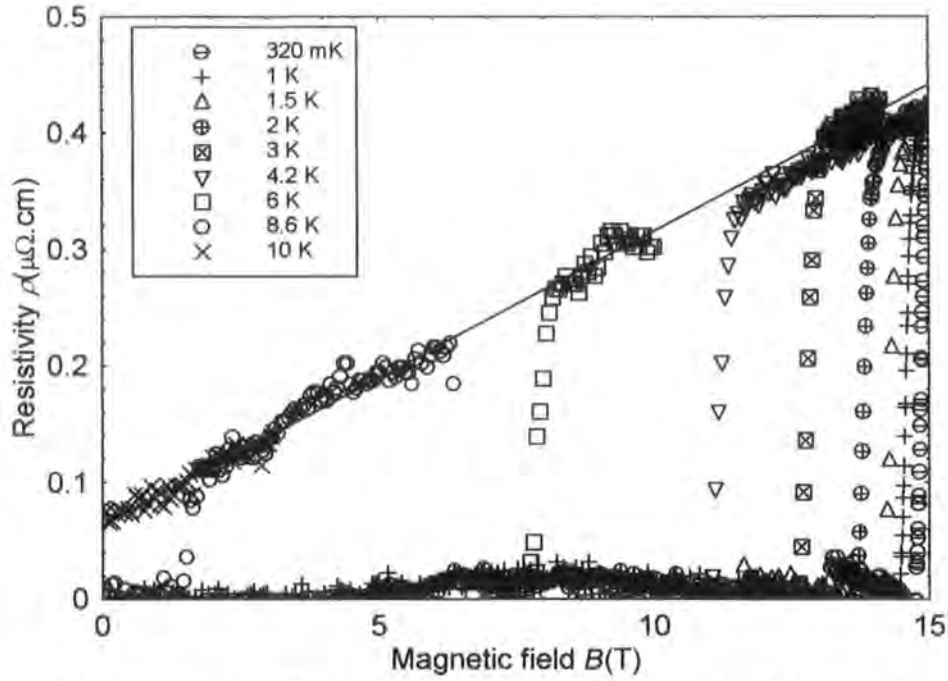

Figure 6.8. Resistivity of NbTi wire as a function of magnetic field and temperature, for $V_{app} = 0.1$ V. The wire was perpendicular to the magnetic field. The solid line is a linear fit to the normal state data.

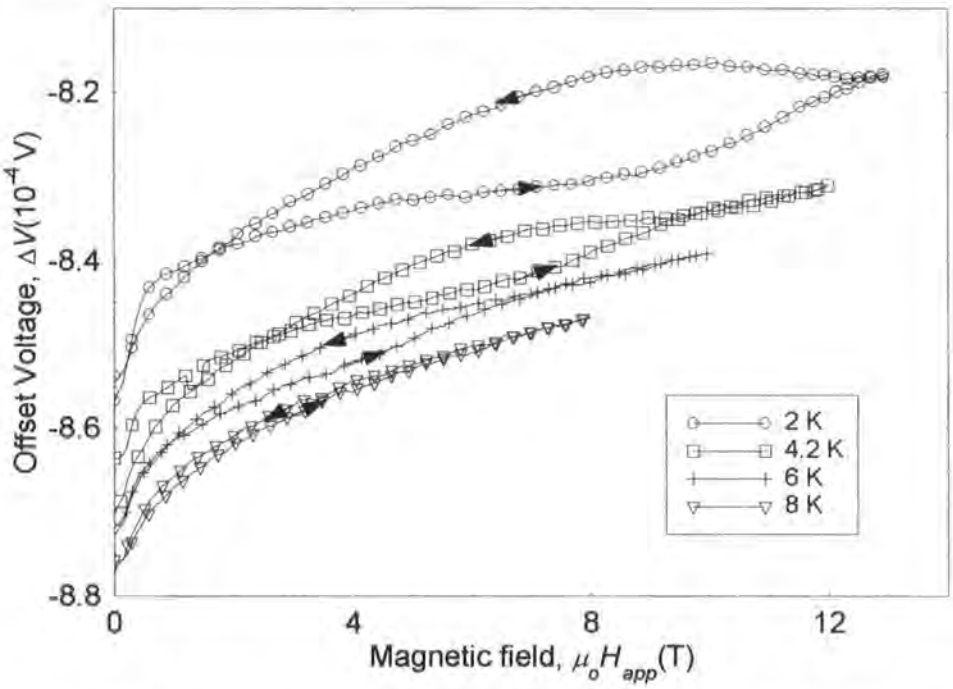

Figure 6.9. Voltage vs. field sweep loops of NbTi wire as a function of magnetic field $\left(\mu_o H_{app}\right)$ and temperature, at the field centre & 180 degrees. The voltage loops were offset along the y-axis, so the loops did not overlap. The arrows indicate the increasing or decreasing magnetic field, during the measurement.

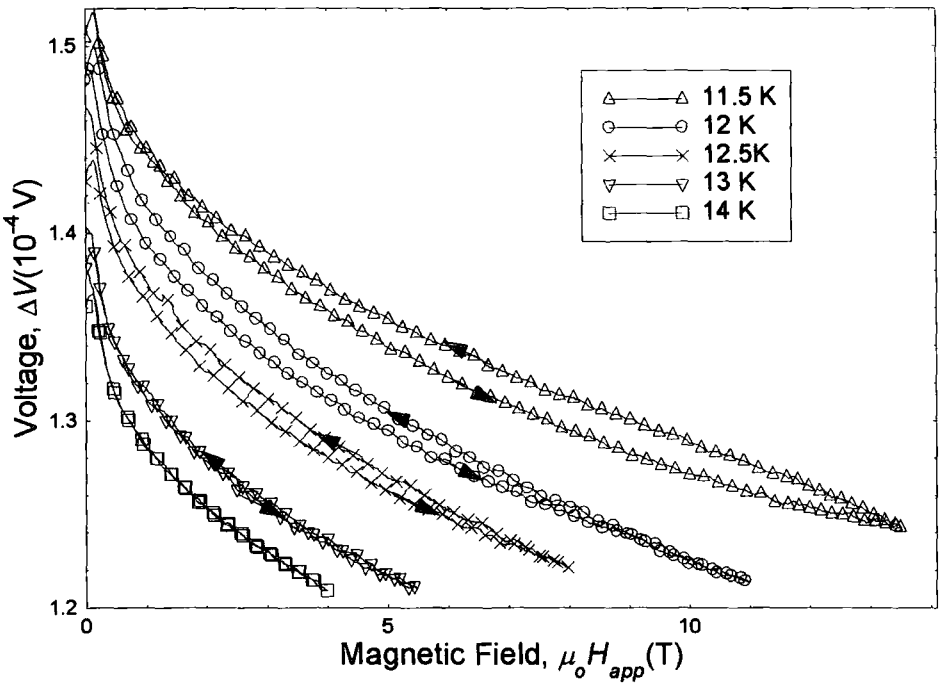

Figure 6.10. Voltage vs. field sweep loops of $PbMo_6S_8$ as a function of magnetic field $\left(\mu_o H_{app}\right)$ and temperature, at the field centre & 5 degrees. The voltage loops were offset along the y-axis, so the loops did not overlap. The arrows indicate the increasing or decreasing magnetic field, during the measurement.

The 1 mm length NbTi wire sample VSM data are in chapter 5 (fig. 5.29). The other three NbTi wire samples were measured at 4.2 K and 8 K to check the consistency of the critical current density (figs. 6.6 & 6.7). The 5 mm length NbTi wire sample was measured with the field perpendicular to the long axis only. The magnetic moments of the NbTi wire samples with the field perpendicular to and parallel to the long axis, have different field dependencies. The magnetic moments hysteresis loops for the field perpendicular to the long axis were symmetric about the *x*-axis. As the length of the NbTi wire increased, the magnetic moments increased as expected (figs. 6.6 & 6.7).

6.3.3 Upper critical field, $B_{c2}(0)$

The torque magnetometer was also used to determine the upper critical field $\left(B_{c2}(T)\right)$ of the samples. The voltage vs. field sweep loops were measured at temperatures close to the critical temperature with the sample at the centre of the magnet.

For $PbMo_6S_8$, the temperatures measured at were 11.5 K, 12 K, 12.5 K, 13 K, and 14 K. The sample was measured at 5° from the reversible angle, hence the voltage vs. field sweep loops were non-reversible (fig. 6.10). This decreased the error for the upper critical field. The resistivity and magnetisation of the 4 mm length $PbMo_6S_8$ sample are presented in chapter 4[1] (fig. 4.4 & 4.7). For NbTi wire, the voltage loops measured at 180° were used, as the loops were non-reversible at $z = 0$ cm (fig. 6.9).

For the torque magnetometer data, the voltage vs. field sweep loops of NbTi wire and $PbMo_6S_8$ were offset along the y-axis, so the change in magnitude of the voltage hysteresis with temperature can be observed (figs. 6.9 & 6.10). From figs 6.9 & 6.10, the magnitude of the hysteresis in the voltage vs. field sweep loops decreased as the temperature increased. The direction of the magnetic field during the measurement for each of the loops' legs was the same for all temperatures.

For the NbTi wire, the resistivity as a function of magnetic field and temperature was measured (fig. 6.8). The upper critical field $B_{c2}^{0.5\rho_N}(T)$ of the NbTi wire, at 300 mK is 14.8 T. The normal state resistivity of NbTi wire has a linear dependence with field.

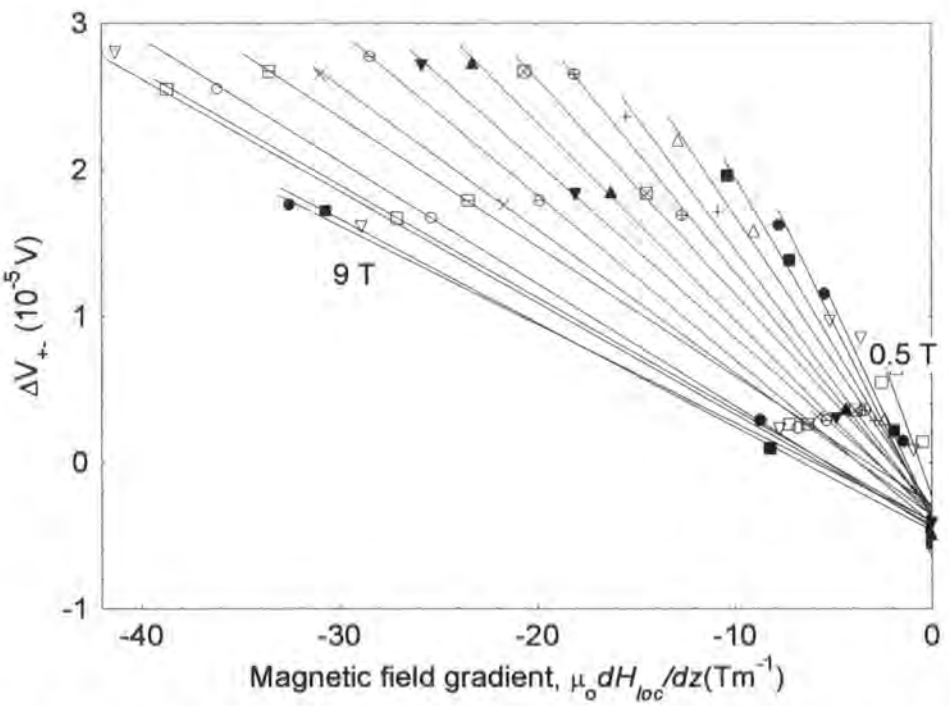

Figure 6.11. Difference in voltage across the voltage vs. field sweep loops (ΔV_{+-}) for $Pb_{0.75}Eu_{0.25}Mo_6S_8$ as a function of local magnetic field (H_{loc}) and magnetic field gradient, at 4.2 K. The solid lines are the best-fit lines through the data.

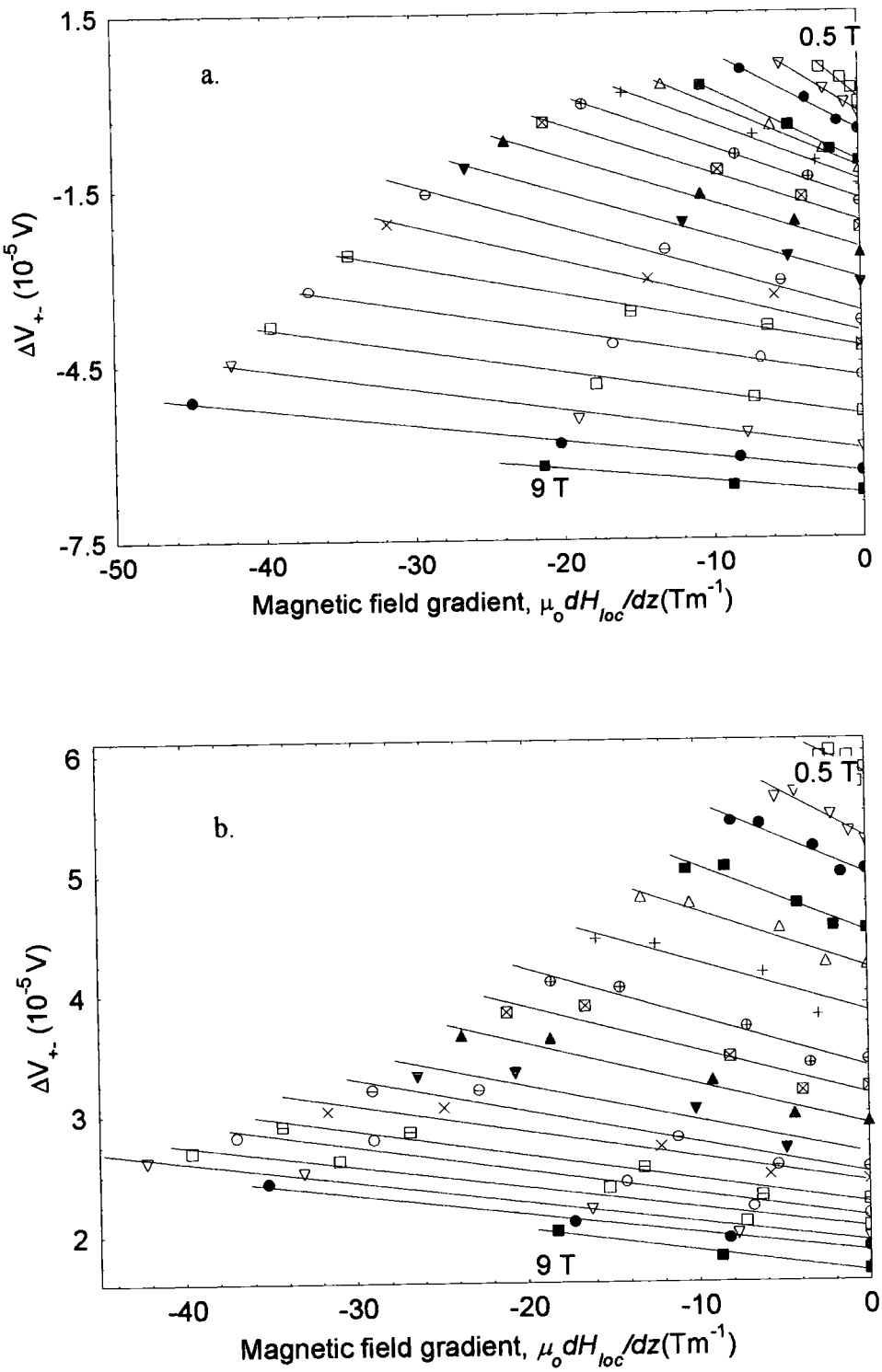

Figure 6.12. Difference in voltage across the voltage vs. field sweep loops (ΔV_{+-}) for $Pb_{0.75}Eu_{0.25}Mo_6S_8$ as a function of magnetic field gradient and local magnetic field, at (a) 5 K and (b) 6 K. The field lines are offset by $\Delta V_{+-} = (0.5\times10^{-5}\mu_o H_{loc})$ where $(\mu_o H_{loc})$ is the magnetic field for the line. The solid lines are the best-fit lines through the data.

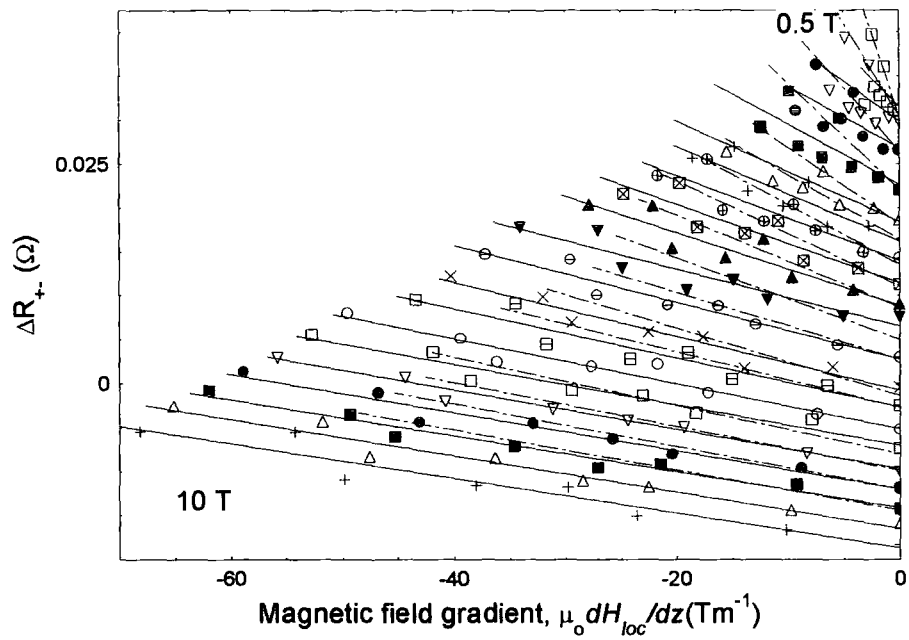

Figure 6.13a. Difference in resistance across the field sweep loop, (ΔR_{+-}) of $PbMo_6S_8$ as a function of magnetic field gradient and local magnetic field, at 0°, 300 mK. The field lines are offset by $\Delta V_{+-} = (0.5\times10^{-5}\mu_o H_{loc})$, where $(\mu_o H_{loc})$ is the magnetic field. The solid lines are the best-fit lines through all the data. The dashed lines are the best-fit lines through the z = 0, 2.5, 4.5, & 6 cm ΔR_{+-} points.

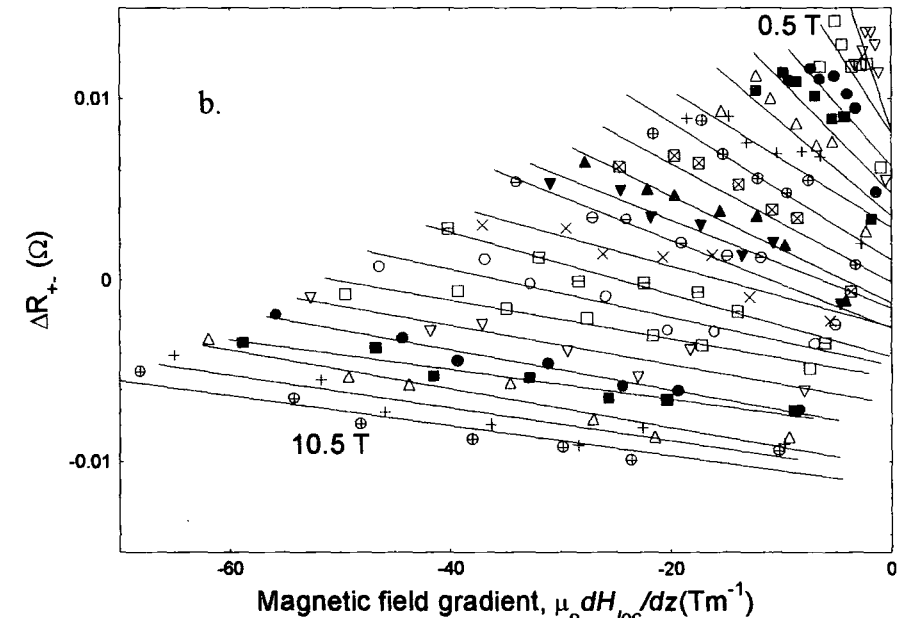

Figure 6.13b. Difference in resistance across the field sweep loop, (ΔR_{+-}) of $PbMo_6S_8$ as a function of magnetic field gradient and local magnetic field, at 0°, 4.2 K. The field lines are offset by $\Delta V_{+-} = (0.5\times10^{-5}\mu_o H_{loc})$, where $(\mu_o H_{loc})$ is the magnetic field for the line. The solid lines are the linear best-fit for the data. The data at z = 0 cm are not plotted on the figure.

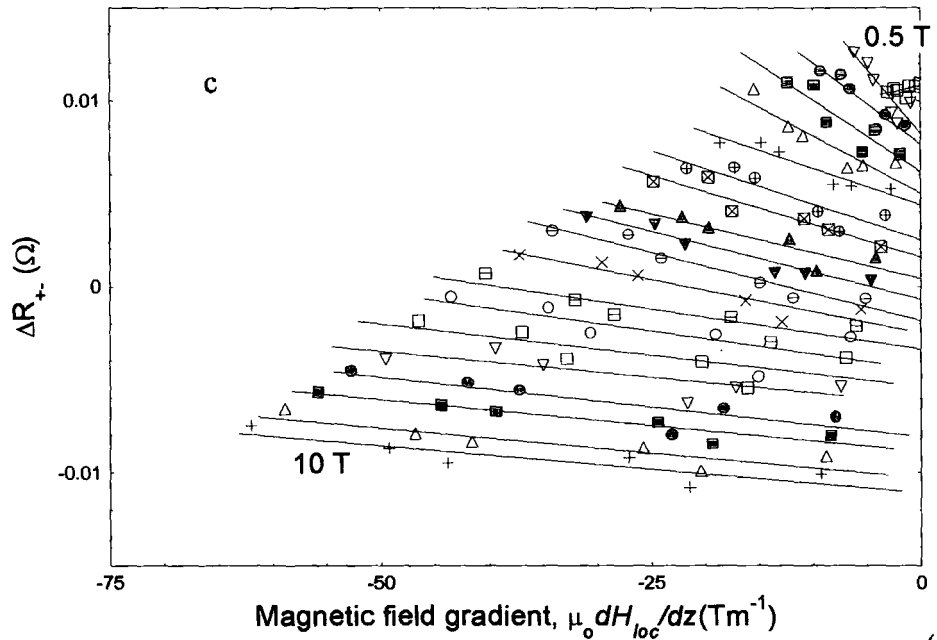

Figure 6.13c. Difference in resistance across the field sweep loop, (ΔR_{+-}) of $PbMo_6S_8$ as a function of magnetic field gradient and local magnetic field, at 0°, 8 K. The field lines are offset by $\Delta V_{+-} = (0.5\times10^{-5}\mu_o H_{loc})$, where $(\mu_o H_{loc})$ is the magnetic field for the line. The solid lines are the linear best-fit for the data. The data at z = 0 cm are not plotted on the figure.

6.4 Analysis

6.4.1 Field-gradient torque magnetometer

6.4.1.1 ΔR_{+-} vs. field gradient

The critical current density of an isotropic superconductor measured at the reversible angle using the torque magnetometer is given by eqn 3.24, using the shape factor $\gamma_{sf} = \frac{4a}{\pi}\left[1-\frac{a}{3h}\right]$. As described in chapter 5, the critical current densities were determined using the LABview programs jccal.vi and gradcal.vi (appendix 3). For each temperature, he difference in resistance across the field sweep loop (ΔR_{+-}) was plotted as a function of local magnetic field gradient $\mu_o\left(\frac{dH_{loc}}{dz}\right)$ and magnetic field. In the figs. 6.12 & 6.13, the data lines are offset along the ΔR_{+-} axis, so they do not overlap, and the splaying out due to the increase of magnetic field is observed.

For $Pb_{0.75}Eu_{0.25}Mo_6S_8$, ΔV_{+-} was calculated rather than ΔR_{+-}, as a function of magnetic field gradient and local magnetic field, as the current through the

Wheatstone bridge was not measured. For the later measurements on NbTi wire and $PbMo_6S_8$, the current through the bridge was measured. Hence if there was a change in current, it could be accounted for by taking the ΔR_{+-} across the loops rather than the ΔV_{+-}. The current changed by less than 1.5 % during a field sweep. The 8 K data had a similar ΔV_{+-} vs. field gradient graph. For fig 6.11, the lines were not offset as the $z = 0$ cm loop was reversible.

For the $PbMo_6S_8$ data (figs. 6.13b & c), the $z = 0$ cm ΔR_{+-} points are not plotted on the graphs, as the $z = 0$ cm ΔR_{+-} data were larger than the $z = 2.5$ cm and $z = 4$ cm ΔR_{+-} data. In fig. 6.13a, all the loops ΔR_{+-} are plotted as a function of magnetic field and field gradient at 300 mK. There are two distinct gradients for each field below 4 T. The first gradient is through the $z = 0$, 2.5, 4.5 and 6 cm ΔR_{+-} points (dashed lines on fig. 6.13a), and the other gradient is through every heights' ΔR_{+-} data (solid line on fig. 13a). Above 4 T, the two different gradients are less distinct, thus one line through all the heights' ΔR_{+-} data can be taken. The ΔR_{+-} vs. field gradient graphs for the NbTi wire sample are in section 5.7 (figs. 5.33).

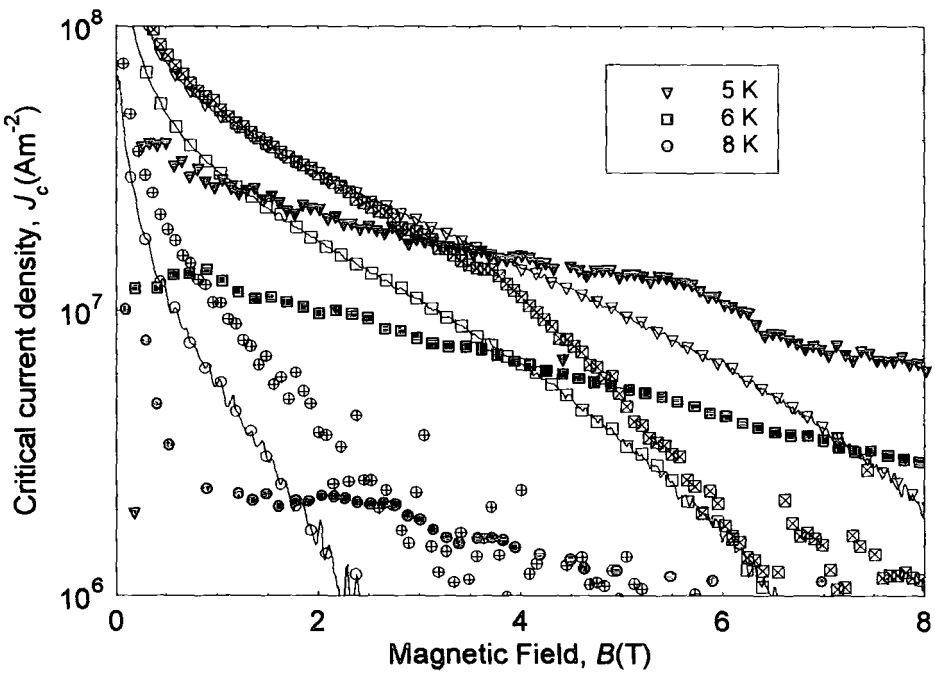

Figure 6.14. Critical current density of $Pb_{0.75}Eu_{0.25}Mo_6S_8$ as a function of magnetic field and temperature. The closed shapes are the 150 μm ∅ torque data, the open shapes are the 4 mm samples' VSM data, and the shapes with crosses inside are the 300 μm ∅ samples' VSM data. The 300 μm ∅ sample was not measured at 5 K.

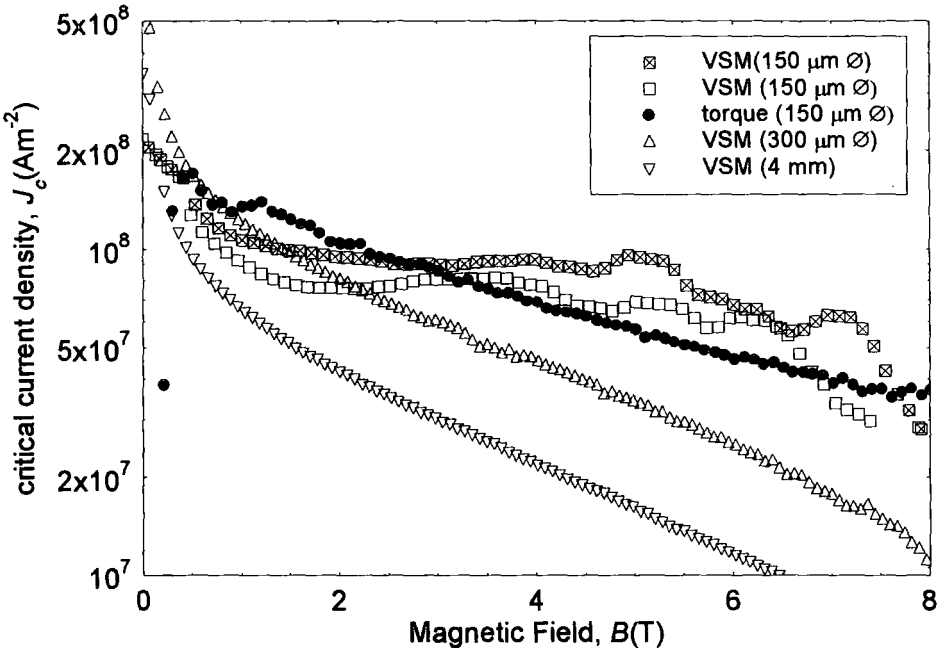

Figure 6.15. Critical current density of $Pb_{0.75}Eu_{0.25}Mo_6S_8$ as a function of magnetic field and experiment, at 4.2 K. For the VSM data the open shapes denote the field perpendicular to the long axis, and the shapes with the cross inside denote the field parallel to the long axis.

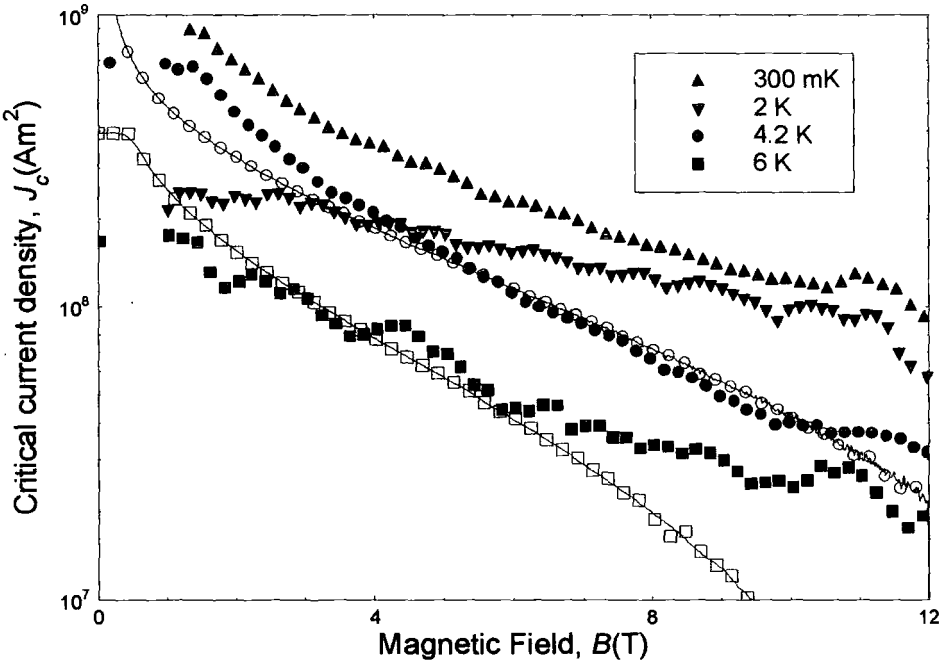

Figure 6.16. Critical current density of $PbMo_6S_8$, as a function of magnetic field and temperature. The open shapes are the VSM data and the closed shapes are the torque data. The 8 K data were the measured background for the sample, so the data were subtracted away from the other temperature critical current densities.

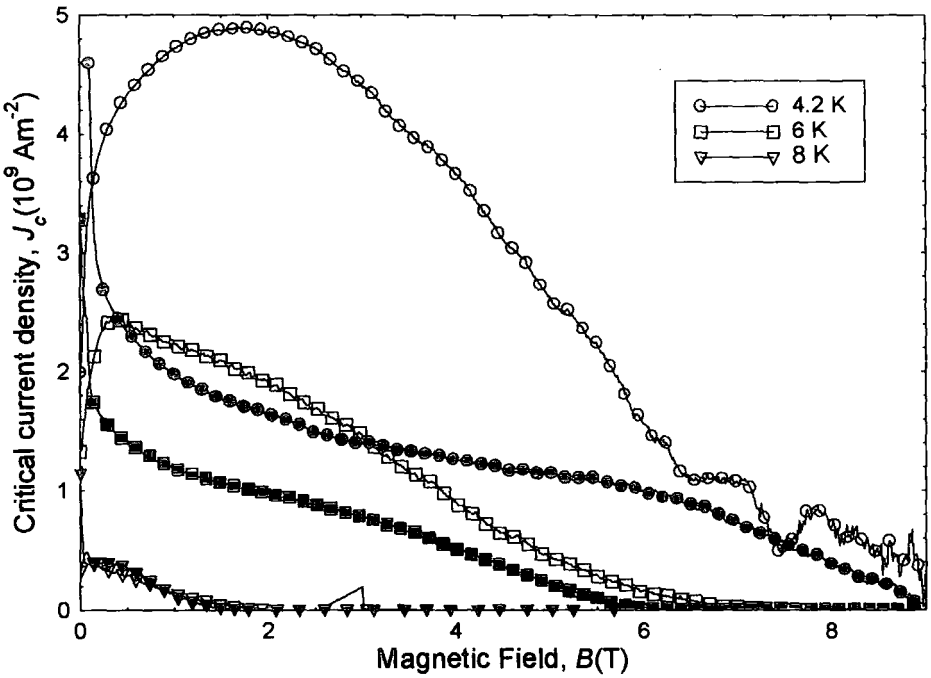

Figure 6.17. Critical current density of the 1 mm length NbTi wire sample, as a function of magnetic field and temperature, measured using the VSM. The open shapes are for the magnetic field parallel to the long axis, and the closed shapes are for the magnetic field perpendicular to the long axis.

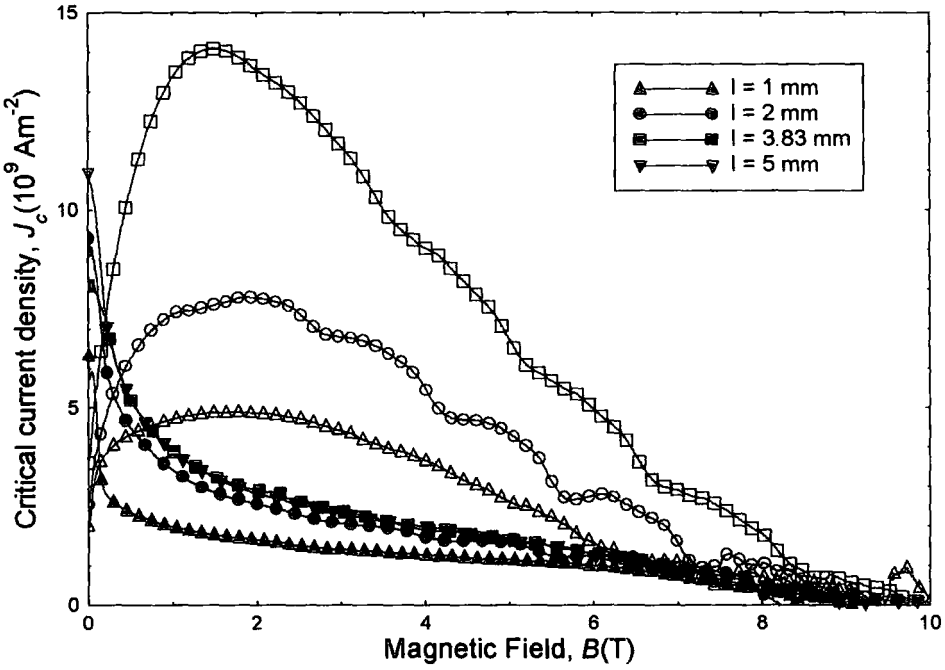

Figure 6.18. Critical current density of NbTi wire, as a function of magnetic field and direction of the magnetic field to the long axis at 4.2 K, measured using the VSM. The samples measured were 1 mm (upwards triangle), 2 mm length (circle), 3.83 mm length (square), and 5 mm length (downwards triangle). The open shapes are for the magnetic field parallel to the long axis, and the closed shapes are for the magnetic field perpendicular to the long axis.

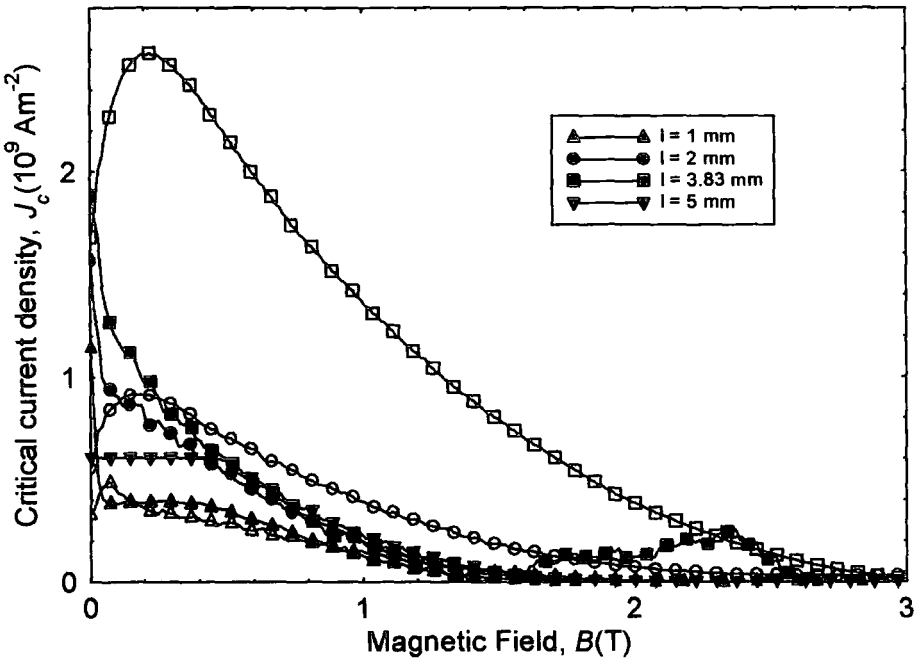

Figure 6.19. Critical current density of NbTi wire, as a function of magnetic field, and direction of the magnetic field to the long axis at 8 K, measured using the VSM. The sample lengths were 1 mm (upwards triangle), 2 mm (circle), 3.83 mm square, and 5 mm (downwards triangle). The open shapes are for the field parallel to the long axis, and the closed shapes are for the field perpendicular to the long axis.

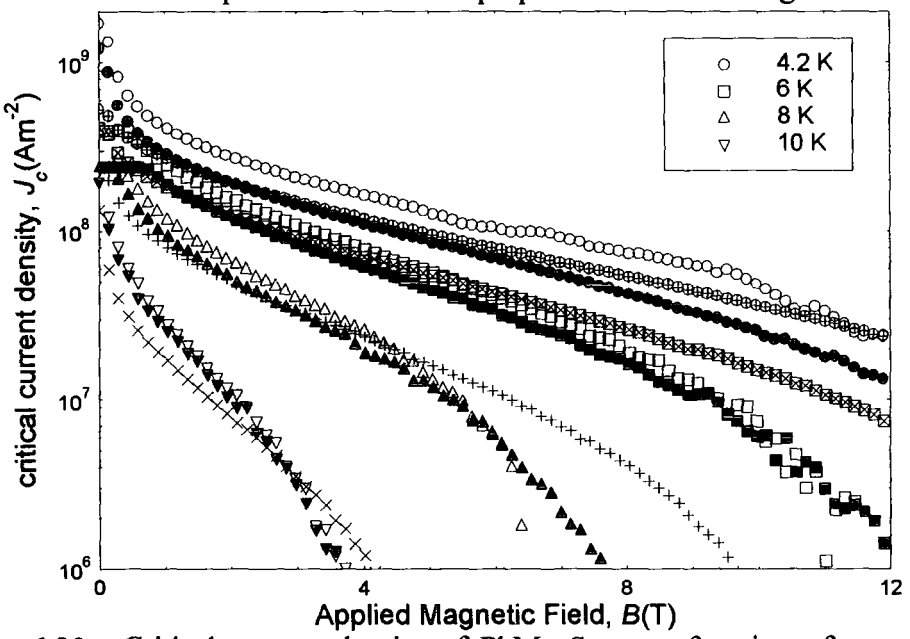

Figure 6.20. Critical current density of $PbMo_6S_8$, as a function of magnetic field, temperature and direction of the magnetic field to the long axis, measured using the VSM. The open shapes are for the magnetic field parallel to the long axis of the 1 mm length sample, and the closed shapes are for the magnetic field perpendicular to the long axis of the 1 mm length sample. The shapes with crosses are for the 4 mm length sample.

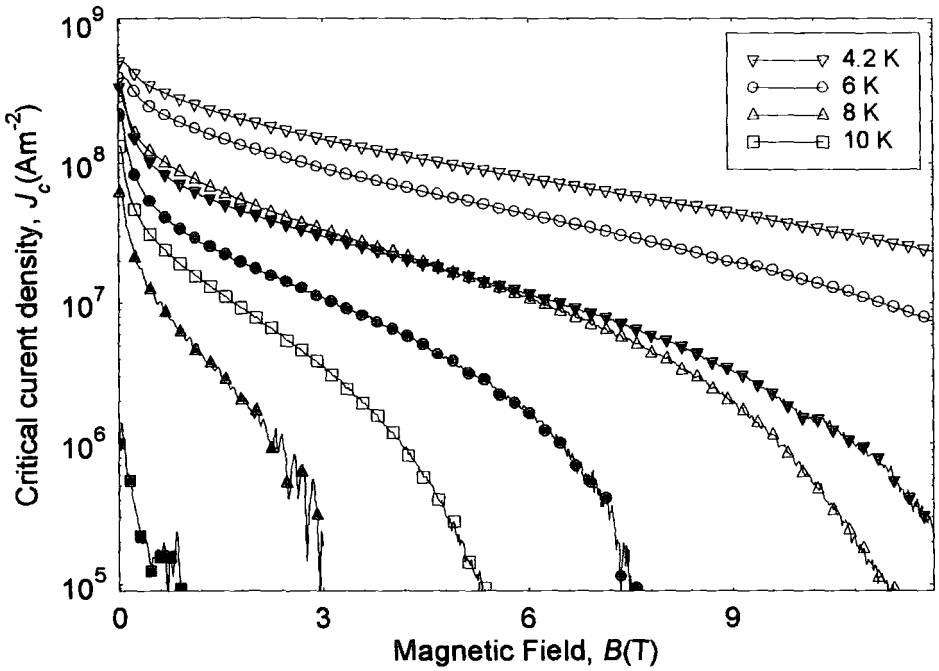

Figure 6.21. Critical current densities of $(Pb_{1-x}Eu_x)Mo_6S_8$ with $x = 0.0$ (open shapes) and $x = 0.25$ (closed shapes), as a function of magnetic field and temperature.

6.4.1.2 Critical current density

The initial torque J_c^{τ} were determined for $Pb_{0.75}Eu_{0.25}Mo_6S_8$ at 0°, as if the sample was at the reversible angle. J_c^{τ} has the same order of magnitude as the 300 μm ∅ and the 4 mm length $Pb_{0.75}Eu_{0.25}Mo_6S_8$ VSM critical current densities but have different field dependencies (fig. 6.14). For the measurement at the reversible angle and 4.2 K, the torque critical current density has the same order of magnitude and similar field dependence as the VSM critical current density for the 300 μm ∅ sample (fig. 6.15). At 10 K, the voltage vs. field sweep loops were reversible, so no background moment was subtracted from the torque data.

The torque critical current densities of $PbMo_6S_8$ have similar field dependence for all temperatures except for 2 K (fig. 6.16). For the $PbMo_6S_8$ data, the 12 K and 8 K critical current densities were similar in magnitude, thus the 8 K data were taken to be the background of the experiment. $J_c^{\tau}(8K)$ was subtracted away from the other temperatures' critical current densities. The 300 mK J_c^{τ} was determined from the dashed lines in fig. 6.13a.

The critical current densities of NbTi wire measured using the torque magnetometer have the similar field dependence for all temperatures (fig. 5.39). At 7 T, the 4.2 K and 2 K have the same magnitude of critical current density. At 10 K, the NbTi wire

data were reversible, so no background J_c was subtracted away from the other temperatures' data.

6.4.2 Vibrating sample magnetometer

6.4.2.1 Critical current density, J_c

The critical current densities for the VSM data were determined from Bean's model[2] (eqn 2.33). The shape factors for a cylindrical sample with the field parallel to the long axis and perpendicular to the long axis are in section 3.7.3. The measured background magnetic moment of the VSM (fig. 5.30) was subtracted away from the samples' magnetic moments measured on the highest amplification of the VSM.

For the NbTi wire and $PbMo_6S_8$ samples measured using the VSM, the critical current density for the magnetic field parallel to the long axis $\left(J_{c\parallel}\right)$, has a different field dependence compared with the critical current density for the magnetic field perpendicular to the long axis $\left(J_{c\perp}\right)$ (figs. 6.17–6.20).

At 4.2 K, the NbTi wire moment data has oscillations in due to fluctuations in the VSM temperature. The magnitude of the 1mm length NbTi wire critical current density was 70 % of the magnitude of the 5 mm length J_c^{VSM}, at 4.2 K (fig. 6.18).

The critical current densities of the 1 mm length $PbMo_6S_8$ sample for both field directions have different field dependence compared with the 4 mm length sample (fig. 6.20). For the $Pb_{0.75}Eu_{0.25}Mo_6S_8$ 4 mm length and the 300 μm ∅ samples, the VSM critical current densities have different field dependencies at 6 K, but almost the same irreversibility field (fig. 6.14). For the 150 μm ∅ sample, the VSM critical current density is unreliable after 2 T, due to the noise on the signal (fig. 6.15).

From figs 4.7, the critical current densities of the 4 mm bulk $PbMo_6S_8$ and $Pb_{0.75}Eu_{0.25}Mo_6S_8$ sample were determined (fig. 6.21). The $PbMo_6S_8$ sample J_c^{VSM} was a factor 5 larger than the $Pb_{0.75}Eu_{0.25}Mo_6S_8$ J_c^{VSM}. Both samples have similar field dependence.

6.4.2.2 Average Magnetisation of the 1 mm length NbTi wire

The VSM average magnetisation data of the 1 mm length NbTi wire were determined by adding the magnetic moment across the hysteresis loops at each field to give the average moment (fig. 6.6). The average moments were then divided by the volume of

the sample $\left(M = \frac{m}{vol}\right)$. From fig. 6.22, the gradient $\left(\frac{dM}{dB}\right)$ of the solid lines through the linear region data close to $B_{c2}(T)$ were determined. Also from fig. 6.22, the upper critical field ($B_{c2}(T)$) was taken to be the field at which the average magnetisation was zero.

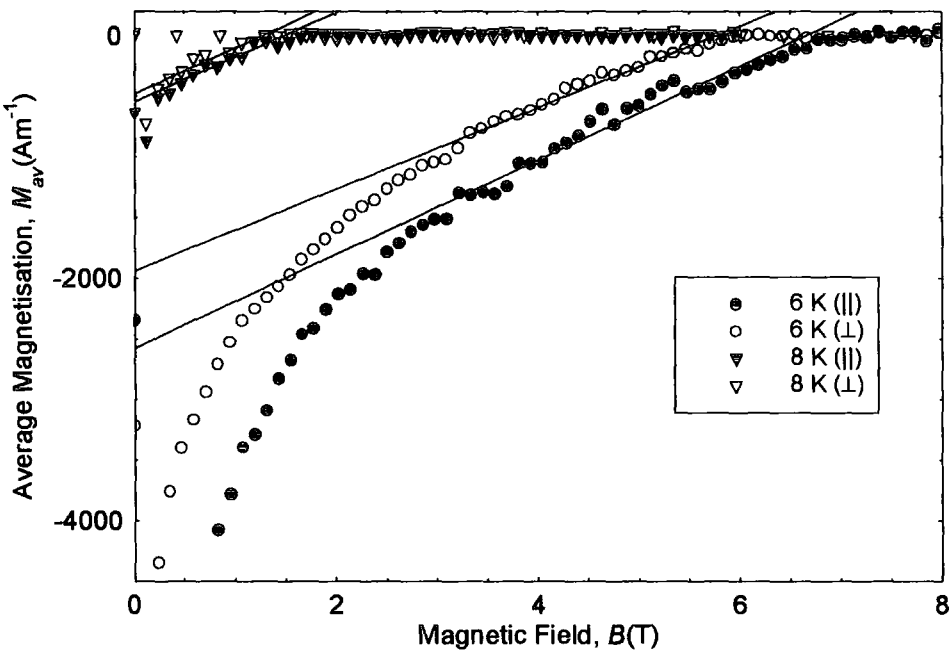

Figure 6.22. Average magnetisation of 1 mm length NbTi wire as a function of magnetic field and temperature. The solid lines are the best-fit lines for the magnetisation region close to the upper critical field. The symbol || and ⊥ represent the field parallel to and perpendicular to the long axis of the sample respectively.

	T_c (K)	$B_{c2}(0)$ (T)	κ	$B_c(0)$ (T)	$B_{c1}(0)$ (T)	$\xi(0)$ (nm)	$\lambda(0)$ (nm)
NbTi (||)	9.0	13	30	0.52	0.031	4.32	131
NbTi (⊥)	8.7	13.3	32	0.51	0.023	4.3	135

Table 6.1. The critical parameters ($B_{c2}(0)$, $B_c(0)$, $B_{c1}(0)$, $\xi(0)$ & $\lambda(0)$) of NbTi 1 mm length wire, for the magnetic field parallel (||) to and perpendicular (⊥) to the long axis.

For each field direction to the long axis of the 1 mm length NbTi wire sample, κ was determined from Abrikosov equation (cf. eqn 2.28):

$$\mu_o\left(\frac{dM}{dB}\right) = \frac{1}{\beta_A\left(2\kappa^2 - 1\right)} \tag{6.1}$$

where β_A is the Abrikosov constant and κ is the GL parameter. Using $B_{c2}(0)$, κ and the GL equations (eqn 4.5 – 4.10), the lower critical field $B_{c1}(0)$, thermodynamic critical field $B_c(0)$, coherence length $\xi(0)$, and penetration depth $\lambda(0)$, of the 1 mm length NbTi wire sample were determined for the field parallel and perpendicular to the long axis.

The average magnetisations for the field parallel to and perpendicular to the long axis have similar field dependence (fig. 6.22). The 8 K data for both field directions to the long axis were the same order of magnitude. The perpendicular field data at 6 K had a similar shape curve to the parallel field data. The 4.2 K average magnetisation was not plotted, due to the oscillations in the data. From table 6.1, both field directions are in good agreement for the fundamental parameters of NbTi wire.

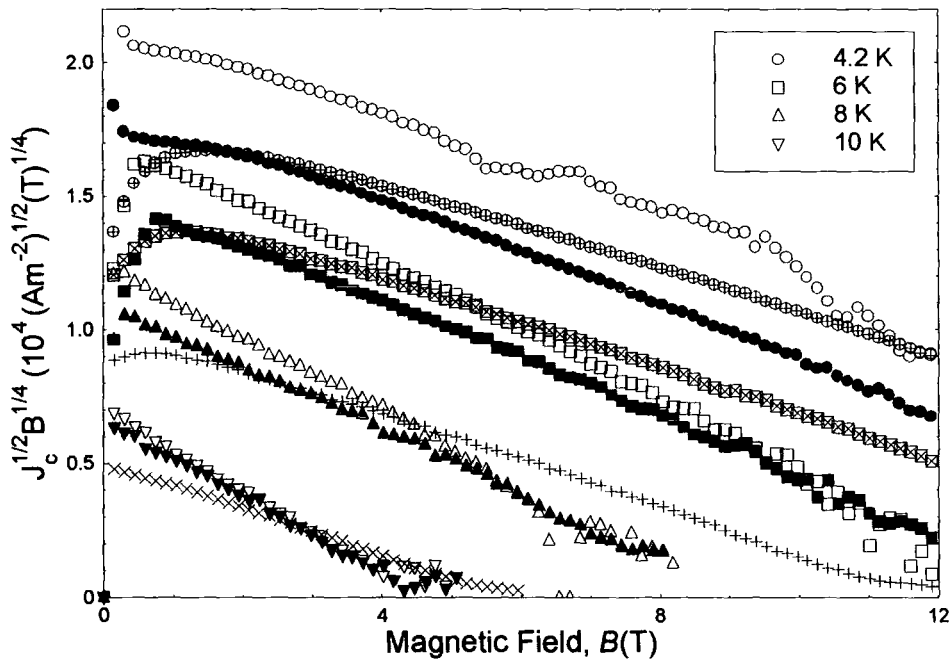

Figure 6.23. Kramer plots $\left(J_c^{1/2}B^{1/4}\right)$ for $PbMo_6S_8$, as a function of magnetic field and temperature measured using the VSM. The open shapes are for the 1 mm length sample with the field parallel to the long axis and the closed shapes are for the 1 mm length sample with the field perpendicular to the long axis. The shapes with crosses inside and the crossed shapes are for the 4 mm length sample.

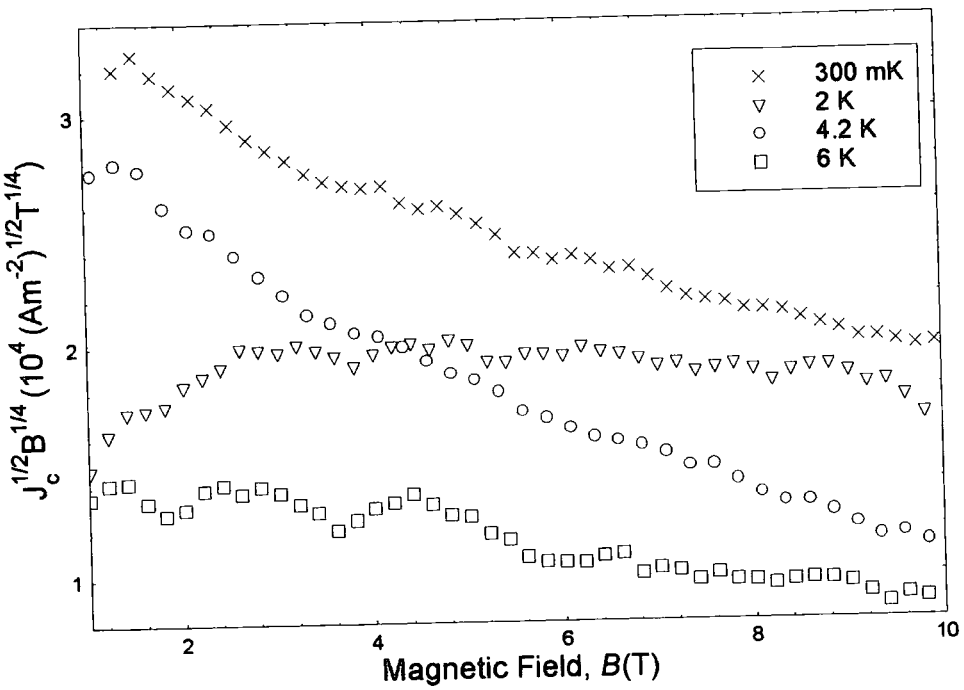

Figure 6.24. Kramer plots $\left(J_c^{1/2}B^{1/4}\right)$ for $PbMo_6S_8$ as a function of magnetic field and temperature, for the 1 mm length sample measured using the torque magnetometer.

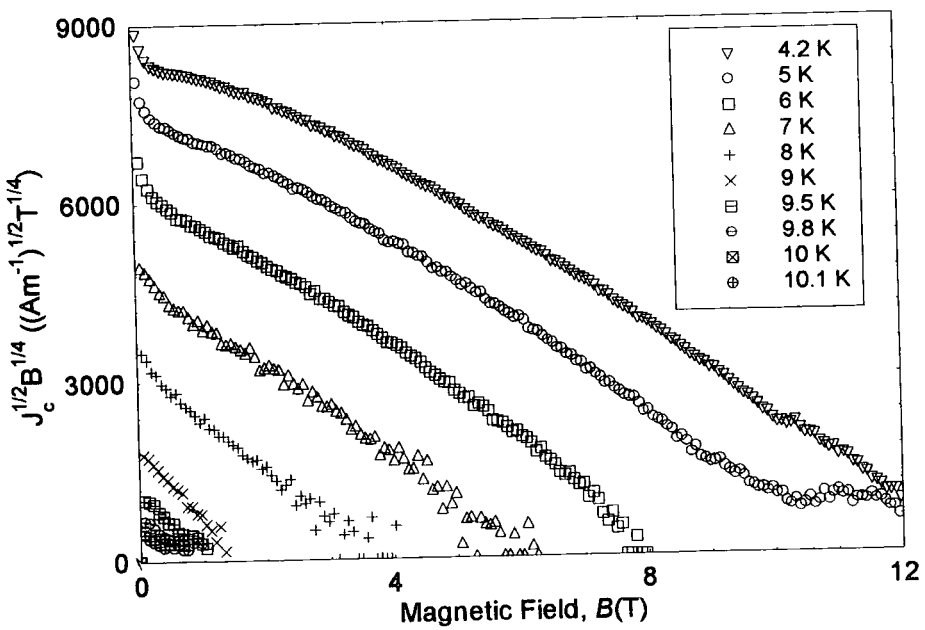

Figure 6.25. Kramer plot $J_c^{1/2}B^{1/4}$, as a function of magnetic field and temperature, for the 4 mm bulk $Pb_{0.75}Eu_{0.25}Mo_6S_8$ sample.

	B_{irr} at 4.2 K (T)	B_{irr} at 6 K (T)	B_{irr} at 8 K (T)
4 mm length sample VSM	24.2 ± 0.1	18.7 ± 0.03	12.1 ± 0.03
1 mm length sample VSM (⊥)	19.2 ± 0.1	14.2 ± 0.02	9.1 ± 0.04
1 mm length sample VSM (∥)	21.7 ± 0.04	13.8 ± 0.03	8.8 ± 0.03
1 mm length sample torque	19.8 ± 0.2	18.0 ± 0.9	-

Table 6.2. Table of the irreversibility fields (B_{irr}) of the different size $PbMo_6S_8$ samples, measured using the VSM and the torque magnetometer. The irreversibility fields were determined from Kramer plots where $J_c^{1/2}B^{1/4} = 0$. The errors were determined from standard error analysis.

6.4.3 Irreversibility fields, B_{irr}

For the $PbMo_6S_8$ data measured on both magnetometers and the 4 mm bulk $Pb_{0.75}Eu_{0.25}Mo_6S_8$ sample measured on the VSM , the Kramer scaling law[3] $\left(J_c^{1/2}B^{1/4}\right)$ against magnetic field were plotted (figs 6.23 - 6.25). For each temperature, the irreversibility field (B_{irr}) (cf. section 2.7.2) was determined from the equation:

$$J_c^{1/2}B^{1/4} = \alpha_K\left(B_{irr} - B\right) \qquad (6.2)$$

where α_K is a constant. The irreversibility field is the field at which the critical current density is zero. For the torque data and the VSM data, B_{irr} was determined from the Kramer plots, by fitting a straight line through the data at each temperature.

The VSM 1 mm length $PbMo_6S_8$ sample data had different field dependence to the 4 mm length sample data (fig. 6.23). From fig. 6.24, the torque 300 mK and 4.2 K data have similar field dependence. From table 6.2, the B_{irr} of the 4 mm length VSM sample and the 1 mm length torque sample agree at 6 K. The torque B_{irr} is 18 T, which is 4 T larger than the B_{irr} of the 1 mm length VSM sample for both field directions. From fig. 6.23 & 6.25, the 4 mm bulk $PbMo_6S_8$ and $Pb_{0.75}Eu_{0.25}Mo_6S_8$ samples have straight lines for the Kramer plots, which are equidistant. NbTi does not have a reversible magnetisation region (fig. 6.22).

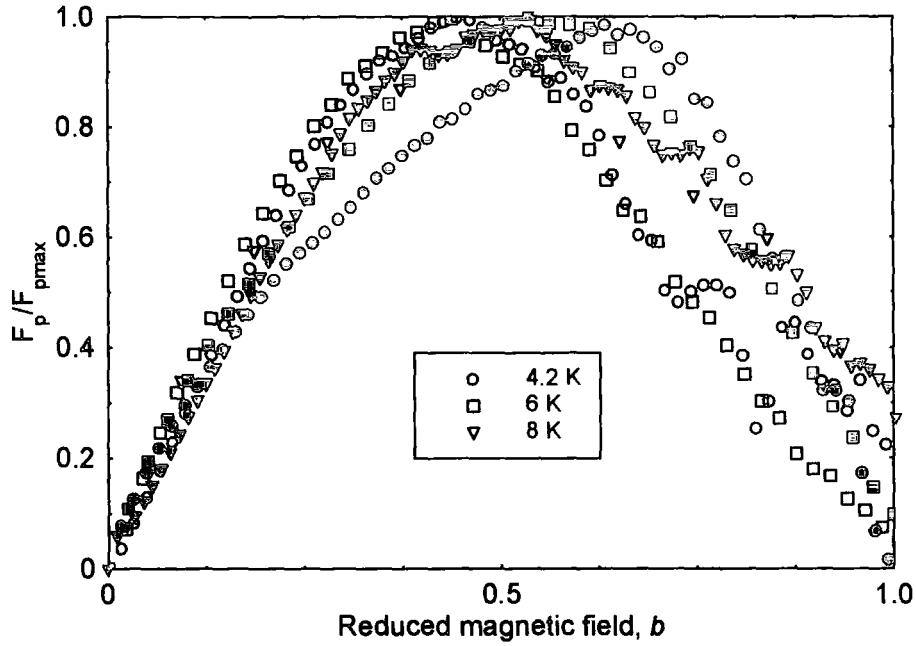

Figure 6.26. Normalised flux pinning force of the 1 mm length NbTi wire sample, as a function of reduced magnetic field, field direction to the long axis and temperature, measured using the VSM. The open shapes are for the field parallel to the long axis and the closed shapes are for the field perpendicular to the long axis.

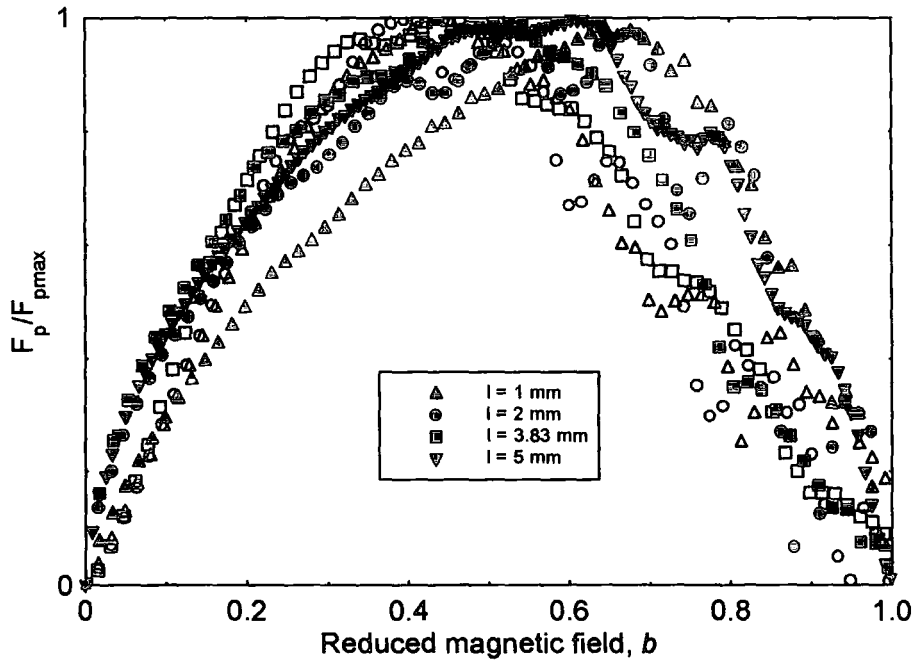

Figure 6.27. Normalised flux pinning force of NbTi wire, as a function of reduced field and field direction to the long axis, at 4.2 K. The sample lengths were 1 mm (upwards triangle), 2 mm (circle), 3.83 mm (square), and 5 mm (downwards triangle). The open shapes are for the field parallel to the long axis, and the closed shapes are for the field perpendicular to the long axis.

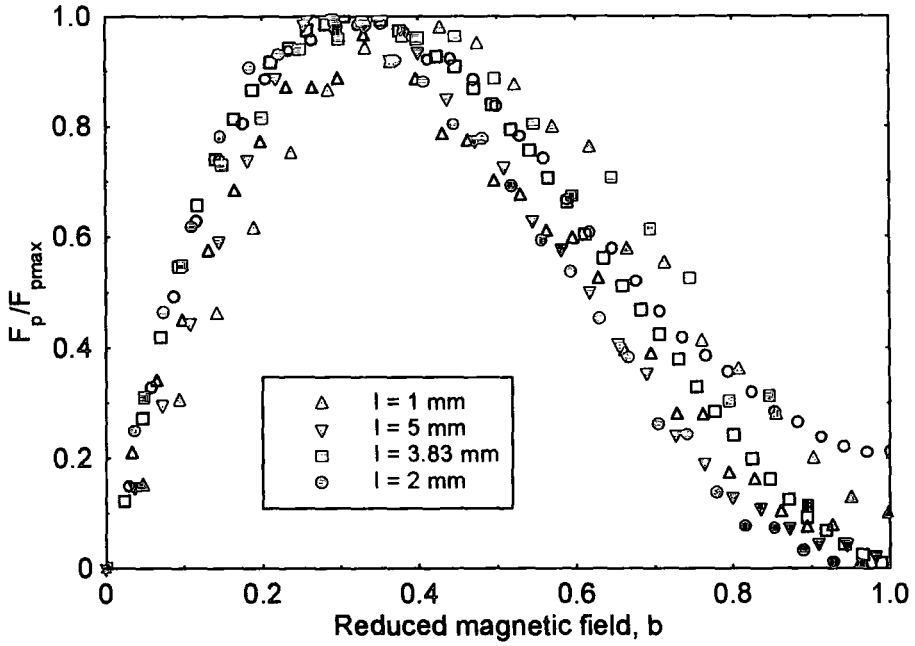

Figure 6.28. Normalised flux pinning force of NbTi wire, as a function of reduced field and field direction to the long axis, at 8 K. The sample lengths were 1 mm (upwards triangle), 2 mm (circle), 3.83 mm (square), and 5 mm (downwards triangle). The open shapes are for the field parallel to the long axis, and the closed shapes are for the field perpendicular to the long axis.

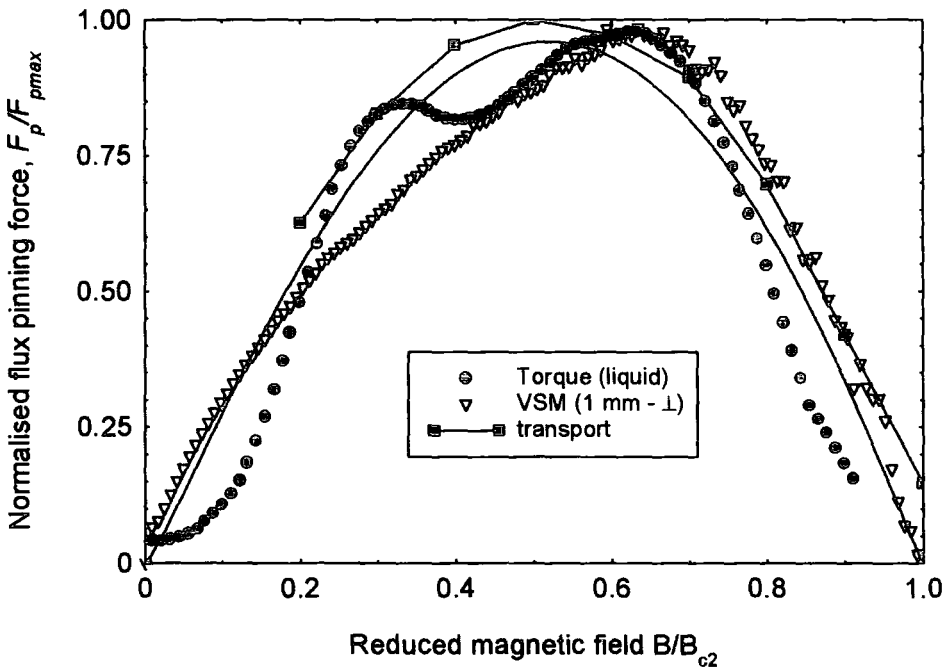

Figure 6.29. Normalised flux pinning force of the 1 mm length NbTi wire as a function of reduced magnetic field at 4.2 K. The solid line represents $F_p / F_{p\max} = \alpha_p(B_{c2}) b(1-b)$. C. Friend took the transport data[4]. The VSM, transport and torque data are taken from fig. 5.37.

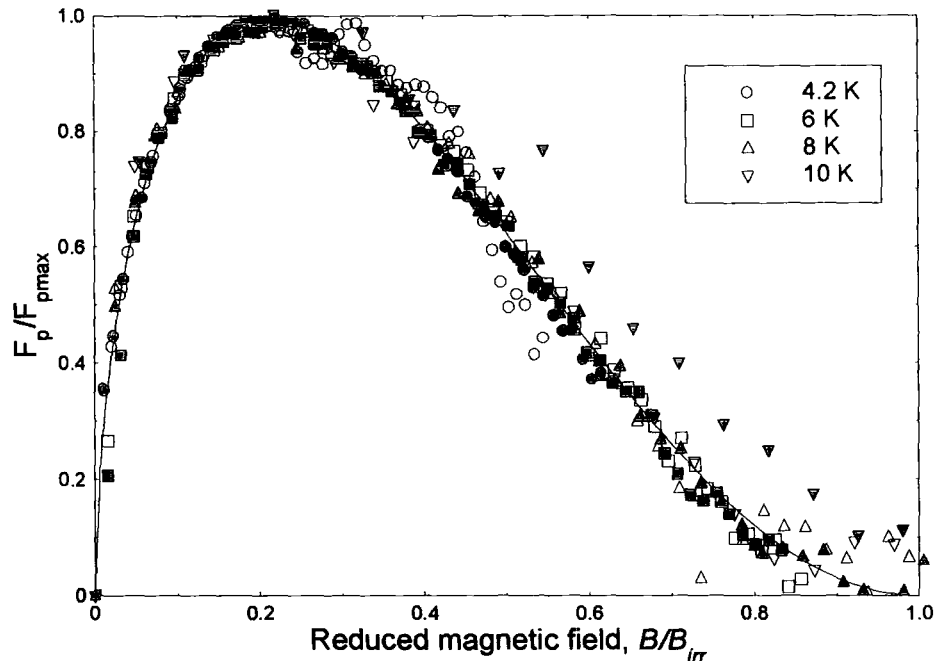

Figure 6.30. Normalised flux pinning force of the 1 mm length $PbMo_6S_8$ sample as a function of reduced field, and temperature, measured using the VSM. The open shapes are for the field parallel, and the closed shapes for the field perpendicular. The solid line is $\frac{F_p}{F_{pmax}} = \alpha_p (B_{c2})(1-b)^q b^p$ fitted to the data, with $p = 0.5$ & $q = 2$.

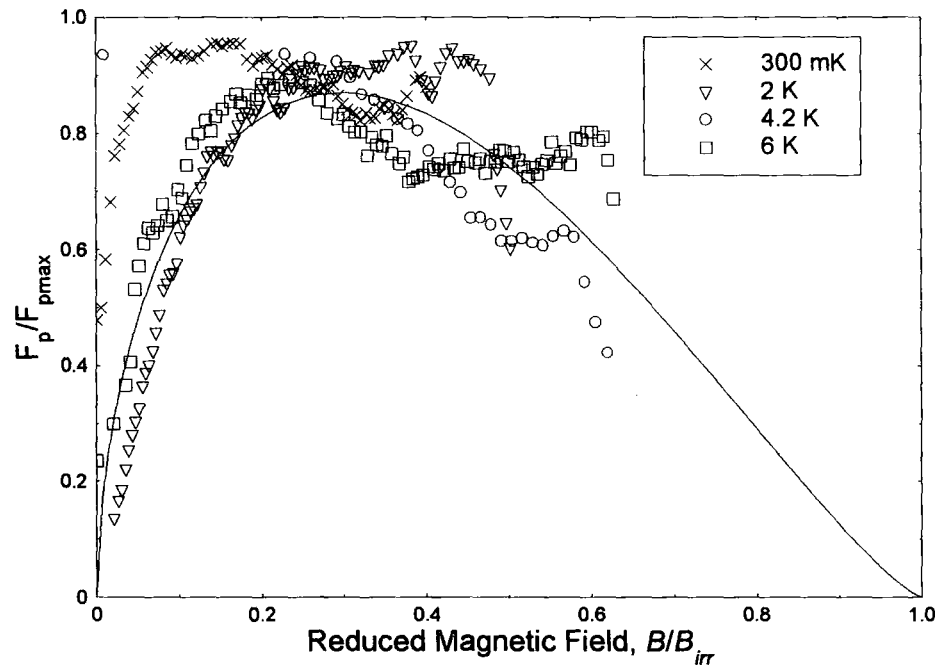

Figure 6.31. Normalised flux pinning force of $PbMo_6S_8$ as a function of reduced magnetic field and temperature. The 1 mm length sample was measured using the torque magnetometer. The solid line is $\frac{F_p}{F_{pmax}} = \alpha_p (B_{c2})(1-b)^q b^p$ fitted to the data with $p = 0.5$ & $q = 1.42$.

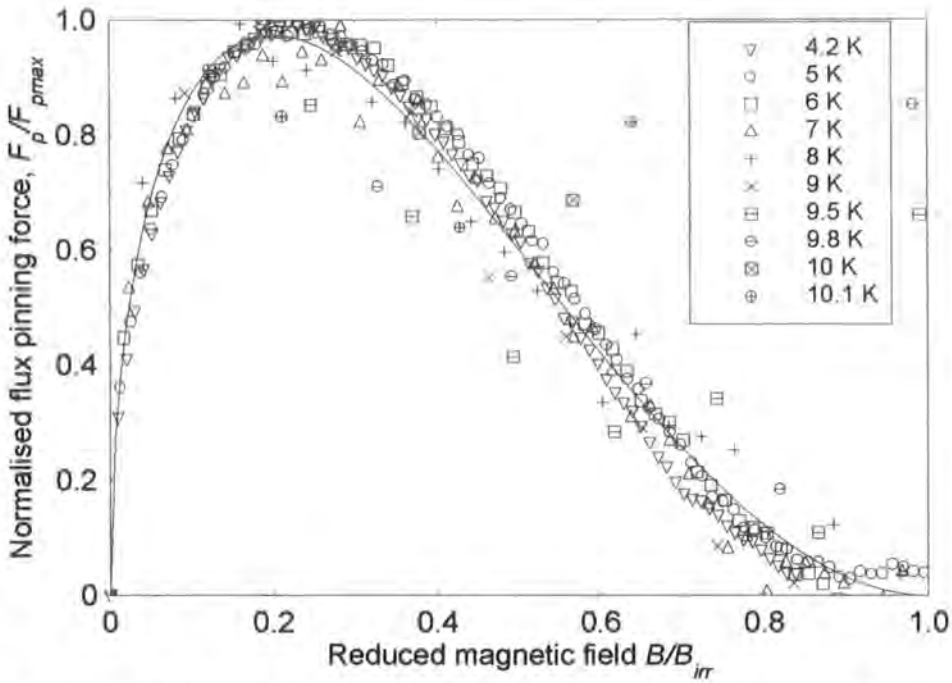

Figure 6.32. Normalised volume pinning force $\left(F_p/F_{\max}\right)$ as a function of reduced magnetic field and temperature for $Pb_{0.75}Eu_{0.25}Mo_6S_8$. The solid lines represent $F_p = \alpha_p B_{irr}^n b^p (1-b)^q$, with $p = 0.5$, and $q = 2$.

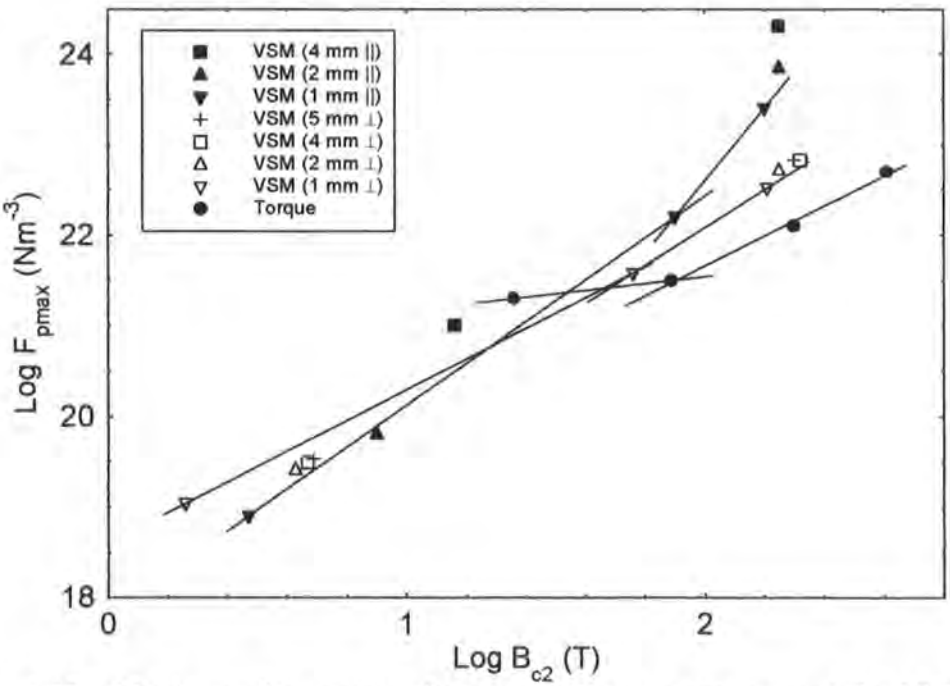

Figure 6.33. Maximum flux pinning force (at different temperatures) for NbTi wire as a function of B_{c2}. The solid lines are linear fit to the 1 mm length sample data. The gradients of the solid lines gave n, for each sample and experiment.

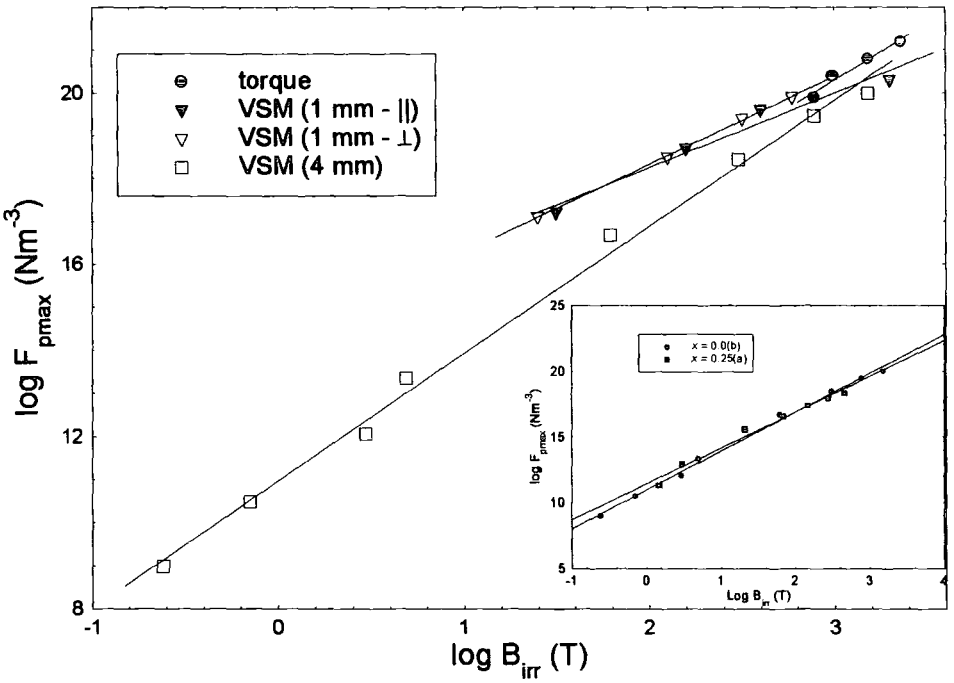

Figure 6.34. Maximum flux pinning force (at different temperatures) for $PbMo_6S_8$ as a function of irreversibility field *(B_{irr})*. The solid lines are the linear fit to the data. The gradients of the solid lines gave *n*, for each sample and experiment. **Inset:** Max flux pinning force for $Pb_{0.75}Eu_{0.25}Mo_6S_8$ and $PbMo_6S_8$ as a function of irreversibility field. The solid lines are the linear fit to the data.

6.4.4 Flux pinning scaling law

6.4.4.1 General considerations

For the NbTi wire samples, the $PbMo_6S_8$ samples and the 4 mm bulk $Pb_{0.75}Eu_{0.25}Mo_6S_8$ sample, the normalised flux pinning force was determined from the VSM and torque magnetometer data. Fietz-Webb scaling law[5] for the volume flux pinning force is given by:

$$F_p(B,T) = \alpha_p(T) B_{c2}^n(T) b^p (1-b)^q \tag{6.3}$$

where α_p, n, p and q are variables that depend on the pinning mechanism of the superconductor and b is the reduced magnetic field. For the $PbMo_6S_8$ and the $Pb_{0.75}Eu_{0.25}Mo_6S_8$ data, B_{irr} was used instead of $B_{c2}(T)$, as they have high $B_{c2}(0)$ (~ 60 T), which means that $B_{c2}(T)$ can only be determined for temperatures close to T_c. From the Kramer plots (figs. 6.23 - 6.25), the irreversibility field (B_{irr}), can be determined over a wider temperature range, so is a convenient magnetic field limit to use. For the NbTi wire the reduced magnetic field was $b = \frac{B}{B_{c2}}$, while for $PbMo_6S_8$

and $Pb_{0.75}Eu_{0.25}Mo_6S_8$ the reduced magnetic field was $b = \frac{B}{B_{irr}}$. The flux pinning force is a maximum at the reduced field $b_{max} = \frac{p}{p+q}$. Eqn 6.3 was fitted to the NbTi wire, $PbMo_6S_8$ and $Pb_{0.75}Eu_{0.25}Mo_6S_8$ data as a function of reduced magnetic field, b.

	n	p	q
NbTi wire literature[6]	2 – 2.3	1 (4.2 K) 0.5 (8 K)	1 (4.2 K) 1.5 (8 K)
NbTi (VSM - ⊥)	2.0 (4.2 K – 6 K) 1.7 (6 K – 8 K)	1.08 ± 0.01 (4.2 K) 1.04 ± 0.04 (8 K)	0.87 ± 0.01(4.2 K) 2.18 ± 0.04 (8 K)
NbTi (VSM - ‖)	4 (4.2 K – 6 K) 2.3 (6 K – 8 K)	1.11 ± 0.03 (4.2 K) 0.92 ± 0.03 (8 K)	1.37 ± 0.03 (4.2 K) 1.94 ± 0.03 (8 K)
NbTi (torque –liquid)	-	1.62 ± 0.07	1.49 ± 0.06
NbTi (torque –vacuum)	1.7 (300 mK – 6 K) 0.4 (6 K – 8 K)	0.2 ± 0.01 (4.2 K) 0.15 ± 0.01 (8 K)	0.23 ± 0.01 (4.2 K) 0.72 ± 0.03 (8 K)
Chevrel Phase literature[7]	2.3	0.5	2
$PbMo_6S_8$ (VSM – 4 mm)	2.9 ± 0.3	0.57 ± 0.005	2.15 ± 0.02
$PbMo_6S_8$ (VSM – 1 mm ‖)	1.75 ± 0.2	0.57 ± 0.01	2.13 ± 0.01
$PbMo_6S_8$ (VSM – 1 mm ⊥)	2.1 ± 0.04	0.59 ± 0.01	2.18 ± 0.02
$PbMo_6S_8$ (torque – vacuum)	2.62 ± 0.3	0.55 ± 0.01	1.42 ± 0.04
$Pb_{0.75}Eu_{0.25}Mo_6S_8$ (VSM – 4 mm)	2.75 ± 0.02	0.56 ± 0.006	2.08 ± 0.02

Table 6.3. A summary of normalised flux pinning force variables for the 1 mm length NbTi wire and $PbMo_6S_8$ determined from the torque magnetometer and the VSM data. For NbTi wire, the p & q variables were determined for 4.2 K and 8 K. The n values were determined for fig. 6.27, for the two distinct gradients. The $PbMo_6S_8$ p & q variables were determined at all temperatures, excluding 300 mK.

6.4.4.2 NbTi wire

For the 1 mm length NbTi wire the reduced field at the maximum volume pinning force moved from $b_{max} = 0.65$ at 4.2 K to $b_{max} = 0.53$ at 8 K for the field perpendicular to the long axis (fig. 6.26). Similarly the reduced field at the maximum volume pinning force for the 2 mm, 3.83 mm and 5 mm length samples was at $b_{max} = 0.54$ for 4.2 K, and at $b_{max} = 0.32$ for 8 K (figs. 6.27 & 6.28). For the torque data, the maximum volume pinning force moved from $b_{max} = 0.8$ at 300 mK to $b_{max} = 0.3$ at 8 K. The torque data normalised flux pinning force curves have a different shape to the VSM data. The 1 mm length NbTi wire torque data taken in liquid helium was in good agreement with the 1 mm length VSM sample at 4.2 K (fig. 6.29).

The maximum volume pinning force for the parallel field data were at different reduced fields to the perpendicular field data. For the 1 mm length sample at 6 K, the perpendicular field data maximum force was at $b_{max} = 0.55$, while the parallel field data maximum force was at $b_{max} = 0.44$.

The variable n was determined for NbTi wire by plotting the log of the max volume pinning force against the log of the upper critical field $B_{c2}(T)$ (fig. 6.33). The n values for the parallel field data differed from the perpendicular field data. There were two different n values for each field direction to the long axis. This was because of the temperature dependence of the flux pinning force peak. For each field direction the n values for the lower temperatures (below 6 K) were larger than the higher temperature n values.

From table 6.3, the p & q values for NbTi wire change with temperature and the field direction to the long axis. For the 1 mm length sample with the field perpendicular to the long axis at 4.2 K, the p value is slightly higher and the q value is slightly lower than the values in the literature. The 1 mm length torque data, the p & q values differ from the literature and the VSM data.

6.4.4.3 $PbMo_6S_8$

For the VSM 1 mm length $PbMo_6S_8$ data for both field directions, the normalised volume pinning curves had similar form for all temperatures (fig. 6.30), the solid line is proportional to $b^{1/2}(1-b)^2$. For the field parallel and perpendicular to the long axis of the $PbMo_6S_8$ sample, the flux pinning force peaks occurred at $b_{max} = 0.22$.

For the torque magnetometer data, the volume pinning force curves have different shapes to the VSM data. In fig. 6.31, the solid line through the data is proportional to $b^{0.5}(1-b)^{1.42}$. For all temperatures above 2 K, the reduce field at the maximum volume pinning force was b_{max} = 0.24 (fig. 6.31). At 300 mK, the maximum volume pinning force was at b_{max} = 0.15.

To determine the *n* value for each data set, the irreversibility field was plotted instead of the upper critical field. From fig. 6.34, the *n* value was dependant on the size of the sample and the direction of the field to the long axis. For the samples measured using the VSM, the *n* values range from 1.75 to 2.95. The literature *n* value and the torque magnetometer data *n* value are within this range. The errors on *n* were determined from the best-line fit through the data on fig. 6.34. For the 4 mm length and 1mm length samples measured using the VSM, the *p* & *q* values are in agreement (table 6.4). The *p* & *q* values are slightly higher than the literature values.

6.4.4.4 Comparison between $Pb_{0.75}Eu_{0.25}Mo_6S_8$ and $PbMo_6S_8$

For the 4 mm bulk $PbMo_6S_8$ sample $p = 0.57 \pm 0.005$ and $q = 2.15 \pm 0.02$ and for the 4 mm bulk $Pb_{0.75}Eu_{0.25}Mo_6S_8$ sample $p = 0.56 \pm 0.006$ and $q = 2.08 \pm 0.02$ (table 6.3). The normalised flux pinning curve was the same shape at each temperature. From figs 6.30 & 6.32 the pinning mechanisms for both samples are the same, as they have the same flux pinning constants.

The constant *n* is the temperature-scaling component of the flux pinning scaling law. The values of *n* were found by plotting the maximum flux pinning force against the irreversibility field, for each temperature (fig. 6.34). The gradient of the line gave *n* for the sample. For $PbMo_6S_8$, *n* was 2.95 ± 0.01 and for $Pb_{0.75}Eu_{0.25}Mo_6S_8$, *n* was 2.75 ± 0.02. As the log of the maximum flux pinning has a linear relation with the log of the irreversibility field, the pinning mechanism is the same at all temperatures. The high temperature data for both samples did not fit on the same flux pinning curve, as the irreversibility field for each temperature was less than 1 T.

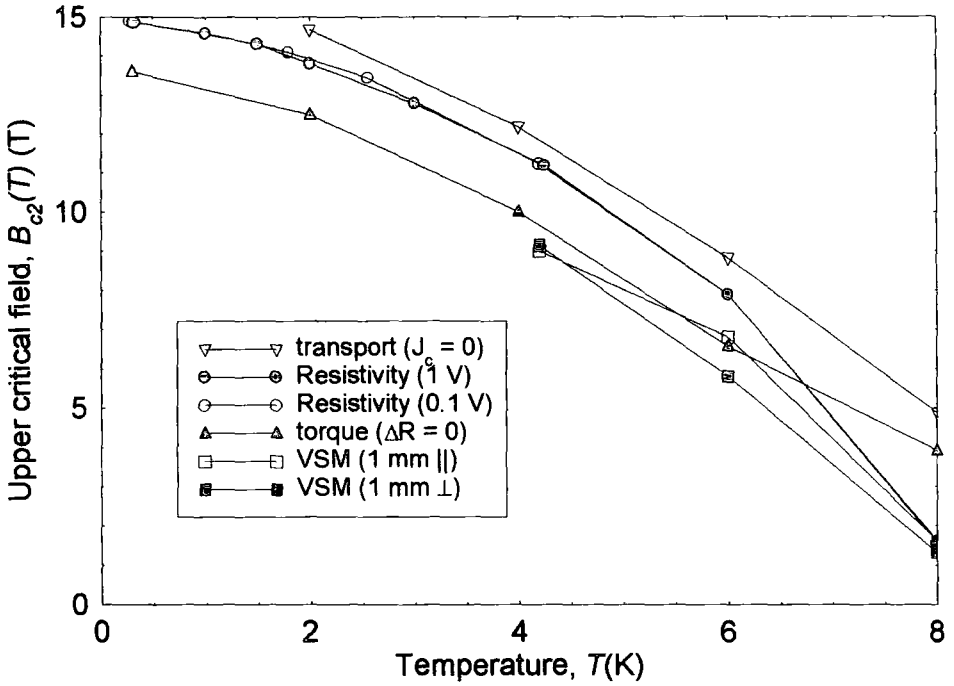

Figure 6.35. The upper critical field of NbTi wire as a function of temperature and experimental technique. The torque data and the VSM data are for the 1 mm length sample. C. Friend took the transport data[4].

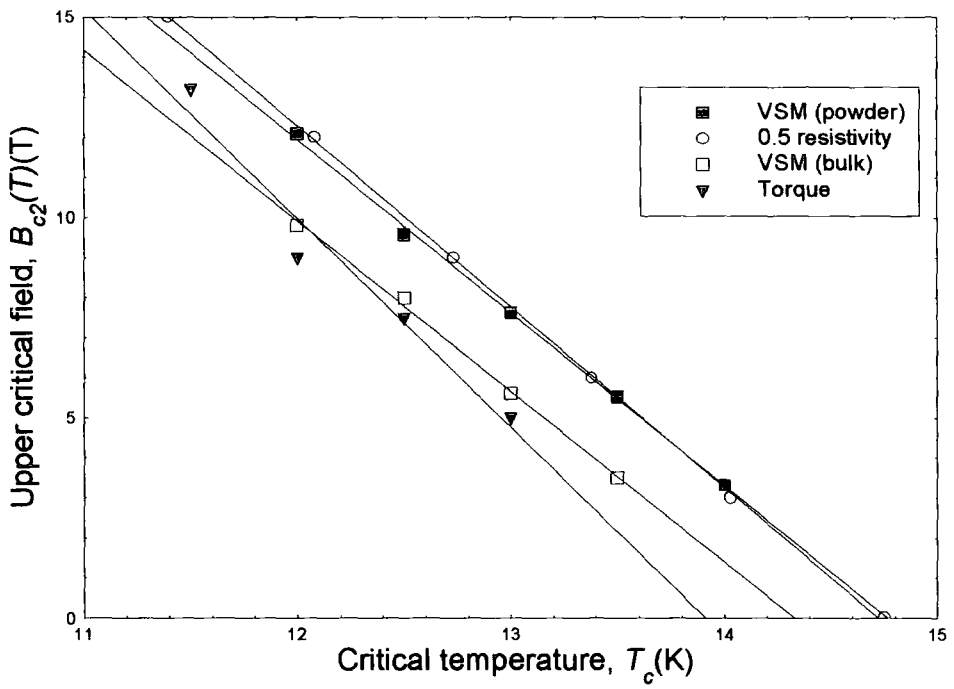

Figure 6.36. The upper critical field of $PbMo_6S_8$ as a function of temperature and experimental technique. The VSM data are for the 4 mm length sample. The solid lines are the linear fit to the data.

6.4.5 Upper critical field, $B_{c2}(0)$

For NbTi wire, different criteria were used for the determination of $B_{c2}(T)$ from the data. For the resistivity data, $B_{c2}^{0.5\rho_N}(T)$ was the field at 50 % of the superconducting transition for each temperature (fig. 6.8). For the transport data, the field at which $J_c = 0$ was taken to be $B_{c2}^{J_c=0}(T)$. For both magnetometers' data the irreversible fields were determined, for the NbTi wire. For the VSM data, $B_{irr}^{M\to 0}(T)$ was the field at which the average magnetisation was zero on fig. 6.22. For the torque data, $B_{irr}^{\tau}(T)$ was the field at which the voltage vs. field sweep loop became reversible at z = 0 cm (fig. 6.9). The upper critical field of NbTi wire at 0 K, was determined by extrapolation from the high temperature data to 0 K. From the resistivity data, the $B_{c2}(0)$ was 15 T. The torque $B_{irr}^{\tau}(T)$ data are in good agreement with the VSM data (fig.6.35). No heating occurred during the resistivity measurement, as the V_{ac} = 0.1 V data and the V_{ac} = 0.01 V data, have the same $B_{c2}^{0.5\rho_N}(T)$ at each temperature.

For $PbMo_6S_8$, the criterion for the torque data $B_{irr}^{\tau}(T)$ (fig. 6.10), thus $B_{irr}^{\tau}(T)$ and the 4 mm length bulk and powder VSM data $B_{c2}^{M\to 0}(T)$ are the same as the NbTi wire methods. For the 4 mm length sample resistivity data, $B_{c2}^{0.5\rho_N}(T)$ and VSM data $B_{c2}^{M\to 0}(T)$ the values are determined in section 4.6.1.

For the Chevrel phase superconductors, WHH theory[8] is used to determine the upper critical field at 0 K. The theory gives the upper critical field to be:

$$B_{c2}(0) = -0.7T_c \left.\frac{dB_{c2}}{dT}\right|_{T=T_c} \tag{6.4}$$

where the gradients $\frac{dB_{c2}}{dT}$ are the solid lines through the data in figure 6.36. In fig. 6.36, the gradients for the different data sets are consistent.

From the upper critical field vs. temperature graphs (figs. 6.35 & 6.36), the critical temperature for each measurement were determined by extrapolating the line back to 0 T. From table 6.4, for the NbTi wire, the upper critical fields from the VSM and torque experiment are in good agreement. Similarly for $PbMo_6S_8$, the T_c, $B_{c2}(0)$ and J_c are consistent for the different measurements. The errors for T_c, and $B_{c2}(0)$ were determined by standard error analysis.

	Critical temperature (T_c) (K)	Upper critical field ($B_{c2}(0)$) (T)	Critical current density ($J_c(4.2\ K, 5\ T)$) (Am^{-2})	$-\frac{dB_{c2}}{dT}$ (TK^{-1})
NbTi wire (VSM 1 mm ⊥)	8.7 ± 0.7	13.4 ± 0.5	1.232×10^9	1.849 ± 0.11
NbTi wire (resistivity)	9.2 ± 1	15 ± 0.1	-	1.65 ± 0.17
NbTi wire (transport)[4]	11.2 ± 0.9	15.5 ± 0.5	8.05×10^8	1.64 ± 0.12
NbTi wire (torque)	10.5 ± 0.5	13.8 ± 0.8	5.375×10^8	1.47 ± 0.06
$PbMo_6S_8$ (VSM – bulk)	14.3 ± 0.7	43 ± 2.7	1.44×10^8	4.26 ± 0.16
$PbMo_6S_8$ (VSM- powder)	14.8 ± 0.4	45 ± 1.6	-	4.32 ± 0.1
$PbMo_6S_8$ (resistivity)	14.7 ± 0.16	47 ± 0.7	-	4.52 ± 0.04
$PbMo_6S_8$ (torque)	13.9 ± 1	51 ± 5	1.38×10^8	5.22 ± 0.5
$Pb_{0.75}Eu_{0.25}Mo_6S_8$ (VSM – bulk)	10.7 ± 0.5	12 ± 5	1.55×10^7	1.54 ± 0.3
$Pb_{0.75}Eu_{0.25}Mo_6S_8$ (VSM – powder)	11.5 ± 0.5	30 ± 5	-	3.34 ± 0.35
$Pb_{0.75}Eu_{0.25}Mo_6S_8$ (torque)	-	-	5.66×10^7	-

Table 6.4. Comparison of the critical temperature, upper critical field and critical current density of NbTi wire, $PbMo_6S_8$ and $Pb_{0.75}Eu_{0.25}Mo_6S_8$. The experimental technique for each data set is given in the brackets. For the NbTi wire, the VSM data and the torque data are for the 1 mm length sample. For $PbMo_6S_8$ and $Pb_{0.75}Eu_{0.25}Mo_6S_8$, the VSM data and the resistivity data are for the 4 mm length sample, and the torque data are for the 1 mm length sample.

6.5 Discussion

6.5.1 Critical current Density

6.5.1.1 Field-gradient torque magnetometer

The initial measurements on the torque magnetometer were made on $Pb_{0.75}Eu_{0.25}Mo_6S_8$ at 0°. For 5 K & 6 K, the critical current densities have similar order of magnitude but different field dependence compared to the J_c^{VSM} (fig. 6.14). The measurements were made before the proper calibration of the torque chips. One reason for the different field dependence at 5 K, & 6 K could be due to the fact that voltage vs. field sweep loops taken at 0° and z = 0 cm were non-reversible (figs. 6.1). The 8 K data had different field dependence to other temperatures, as the moment was on the limit of the sensitivity of the torque magnetometer.

At the reversible angle the J_c^r measured at 4.2 K (fig. 6.15), has different field dependence to the 5 K & 6 K data. This could be due to improvements having been made to the experiment, including the calibration of the QD chip, better thermal linking to the sample, and the data being taken at the reversible angle. The $Pb_{0.75}Eu_{0.25}Mo_6S_8$ sample was not measured at 300 mK.

For $PbMo_6S_8$, measured at the reversible angle, the field dependence of the critical current density was similar for 300mK, 4.2 K and 6 K to the VSM data (fig. 6.16). The 2 K critical current density had different field dependence below 5 T compared to the other temperatures. At 300 mK, if the gradient was taken through all the ΔR_{+-} points (solid line on fig. 6.13a), the J_c^r determined had a similar low field dependence to the 2 K data. During the 300 mK measurement the liquid helium-3 had to be re-condensed four times, as the hold time at 300 mK was ~ 5 hours. The loops measured directly after each re-condensation were at z = 0, 2.5, 4.5 & 6 cm. For these four voltage loops, the magnitude of the difference in voltage across the loop below 4 T increased linearly with field gradient (dashed lines in fig. 6.13a). Hence the J_c^r determined has similar field dependence to the 4.2 K data. For the voltage vs. field sweep loops taken at the other heights, the difference in voltage across the loops were similar up to 4 T, hence the voltage vs. field sweep loops taken at z = 0, 2.5, 4.5 & 6 cm were used to determine J_c^r. The reason for this difference between the hysteresis in the voltage loops is still uncertain. When the temperature of the helium-3 pot and the sample is 300 mK, the 1 K plate temperature is 1.6 K, thus any helium gas in the

IVC will condense on to the sample, as it is at the lowest temperature. Hence the first voltage loops measured at 300 mK after re-cooling were not affected by heating, due to the condensed helium on the sample. For consecutive loops, heating of the sample could have caused the helium to evaporate, thus cause the data under 5 T to be inaccurate. When the helium-3 pot and the sample are at 2 K, the 1 K plate temperature is 1.6 K, so any helium gas in the IVC will condense onto the 1 K plate rather than the sample. Any heating which occurs will affect the voltage loops measured. Above 5 T, the excess heat appears to have been removed for both temperatures, so the critical current densities had the correct field dependence. For the 6 K J_c^T the field dependence above 8 T, differs from the VSM data, due to the large SNR noise on the data at high fields. The 8 K and 12 K data were the same order of magnitude, as the noise was greater than the signal, at these temperatures, hence the 8 K data were taken to be the background of the chip in the magnetic field.

At 300 mK, the critical current densities of NbTi wire and $PbMo_6S_8$ were measured. The critical current density of $PbMo_6S_8$ bulk sample had been measured at 4.2 K[9, 10] and for $PbMo_6S_8$ wire at 1.9 K[11, 12, 13]. The critical current density was $2.98 \pm 0.67 \times 10^8$ Am^{-2}, at 300 mK, 5 T (fig. 6.16).

From literature the critical current density of NbTi has been measured at 2 K[14]. Thus the critical current density of NbTi wire at 300 mK was $8.34 \pm 1.7 \times 10^8$ Am^{-2}, at 5 T (fig. 5.39). The critical current density at 4.2 K was 50 % of the J_c^{VSM}. The lower value may have been due to Eddy heating and the small signal to noise ratio (SNR).

6.5.1.2 VSM – $Pb_{0.75}Eu_{0.25}Mo_6S_8$

For the $Pb_{0.75}Eu_{0.25}Mo_6S_8$ 4 mm length sample and the 300 μm ∅ sample measured on the VSM, the field dependence and magnitude of the critical current densities were different (fig. 6.14). The difference was not due to the ac-field associated with the VSM[15], as the irreversibility fields at 6 K, for both samples were 6.5 T, hence the difference was due to the shape of the samples. The 4 mm length sample was a parallelepiped, while the 300 μm ∅ sample was a cylinder. Also the samples were taken from different parts of the large HIP'ed sample, which also means the difference could be due to inhomogeneity in the large sample. Therefore the 300 μm ∅ sample had a larger J_c^{VSM} than the 4 mm length sample at lower fields. At 4.2 K, the 150 μm ∅ sample magnetic moment was on the limit of the sensitivity of the

VSM, so for fields above 2 T, the background noise was greater than the signal. Thus the J_c^{VSM} for the 150 μm ∅ sample had a different field dependence and magnitude than the 4 mm length and 300 μm ∅ samples.

6.5.1.3 VSM - $PbMo_6S_8$

For $PbMo_6S_8$, the critical current densities determined from the VSM data of the 1 mm length sample differed from the 4 mm length samples (fig. 6.20). From Bean's model[2] the critical current density should be the same for both samples, as they were taken from the same large HIP'ed sample. The difference in the magnitude of the critical current densities could have been due to the ends of the samples not being perfectly flat. This would alter the critical currents which flowed, thus the shape factor used in the calculations would be incorrect. Another reason could be due to the samples being different shapes. The 4 mm length sample was a parallelepiped, while the 1 mm length sample was a cylinder. If there were any inhomogeneity of the superconducting parameters in the large HIP'ed sample, this would also change the critical current density between the samples. This is because the samples were cut from different parts of the large HIP'ed sample.

The difference in the field dependence of the critical current densities between the 4 mm length sample and the 1 mm length sample was due to the ac-field associated with the VSM (fig. 6.20)[15]. The ac-field completely penetrated the 1 mm length sample at lower fields than the 4 mm length sample, which caused the critical current density of the 1 mm length sample to reduce to zero at a lower field, than the 4 mm length sample.

6.5.1.4 Anisotropy of the $PbMo_6S_8$ critical current density

For the 1 mm length $PbMo_6S_8$ sample, the critical current density measured with the field perpendicular to the long axis, $J_{c\perp}$ was lower in magnitude than the critical current density measured with the field parallel to the long axis, $J_{c\parallel}$ (fig. 6.20). The anisotropy ratio $\left(J_{c\parallel} / J_{c\perp}\right)$ between the critical current densities decreased as the temperature was increased. At 10 K, between 0 T and 3 T, the ratio was a constant of value 1.15, and at 8 K the ratio was 1.26, between 0.5 T and 5 T. At fields close to B_{irr}, the ratio decreased towards zero. At 6 K, the ratio decreased linearly from 1.33 at

0.5 T to 1.18 at 10 T, then decreased non-linearly to zero. At 4.2 K, the ratio was less well defined, due to noise on the parallel field data, thus the ratio at 4.2 K, between 0.5 T and 6 T, linearly increased from 1.41 to 1.49.

Anisotropy in J_c is often due to the flux pinning mechanism in the superconducting sample[16], which is unlikely for $PbMo_6S_8$, as the pinning centres are at the grain boundaries[7]. The grain boundaries should be isotropic, as the material was hot isostatically pressed (HIP'ed), hence the grains were pushed together with the same pressure from all direction. If during HIP'ing, one direction was more favourable than the others, this would introduce anisotropy into the structure of the material. The more probable reason is the shape of the sample. If the 1 mm length sample was not perfectly cylindrical, this would change the critical current density.

6.5.1.5 Comparison between the $PbMo_6S_8$ and $Pb_{0.75}Eu_{0.25}Mo_6S_8$

The critical current density is limited by two material properties in bulk Chevrel phase superconductors. The first is the connectivity of the grains[10, 17, 18]. Ramsbottom *et al*, showed that HIP'ing improved the density of Chevrel phase superconductors, and thus increased the critical current density[10]. This was because the HIP'ed samples had better homogeneity and connectivity across the grains. The second is the flux pinning in the sample[19, 7, 20]. Wördenweber proved the magnetic flux was pinned at the grain boundaries in Chevrel phase superconductors[21], hence reducing the size of the grains or increasing the number of pinning sites, will increases the critical current density[19]. From the data, at 4.2 K, 4 T, the critical current density of $Pb_{0.75}Eu_{0.25}Mo_6S_8$ was 2.23 x 10^7 Am^{-2} compared with 1.18 x 10^8 Am^{-2} for $PbMo_6S_8$. The critical current density decreased by a factor 5, with the addition of Eu ions, which means either the Eu ions decreased the connectivity of the grains or reduced the pinning at the grain boundaries. From the resistivity measurements the Eu ions formed second phase materials on the edge of the grains and in the grain boundaries (section 4.7.2), which produced dirty boundaries, so reduced the critical current density. Another reason could have been the Eu ions repelled the magnetic flux, rather than attracted. If the Eu ions had acted as pinning sites, by attracting the flux the critical current density would have increased, in comparison with the critical current density of $PbMo_6S_8$. The critical current densities of $PbMo_6S_8$ and $Pb_{0.75}Eu_{0.25}Mo_6S_8$ had similar field dependence (fig. 6.21), which suggests the pinning mechanism was the same.

6.5.1.6 VSM - NbTi wire

The critical current density of NbTi wire is a well documented subject[16, 22]. It depends on the percentage of titanium in the wire[14, 23], the microstructure of the sample[24, 25] and the fabrication process[26]. From the literature, the optimum composition, which has the largest J_c is Nb50.4%Ti. For this composition, $B_{c2}(0)$ = 15 T, $T_c \sim 9$ K and $J_c = 2.7 \times 10^9$ Am^{-2} (4.2 K, 5 T)[14, 23]. Reducing the percentage of Ti, decreases the J_c, but increases $B_{c2}(0)$ [14], while increasing the percentage of Ti, decreases the J_c and $B_{c2}(0)$ [14]. The composition of the NbTi wire used in this experiment was Nb46.5wt%Ti in a multi-filamentary wire.

For NbTi wire, with the field perpendicular to the long axis at 4.2 K, the 3.83 mm length and 5 mm length NbTi wire samples critical current densities were the same magnitude (fig. 6.18). The 1 mm length NbTi wire critical current density was 70 % of the 5 mm length critical current density. One reason for the reduction could be due to the ends of the wire not being perfectly flat, which would affect the critical current density, by changing the loop around which the current flows. Another possible reason is the ac-field associated with the VSM[15]. As the length of the wire decreases, the ac-field will fully penetrate the smaller samples at lower magnetic fields. Thus the ac-field will penetrate the 1 mm length sample at fields lower than the 5 mm length sample. At 4.2 K, the $B_{c2}(T)$ for all the samples were similar, suggesting that the ac-field did not penetrate the 1 mm length sample completely. At 8 K, for both field directions, the $B_{c2}(T)$ decreased, as the length of the sample was reduced. For the 1 mm length sample perpendicular to the magnetic field, $B_{c2}(T)$ was 1.3 T, while for the 5 mm length sample, $B_{c2}(T)$ was 1.7 T, hence the ac-field associated with the VSM did completely penetrate the 1 mm length sample.

6.5.1.7 Anisotropy of the NbTi critical current density

For the NbTi wire samples, the $J_{c\perp}$ had different field dependence compared with the $J_{c\parallel}$ (fig. 6.17). Jungst investigated the change in NbTi wires' critical current as a function of the angle between the long axis of the sample and the magnetic field[27]. The shape of the critical current curves for the field parallel to and perpendicular to the sample's long axis are similar to those determined in this chapter. Thus the difference in curve shape is a generic result, rather than a heating problem.

Mathur *et al* investigated the anisotropy of the critical current density of NbTi wire[28]. They found that the critical current density was larger with the field parallel to the long axis, compared with the field perpendicular to the long axis. The anisotropy ratio $\left(J_{c\parallel} / J_{c\perp}\right)$ increased as the field magnitude was increased, up to the maximum applied field of 3.5 T. From the J_c VSM data for the NbTi wire (figs. 6.17 – 6.19), the anisotropy ratio between $J_{c\perp}$ and $J_{c\parallel}$ increased to a maximum value and then decreases down to zero at $B_{c2}(T)$. The ratio was larger for the 3.83 mm length NbTi wire sample compared to the 1 mm length sample. The ratio for both samples decreased as the temperature was increased. At 4.2 K, the maximum ratio was over the field range 2.5 – 3.2 T. For 6 K the maximum ratio was in the field range 1.4–2.1 T. At 8 K, the ratio gradually increased with field, as the $B_{c2}(T)$ and J_c for the field parallel were higher than the $B_{c2}(T)$ and J_c for the field perpendicular to the long axis. The peak ratio value at 4.2 K ranged from 3.17 for the 1 mm length sample to 4.96 for the 3.83 mm length sample. They are slightly higher than the Mathur's values, which ranged from 1.8 to 3.4 at 3 T.

The anisotropy in the NbTi wire critical current density is due to the pinning mechanism. The flux is pinned on the dislocated cell well structure and the ribbon-like α-Ti precipitates[22], which are along the long axis, hence the pinning centres have an anisotropy associated with them.

The anisotropic microstructure does not affect the fundamental parameters measured for the two different magnetic field directions to the long axis. The GL parameter and the critical fields ($B_c(0)$ & $B_{c1}(0)$) were in agreement between the parallel field data and the perpendicular field data, for the 1 mm length sample (table 6.1).

6.5.2 Irreversibility fields

The irreversibility field $\left(B_{irr}\right)$ of a superconductor is the field at which the critical current density goes to zero. Daniel *et al*, suggests that the irreversibility field $\left(B^*_{irr}\right)$ measured from VSM magnetisation measurements was not the actual irreversibility field $\left(B_{irr}\right)$ of the sample[15]. In a VSM, the sample is vibrated over a throw distance at the magnet centre. The magnetic field is not homogenous over the whole throw distance, so the sample experiences a field gradient. The movement in the field gradient produces an ac-magnetic field, which penetrates the sample. When the ac-

field fully penetrates, it cancels out the self-field $\left(B_{sf} = \mu_o J_c r_m\right)$ of the superconductor. This reduces the measured magnetic moment to zero. The irreversibility fields $\left(B^*_{irr}\right)$ for both samples were determined from the Kramer plots (fig. 6.23 & 6.25). For $PbMo_6S_8$ the irreversibility fields $\left(B^*_{irr}\right)$ were a factor 2 or higher, less than the $B_{c2}(T)$, for the same temperature. For $PbMo_6S_8$, the reversible region was 11 T, at 12 K, thus $PbMo_6S_8$ has a large reversible magnetisation region, or the measured B^*_{irr} was not the actual B_{irr}, due to the ac field associated with the VSM.

The irreversibility fields, for $PbMo_6S_8$ were determined from the Kramer plots for both magnetometers' data (figs 6.23 & 6.24). At 4.2 K, the irreversibility fields measured were in the range 19.2 T to 24.2 T (table 6.2). The wide range of values was due to the inaccuracy of the VSM measurements at 4.2 K. Thus the 1 mm length perpendicular sample B_{irr} was 5 T lower than the 4 mm length samples' B_{irr}, but was in agreement with the B_{irr} of the torque measurement. At 6 K, the torque 1 mm length sample and 4 mm length VSM sample irreversibility fields were 18 T, while the 1 mm length VSM irreversibility fields for both field directions were 14 T. This difference of 4 T was due to the ac-field fully penetrating the 1 mm length sample at a lower magnetic field[15]. Hence the torque magnetometer gave a more reliable value of B_{irr} than the VSM for the same sample, and the ac-field due to the vibration of the sample in the VSM does affect the data taken for samples smaller than a certain size.

From the torque magnetometer measurement (fig. 6.24), the irreversibility field of $PbMo_6S_8$ at 300 mK was 28.8 ± 0.2 T. This is roughly two thirds the size of the $B_{c2}(0)$, for the sample (table 6.4), which suggests $PbMo_6S_8$ has a large reversible magnetisation region.

6.5.3 Flux pinning force scaling law

6.5.3.1 $PbMo_6S_8$

For $PbMo_6S_8$ the VSM 4 mm length sample and 1 mm length sample values of p & q were consistent with each other (table 6.3). From section 6.5.3.1, they are slightly higher than the literature values of $p = 0.5$ & $q = 2$[7, 17], which suggests the flux pinning was at the grain boundaries[21, 10, 29]. The n values differ between the 4 mm length VSM data, the 1 mm length VSM data and the torque data. The range of VSM values was $n = 1.75$ to 2.9, with the literature value of $n = 2.5$, and the torque value of

n = 2.62 in this range. As n is the temperature dependant variable in the scaling law, the different irreversibility fields for each sample due to the VSM ac-field reducing B_{irr}[15], caused n to vary between the torque data and the VSM data. From table 6.3, the torque sample and the 4 mm length sample n values are consistent within errors. The torque flux pinning variables were p = 0.55 & q = 1.42, hence the p value is in agreement while the q value differs from the VSM values as the highest temperature measured on the torque magnetometer was 6 K. Hence the B_{irr} for all the temperatures were greater than the maximum applied field (~ 13 T), so there was no data at high reduced fields (fig. 6.31), which meant the scaling law (eqn 6.3) was fitted to the normalised volume pinning force data, at low reduced fields. The maximum volume pinning force for the 1 mm length VSM data was at b_{max} = 0.22 ± 0.01, and the torque data max volume pinning force was at b_{max} = 0.24 ± 0.01. These reduced fields are in agreement with each other and with the literature[10]. As the perpendicular field and parallel field VSM data have the same reduced field for the max volume pinning force, the pinning centres must be isotropic.

6.5.3.2 Comparison between $PbMo_6S_8$ and $Pb_{0.75}Eu_{0.25}Mo_6S_8$

Wördenweber proposed the modified flux line shear (FLS) model, which describes the pinning of flux in weakly pinned channels[21]. These channels are assumed to be at the grain boundaries in bulk polycrystalline materials[20]. Cattani *et al* also suggested there was strong intragrain pinning as well as intergrain pinning in Chevrel phase materials[18]. From the Kramer plots (fig 6.23 & 6.25) both $PbMo_6S_8$ and $Pb_{0.75}Eu_{0.25}Mo_6S_8$ have straight-line plots at each temperature, which were equidistant apart. From theory[3] the straight lines means there was only one pinning mechanism in the samples. The normalised flux pinning curves, were fitted to the Fietz-Webb[5] scaling law for bulk pinning (figs 6.30 & 6.32). The constants for $PbMo_6S_8$ were p = 0.58 and q = 2.15 and for $Pb_{0.75}Eu_{0.25}Mo_6S_8$ were p = 0.56 and q = 2.07, with the errors less than 1 %. Hence these values of p & q are higher than the theory[29], and experimental[7, 9] values of p = 0.5 and q = 2 found in the literature. At all temperatures the normalised flux pinning curve have the same shape, with a peak at the reduced field b_{max} = 0.21 for $PbMo_6S_8$ and b_{max} = 0.23 for $Pb_{0.75}Eu_{0.25}Mo_6S_8$, which again is consistent with the flux model with pinning at the grain boundaries[20]. The constant n is the temperature scaling component for the scaling law. The constant n for $PbMo_6S_8$

was 2.9 and for $(Pb_{0.75}Eu_{0.25})Mo_6S_8$ was 2.75. From the Kramer scaling law the theory value of n is 2.5[3]. The measured values in the literature range from 1.8[30] to 2.4[10]. Thus the measured n values were slightly higher, which suggests the distribution of $B_{c2}(T)$ in the samples has increased the n value.

6.5.3.3 NbTi wire – variation with temperature

The volume flux pinning mechanisms in NbTi are dependent on the microstructure[24, 25] and the fabrication process[26]. In NbTi wires, the pinning centres are due to the material having a dislocation cell structure of subgrain boundaries, and fine scale α–titanium precipitation[16] along the long axis of the wire. The dislocation cell structure is achieved by the extensive cold work on the wire, while the α–Ti precipitates have to be about 5 to 20 nm in size to act as flux pinning sites.

Anisotropy in the microstructure of NbTi is used to explain the change in position of the maximum volume pinning force with temperature, magnetic field direction to the long axis and sample length (figs. 6.26 - 6.28).

Meingast and Larbalestier suggested there were two types of flux pinning, which occur in NbTi wire[31]. They proposed the different pinning mechanisms had different temperature dependencies. These pinning mechanisms are $\delta\kappa$ pinning and δH_c pinning and are due to the fabrication process of the NbTi. The $\delta\kappa$ pinning is due to the dislocation cell structure, which pins at high reduced fields, while δH_c pinning is due to α–Ti precipitation in the sample, which pins at low reduced fields. From this chapter, for an increase in temperature, the NbTi wire maximum volume pinning force moved to lower reduced fields in both the VSM data and the torque data (fig. 6.26). From the perpendicular field VSM data, the max volume pinning force of the 2 mm length sample was at $b_{max} = 0.54$ at 4.2 K, and moved to $b_{max} = 0.3$ at 8 K (figs. 6.27 & 6.28), which is consistent with the measurements taken by Meingast[31]. The reason is at low temperatures both pinning mechanisms occur, hence the volume flux pinning force has two contributions, which broaden the curve, and the max force is at $b = 0.5$. Close to T_c, the δH_c pinning dominates, thus the flux is pinned on the α-Ti particles, and the pinning occurs at low reduced fields. The move max volume pinning force as a function of temperature was also observed in the 3.83 mm and 5 mm length samples' perpendicular data (figs. 6.27 & 6.28). For the 1 mm length sample the max force was at $b_{max} = 0.65$ at 4.2 K and moved to $b_{max} = 0.53$ at 8 K.

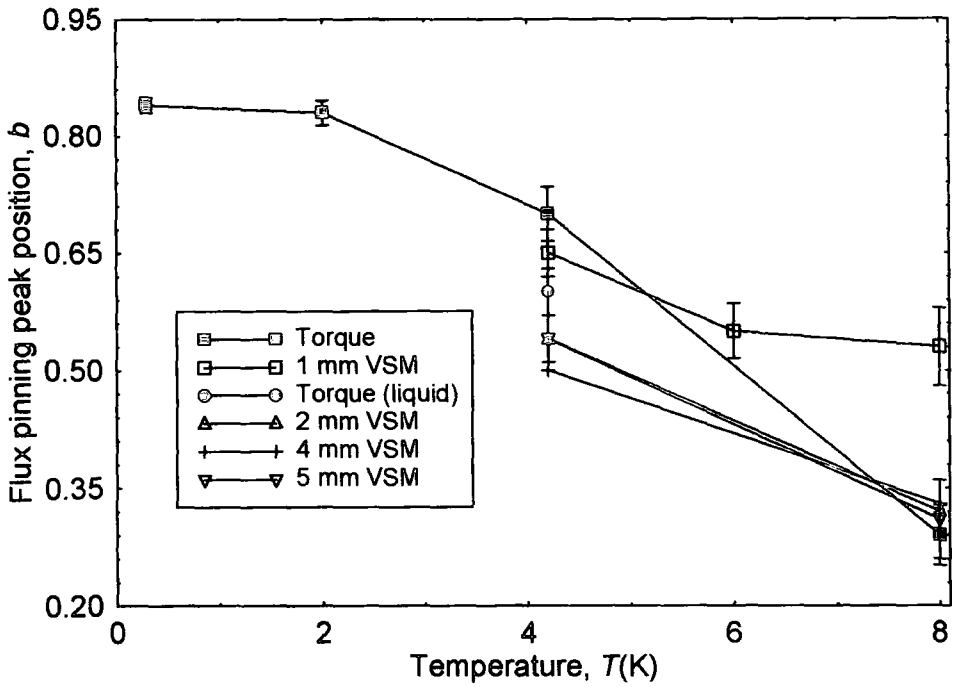

Figure 6.37. The reduced field at the max volume pinning force, of NbTi wire as a function of temperature and experiment. For the VSM data the field was perpendicular to the long axis. The error bars were determined from the errors for the reduced field peaks and the upper critical field data.

From the torque normalised flux pinning force data, the reduce field at the max volume pinning force moves from b_{max} = 0.84 at 300 mK to b_{max} = 0.3 at 8 K. The high temperature data agrees with theory[31] and the VSM data. At 300 mK, the max volume pinning force is at b_{max} = 0.84 (fig. 6.37), which suggests the $\delta\kappa$ pinning is the principal mechanism, as $\delta\kappa$ pinning occurs at high reduced magnetic fields. The δH_c pinning probably does not contribute. The shape of the curve at 300 mK is given by $b(1-b)^{1/4}$. Hampshire *et al*[6] found for NbTi wire which had been annealed at 250 °C for 1 hr, the flux peak was at b_{max} = 0.73, while the wire annealed at 500 °C for 1 hr, had a peak at b_{max} = 0.3. The second set data has an inflexion at b_{max} = 0.8. Hampshire *et al*[6] concluded that the $\delta\kappa$ pinning was the weaker pinning mechanism, but was seen at low temperatures and high reduced fields, which is consistent with the torque data at 300 mK. Therefore the torque data shows the change in pinning mechanisms in NbTi wire as a function of temperature. Also the torque data value of n = 1.65 at low temperatures is consistent with Hampshire's n value[6]. For the torque

data taken in liquid helium (fig. 6.29) the maximum volume pinning force is at b_{max} = 0.59, which is consistent with the VSM data (fig. 6.37).

The error for the reduced field at the max volume pinning force, b_{max}, at each temperature was determined from the error for the $B_{irr}(T)$ from the data and standard error analysis. Thus the change in the reduced field at the max volume pinning force is a definite result, rather than an error in calculating $B_{irr}(T)$ (fig. 6.37). For the torque magnetometer data, the error for $B_{irr}^{\tau}(T)$ increased as the temperature increased, as at higher temperatures the magnitude of the hysteresis in the voltage loop at z = 0 cm was reduced. Thus it was more difficult to determine the field at which the loop became reversible (fig. 6.9). At the low temperatures, $B_{irr}^{\tau}(T)$ was easier to determine as the magnitude of the hysteresis in the loop was large compared to the noise. The errors for the VSM $B_{irr}^{M\to 0}(T)$ at 4.2 K were due to the oscillations in the data (figs 6.6 – 6.7), which made it difficult to determine the exact field at which the average magnetisation was zero. Hence the error at 4.2 K for the torque data and the VSM data in determining the reduced field at the max volume pinning force was ± 0.2 T. At 8 K, the error for $B_{irr}^{M\to 0}(T)$ from the VSM was due to the VSM amplifier being on the highest amplification possible. The noise on the data increased on this setting. Thus the error for the reduced field from the torque measurement was smaller than the VSM error. Hence the movement of the max volume pinning force from b_{max} = 0.8 to 0.3 as the temperature increases is a generic result. It also proves that there are two different pinning mechanisms in NbTi wire. These mechanisms have different temperature and reduced field dependence.

For the VSM data, the p & q values also change as the temperature is increased, and the principal pinning mechanism changes. At 4.2 K for the 1 mm length perpendicular field data p = 0.86 & q = 0.93 (table 6.3). Thus the curve shape is $b(1-b)$, which is consistent with the literature[6]. While at 8 K, p = 1.04 & q = 2.18, which differs from the Meignast 8 K values[31]. Meignast showed the curve shape was $b^{1/2}(1-b)^2$ at 8 K, due to the δH_c pinning being the principal mechanism[31]. At 8 K the p & q variables are consistent with the McKinnell high concentration Ti data[23]. McKinnell *et al* determined for 62%Ti the shape of the pinning curve was $b(1-b)^2$, which was due to the δH_c pinning being the principal mechanism, as the high

concentration of Ti increased the α-Ti particles' size[23]. Thus for the data at 8 K, the mechanism was δH_c pinning, as the data have the curve shape $b(1-b)^2$.

6.5.3.4 NbTi wire – variation with applied magnetic field direction

The normalised flux pinning scaling curves were different for the parallel VSM data and perpendicular field VSM data. Küepfer and Matsushita[32] investigated the difference in volume flux pinning force when the NbTi wire long axis was parallel to and perpendicular to the magnetic field. The difference was due to the highly anisotropic pinning centres. Küepfer expected that for the field parallel to the long axis, the flux motion would be along the cell wall, which would mean the volume flux pinning force with the field parallel to the long axis would be less than the perpendicular field volume flux pinning force. Küepfer *et al* found the volume flux pinning force was larger for the field parallel to the long axis, which is consistent with the volume flux pinning forces determined in this work. From Küepfer data, at 4.2 K the field at the maximum volume pinning force taken from the paper, were 5 T for the parallel field data and 6.25 T for the perpendicular field data. Both field directions had the same $B_{c2}(T)$, hence the max force occurred at b_{max} = 0.47 for the parallel field data and b_{max} = 0.58 for the perpendicular field data. From this chapter the max volume pinning force, at 4.2 K was at 4 T for all the samples with the field parallel to the long axis, and at 5 T for all the samples, with the long axis perpendicular to the field excluding the 1 mm length sample. From fig. 6.27, the max volume pinning force peak for the field parallel to the long axis was at $b_{max} = 0.45 \pm 0.03$ compared to $b_{max} = 0.54 \pm 0.03$ for the field perpendicular to the long axis. These reduced fields are in good agreement with Küepfer's[32]. The pinning force mechanisms for each field direction were independent of the length of the sample.

At 4.2 K, the variables p & q were different for the two field directions. For the perpendicular field direction, p = 0.86 and q = 0.93, while for the parallel field direction p =1.16 and q = 1.5. The perpendicular data has the classic $b(1-b)$ shape[6] that occurs at low temperatures in NbTi. While the parallel data has the shape $b(1-b)^{3/2}$, due to the anisotropy of the pinning centres in the NbTi wire.

The exponent n is the temperature dependence parameter of the flux pinning scaling law. Due to the change in the principal pinning mechanism with temperature, there were two distinct gradients seen for the torque data and the VSM parallel data (fig.

6.33). For NbTi wire the variable n in the literature varies from 1.7[6, 31] to 2.5[5]. The measured n values for both field directions below 6 K lie within these limits (table 6.3). The n values for the data below 6 K were higher than the values for the data above 6 K. For the 2 mm and 3.83 mm length samples, the data taken with the field parallel to the long-axis, the 4.2 K data points lie about the 1 mm length parallel data line. Similarly the perpendicular 4.2 K for both samples data are on the 1 mm length perpendicular line. At 8 K, the 2 mm, 3.83 mm and 5 mm length samples parallel field data points and the perpendicular field data points lay close to their respective n line, which suggests the n values were constant for the different sample lengths in each field direction.

6.5.4 Upper critical field, $B_{c2}(0)$

From fig. 6.36, the upper critical field of $PbMo_6S_8$ was determined using WHH theory[8]. The torque data were in good agreement with the resistivity and VSM data (table 6.4). Thus the upper critical field of the 1 mm length $PbMo_6S_8$ sample measured by the torque magnetometer was $B_{c2}^{\tau}(0) = 51$ T.

From fig. 6.35, the upper critical field of NbTi wire was determined, for the different experimental techniques. The torque data were in good agreement with the resistivity and VSM data. From the resistivity measurement, the NbTi wire upper critical field $B_{c2}(0)$ is 15 T, which is in good agreement with data in the literature[16, 33]. From the literature, the lowest temperature that $B_{c2}(T)$ was measured at was 2 K[33, 14]. Using the Heliox probe, the resistivity $B_{c2}^{0.5\rho_N}(T)$ at 300 mK was 14.8 T and the 1 mm length torque data $B_{irr}^{\tau}(T)$ was 13.6 T. These experiments have confirmed that $B_{c2}(0)$ for NbTi wire is 15 T, rather than the GLAG theory value of 18 T[16].

The field-gradient torque magnetometer is a reliable method of determining the upper critical field of isotropic superconductors.

Friend measured the $B_{c2}(T)$ dependence on magnetic field direction to the long axis from resistivity measurements[4]. He found the ratio of the $B_{c2}^{0.5\rho_N}(T)$, for the field parallel to the long axis by the field perpendicular to the long axis was a constant value of 1.1, between 2 K and 7 K, and then increased as T_c was approached. From the VSM data the ratio of $B_{irr}^{M\to 0}(T)$ at 4.2 K is 1 for the 1 mm length, 2 mm length and 3.83 mm length samples, due to the oscillations in the moment data introducing

errors into determining $B_{irr}^{M\to 0}(T)$. At 6 K, for the 1 mm length sample the ratio is 1.17, which is consistent with Friend's measurements. Similarly at 8 K, the ratio has increased, for the 1 mm length sample the ratio is 1.23, compared to 1.64 for the 3.83 mm length sample. The reason for this anisotropy in the $B_{irr}^{M\to 0}(T)$ is again due to the microstructure of the NbTi wire, having elongated α-Ti precipitates along the long axis of the wire.

6.6 Conclusion

The field-gradient torque magnetometer was used to determine the critical current density at 300 mK, 5 T, for $PbMo_6S_8$ $J_c^{\tau} = 2.98 \times 10^8$ Am^{-2} and for NbTi wire $J_c^{\tau} = 8.34 \times 10^8$ Am^{-2}.

The upper critical field ($B_{c2}(0)$) of NbTi wire is 15 T, which was determined from resistivity measurements from 300 mK up to T_c and in fields up to 15 T. The field-gradient torque magnetometer was also used to determine the upper critical field. For NbTi wire $B_{irr}^{\tau}(T)$is 13.8 T which agrees with the VSM $B_{irr}^{M\to 0}(T)$ = 13.4 T. Similarly for $PbMo_6S_8$ $B_{c2}^{\tau}(0)$ is 51 T, which is slightly higher than with the VSM $B_{c2}^{M\to 0}(0) = 45$ T.

The irreversibility fields (B_{irr}) of $PbMo_6S_8$ were determined from the VSM and torque magnetometer Kramer plots. At temperatures above 6 K, the VSM ac-field reduced the 1 mm length sample's B_{irr} by 4 T in comparison to the VSM 4 mm length sample and the 1 mm length torque data value of 18 T. The B_{irr} of $PbMo_6S_8$ at 300 mK is 28.8 T. This is a third smaller than the $B_{c2}^{\tau}(0)$ measured, thus $PbMo_6S_8$ has a large reversible magnetisation region.

From the VSM data, the critical current densities of the 1 mm length $PbMo_6S_8$ sample, for both field directions, had different field dependencies compared to the 4 mm length sample. Similarly the 1 mm length $Pb_{0.75}Eu_{0.25}Mo_6S_8$ sample had a different field dependence to the 4 mm length sample. This was due to the ac-field associated with the VSM completely penetrating the 1 mm length samples at lower fields than the 4 mm length samples. At 4.2 K the magnitude of critical current density of the VSM 1 mm length $PbMo_6S_8$ sample measured with the field perpendicular to the long axis, was 70 % of the magnitude of the critical current

density for the field parallel to the long axis. The critical current density of $Pb_{0.75}Eu_{0.25}Mo_6S_8$ was a factor 5 lower than $PbMo_6S_8$.

The maximum volume pinning force for the VSM $PbMo_6S_8$ 4 mm length and 1 mm length samples and the torque 1 mm length sample were at $b_{max} \approx 0.2$, which is consistent with pinning at the grain boundaries. As the reduced field at the max volume pinning force for the VSM 1 mm length sample for both field directions was 0.2, the grain boundaries in the sample are isotropic. The VSM 4 mm length and 1 mm length samples p & q values were in agreement with each other. The values were $p = 0.57$ and $q = 2.15$, which are slightly higher than the literature values. The torque magnetometry values were $p = 0.55$ & $q = 1.42$. For both magnetometer measurements, the n values were in the range 1.75 to 2.9. While for $Pb_{0.75}Eu_{0.25}Mo_6S_8$, $p = 0.56$, $q = 2.08$ and $n = 2.75$, hence the pinning for both materials was at the grain boundaries.

From the VSM measurements, the critical current density of NbTi wire decreased, as the length of wire samples decreased. At 4.2K, 5T, for the field applied perpendicular to the long axis, the 1 mm length NbTi wire critical current density was 70 % the 5 mm length wire J_c. The critical current density field dependence and magnitude depended on the direction of the field to the long axis of the wire. At 4.2 K, 5 T, the magnitude of the perpendicular critical current density was 45 % of the parallel J_c. The difference in J_c was due to the anisotropic pinning centres in the NbTi wire.

For NbTi wire, the normalised flux pinning force curves were temperature dependent, due to the two pinning mechanisms in NbTi wire having different temperature dependencies. They are observed as a change in the reduced field at the max volume pinning force. At 300 mK, the mechanism is $\delta\kappa$ pinning, as the max force is at $b_{max} = 0.84$, while at 4.2 K, both mechanisms contribute to the flux pinning, so the max force is at $b_{max} = 0.5$. At 8 K, δH_c pinning is the principal mechanism, so the max force is at $b_{max} = 0.3$. The change in the reduced field at the max volume pinning force, as a function of temperature is observed in the torque magnetometer data. The data confirms that the $\delta\kappa$ pinning is the principal pinning mechanism for temperatures below 4.2 K. From the VSM data, the movement of the max force from $b_{max} = 0.54$ at 4.2 K to $b_{max} = 0.3$ at 8 K is observed in the 2 mm and 3.83 mm length samples' data.

For NbTi wire, the flux pinning force was also dependent on the direction of the magnetic field to the long axis of the wire. For the 2 mm length wire with the field perpendicular to the long axis the max volume pinning force was at $b_{max} = 0.54$, while for the field parallel the max force was at $b_{max} = 0.45$. This change in reduced field is due to the anisotropy of the pinning centres in the NbTi wire. For each field direction to the long axis, the flux pinning force was independent of the sample length.

References for Chapter 6

1 N. A. Morley, N. R. Leigh, H. Niu, et al., IEEE Transactions on Applied Superconductor **11**, 3599 (2001).

2 C. P. Bean, Reviews of Modern Physics **36**, 31 (1964).

3 E. J. Kramer, Journal of Applied Physics **44**, 1360 (1972).

4 C. M. Friend, "Transport critical current density measurements on high and low temperature superconductors in magnetic fields up to 15 T" *Dept. of Physics,* University of Durham, (1994).

5 W. A. Fietz and W. W. Webb, Physical Review **178**, 657 (1969).

6 R. G. Hampshire and M. T. Taylor, Journal of physics F: Metal Physics **2**, 89 (1971).

7 A. Gupta, M. Decroux, P. Selvam, et al., Physica C **234**, 219 (1994).

8 N. R. Werthamer, E. Helfand, and P. C. Hohenberg, Physical Review **147**, 295 (1966).

9 D. N. Zheng, H. D. Ramsbottom, and D. P. Hampshire, Physical Review B **52**, 12931 (1995).

10 H. D. Ramsbottom and D. P. Hampshire, Physica C **274**, 295 (1997).

11 H. Yamasaki, M. Umeda, and S. Kosaka, Journal of Applied Physics **72**, 1180 (1992).

12 M. Decroux, P. Selvam, J. Cors, et al., IEEE Transactions on Applied Superconductivity **3**, 1502 (1993).

13 N. Cheggour, M. Decroux, O. Fischer, et al., Journal of Applied Physics **84**, 2181 (1998).

14 K. F. Hwang and D. C. Larbalestier, IEEE Trans. Mag. **15**, 400 (1979).

15 I. J. Daniel and D. P. Hampshire, Physical Review B **61** (2000).

16 D. C. Larbalestier, Advances in Cryogenic Engineering **26**, 10 (1980).

17 P. Selvam, D. Cattani, J. Cors, et al., Journal of Applied Physics **72**, 4232 (1992).

18 D. Cattani, J. Cors, M. Decroux, et al., Physica B **165 & 166**, 1409 (1990).

19 L. A. Bonney, T. C. Willis, and D. C. Larbalestier, Journal of Applied Physics **77**, 6377 (1995).

20 D. Dew-Hughes, Philosophical Magazine B **55**, 459 (1987).

21 R. Wordenweber, Rep. Prog. Phys. **62**, 187 (1998).

[22] E. W. Collings, *Applied superconductivity, Metallurgy, and physics of titanium alloys* (Plenum, 1986).

[23] J. C. McKinnell, P. J. Lee, and D. C. Larbalestier, IEEE Transactions on Magnetics **25**, 1930 (1989).

[24] D. C. Larbalestier and A. W. West, Acta Metallurgica **32**, 1871 (1984).

[25] D. C. Larbalestier, IEEE Transactions on Magnetics **mag-21**, 257 (1985).

[26] T. Matsushita and H. Kupfer, Journal of Applied Physics **63**, 5048 (1988).

[27] K.-P. Jungst, IEEE transactions on Magnetics **11**, 340 (1975).

[28] M. P. Mathur, M. S. Walker, D. W. Deis, et al., Journal of Applied Physics **43**, 3831 (1972).

[29] D. Dew-Hughes, Philos Mag **30**, 293 (1974).

[30] D. N. Zheng, S. Ali, H. A. Hamid, et al., Physica C: Superconductivity **291**, 49 (1997).

[31] C. Meingast and D. C. Larbalestier, Journal of Applied Physics **66**, 5971 (1989).

[32] H. Kuepfer and T. Matsushita, Journal of Applied Physics **63**, 5060 (1988).

[33] C. Meingast, P. J. Lee, and D. C. Larbalestier, Journal of Applied Physics **66**, 5962 (1989).

Chapter 7

Comparison between CuBe and Ti alloys magnetic susceptibility

7.1 Introduction

This chapter reviews the magnetic susceptibility measurements of titanium and copper-beryllium (section 7.2). It is an independent piece of work, which is unrelated to the previous three chapters. The mass susceptibility temperature dependence of two titanium alloys and copper-beryllium were measured (section 7.3, 7.4 & 7.5). The difference in mass susceptibility is discussed with relation to the change in absolute magnitude from room temperature to 5 K (section 7.6).

Titanium, titanium alloys and copper-beryllium are some of the strongest metals available. Titanium is used in the aerospace industry and for medical application. This is because it is strong and lightweight. Copper-beryllium is used for springs and resistance welding electrodes. It has high strength and high conductivity. Both metals are corrosion resistant. Cryogenic magnetic measurements involving high-pressures[1, 2] or strain[3] require high strength metals with small magnetic susceptibility. The Durham group has experience in using CuBe. In this chapter in order to investigate whether other materials are more suitable, the susceptibilities as a function of temperature of titanium and titanium alloys were measured and compared with the CuBe susceptibility.

7.2 Review of magnetic susceptibility in the literature

Collings measured the mass susceptibility of titanium as a function of temperature[4]. Titanium is a paramagnetic metal. At 300 K the mass susceptibility is 3.99×10^{-8} m^3kg^{-1}. At 100 K the mass susceptibility is 3.71×10^{-8} m^3kg^{-1}. This is a change of 2.89×10^{-9} m^3kg^{-1}, over 200 K. At temperatures from 100 K down to 4.2 K, the susceptibility is almost constant with temperature[5]. Adding impurities changes the strength of the alloy. It also changes the magnetic behaviour. The impurities added into titanium form either α, α/β or β Ti alloys. Copper-beryllium is diamagnetic at 300 K, with a susceptibility of -2×10^{-10} m^3kg^{-1}[2]. At 4.2 K it is paramagnetic[6] with a susceptibility of 4×10^{-9} m^3kg^{-1}[2]. This is a change of 4.02×10^{-9} m^3kg^{-1} over 300 K.

Material	Impurities percentage	Alloy type	Density (10^3 kgm^{-3})	Sample volume (10^{-8} m^3)	Tensile strength (MPa)
Pure Titanium	-	α	4.51	3.22 x 3.05 x 0.73	270 – 350
Ti – 64	Al–6%, V–4%	α/β	4.42	3.04 x 3.09 x 0.74	960 – 1270
Ti – 550	Al-4%, Mo-4%, Sn-2%, Si-0.5%	α/β	4.60	3.30 x 3.25 x 0.85	1100 – 1280
Ti – 21S	Mo-15%, Nb-3%, Al-3%, Si-0.2%	β	-	3.27 x 3.30 x 0.72	-
Ti – 75	O < 1%	α	4.51	3.29 x 3.27 x 0.75	570 – 730
Cu – Be	~ 1 % Ni or Co	–	8.25	3.38 x 3.46 x 0.87	500 - 1300

Table 7.1. Summary of the titanium alloys and copper-beryllium investigated in this chapter

The change in magnetism is because magnetic ions (either nickel or cobalt) are doped into the alloy. They are added as precipitation-hardening impurities.

7.3 Experimental procedure and samples measured

The samples measured were copper-beryllium, pure titanium, and the titanium alloys Ti-64, Ti-550, Ti-75, and Ti-21S. The titanium and titanium alloys were from TIMETAL, who specialise in titanium. The mechanical properties were taken from the TIMETAL technical specification. The copper-beryllium was from Brush-Wellman. The copper-beryllium mechanical properties were taken from the Goodfellows Ltd website.

From the TIMETAL documentation the strength of titanium improves by adding impurities (table 7.1). The magnetic moments were measured on the VSM at Birmingham. The temperature dependent susceptibilities of Ti–64, Ti–550 and CuBe were measured. The susceptibilities of the other three titanium alloys were measured,

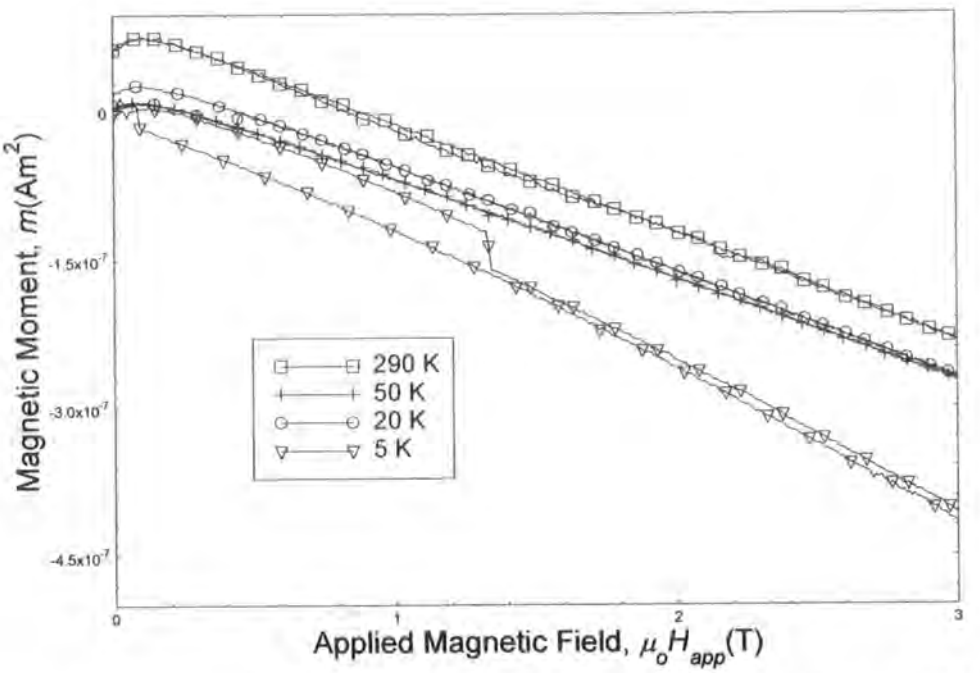

Figure 7.1. Magnetic moment as a function of applied magnetic field and temperature, for the background components of the VSM.

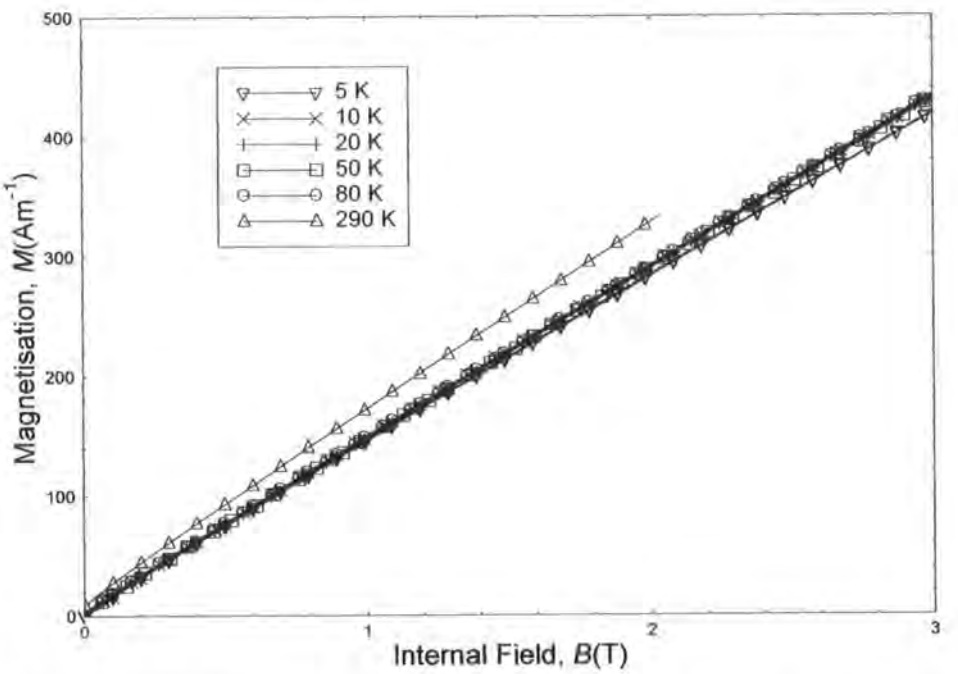

Figure 7.2. Magnetisation of Ti – 550 alloy as a function of internal magnetic field and temperature.

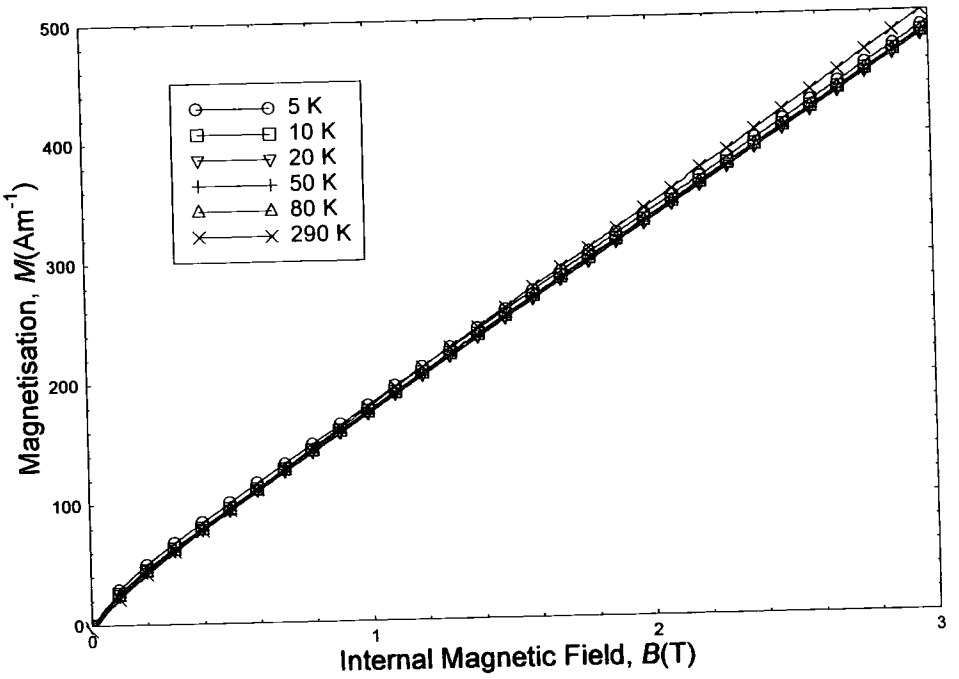

Figure 7.3. Magnetisation of Ti – 64 alloy as a function of internal magnetic field and temperature.

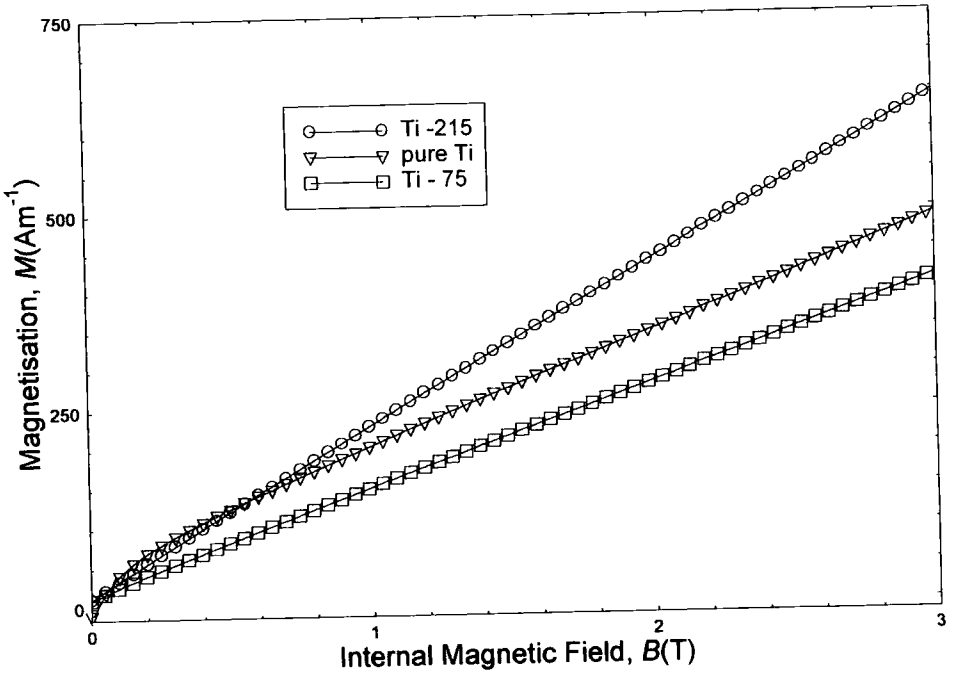

Figure 7.4. Magnetisation as a function of internal magnetic field for pure Ti, Ti - 75 alloy and Ti - 21S alloy at 290 K.

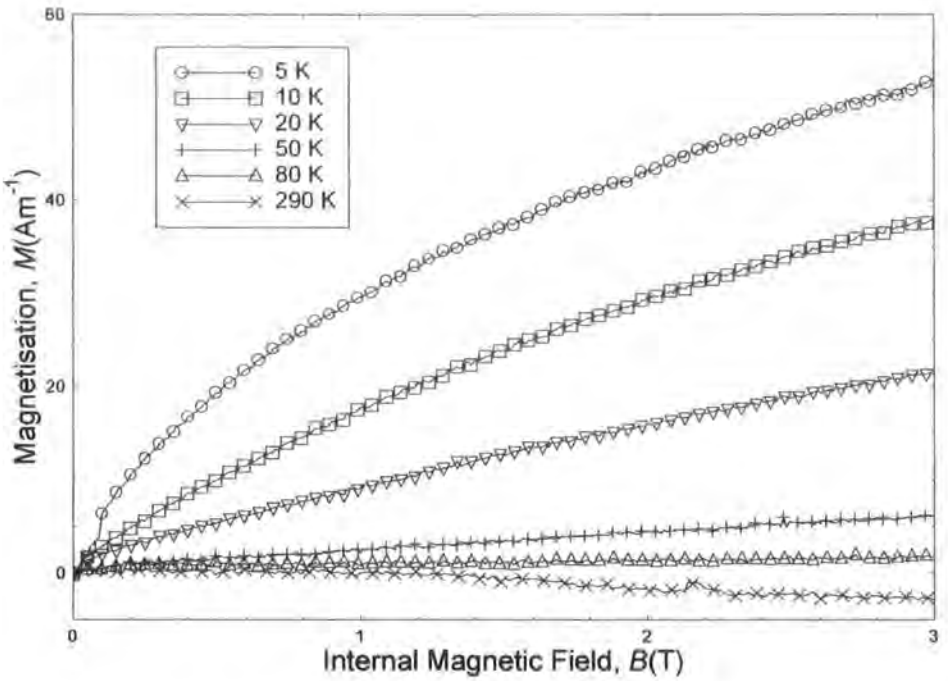

Figure 7.5. Magnetisation of Copper-beryllium as a function of internal magnetic field and temperature.

at 290 K. At each temperature, the magnetic field was swept to 3 T, and back to zero. The magnetic moment was measured at different sweep rates, at 290 K. The field sweep rate used to obtain all data shown was 100 Oemin^{-1}. This was the highest sweep rate, which showed no Eddy current heating. The samples were attached to a clear plastic straw, using double-sided sticky tape, with PTFE tape wrapped three times around. The straw was attached to the bottom of the VSM rod.

7.4 Results

The magnetic moments were measured on the highest sensitivity of the amplifier. They were of similar magnitude to the background. The magnetic moment from the background was due to the plastic straw, with the double-sided sticky tape and PTFE. From fig. 7.1 this magnetic moment changes with temperature. The background magnetic moment was subtracted away from the samples' magnetic moments. The magnetization was calculated by dividing the moment by the volume (c.f. eqn 3.18).

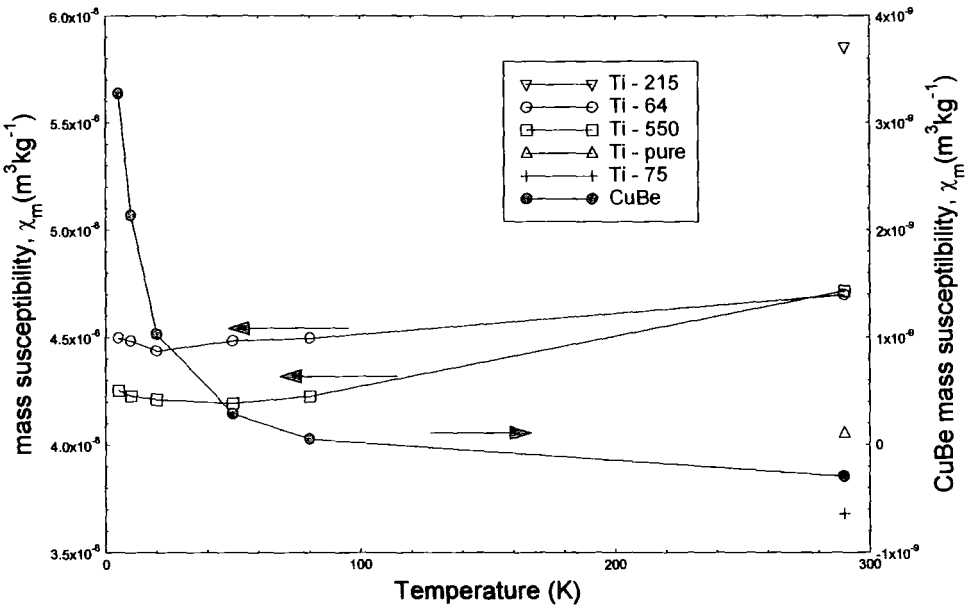

Figure 7.6. The mass susceptibility of the titanium alloys (open shapes) and CuBe (closed shapes) as a function of magnetic field and temperature.

The demagnetisation factor for a flat disc was used to calculate the internal field of the samples (cf. section 3.8.2). The factors are given by:

$$N_{\parallel} = 0.73 \;\&\; N_{\perp} = 0.13 \tag{7.1}$$

From figs. 7.2 & 7.3 the magnetisation of the titanium alloys is almost constant with temperature. The magnetisation for each of titanium alloys is dependent on the impurities added. This is seen in fig. 7.4, where the magnetisation of the two alloys and pure titanium differ with field. From fig. 7.5 the magnetisation of copper-beryllium changes from paramagnetic to diamagnetic over the temperature range. The magnetisation of copper-beryllium is a factor 10 smaller than the titanium, at 5 K.

7.5 Analysis

The mass susceptibilities for the samples are determined from[7]:

$$\chi_m = \frac{\chi_{vol}}{\rho} = \frac{1}{\rho}\frac{\mu_o M}{B} \tag{7.2}$$

where ρ is the density.

At temperatures below 50 K, CuBe has a positive susceptibility (fig. 7.5). A Brillouin function (eqn 3.2) has been fitted to the data at 5 & 10 K. The variables for the magnetic ions are $J = 4.38$, $g_J = 1.27$ and $N = 1.46 \times 10^{20}$ m^{-3}.

	Mass susceptibility 290 K (m^3kg^{-1})	Mass susceptibility 5 K (m^3kg^{-1})	Tensile strength (MPa)	Elongation (%)	Young's Modulus (GPa)
CuBe	-2.88×10^{-10}	3.27×10^{-9}	500 - 1300	< 50	120 - 160
Pure Ti	4.05×10^{-8}	-	230 - 460	25	115
Ti – 64 alloy	4.7×10^{-8}	4.5×10^{-8}	960 - 1270	8	105 - 120
Ti – 550 alloy	4.7×10^{-8}	4.25×10^{-8}	1100 - 1280	9	110 - 130
Ti – 75 alloy	3.68×10^{-8}	-	570 - 740	15	105 - 120
Ti – 215 alloy	5.86×10^{-8}	-	-	-	-

Table 7.2. The magnetic susceptibilities and mechanical properties of CuBe, Ti and Ti alloys. The tensile strength, elongation, and Young's modulus for the Ti alloys were taken from the TIMETAL document. CuBe values were taken from the Goodfellows Ltd web page.

This suggests that the impurity ion is Co^{2+}, where $J = 4.5$ and $g_J = 1.33$[7]. At temperatures below 50 K, the mass susceptibility (fig 7.6) of CuBe has been fitted to Curie's law (eqn 3.4). This gives the Curie constant to be $C = 1.744 \times 10^{-8}$ Km^3kg^{-1}. This is in agreement with the Curie constant calculated from the Brillouin function, which gives 1.75×10^{-8} Km^3kg^{-1}.

7.6 Discussion

Copper-beryllium contains magnetic ions (either Ni or Co), to help stabilize it. At 290 K, the susceptibility of CuBe is negative, as the magnetic ions have no long-range order. At low temperatures, the susceptibility of CuBe is positive[6], as the magnetic ions interact. This changes the mass susceptibility by two orders of magnitude. From literature[2], the mass susceptibility at 300 K is -2×10^{-10} m^3kg^{-1} compared with our measurement of -2.88×10^{-10} m^3kg^{-1} (table 7.2). The mass susceptibilities are in

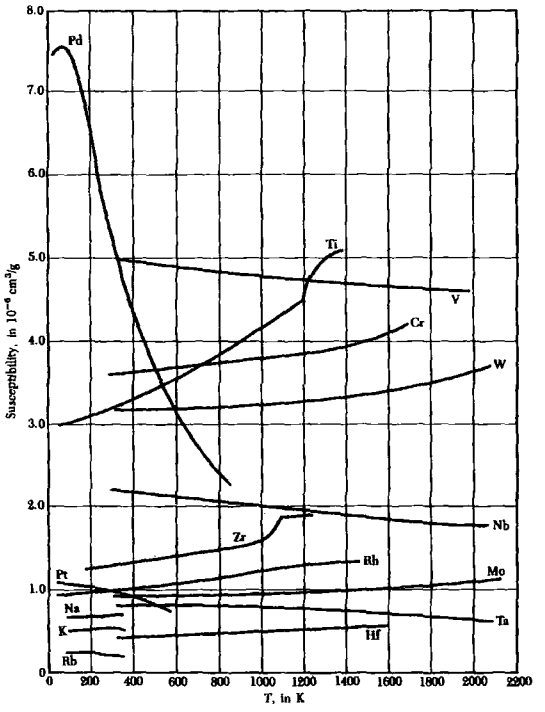

Figure 7.7. The mass susceptibility for various elements, as a function of temperature. Taken from Kittel[7].

good agreement. The small difference is due to the slight difference in the percentages of impurities.

Titanium metal is paramagnetic. The measured mass susceptibility of pure Ti is 4.05 x 10^{-8} m^3kg^{-1} (fig. 7.6). The value in the literature[4] is 3.99 x 10^{-8} m^3kg^{-1}. The titanium alloys are also paramagnetic at all temperatures. The ions added to form the alloys give different temperature dependant susceptibility. The alloys do not obey Curies' law.

From fig. 7.7, the temperature dependent susceptibilities of some elements are plotted. The susceptibility of titanium[4] decreases with temperature whereas the susceptibility of vanadium and aluminium[8] increases with temperature. In fig. 7.6 the susceptibility for Ti–64 (which contains Al and V) decreases with temperature from 300 K to 20 K, and then increases from 20 K to 5 K. This is due to the competition between the V susceptibility, the Ti susceptibility and the Al susceptibility.

Both Ti and CuBe are used for their strength in cryogenic measurements. They are often used in high magnetic fields, therefore the magnetic susceptibility is important.

Their susceptibility has to be as small as possible. From table 7.2, CuBe and the Ti alloys are both paramagnetic at 5 K. The mass susceptibility of CuBe is a factor 10 smaller than the Ti alloys. At 290 K, CuBe has a negative susceptibility, and all the Ti alloys are paramagnetic. The magnitude of the mass susceptibility of CuBe is a factor 100 smaller than all the Ti alloys measured. For magnetic measurements taken at a single temperature eg 4.2 K, 300 K, copper-beryllium has the lowest susceptibility so should be used.

For magnetic experiments, over a temperature range (5 K – 20 K), the absolute change in susceptibility is important. Ideally the susceptibility is constant. The change in susceptibility for CuBe between 5 K and 20 K is 2.261×10^{-9} m^3kg^{-1}, compared with 5.4×10^{-10} m^3kg^{-1} for Ti–64 and 4×10^{-10} m^3kg^{-1} for Ti–550. Thus the Ti alloys susceptibilities are almost constant with temperature. For variable temperature measurements the Ti alloys should be used.

7.7 Conclusions

At 5 K, the mass susceptibility of copper-beryllium is a factor 10 smaller than the titanium alloys. However between 5 K and 20 K, the change in mass susceptibility for CuBe is a factor 5 larger than the Ti alloys. Hence CuBe has a smaller mass susceptibility, but the Ti alloys should be used for variable temperature magnetic measurements.

References for chapter 7

1 K. Koyama, S. Hane, K. Kamishima, *et al.*, Review of Scientific Instruments **69**, 3009 (1998).

2 K. Kamishima, M. Hagiwara, and H. Yoshida, Review of Scientific Instruments **72**, 1472 (2001).

3 N. Cheggour and D. P. Hampshire, Review of Scientific Instruments **71**, 4512 (2000).

4 E. W. Collings and J. C. Ho, Physical Review B **2**, 235 (1970).

5 I. Bakonyi, H. Ebert, and A. I. Liechtenstein, Physical Review B **48**, 7841 (1993).

6 Z. Xia, J. Bray-Ali, J. Zhang, *et al.*, Journal of Low Temperature Physics **126**, 655 (2002).

7 C. Kittel, *Introduction to solid state physics* (John Wiley & Sons, 1996).

8 J. R. Cooper and M. Miljak, Journal of Physics F: Metal Physics **6**, 2151 (1976).

Chapter 8

Conclusions & Future Work

8.1 Conclusions

A field-gradient torque magnetometer has been constructed which can measure the magnetic moment of isotropic superconductors in the temperature range 300 mK to 20 K, in magnetic fields up to 15 T. The probe uses a QD silicon piezoresistive torque chip to measure the moment in magnetic field gradients. The torque magnetometer data is used to determine the critical current density and upper critical field $B_{c2}(0)$.

For NbTi wire and $PbMo_6S_8$, the critical current densities were determined from 300 mK to T_c in fields up to 15 T. For the same $PbMo_6S_8$ sample, the torque magnetometer's critical current densities were consistent with the vibrating sample magnetometer's (VSM) critical current densities.

The field-gradient torque magnetometer data was also used to determine the upper critical field. $B^{r}_{c2}(T)$ was determined from voltage vs. field sweep loops measured at the field centre, for temperatures close to T_c. For $PbMo_6S_8$ $B^{r}_{c2}(0)$ = 51 T which is slightly higher than the VSM $B^{M\to 0}_{c2}(0)$ = 45 T. For NbTi wire at 300 mK the resistivity $B^{0.5\rho_N}_{c2}(T)$ = 14.8 T, thus the $B^{0.5\rho_N}_{c2}(0)$ is 15 T. The torque magnetometer $B^{r}_{c2}(0)$ = 13.8 T, which is slightly lower than the resistivity value.

The temperature dependence of the different pinning mechanisms in NbTi wire were observed in the torque magnetometer normalised flux pinning force data. The peak of the normalised pinning force moved from b_{max} = 0.8 at 300 mK to b_{max} = 0.3 at 8 K. This means at low temperatures (below 2 K), $\delta\kappa$ pinning is dominant, and at temperatures close to T_c, δH_c pinning is dominant. This result was confirmed by the VSM data, where the b_{max} = 0.55 at 4.2 K and moves to b_{max} = 0.3 at 8 K.

From the VSM data, the irreversibility fields (B_{irr}) of the 4 mm length $PbMo_6S_8$ sample and the 1 mm length $PbMo_6S_8$ sample were different values due to the ac-field associated with the VSM. At 6 K, for the 1 mm length sample measured on the torque magnetometer B_{irr} = 18 T, which agreed with the VSM measured value for the 4 mm length sample B_{irr} = 18.7 T rather than the 1 mm length sample B_{irr} = 14 T.

The change in the superconducting parameters of the Chevrel phase superconductor $PbMo_6S_8$ with the addition of Eu ions have been investigated. The superconductor $Pb_{0.75}Eu_{0.25}Mo_6S_8$, the magnetisation and specific heat data had paramagnetic and superconducting contributions. The addition of Eu ions into $PbMo_6S_8$ decreased the critical temperature from 15.16 K to 12.6 K, and decreased the critical current density from 2.23 x 10^7 Am^{-2} to 1.18 x 10^8 Am^{-2}. The Sommerfeld constant (γ) was reduced by a factor 2, to 276 $JK^{-1}m^{-3}$ for $Pb_{0.75}Eu_{0.25}Mo_6S_8$. The upper critical field measured from resistivity measurements $B_{c2}^{0.5\rho_N}(0)$ increased from 51 T to 56 T, while $B_{c2}^{M\to 0}(0)$ measured from magnetisation data decreased from 50 T to 30 T. This difference was due to a distribution of $B_{c2}(T)$ in the $Pb_{0.75}Eu_{0.25}Mo_6S_8$ sample. For $Pb_{0.75}Eu_{0.25}Mo_6S_8$ and $PbMo_6S_8$ the powder samples were used to determine κ over the temperature range 6 K to T_c.

8.2 Future work

From this thesis there are two areas for which future work could be considered. The first area is expanding the different types of samples or superconductors measured by the field-gradient torque magnetometer.

The different types of samples could include single crystals. This is because the QD torque chip platform area is 2 x 2 mm^2, which means small samples (mass < 10 mg) can be measured. Thus it is ideal for materials such as $PbMo_6S_8$ and $DyMo_6S_8$, whose single crystal volume is of order 1 x 0.8 x 0.3 mm^3. The measurement of the critical current density of single crystals is important. There are no grain boundaries in the crystal. Thus only the intragrain flux pinning in the Chevrel phase superconductors will be measured. Other samples, which could be measured include magnetic superconductors such as $DyMo_6S_8$. These materials have critical temperatures below 2 K. As the torque magnetometer's base temperature is 300 mK, the critical current density and upper critical field can be determined. The behaviour of $DyMo_6S_8$ in a magnetic field can also be investigated using the torque magnetometer.

The torque magnetometer could also be used to investigate the critical current densities of anisotropic superconductors. Anisotropic superconductors have only been measured at the field centre using piezoresistive cantilevers, to determine their anisotropy. The critical current densities measured were direction dependent. The field-gradient torque magnetometer provides a method of measuring the critical

current density at different angles to the magnetic field, by measuring the magnetic moment of the superconductors at different field-gradients. This would be useful to observe how the anisotropy affects J_c as a function of angle.

The second area is to improve the field-gradient torque magnetometer. These improvements could include decreasing the base temperature further by using adiabatic demagnetisation. In decreasing the temperature below 250 mK, the behaviour of the superconductors and their critical current density could be observed. For materials such as NbTi wire this could give an increased insight to whether $B_{c2}(0)$ = 15 T, or if it increases rapidly to 18 T as predicted by GLAG theory below 250 mK. It would also be used to determine whether the flux pinning mechanisms in superconductors such as NbTi and $PbMo_6S_8$ changes at very low temperatures, or whether they are consistent for the whole temperature range. The critical current density can also be investigated to determine if it increases linearly at temperatures below 250 mK.

The second improvement would be to improve the thermal linking between the sample and the helium-3 pot. This would reduce the possibility of heating occurring in the sample. It would also improve the base temperature of the sample. One method could be to directly attach a wire to the sample rather than the QD chip. Another method could be to attach a thermometer to the thick outside edge of the QD chip. The thermometer leads would act as the thermal link from the helium-3 pot to the sample. The other advantage would be that the actual temperature of the sample would be known, rather than the temperature of the tufnol platform.

Other improvements could include reducing the backlash of the gears on the rotator platform. Using the grub screw tightened against the lowest gear decreased the backlash, although it was not perfect. Therefore using anti-backlash gears, or an arrangement where the gears are held stationary at the required angle, could be investigated.

Appendix 1. Publications

[1] N. A. Morley, N. R. Leigh, H. Niu, and D. P. Hampshire, "High upper critical field in the Chevrel phase superconductor lead-molybdenum-sulphide doped with europium," *IEEE transactions on applied superconductor*, vol. 11, pp. 3599 - 3602, 2001.

[2] H. Niu, N. A. Morley, and D. P. Hampshire, "Chevrel phase $(Pb_{1-x}Cu_{1.8x})Mo_8S_6$ with a mixed structure and high critical parameters," *IEEE Trans. Appl. Supercond.*, vol. 11, pp. 3619 -3622, 2001.

[3] K. Osamura, M. Sugano, A. Nyilas, H. S. Shin, H. Weijers, D. P. Hampshire, N. Morley, K. Morley, S. Keys, M. Leghissa, W. Herkert, K. Katagiri, and T. Ogata, "The tensile property of commercial BI2223 tapes: a report on the international round-robin test," *Superconductor science and technology*, vol. 15, pp. 888 - 893, 2002.

Appendix 2. Conferences and Courses

Conferences Attended

April 2003	Queen's University, Belfast	CMMP 2003

- Second prize in the poster competition.

April 2002	Brighton, Sussex	CMMP 2002
January 2002	University of Cambridge	Superconductivity Meeting
December 2000	University of Bristol	CMMP 2000
September 2000	Virginia Beach, Virginia	ASC'2000
April 2000	University of Birmingham	Superconductivity Meeting
December 1999	University of Leicester	CMMP 1999

Courses Attended

2001	Superconductivity Winter School (Cambridge University)
2000	Using Microsoft Excel 97 (Durham University ITS)
2000	Using Microsoft PowerPoint 97 (Durham University ITS)
1999	Endnotes (Durham University ITS)
1999	Low Temperature techniques course (Aston University)
1999	Mechanical workshop course (Durham University)

Appendix 3. Computer Programs

This appendix contains a comprehensive description of the LABview computer programs required to run the torque field-gradient magnetometer, and the Ressus probe. Also included is the Maple VI program used to calculate the best-fit paramagnetic magnetisation.

LABview torque field-gradient magnetometry programs

For the torque magnetometer experiments each have their own front program, which is made up of separate subprograms. These subprograms read and write to the different instruments and carry out analysis. For most of the experiments carried out the instruments are the same and therefore the same subprograms are used for each.

Instruments programs

The following programs are used for the IPS magnet power supply:

Setupd.vi

Sets the power supply up at the beginning of an experiment

SwitchMbc.vi

Switches the superconducting magnet switch on

Setcur.vi

Writes a current value to the power supply

Setfield.vi

Writes the maximum/target magnetic field to the power supply

Readfield.vi

Reads the magnetic field of the magnet from the power supply

Chkspeedsuperbcrot.vi

Reads the magnetic field of the magnet, and checks the ramp rate is correct for that field. Changes ramp rate at set magnetic fields.

The following programs are used for the Oxford Instruments ITC:

Settemprot.vi

Writes the fixed temperature to the ITC. Sets the correct thermometer, for the temperature range.

PIDhe.vi

Writes the PID parameters to the ITC

Buscmd.vi

Is a control vi, which can be used to read or write from the ITC

The following programs are used for the Stanford 850 lockin amplifier:

SetupG.vi

Sets up the lockin amplifier for the experiment including the frequency and the voltage range.

SR850data.vi

Reads the voltage of each of the output channels of the lockin amplifier

The following programs are used for the Keithley voltmeters:

SetupB.vi

Sets the Keithley voltmeters up for the experiment

Keidata.vi

Reads the Keithley voltage – for torque experiment it was the voltage across the RuO_2 thermometer

Keidata3.vi

Reads the Keithley voltage – for torque experiment it was the voltage across the Hall chip

Keidata5.vi

Reads the Keithley voltage – for torque experiment it was the voltage across the 10 Ohms resistor, used to determine the current through the Wheatstone bridge.

The following programs are used for the Lakeshore temperature controller:

Setupf.vi

Sets the Lakeshore up for the experiment

Readtempche.vi

Reads the resistance off the Lakeshore – for the torque experiment the resistance was the cernox thermometer

Analysis programs

The following programs are used in the torque magnetometer experiment to display or analysis the data from the instruments.

Chartres.vi

In real time plots the temperature of the helium-3 pot, and the sample against magnetic field. Also plots the change in voltage across the Wheatstone bridge as a function of magnetic field.

Cx2rot.vi

Converts the resistance across the cernox thermometer into the temperature of the cernox

Calruo2.vi

Converts the resistance of the RuO_2 thermometer into the temperature of the thermometer

Rotdata.vi

This subprogram runs the reading of the different instruments. Every 30 seconds, the program runs the following sub programs and commands:

Ckspeedsuperbcrot.vi – Readfield.vi - reads the temperature of the helium-3 pot – Keidata.vi – Readtempche.vi – Keidata3.vi – Kedata5.vi – SR850data.vi – chartres.vi – writes all the read data to the opened data file.

This is repeated until the target magnetic field is reached.

Zerorotdata.vi

This sub program sets the target magnetic field to 0 T, then runs the Rotdata.vi

Experiment front programs

Each experiment has a front program, which is the program opened from the main LABview menu. This front program is generally made up of a sequence of subprograms, which run one after the other during the experiment process. The front program has a screen where experimental information is typed in.

For the calibration of the torque chips in liquid nitrogen using the copper solenoid magnet, the following program is used:

Chipcal.vi

On the opening screen the maximum current though the magnet and data filename are typed in.

The program runs the following sub programs every 30 seconds (similar to the Rotdata.vi):

Readfield.vi - setcur.vi - Keidata.vi - Readtempche.vi - Keidata3.vi - Keidata5.vi - SR850data.vi - chartres.vi-writes all the read data to file.

This is repeated until the max current is reached.

For the experiments in the superconducting magnet, the general program structure is the same; the only thing, which changes between the liquid helium and vacuum measurements, is the ramp rate of the magnetic field. Thus the front programs for the two experiments are:

In liquid helium the program is: GO3rota.vi

In vacuum the program is: GO3rotc.vi

On the opening screen the number of runs, the target field, the temperatures at which the experiment is being carried out, and the data filename are entered. The sequence the sub programs and commands are carried out is:

Settemprot.vi – PIDhe.vi – Setfield.vi – Rotdata.vi – Zerorotdata.vi

The program is then repeated for the next temperature.

LABview resistivity and ac-susceptibility program

The resistivity and susceptibility experiment is also controlled using LABview programs. As the same instruments are used to measure the temperature and voltages as for the torque magnetometry experiment, the same sub programs are used to read and write to the instruments.

The front program for the Ressus probe in the superconducting magnet is:

GoBC.vi - The program is split into three large sub programs, which are:

Setup.vi

This program set-up all the instruments in the experiment in the following order:

SetupB.vi – SetupC – Setupd – switchmc.vi – setupf.vi – setupG.vi

where setupc.vi set up the EG&G lockin amplifier

GO1.vi

This program asks for the following information: set field, temperature range, temperature ramp rate, number of points, data filename.

GO2BC.vi

This program runs the major part of the experiment, for every field the program sequence is:

PID.vi – Setfield.vi – settempbase.vi – takedata.vi – settempbase.vi

The settempbase.vi writes the start temperature to the ITC. Settemp.vi writes the set point temperature to the ITC. takedata.vi is the subprogram, which reads and writes to the instruments, with the following sequence:

Settemp.vi – Keidata.vi – SR850data.vi – EGGdata.vi – Readtempche.vi – chartres.vi – writes all data to file.

This program repeats this sequence every 30 seconds until the max temperature is reached.

LABview critical current density programs

LABview programs are used to calculate the critical current density of the superconductor from the data. Two different programs are used. The initial data sets have the following columns of data, for a fixed temperature and height z: magnetic field (B), magnetic field gradient at B, corresponding ΔR_{+-} across the loop.

Jccal.vi

Reads the initial data file. For each B, writes the magnetic field gradient and corresponding ΔR_{+-} to a separate data file for that field. The program is repeated for each height.

Gradcal.vi

Reads the jccal.vi data file for each magnetic field. Puts a straight line through the ΔR_{+-} vs. magnetic field gradient points for each file. Writes the magnetic field and corresponding gradient $\left(\frac{d\Delta R_{+-}}{d\frac{dB}{dz}}\right)$ into the final data file.

Maple VI

Maple VI was used to calculate the best-fit paramagnetic magnetisation.

Mag4.mws

Adapted from N. Leigh's' param.mws program, it calculates and determines the magnetisation of a paramagnetic material, as a function of magnetic field and temperature.